ABSTRACT

Title of dissertation: COMPREHENSIVE AEROELASTIC

ANALYSIS OF HELICOPTER ROTOR WITH

TRAILING-EDGE FLAP FOR PRIMARY

CONTROL AND VIBRATION CONTROL

Jinwei Shen, Doctor of Philosophy, 2003

Dissertation directed by: Professor Inderjit Chopra
Department of Aerospace Engineering

A comprehensive aeroelastic analytical model of helicopter rotors with trailing-edge flaps for primary and vibration controls has been developed. The derivation of system equations is based on Hamilton principles, and implemented with finite element method in space and time. The blade element consists of fifteen degrees of freedom representing blade flap, lag, torsional, and axial deformations. Three aerodynamic models of flapped airfoils were implemented in the present analysis, the unsteady Hariharan-Leishman model for trailing-edge flaps without aerodynamic balance, a quasi-steady Theodorsen theory for an aerodynamic balanced trailing-edge flap, and table lookup based on wind tunnel test data. The trailing-edge flap deflections may be modeled as a degree of freedom so that the actuator dynamics can be captured properly. The coupled trim

Report Documentation Page

1. REPORT DATE **2003**	2. REPORT TYPE	3. DATES COVERED **00-00-2003 to 00-00-2003**

4. TITLE AND SUBTITLE **Comprehensive Aeroelastic Analysis of Helicopter Rotor with Trailing-Edge Flap for Primary Control and Vibration Control**	5a. CONTRACT NUMBER
	5b. GRANT NUMBER
	5c. PROGRAM ELEMENT NUMBER
6. AUTHOR(S)	5d. PROJECT NUMBER
	5e. TASK NUMBER
	5f. WORK UNIT NUMBER
7. PERFORMING ORGANIZATION NAME(S) AND ADDRESS(ES) **University of Maryland,Department of Aerospace Engineering,College Park,MD,20742**	8. PERFORMING ORGANIZATION REPORT NUMBER
9. SPONSORING/MONITORING AGENCY NAME(S) AND ADDRESS(ES)	10. SPONSOR/MONITOR'S ACRONYM(S)
	11. SPONSOR/MONITOR'S REPORT NUMBER(S)

12. DISTRIBUTION/AVAILABILITY STATEMENT
Approved for public release; distribution unlimited

13. SUPPLEMENTARY NOTES

14. ABSTRACT

A comprehensive aeroelastic analytical model of helicopter rotors with trailingedge flaps for primary and vibration controls has been developed. The derivation of system equations is based on Hamilton principles, and implemented with finite element method in space and time. The blade element consists of fifteen degrees of freedom representing blade flap, lag, torsional, and axial deformations. Three aerodynamic models of flapped airfoils were implemented in the present analysis, the unsteady Hariharan- Leishman model for trailing-edge flaps without aerodynamic balance, a quasi-steady Theodorsen theory for an aerodynamic balanced trailing-edge flap, and table lookup based on wind tunnel test data. The trailing-edge flap deflections may be modeled as a degree of freedom so that the actuator dynamics can be captured properly. The coupled trim procedures for swashplateless rotor are solved in either wind tunnel trim or free flight condition. A multicyclic controller is also implemented to calculate the flap control inputs for minimization of vibratory rotor hub loads. The coupled blade equations of motion are linearized by using small perturbations about a steady trimmed solution. The aeroelastic stability characteristics of trailing-edge flap rotors is then determined from an eigenanalysis of the homogeneous equations using Floquet method. The correlation studies of a typical bearingless rotor and an ultralight teetering rotor are respectively based on wind tunnel test data and simulations of another comprehensive analysis (CAMRAD II). Overall, good correlations are obtained. Parametric study identifies that the effect of actuator dynamics cannot be neglected, especially for a torsionally soft smart actuator system. Aeroelastic stability characteristics of a trailing-edge flap rotor system are shown to be sensitive to flap aerodynamic and mass balances. Key parameters of trailing-edge flap system for primary rotor control are identified as blade pitch index angle, torsional frequency, flap location, flap length, and overhang length. The swashplateless rotor is shown to achieve better rotor performance and overall more stable than the conventional configuration. Simulations of flaps performing both primary control and active vibration control are carried out, with the conclusion that trailing-edge flaps are capable of trimming the rotor and simultaneously minimizing vibratory rotor hub loads.

15. SUBJECT TERMS

16. SECURITY CLASSIFICATION OF:			17. LIMITATION OF ABSTRACT	18. NUMBER OF PAGES	19a. NAME OF RESPONSIBLE PERSON
a. REPORT **unclassified**	b. ABSTRACT **unclassified**	c. THIS PAGE **unclassified**	**Same as Report (SAR)**	**300**	

procedures for swashplateless rotor are solved in either wind tunnel trim or free flight condition. A multicyclic controller is also implemented to calculate the flap control inputs for minimization of vibratory rotor hub loads. The coupled blade equations of motion are linearized by using small perturbations about a steady trimmed solution. The aeroelastic stability characteristics of trailing-edge flap rotors is then determined from an eigenanalysis of the homogeneous equations using Floquet method.

The correlation studies of a typical bearingless rotor and an ultralight teetering rotor are respectively based on wind tunnel test data and simulations of another comprehensive analysis (CAMRAD II). Overall, good correlations are obtained. Parametric study identifies that the effect of actuator dynamics cannot be neglected, especially for a torsionally soft smart actuator system. Aeroelastic stability characteristics of a trailing-edge flap rotor system are shown to be sensitive to flap aerodynamic and mass balances. Key parameters of trailing-edge flap system for primary rotor control are identified as blade pitch index angle, torsional frequency, flap location, flap length, and overhang length. The swashplateless rotor is shown to achieve better rotor performance and overall more stable than the conventional configuration. Simulations of flaps performing both primary control and active vibration control are carried out, with the conclusion that trailing-edge flaps are capable of trimming the rotor and simultaneously minimizing vibratory rotor hub loads.

COMPREHENSIVE AEROELASTIC ANALYSIS OF

HELICOPTER ROTOR WITH TRAILING-EDGE FLAP

FOR PRIMARY CONTROL AND VIBRATION CONTROL

by

Jinwei Shen

Dissertation submitted to the Faculty of the Graduate School of the
University of Maryland, College Park in partial fulfillment
of the requirements for the degree of
Doctor of Philosophy
2003

Advisory Committee:

> Professor Inderjit Chopra, Chairman/Advisor
> Associate Professor James Baeder
> Professor Roberto Celi
> Professor J. Gordon Leishman
> Associate Professor Tobias von Petersdorff, Dean's Representative

ACKNOWLEDGMENTS

and Ron.

Above all, I would like to express my gratitude to my wife, Hui (卉), for her love and patience (as well as drawing technical sketches and typesetting this manuscript) during this research work. I offer thanks to my parents for their unceasing love; to my parents-in-law, grandparents, and brother Jinhui for their encouragement and support. Last but not least, I thank my daughter Maggie (斯言) for her love and being such a good kid.

TABLE OF CONTENTS

Bibliography   256

LIST OF FIGURES

xv

LIST OF TABLES

Nomenclature

C_D Drag

C_{FF} Flap damping

C_{FR} Flap-blade damping vector

C_F Trailing-edge flap force

C_N Normal force

C_Q Rotor torque coefficient

C_{RF} Blade-flap damping vector

C_{RR} Blade damping matrix

C_S Leading-edge suction force

C_T Rotor thrust coefficient

C_W Gross weight coefficient

C_d Sectional drag coefficient

C_h Sectional flap hinge moment coefficient

C_l Sectional lift coefficient

C_{lf} Sectional flap hinge lift coefficient

C_m Sectional pitch moment coefficient

FM Figure of merit

F_x Longitudinal hub force

F_y Lateral hub force

F_z Vertical hub force

H Flap hinge moment (positive flap down)

I_f Flap second mass moment of inertia about flap hinge, $\int \int {y_f}^2 \, dm$

J Scalar nondimensional vibration objective function

K_{FF} Flap stiffness

K_{FR} Flap-blade stiffness vector

K_{RF} Blade-flap stiffness vector

K_{RR} Blade stiffness matrix

M Mach number

M_{FF} Flap mass

M_{FR} Flap-blade mass vector

M_{RF} Blade-flap mass vector

M_{RR} Blade mass matrix

M_h Trailing-edge flap hinge moment

M_x Roll hub moment

M_y Pitch hub moment

M_z Yaw hub moment

N_b Number of rotor blades

P_f Trailing-edge flap actuation power

Q_F Trailing-edge flap deflection

Q_R Modal blade displacement vector

R Rotor radius

S_f Flap first mass moment of inertia about flap hinge, $\int \int y_f dm$

T Kinetic energy

$T_{1\sim29}$ Theodorsen flap constants

U Strain energy

U_p Downwash velocity

U_t Air velocity tangential to blade chord

W Virtual work

X N_b/rev longitudinal vibratory hub shear

Y N_b/rev lateral vibratory hub shear

Z N_b/rev vertical vibratory hub shear

ΔL Flap incremental lift (positive up)

ΔM Flap incremental pitching moment (positive airfoil leading-edge up)

$\frac{dC_l}{d\delta}$ Lift increment sensitivity to flap deflection

$\frac{dC_m}{d\delta}$ Moment increment sensitivity to flap deflection

$\frac{f}{A}$ Parasite drag area ratio

a Lift curve slope

c Blade chord

c_a Flap actuator torsional damping

c_b Flap overhang length

c_f Flap chord

c_{cg} Flap CG offset (positive backward)

d Offset of flap hinge from blade elastic axis

e Flap leading edge location aft of midchord, in semichords.

k_a	Flap actuator torsional stiffness
l	Offset of flap hinge from flap leading edge
l_f	Flap length
r_{mid}	Trailing-edge flap middle section location
t	Time
u	Blade elastic axial displacements
v	Blade elastic lag displacements
w	Blade elastic flap displacements
x	Blade spanwise position
α	Angle of attack
β_{1c}	Longitudinal tip-path-plane tilt angle
β_{1s}	Lateral tip-path-plane tilt angle
β_p	Blade precone angle
δ	Trailing-edge flap deflection (positive flap down)
δ_0	Trailing-edge flap collective angle
δ_{1c}	Trailing-edge flap lateral cyclic
δ_{1s}	Trailing-edge flap longitudinal cyclic

δ_a Actuator deflection (positive flap down)

δ_f Flap deflection (positive flap down)

δ_f Trailing-edge flap deflection (positive flap down)

$\overset{\star}{\delta}$ Trailing-edge flap rate

η Leading-edge suction recovery factor

γ Lock number

$\hat{\phi}$ Blade elastic twist

μ Advance ratio

ϕ_{twist} Elastic torsion deflection (positive nose upward)

ψ Azimuth angle

σ Rotor solidity

θ Blade section pitch (positive nose upward)

θ_0 Blade collective pitch

θ_{1c} Blade lateral cyclic pitch

θ_{1s} Blade longitudinal cyclic pitch

θ_{index} Blade indexing angle (positive nose upward)

θ_{root} Blade pitch motion at blade root spring

ξ Blade modal response

ζ Damping ratio

δT   Variation in kinetic energy

δU   Variation in strain energy

δW   Virtual work

Subscripts

$0, 1c, 1s, .., pc, ps, .., \infty$ Harmonics of a sine/cosine Fourier series representation of a periodic function

a   Actuator

b   Blade

f   Trailing-edge flap

CG   Center of gravity

GJ   Torsional stiffness

OtherSymbols

$\mathbf{F}(\ldots)$ Function of $\ldots$

$(..)'$ $\frac{d}{dx}$

$\Delta(.)$ $(.)_n - (.)_{n-1}$, perturbation

$\delta(.)$ Virtual variation

$\overset{\star}{(..)}$ $\frac{d}{d\psi}$

$\overset{\star\star}{(..)}$ $\frac{d^2}{d\psi^2}$

Chapter 1

Introduction

1.1 Problem Statement

Helicopters, with their hover and forward flight flight capabilities, occupy a unique role in man-made flying vehicles. The evolution of helicopter development is a long journey through human history: from the "Chinese top", a spin-flying toy, to the famous sketch of da Vinci [1], to the golden ages of early 20th century full of enthusiastic and talented helicopter pioneers [2, 3]. Its evolution has not stopped, however, many obstacles and challenges are still faced by helicopter designers worldwide.

One of the key challenges faced by modern helicopter designers is vibration suppression. Helicopters are susceptible to excessive vibration because of the unsteady aerodynamic environment at the rotor disk, nonlinear inertial couplings of slender rotating blades, and complex rotor-fuselage interaction effects. The need for vibration control is critical. Small vibration levels will prolong the lifetime of onboard equipments and increase system reliability. Furthermore, it will improve the ride quality of passengers and crew, thus increasing the public acceptance of helicopters for public transportation. The

1

vibration problem is also associated with fatigue of both rotating and fixed system components due to vibratory loading. This high level of vibration limits the helicopter performance, reduces structural life of dynamic systems, and increases maintenance costs. In addition to the dominant main rotor vibration, helicopters are also subject to vibrations originating from the engine and transmission system, and the aerodynamic interactions among rotor, fuselage, and tail rotors. ADS-27, a set of vibration regulations specified for U.S. Army helicopters, has been proposed to use on civil helicopters as well.

One area where great improvements have been made in helicopter development in recent years is the main rotor hub design. It has been advanced from fully articulated design to the hingeless configuration, and more recently to the state-of-the-art, bearingless design. The main goal is to reduce the weight and part count of main rotor hub, and hence decrease manufacturing and maintenance costs. A less complex rotor hub also significantly reduces the overall drag of the helicopter, thereby increasing the rotor performance and cruise efficiency. Despite these advancements, the main rotor hub remains a complex and aerodynamically inefficient device. Nonetheless, innovations in the flight control system could lead to further simplification of rotor hub. A helicopter flight control system has characteristically been one of the most complex and flight critical components. It generally has numerous exposed linkages, bearings, swashplate, push rods and hinges. These components are maintenance intensive, costly and act as a significant source of drag. The basic swashplate control concept, invented in the 1930s during the early stage of helicopter development, is still routinely installed on nearly all modern helicopters. The weight, drag, cost, and the probability of failure of the mechanical components of swashplate control system provide an impetus to search for alternative forms of main

rotor pitch control.

In summary, the modern advancement in helicopter development is to reduce the cost of manufacturing and maintenance, expand operational speed and range, increase cruise efficiency, improve survivability, advance handling qualities, and minimize vibration and noise. To achieve these goals, innovative configuration concepts must be introduced, active and adaptive control systems must be devised, and design tools must be developed. The present research investigates the feasibility of using plain trailing-edge flaps for primary rotor and vibration controls. The focus of this dissertation is on the development of a comprehensive aeroelastic analysis of trailing-edge flap helicopter rotors. The analytical model provides an important design tool for trailing-edge flap systems.

1.2 Background and Motivation

This dissertation addresses the control effectiveness, actuation requirements, and performance and stability characteristics of a helicopter rotor with plain trailing-edge flaps for primary rotor and vibration control. This section describes the sources of main rotor vibration. It then discusses the history of the helicopter primary control system, and compares the various candidates that would replace the conventional swashplate control system.

1.2.1 Helicopter Main Rotor Vibration

Helicopter rotors are susceptible to high vibrations because flexible rotor blades operating in an unsteady aerodynamic environment results in complex aeroelastic couplings. As

illustrated in Figure 1.1, the main rotor of a helicopter in forward flight, may encounter transonic flow on the advancing blades, dynamic stall on the retreating blades, and radial flow on the front and back blades. The flow field is inherently unsymmetrical with reverse flow occurs on the retreating blades. Inflow distribution is nonuniform, resulting from the complex rotor wake geometry. Blade vortex interactions (BVI) are the main source of helicopter noise, especially during low speed descending flight, as well as being a significant source of main rotor vibrations. Nonetheless, all these factors causing main rotor vibrations may not necessarily manifest through all flight conditions. Some are more dominant at low speeds whereas others are only significant in high speed flight conditions. For a typical helicopter, main rotor vibration is most pronounced in the transition flight regime at advance ratios of approximately 0.1 and in high speed flight at advance ratios above 0.3. In the transition regime from hover to forward flight, factors such as BVI and nonuniform inflow are the dominant ones. This is because blade tip vortices remain close to the blades and collide with passing of following blades at low speed forward flight. This results in high levels of vibration and noise. Furthermore, the wake geometry is also close to the rotor in low speed flight, which results in a complex inflow distribution that also contributes significantly to the main rotor vibration. In high speed flight conditions, vibration is not normally associated with BVI and nonuniform inflow distribution. This is because the blade tip vortices are quickly pushed downstream because of high forward speed and inflow velocity, and as a result, a somewhat less complex inflow distribution is generated by the wake structure behind the rotor. However, transonic flow, dynamic stall, and three-dimensional effects will contribute to the main rotor vibration in high speed flight conditions.

Besides the complex aerodynamic environment, other factors also contribute to main rotor vibration. In steady, level flight, a 1/rev pitch input is required to maintain trimmed condition, which contributes to vibratory components in the blade loading. Furthermore, long and flexible rotor blades excited by the aerodynamic and inertial forces produce complex elastic deformations that involve multiharmonic flapping, lagging, and torsional twists. The blade response, aerodynamic, and inertial loads are closely coupled, resulting in complex aeroelastic effects. Figure 1.2 shows the blade angle of attack distributions in hover and forward flight. It shows a blade airfoil section undergoing very complex angle of attack variations in one rotor revolution, especially in the high speed forward flight condition. It is expected that the resulting aerodynamic force generated is nonlinear and vibratory in nature.

Although the blade loads consist of multiple harmonic components, the hub loads observed in fixed system occur only in harmonics that are integer factors of total number of blades. For example, a rotor with N_b identical blades will only generate hub loads in harmonics of iN_b/rev where i is an arbitrary integer ($i = 0, 1, 2, \ldots \infty$). This is because the other harmonics of blade loads are canceled out by the other blades when transferred to the hub. Among the iN_b/rev hub loads, the N_b/rev is typically the largest. It is well known that the iN_b/rev longitudinal and lateral hub forces as well as hub pitching and rolling moments resulting from $iN_b \pm 1$ blade loads whereas the iN_b/rev vertical hub force result from iN_b blade loads. This discussion, however, is based on the assumption that the rotor consists of identical blades. In practice, dissimilarities between rotor blades may result from the manufacturing process and mechanical faults. A dissimilar rotor will generate large 1/rev hub loads that in turn excite the fuselage at 1/rev.

It is worth to note that vibration predictions of current comprehensive analytical models are less than satisfactory, despite the continuous attention from helicopter researchers. A recent study [4] compares the predictions of state-of-the-art rotorcraft analyses with the Lynx flight test measurement, and shows the accuracy of predicted vibratory loads is less than 50% for all the various analyses. This prediction difficulty is normally attributed to imprecise modeling of the complex aerodynamics. Nonetheless, there is ongoing research [5, 6] addressing this problem, and the accuracy of vibratory load predictions may be improved by consisting coupling of the comprehensive rotorcraft analyses with CFD calculations of aerodynamic loads.

1.2.2 Concepts of Helicopter Vibration Control

As described in previous section, helicopters are inherently prone to high vibration. The vibration level is unacceptably large if left uncontrolled, therefore, most production helicopters have vibration reduction devices installed. The indication of vibration level is measured in terms of acceleration at critical locations on the fuselage, such as the pilot seat, copilot seat, CG, and tail rotor. Helicopter fuselage, being elastic in nature, responds to the excitation of iN_b/rev hub loads described in the previous section. The goal of vibration reduction is to reduce the acceleration levels at key locations. The concept of helicopter vibration control may be thought of as elements in a "long chain running from the tip of blade to the cabin seats" [7]. These approaches may be classified into five categories according to their applications [7]:

1. *Cabin suppressors*: devices mounted on selected locations of fuselage to increase

the fuselage apparent impedance, or control the location of a node of important modes. These are typically passive spring-mass combinations tuned to near N_b/rev [8]. Recent research has been directed towards investigating active cabin suppressors [9, 10]. The drawbacks of this type of device include large weight penalty, the localized nature of vibration reduction, and the poor off-design performance.

2. *Isolators*: devices installed between fuselage and main rotor/transmission assembly to decouple the dynamics of the main rotor from the fuselage, and reduce the amplitude of fuselage response to a given main rotor vibratory loads [11, 12]. The disadvantages of this device are high weight penalty, and potential reliability and maintenance issues.

3. *Absorbers*: pendulum like devices mounted on the rotor hub tuned to cancel dominant N_b/rev hub loads [13, 14] using its centrifugal force. These devices are simple in operation, however, incur weight and drag penalties.

4. *Attenuators*: devices installed on the blades in the rotating frame to adjust blade structure dynamics so as to reduce the vibratory loads at blade root. These are typical discrete masses mounted at the blade tip or midspan favorably to adjust the blade natural frequencies and modes. One example of such a device maybe found on the SH-2 rotors where brackets are used to adjust the flap frequency above 3/rev [15]. This category of vibration reduction concepts is closely related to the topic of blade structural optimization [16]. While it is a promising concept for reducing vibration, it cannot be changed once the design is complete and in production.

5. *Rotor excitation reducers*: devices installed on the blades that work directly at the source of the vibration by reducing the aerodynamic excitations on the blades. These systems counteract the blade vibratory aerodynamic loads with carefully phased aerodynamic inputs to the blade. The advantages of this type of device are that it reduces not only vibratory hub loads, but also vibratory loads in the blades, pitch links, and other dynamic components, thus improving the reliability of the system.

The first four concepts in the above list have proved effective to reduce vibration to some degree, and warrant their continuing application on helicopters. However, they also share the common disadvantage of incurring large weight penalties and poor off-design performance. The rotor excitation reduction devices have the potential of reducing vibration level with greater effectiveness and flexibility than the other concepts. These can be further classified into two categories: Higher Harmonic Control (HHC) and Individual Blade Control (IBC) [17]. *Higher Harmonic Control* usually refers to devices whose control inputs are actuated in the fixed system, typically through swashplate. It has been shown that HHC is effective in vibration reduction [18, 19] and helicopter performance improvement [20]. The drawbacks of the HHC system are high power requirements, weight penalty, high pitch link loads, and most importantly, are limited to the N/rev swashplate frequency which prevents their application on vibration reduction of dissimilar rotors blades. *Individual Blade Control* refers to a system where control inputs are installed in the rotating system, and every blade is controlled independently at any desired frequency. The early actuation mechanism of IBC is through the hydraulic slip ring unit

that is very complex and incurs high actuation power and weight penalty [17]. Recently, the emergence of smart material actuators has opened up new frontiers for innovative concepts in vibration reduction. Smart materials such as piezoceramics can provide high bandwidth actuation and possess high energy densities, and thus are suitable for compact and low-weight on-blade actuation.

The primary concepts of smart rotor systems include active flap rotors, active twist rotors, and composite coupled rotors [21]. Among these concepts, the trailing-edge flap system is an attractive option because of its high control authority, low actuation power, low aerodynamic drag, and less intrusiveness in blade structure integrity. This control system can be used for multifunctional roles such as to suppress vibration and noise, increase aeromechanical stability, improve rotor performance, and potentially replace the swashplate system to provide primary rotor control.

1.2.3 Helicopter Primary Control System

The helicopter main rotor produces the lift that sustains the weight of aircraft , the propulsive force to fly forward, and the primary control forces to maneuver. The role of the helicopter primary control system is to control the magnitude and direction of rotor thrust, and thus control the attitude of the vehicle. The magnitude of rotor thrust is determined by the lift generated collectively by individual blades, which in turn is controlled by the collective pitch angle. The direction of rotor thrust is approximately perpendicular to the Tip-Path-Plane (TPP). Rotor cyclic pitch angles, which cause blade flapping up and down, control the direction of TPP. Therefore, helicopter primary rotor control essentially

consists of collective and cyclic control of rotor blade pitch angles.

The pitch control device for a helicopter rotor blade was one of the great design challenges faced by the earliest rotorcraft engineers, and it remains one of the most complex, precise and flight critical devices on rotorcraft today. The rotorcraft pioneers invented two means of altering blade pitch: the swashplate mechanism and the trailing-edge flap system, and these two devices are still the dominant design concepts of modern helicopter primary control system.

Hafner [22], in the late 1920s, developed a swashplate mechanism, which was to become the standard means of providing pitch control on modern helicopters [2]. Figure 1.3 illustrates a swashplate system of a modern bearingless rotor MD-900 Explorer. The swashplate assembly is the transition between the rotating rotor and the stationary control rod inputs. It consists of a lower nonrotating ring, which receives the boosted control inputs from the pilot cyclic and collective pitch sticks, and an upper rotating ring that transfers those inputs through pitch links to each blade's torque tube. The collective input is transferred to blade collective pitch angle change by the up and down movement of the swashplate whereas the cyclic inputs are passed to blade cyclic pitch changes through the inclination of the swashplate.

The concept of a trailing-edge flap for helicopter primary control essentially originated with Pescara's helicopter of 1922 [23], which featured plain flaps for 1/rev blade pitch control. Servo flaps, introduced by d'Ascanio [24] in his co-axial helicopter design around 1930, have been a feature of Kaman aircraft [25] since the late 1940's. Figure 1.4 illustrates a servo-flap system installed on a production composite blade of modern Kaman helicopter. The servo flap is a small auxiliary airfoil located at about 75%

span of the rotor blade, situated aft of the trailing edge of main rotor blade. These flaps are controlled by the pilot through push-pull control rods. A more-or-less conventional swashplate mechanism, with control rods going through the centers of hollow rotor shafts, was used to transfer pilot inputs in fixed system to the push-pull rods in rotating frame. The flaps are controlled by pilot to deflect against servo-flap hinge to produce pitching moment changes. This in turn impels the main blades to pitch against the feathering bearing to achieve aerodynamic equilibrium, thereby producing the desired collective and cyclic blade pitch. Servo-flap system requires a torsional soft rotor to increase the control effectiveness of servo-flaps, and this is achieved by using a very soft torsional spring (tension-torsion straps) to restrain the blade about pitch bearing [26]. Some early production servo-flap rotor designed by Kaman replaces the pitch bearing with torsionally soft retention strap, and this simplifies rotor hub considerably.

The reason that Kaman is the sole company using the servo-flap control system whereas all others are all opt for the swashplate system, is hard to comprehend. Nonetheless, it should not be attributed to inherent flaws in the servo-flap system. Compared with conventional swashplate control system, the servo-flap system has the following advantages and disadvantages [15, 26, 27].

1. Servo-flap system requires a smaller control force. Conventional swashplate control system moves the entire blade whereas servo-flap system only works on the small flap surface. Therefore, conventional system typically requires the complex and heavy hydraulic system whereas servo-flap system may be driven by pilot without boosting devices. Besides the weight and power reduction, small control force also

provides excellent flying quality and aerodynamic control sensitivity.

2. The servo-flap system has a cleaner hub design. The low control forces translate into a lighter control system, and this enables a cleaner hub system. It also has a great potential to fly the helicopter by wire, thereby, complete eliminating the swashplate system to reduce significantly the weight and drag penalty and cost involved in the conventional system.

3. Servo-flap system enhances rotor stability characteristics. The blade pitching moment generated by the servo-flap airload makes the main rotor thrust derivative negative, which generates a stabilizing effect on the entire rotor.

4. A rotor with a servo-flap system may have lower blade induced vibration. Elimination of structure in the primary flight control system eliminates a load path for vibratory control loads transferred to airframe, and thus reduces vibration. A torsional soft rotor is also more sensitive to the dynamic and aerodynamic tuning to reduce vibration.

5. Servo-flap rotor increases the survivability because of control redundancy. Helicopters are designed and built with numerous redundancies and can usually tolerate such failures as loss of engine power, gearbox, tail rotor drive and even the tail rotor itself, but conventional swashplate system consists of a single path in the critical flight control system, and once fails the outcome is often fatal. Swashplate failures, which are primarily caused by bearing malfunctions due to loss of lubrication, have been shown as the cause of several fatal helicopter accidents.

6. Blade structural integrity is a concern for servo-flap rotor because of the mounting of flaps and passing of control rods. The flaps and extra supporting structures will also increase the blade weight.

7. The necessary torsional soft rotor design of servo-flap rotor is sensitive to two types of rotor instability problems: flap/pitch and lag/pitch flutter [28], and must be dealt carefully.

8. There is drag penalty resulted from trailing-edge flap system. This will be slightly compromise in the drag reduction of a clean hub design of servo-flap rotor.

As can be deduced from the description, the servo-flap system is one concept that may be of use in designing next generation of advanced rotor system by maximizing its advantages and addressing its shortcomings carefully.

1.2.4 Concepts of Blade Pitch Control

As described in previous section, the conventional swashplate mechanism is routinely used as the primary control system on most helicopters flying today. However, it has some major drawbacks, such as numerous exposed linkages, bearings, push rods and hinges, which are maintenance intensive, inspection critical, costly and act as a significant source of drag. These inherent drawbacks of swashplate system provide an impetus to search for alternative forms of main rotor pitch control.

A wide range of potentially suitable concepts was studied by various researchers. The concepts can be classified into categories according to their method of operation:

1. Blade camber control – achieved by cyclic excitation with embedded material that is arranged differently on the top and bottom surfaces of the blade sections. Due to the lack of availability of suitable smart materials with sufficient stroke and stiffness, this concept was found infeasible [29, 30].

2. Blade twist control – enables blade twist to be generated from embedded active materials and via the application of a cyclic differential voltage over the span of the blade. Problems with this design include blade structural integrity and requirement for large actuation power [31].

3. Blade pitch control – actuates individual blades in pitch using hydraulic or smart material actuators in the rotating frame. Hydraulic actuation requires installation of complex hydraulic slipring, whereas smart actuation is limited by the relatively small stroke of current smart materials [17].

4. Tilting shaft concept – affects a tilt of the control mast to reorient the direction of the rotor thrust. This concept was found infeasible because of the unacceptably large actuation forces and strokes required, and because of the inherent complexity and weight of the actuation mechanism. This concept is most seen on autogyros [32].

5. Active servo flaps – auxiliary airfoil sections that are located aft of the trailing edge of the main blades as adopted by Kaman. This design involves exposed linkages resulting in large drag penalties [26, 33].

6. Active plain trailing edge flaps – flaps integrated with the main lifting section of the blade are deflected cyclically to change the lift and/or moment characteristics

of the blade section [34].

With the recent emergence of smart material actuators with high energy densities, it appears promising to apply this technology to primary rotor controls through the application of active trailing edge flaps [35]. Furthermore, trailing-edge flaps have also received considerable interest among rotorcraft engineers for the reduction of helicopter vibration and noise [36–41]. The use of a trailing-edge flap for primary control appears attractive in the context of an actively controlled rotor, where embedded flaps can perform multiple functions.

There are primarily two types of flaps suitable for using on helicopter blades: servo flaps and plain flaps (Fig. 1.5). The servo-flap design consists of auxiliary airfoil sections that are located aft of the trailing edge of the main blades. Despite the successful service history of servo-flaps for blade pitch control [33, 42], they are somewhat inefficient because of the high drag resulting from exposure of the hinges and supporting structure, and reduction in aerodynamic efficiency caused by the flap hinge gap [34]. An alternative configuration, the plain flap, is the subject of the present investigation, and coupled with the use of smart materials, provides an attractive solution. In this configuration, the flap is integrated into the rotor blade by placing the flap actuation and support structure, hinge, and linkage assembly within the blade profile, thereby resulting in a reduction in aerodynamic drag, and an increase of flap effectiveness by narrowing the hinge gap. However, compared with servo flaps, plain flaps are located much closer to the blade elastic axis and hence their capability to generate pitching moments is correspondingly reduced. This reduction may be compensated by optimizing other important variables such as pitch in-

dex angle, blade root spring stiffness, flap location and size, etc. so that enough control authority may be achieved. It is worth to note that there is ongoing research [15, 43] in Kaman to explore the feasibility of replacing their traditional servo-flap system with plain trailing-edge flap.

1.3 Literature Survey

The present investigation concerns itself with demonstrating the feasibility of using a plain trailing-edge flap system for helicopter primary and vibration controls. The performance and stability characteristics of trailing-edge flap rotors are examined systematically through parametric studies. This section first discusses state-of-the-art research aimed at using trailing-edge flap for vibration reduction, including both numerical and experimental studies. It then describes the aeroelastic stability study of flapped wings because there are no known studies focusing on stability of trailing-edge flap rotors. Lastly, the investigations concerning trailing-edge flaps for helicopter primary control are reviewed.

1.3.1 Trailing-Edge Flaps for Vibration Control

The concept of using trailing-edge flaps for helicopter vibration control is not entirely new. Payne [44] identified the concept for higher harmonic control in 1958. However, the first focused study of this concept did not occur until 1970's when the Multicyclic Controllable Twist Rotor (MCTR) was developed [45–48]. The MCTR uses a hybrid control system, featuring the conventional swashplate primary control system with the outboard servo flap for vibration control and rotor performance improvement. Full scale

16

wind tunnel tests demonstrated significant reductions in blade flapwise bending moments and actuator control loads [47]. The MCTR concept, however, was not used on production helicopters primarily because of the complexity of electro-hydraulic actuators used in the servo flap control system.

Since the 1990's, the advancement of smart materials opens a new domain of active trailing-edge flap systems driven by smart material actuators. The emergence of these compact, lightweight, high bandwidth, and low power requirement actuators has revived the interest in active trailing-edge flap rotors [35]. Several small scale rotors with a trailing-edge flap system actuated by embedded smart materials have been developed by various researchers, including Prechtl and Hall [49], Lee and Chopra [50], Bernhard and Chopra [51], Koratkar and Chopra [38], Fulton and Ormiston [52], and Janker, *et al.* [53]. A full scale rotor with a smart trailing-edge flap system has been designed by Straub, *et al.* [40], and will be tested in flight. Wind tunnel experiments [38] have shown that helicopter hub vibratory loads can be successfully minimized with actively controlled, trailing-edge flaps with smart actuators. The introduction of Reference [21] contains a detailed review of these works.

In analytical simulation, Millott and Friedmann [36] investigated servo-flaps using a flexible blade model and modified Theodorsen aerodynamics. The servo flap system was found to be as effective as conventional multicyclic control, but with greatly reduced power requirements. The study included parametric studies of flap size, flap location, and blade torsional stiffness. The flap location was determined to be a significant design parameter. However, the study incorporated uniform inflow distribution that limited the level of vibrating loads. Milgram and Chopra [37, 54] presented a comprehensive study

based on UMARC using a compressible unsteady aerodynamic model [55] and the Bagai-Leishman free wake model [56]. The analytical results were validated with wind tunnel experimental data [57]. The Milgram and Chopra study indicates the feasibility of a 10% span, 20% chord trailing-edge flap, with $\pm$ 5 deg. flap travel, in reducing vibratory hub loads. The parametric design study examined the influence of design parameters such as flap length and chord, spanwise location, and controller weighting parameters. The flap length and chord were found of less importance because the controller automatically adjusts for changes in flap authority by varying the input amplitudes. The flap spanwise location was found to be an important parameter. Myrtle and Friedmann [58] presented a rotor code for the active flap using an unsteady aerodynamic model [59] for airfoil/flap based on a rational function approximation approach. Similar levels of vibration reduction are obtained when using quasi-steady Theodorsen aerodynamics and the new unsteady aerodynamic model. Unsteady aerodynamics, including free wake modeling, was shown to be important for obtaining flap actuation power requirements. Zhang, Smith and Wang [60] presented an active/passive hybrid method for vibration reduction by integrating active flap design with blade structural optimization. The study concluded that hybrid design could achieve more vibration reduction with less control efforts compared to retrofit or sequential design. Straub and *et al.* [40,61] modified the comprehensive code CAMRAD/JA to account for the aerodynamics of blade sections with a trailing-edge flap and a simple model of actuator dynamics. The flap aerodynamics is modeled with approximation of potential flow thin airfoil theory or with use of 2D airfoil section table lookup. The recently released CAMRAD II [62, 63] code presented the ability to model the fully coupled blade/flap aerodynamics and dynamics. The steady flap aerodynamics is

18

modeled using 2D airfoil table lookup. Incompressible unsteady loads are obtained using modified classical 2D airfoil/flap theory [64]. Predicted results from CAMRAD/JA and CAMRAD II were compared for blades without flaps and for blades with prescribed flap motion [40]. The study showed that CAMRAD/JA captured the overall rotor response and trailing-edge flap loads with sufficient fidelity, and that CAMRAD II predicated more accurate blade and flap loads.

1.3.2   Aeroelastic Stability of Flapped Wing

With the extensive work regarding the use of active trailing-edge flap for vibration control [35, 38, 40, 52, 65, 66], automated in-flight tracking [67], and primary flight control [68, 69], the aeroelastic stability associated with these flap systems is a concern that has received little attention to date [70, 71]. Satisfactory stability characteristics that include blade aeroelastic stability and ground or air resonance [28] may be critical to the design.

Flutter phenomena of control surfaces in fixed-wing aircraft, such as wing-aileron, tail-elevator and rudder, are well studied. Many of the theories and practices associated with flutter on flaps of fixed-wing aircraft may also be applicable to rotorcraft, and the current investigation may use similar approaches with respect to trailing-edge flaps on rotor blades. Broadbent [72] presented a discussion on flutter of control surfaces and tabs. The nature of aeroelastic stability of wing-aileron systems is explained by considering the aerodynamic forces that arise from the aileron motion and solving the binary flutter equations of wing bending-aileron and wing torsion-aileron. It is explained that the avoidance

19

of control surface flutter can be achieved by using mass-balance, irreversible controls, and adding more damping. Fung [73] explained the flutter phenomenon by considering energy transfer between wing distortion and aileron deflection, and gave historical remarks on flutter analysis development. Theodorsen [74] presented the aerodynamic model for an oscillating airfoil or airfoil-aileron combination with three independent degrees of freedom: wing bending, wing torsion, and aileron deflection. The calculated stability solution is compared with experimental data, and the comparison shows fair to good agreement.

Compared with control surfaces in fixed-wing aircraft, trailing-edge flaps embedded on rotor blades operate in more complex aerodynamic and inertial environment, and thus may induce unique aeroelastic instabilities that must be examined carefully.

1.3.3   Trailing-Edge Flaps for Primary Control

The use of a trailing-edge flap system for primary control dates back to Pescara's helicopter of 1922 [23]. Since the late 1940s, Kaman has been a proponent of servo flap controlled rotors, which is the hallmark of Kaman helicopters (Table 1.1) [26]. The concept of trailing-edge flaps for primary control appears attractive in an actively controlled rotor, where embedded flaps can perform multiple functions. Additionally, multiple on-blade flaps may increase the redundancy of the flight control system. A recently envisaged NASA Revolutionary Concepts (REVCON) program is expected to examine the feasibility of "swashplateless" helicopter flight [75].

Early studies by Lemnios and *et al.* [26, 33] presented modeling and correlation for Kaman's rotors (Table 1.1), which utilizes the servo-flap type system as a primary

Table 1.1: Rotors built by Kaman [26]

Vehicle	Year	Gross Weight	Rotor System	Control
H-43	1956	2000 kg	Synchropter Rotor	Servo Flap
K-17	1958	430 kg	Tip Jet Rotor	Swashplate/Pitch-Horn
SH-2F	1973	3200 kg	Single Main Rotor	Servo Flap
K-1200 K-MAX	1994	2200 kg	Synchropter Rotor	Servo Flap

control device. Lemnios and Jones [26] presented a conceptual design of a high maneuverable/agile servo flap control rotor system. The study proposed a plain trailing-edge flap system driven by electro-hydraulic actuator for primary and multicyclic control. The electro-hydraulic actuators were powered by hydraulic system in fixed frame and pulsating fluid was transferred to the actuator in rotating frame via a hydraulic slip ring. It was concluded that the conceptual design can satisfy the Army's Future Attack Rotorcraft (FAR) requirements and represents a significant advancement in the rotor control technology. Wei and Jones [33] presented an analysis that used a modified version of the rotorcraft flight simulation code C81, with airfoil data tables used to obtain the aerodynamic coefficients of the servo flap. The analytical model of the servo flap was treated as a control system, not a degree of freedom. The analytical results showed good correlations with the SH-2F 101 Rotor flight test data, such as servo flap control position, fuselage attitude, main rotor torque, and bending moment distribution.

More recently, Wei and *et al.* [15, 27, 42, 76] presented research findings concern-

ing improvements to the servo-flap, which may enhance rotor performance and vibration reduction. Wei [76] presented an advanced servo flap rotor system using Variable Blade Index Angle Control (VBIAC) to achieve high performance in hover and low vibration in high speed forward flight. The optimal blade index angle is varied with flight speed, and therefore optimally adjusted in flight. Approximately 9% performance improvement was achieved in hover. Blade stall margin was increased with a trade-off by slightly increasing the blade acceptable vibration level. Aircraft airspeed, vibration level, and pilot control positions were used in the design to feedback the index angle change requirement needed to achieve the design goal. High torque, low speed, and high precision motion control actuators were used to move the blade when the aircraft has a vibration level higher than desired. The variable blade index angle control was designed in parallel with the main rotor flight control system. Reference 42 presented the development of a new production composite main rotor blade that could generate an upload on the servo-flap in hover. This servo-flap upload generated a more uniform blade lift distribution, and thus produced better hover and forward flight performances. Reference 27 presented the design of soft torsion rotor systems. A torsionally soft rotor is inherent to a trailing-edge flap primary control system, and blade torsional frequency is a critical design variable. A soft torsion rotor has very different dynamic and aerodynamic characteristics as compared to a conventional pitch horn torsionally-stiff rotor. One of the major concerns of the soft torsion rotor design is the aeroelastic stability. The study in Ref. [27] addressed the design consideration of soft torsion rotor systems at Kaman as well as their helicopter development programs. Reference 15 presented design considerations of a plain trailing-edge flap to replace Kaman's conventional external servo flap for future helicopter develop-

ments. The study compared the external servo-flap and plain trailing-edge flap rotor, and concluded that the plain trailing-edge flap has better aerodynamic performance because of an inherently higher lift to drag ratio, and improved rotor stability characteristics because of a more forward chordwise center of gravity. The challenges of designing a plain trailing-edge flap rotor were also identified. The reduction in pitching moment of plain trailing-edge flap due to shorter moment arm must be compensated with a larger flap, more radial outboard flap location, and extreme soft torsion stiffness.

There was also research conducted outside Kaman that studied the potential of a trailing-edge flap controlled rotor. Straub and Charles [77] examined the preliminary requirements of the swashplateless design for an Advanced Rotor and Control System (ARCS) concept. Both a servo-flap type system and a combination of plain flap and blade root actuator mechanism were studied. The study concluded that the dual control concept is superior to the servo-flap design in maneuverability and basic performance.

A recent study by Ormiston [34], using a simple rigid rotor model, explored the feasibility of a swashplateless rotor with plain trailing-edge flaps. It was concluded that plain trailing-edge flaps have the potential to satisfy the general requirements for primary flight controls. The study also indicated that the blade fundamental torsional frequency would likely need to be lowered to 1.5 to 2.5/rev and the constraints associated with aeroelastic stability and flutter of rotor blades with such low torsional frequency should be thoroughly investigated.

1.4 Present Research

1.4.1 Objective

The present research investigates the feasibility of using plain trailing-edge flap for helicopter primary and vibration control. The focus of this dissertation is on the development of a comprehensive aeroelastic analysis of trailing-edge flap helicopter rotors.

For most of the previous trailing-edge flaps analyses, the actuator dynamics were neglected. One objective of this research is to present a comprehensive rotor aeroelastic analysis with trailing-edge flap including smart actuator dynamics. Coupling effect among blade, smart actuator and flap is investigated by properly modeling actuator dynamics.

Following this, the aeroelastic stability of a rotor system with trailing-edge flaps is investigated systematically. The study also examines the effects of various key design variables such as flap overhang length, flap CG offset, rotor control system stiffness, blade torsional stiffness, actuator stiffness, and trailing-edge flap size and location on the aeroelastic stability characteristics of a trailing-edge flap rotor system.

The final objective of this study is to develop a comprehensive rotorcraft analysis that includes a swashplateless rotor with trailing-edge flaps, and investigate the feasibility of a trailing-edge flap primary control system. A multicyclic controller is implemented with the swashplateless rotor analysis, and the capability of a trailing-edge flap performing both primary control and active vibration control functions is evaluated. A parametric study of various key design variables involved in the primary control with plain trailing-edge flaps is carried out. The aeroelastic stability characteristics of a swashplateless rotor

system is systematically examined. The performance of a teetering rotor with a plain trailing-edge flap system for primary control is evaluated. This research investigates the effect of various key design variables such as pitch index angle, flap location and size on rotor performance, trailing-edge flap deflections and actuation requirement.

1.4.2 Scope

The focus of this research is to develop a comprehensive aeroelastic analytical model of a helicopter rotor with trailing-edge flaps for primary rotor and vibration control. The derivation of system equations is based on Hamilton principles, and implemented with finite element in space and time. The blade element consists of fifteen degrees of freedom representing blade flap, lag, torsional, and axial deformations. Three aerodynamic models of flapped airfoil are implemented in the present analysis, an advanced unsteady Leishman-Hariharan model for flaps without aerodynamic balance, a quasi-steady Theodorsen theory for an aerodynamic balanced flap, and table lookup based on wind tunnel test data. Bagai-Leishman free wake model based pseudo-implicit predictor-corrector relaxation scheme is used to provide inflow distribution on the rotor disk. Drees linear inflow was also implemented for some preliminary studies. Nonlinear inertial effects of the flap and blade are fully captured. The trailing-edge flap deflections may be modeled as a degree of freedom so that the actuator dynamics can be captured properly. The coupled trim procedures of a conventional or swashplateless rotor are solved in either wind tunnel trim or free flight conditions. The coupled blade equations of motion are linearized by using small perturbations about a steady trimmed solution. Stability is then determined from

an eigenanalysis of the homogeneous equations using either Floquet method or Constant Coefficient Approximations. The trailing-edge flap motion is included as an additional degree of freedom in this study, and the stability of the trailing-edge flap mode is properly predicted. The coupled trim procedure is then modified to model a swashplateless, bearingless helicopter rotor with trailing-edge flaps in a wind tunnel trim condition. Two unique characteristics of a swashplateless rotor, compared with a conventional rotor, are torsionally soft blades and pre-collective angles, both of which are properly modeled in the analysis. The swashplateless rotor model is further enhanced to model an ultralight teetering helicopter rotor with trailing-edge flaps in free flight conditions. An additional degree of freedom involved in teetering rotors, i.e., rotor teetering angle, is added in the system equations. The blade equations of motion are transformed into the hub-fixed system to treat two blades of the teetering rotor simultaneously. A multicyclic controller is also implemented to determine the flap control inputs for minimization of vibratory rotor hub loads. This controller may be used for vibration control in both the conventional and swashplateless rotors with trailing-edge flaps. This comprehensive trailing-edge flap helicopter model provides a design tool to investigate the effect of flap configurations of arbitrary locations, length, chord ratio, overhang length and mass properties on flap effectiveness to provide primary and vibration controls, actuation requirements, and aeroelastic stability characteristics.

A correlation study for the baseline bearingless rotor without trailing-edge flaps is performed using wind tunnel experimental data. The predictions of rotor trim angles, rotor performance, blade sectional loads, vibratory hub loads, and aeroelastic stability characteristics are compared with wind tunnel measurements at different flight conditions.

26

The impact of actuator dynamics on control effectiveness and actuation requirements of a trailing-edge flap system as a vibration reduction device is also investigated. The parametric study is conducted to examine flap location using both coupled and prescribed flap motion models.

The aeroelastic stability characteristics of a trailing-edge flap rotor system are then examined by a parameter study on various key design variables such as flap overhang length, flap CG offset, rotor control system stiffness, blade torsional stiffness, actuator stiffness, and trailing-edge flap size and location. Simulations for several advance ratios and various collective pitches are performed.

The actuation requirements of a primary control system are then evaluated for MDART bearingless rotor in wind tunnel trim conditions. The feasibility of trailing-edge flaps performing both primary control and active vibration control is examined. A parametric design study is conducted for a helicopter primary control system using trailing-edge flaps. The swashplateless rotor design is based on MD-900 bearingless rotor, with plain trailing-edge flaps as a primary control device. The primary design parameters studied are blade index angle, blade root spring stiffness, blade torsional stiffness, trailing-edge flap chordwise and spanwise size, location, and overhang length.

The teetering rotor of an ultralight helicopter with trailing-edge flap as primary flight control is evaluated in free flight trim conditions. The study examines the effects of various key design variables such as pitch index angle, flap location and geometry on rotor performance, and trailing-edge flap deflections. The prediction capability of the present analysis of a baseline teetering rotor is correlated with the predictions of another comprehensive analysis, CAMRAD II. The correlation is carried out for the baseline ro-

tor without trailing-edge flaps embedded. The predicted blade natural frequencies, blade flapping and pitch angles and rotor shaft tilt are compared. The performance of swashplateless rotor is examined by comparing with the conventional swashplate controlled rotor at different flight conditions and at various thrust levels.

1.5   Overview of Dissertation

The dissertation is organized in four chapters as described below:

Chapter 1 Introduction   This chapter presents the background and motivations that lead to the objective and scope of this dissertation. It also includes a brief comparison of a conventional swashplate controlled rotor and a trailing-edge flap rotor as well as a literature survey of numerical studies of trailing-edge flap rotor systems.

Chapter 2 Analytical Model   This chapter presents the formulation of the analysis, including the basic aeroelastic analysis of trailing-edge flap rotor, aeroelastic stability, and swashplateless rotor coupled trim procedures.

Chapter 3 Results and Discussion   This chapter presents the validation study of a baseline bearingless and teetering rotor without trailing-edge flaps. Next, predictions of trailing-edge flap rotor are correlated with the calculations of another analysis, CAMRAD II. Parameter study is then presented to investigate the potential of trailing-edge flap performing both vibration reduction and primary rotor control. Aeroelastic stability characteristics of trailing-edge flap rotors are examined as well.

Chapter 4 Summary and Conclusion

This final chapter will summarize the significant conclusions of this study and present the recommendations for future work.
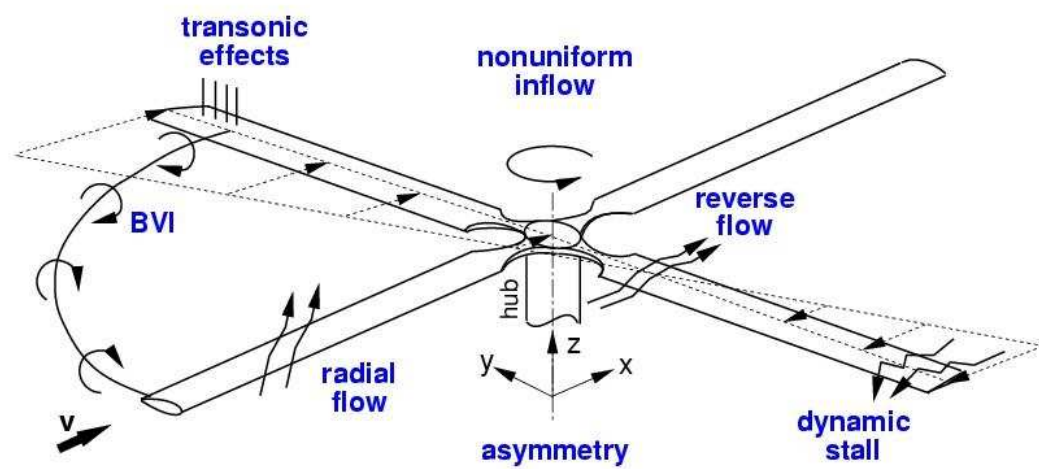
Figure 1.1: Aerodynamic sources of helicopter main rotor vibration
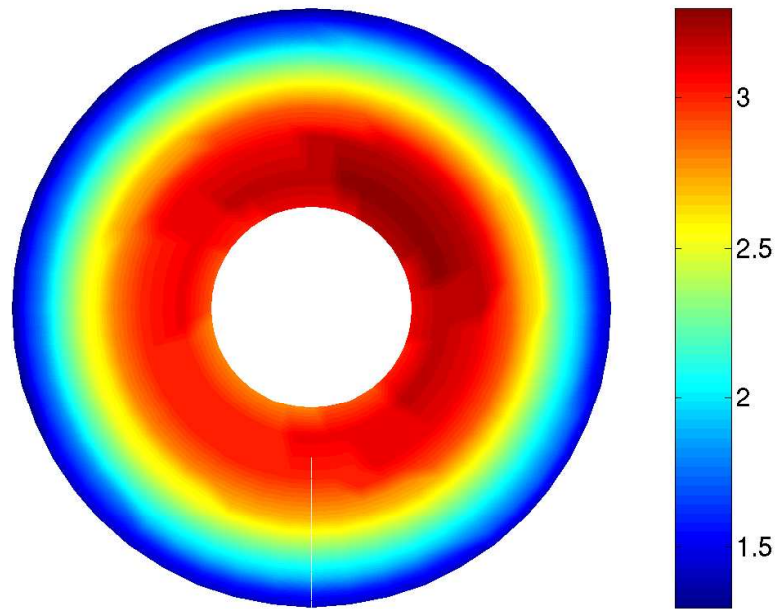
(a) hover
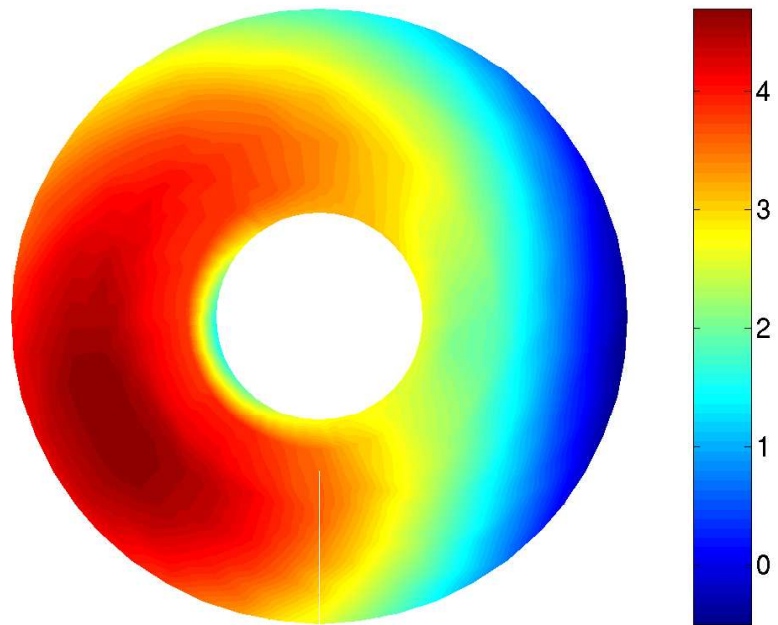
(b) forward flight, $\mu = 0.16$

Figure 1.2: Blade angle of attack distributions in hover and forward flight
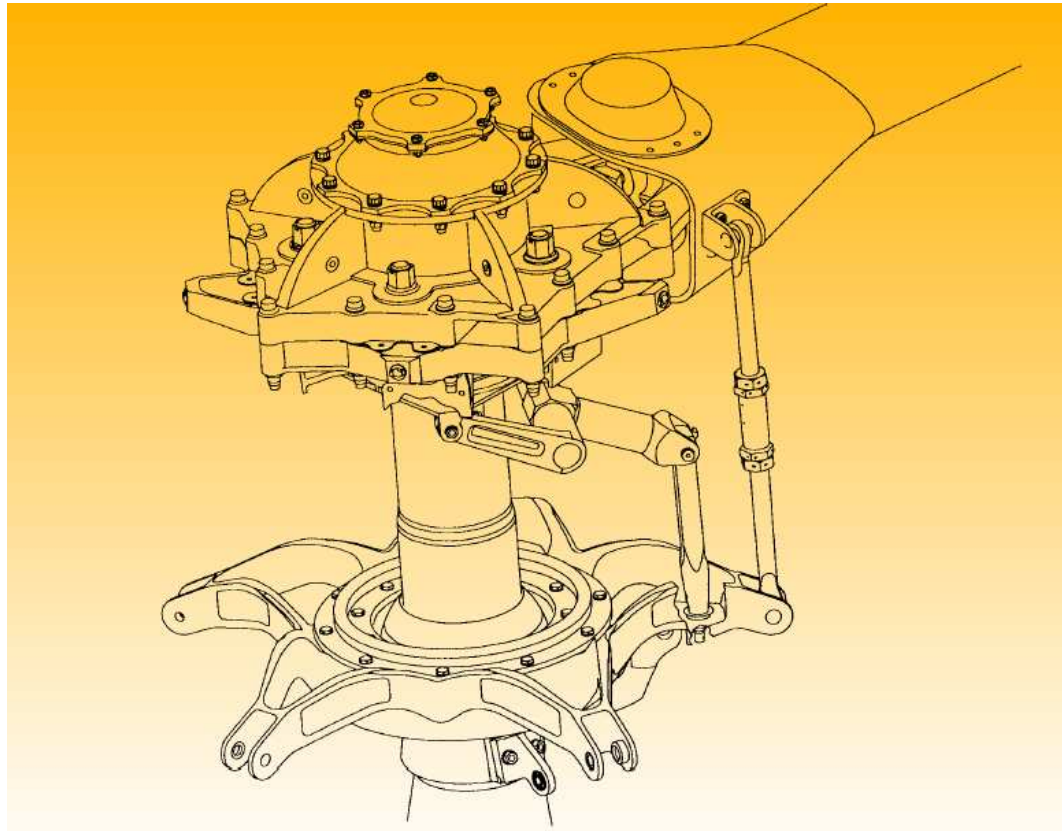
Figure 1.3: MD900 swashplate system [78]
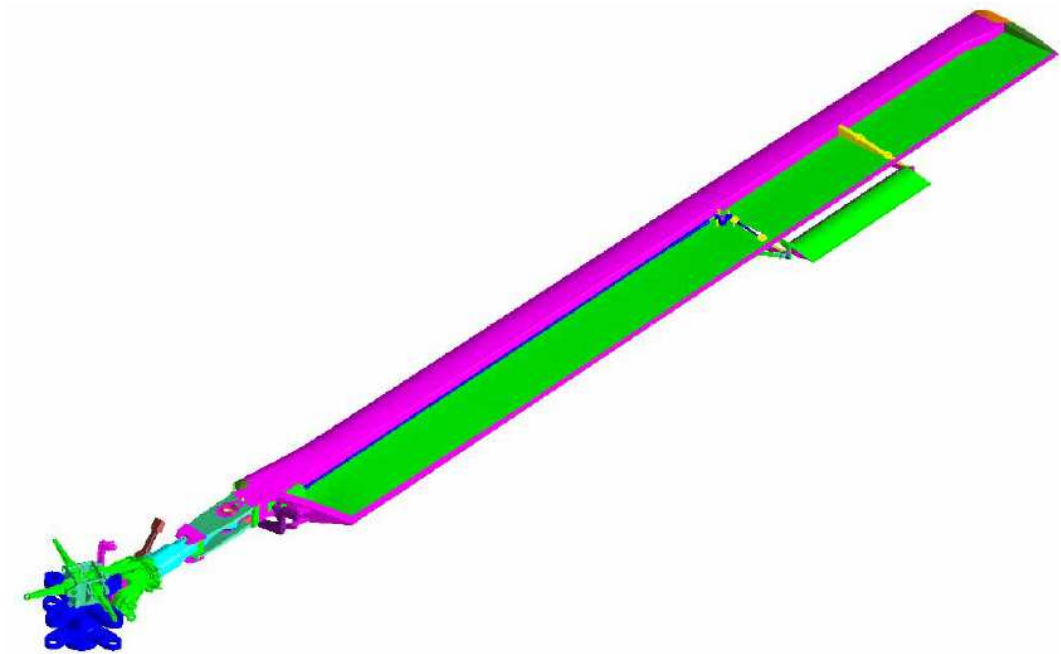
Figure 1.4: Servo flap on a production composite rotor of Kaman helicopter [15]

Servo Flap
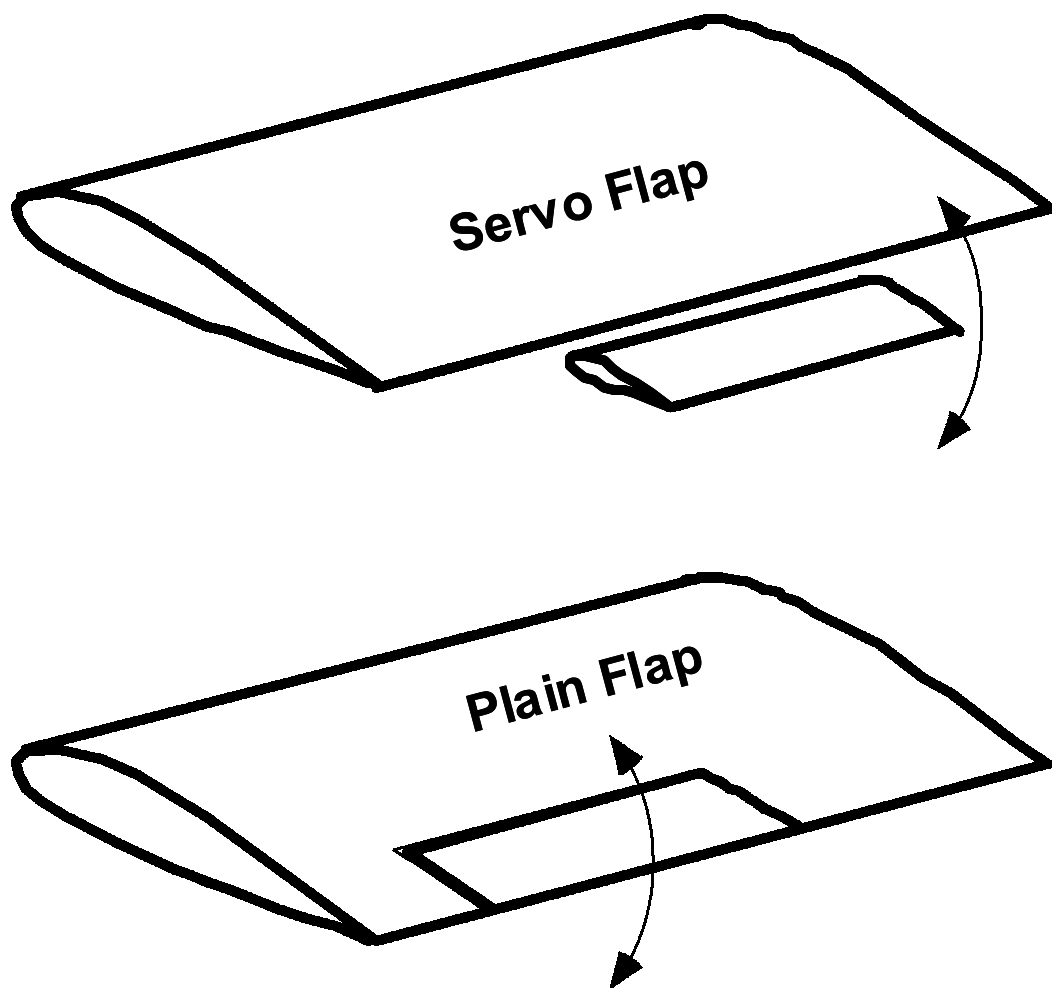
Plain Flap

Figure 1.5: Servo-flap and plain flap

Chapter 2

Analytic Model

This chapter describes the aeroelastic analysis for a helicopter rotor with trailing-edge flaps. The analysis is based on the derivation and implementation of trailing-edge flap rotor equations of motion in a level flight condition. It calculates the aeroelastic response and stability characteristics of the rotor blade and trailing-edge flap using a coupled trim procedure. The rotor can be either in a free flight propulsive trim or wind tunnel trim condition. The equations of motion are derived using Hamilton principle [79], and implemented using finite element methods. The temporal equations of motion are solved using finite element in time procedure coupled with the rotor trim equations. The aeroelastic stability characteristics are then calculated using linearizion of equations of motions by using small perturbations about a steady trimmed solution. Stability is determined from an eigenanalysis of the homogeneous equations using Floquet theory.

There are two types of trailing-edge flap models in the present investigations with different levels of fidelity. The "prescribed trailing-edge flap motion model" assumes a prescribed motion of trailing-edge flaps, and hence neglects the trailing-edge flap actuator dynamics. However, flap inertial contributions are included in both the formulation

of the blade equations of motion and the computation of hub loads. The "coupled rotor/flap/actuator model" calculates the trailing-edge flap motion along with blade elastic deflection with prescribed actuator inputs. Trailing-edge flaps are connected to the rotor blade via smart material actuator, and the blade deflection and trailing-edge flap motion are coupled through the inertial and aerodynamic loads generated by the flap including hinge moments of the flap. The actuator is modeled as a combination of a linear spring and a damper.

The trailing-edge flaps are used for two different functions: active vibration control and primary rotor controls. First, the implementation of multicyclic controller used to study the effectiveness of the trailing-edge flap system in helicopter vibration control is described. This controller is based on the "T" matrix method that is widely used in both analytic and experimental investigations of Higher Harmonic Control (HHC) system. The inputs to this controller are the helicopter rotor vibratory hub loads, and the outputs are the optimum trailing-edge flap motions used to minimize the vibration level.

Second, the analysis of a swashplateless trailing-edge flap helicopter rotor is developed based on the formulation of nonlinear equations of motion. Trailing-edge flaps replace the swashplate system to provide helicopter primary rotor controls. Blade pitch angles required to trim are controlled by trailing-edge flap inputs rather than directly imposed in the conventional swashplate control system. The flaps produce pitching moment changes, which impel the main blades to twist against the root spring to achieve equilibrium with aerodynamic forces, and thereby producing the desired collective and cyclic blade pitch angles. This mechanism requires a torsionally soft rotor, which can be achieved using soft root springs. This will result in a large torsion motion against

36

the root spring. The formulation of modeling this large torsion motion is described in Section 2.9.2. The multicyclic controller was implemented with the swashplateless rotor analysis in order to investigate feasibility of trailing-edge flap performing both primary control and active vibration control.

2.1 Coordinate Systems

This section presents the coordinate systems used to describe the blade and trailing-edge flap motions. All systems are right handed and are defined in consistent with the UMARC (University of Maryland Advanced Rotorcraft Code) methodology [80, 81]. Their definitions are shown below:

1. The *Hub fixed non-rotating coordinate system* ("H") (Fig. 2.1), x_H, y_H, z_H, is a non-rotating Cartesian coordinate system fixed at the intersection of the rotor shaft axis and the blade elastic axis. Its unit vector, $\hat{i}_H, \hat{j}_H, \hat{k}_H$, is defined below:

   $\hat{i}_H$ perpendicular to the rotor shaft axis; points toward the helicopter tail

   $\hat{j}_H$ perpendicular to the rotor shaft axis; points starboard

   $\hat{k}_H$ coincident with the rotor shaft axis; points up

2. The *Hub rotating coordinate system* ("R") (Fig. 2.1), x_R, y_R, z_R, with unit vector, $\hat{i}_R, \hat{j}_R, \hat{k}_R$, rotating at constant angular velocity $\Omega \hat{k}_R$ with respect to the hub-fixed non-rotating coordinate system.

3. The *Undeformed blade coordinate system* ("U"), (Fig. 2.1), x_U, y_U, z_U, with unit vector, $\hat{i}_U, \hat{j}_U, \hat{k}_U$, also rotating with the blades and is defined as "R" system rotated

about j_R by the blade precone angle, β_p. The x_U axis is coincident with the blade undeformed elastic axis.

4. The *Local undeformed blade coordinate system* ("L"), (Fig. 2.1), x_L, y_L, z_L, with unit vector, $\hat{i}_L, \hat{j}_L, \hat{k}_L$, identical to the "U" system except with an origin at an arbitrary blade station $r/R = x$. This is the coordinate system in which the blade deformations are defined.

5. The *Deformed blade coordinate system* ("D"), (Fig. 2.1), x_D, y_D, z_D, with unit vector, $\hat{i}_D, \hat{j}_D, \hat{k}_D$, with the same origin as the "L" system and is defined as "L" system rotated through transformation matrix T_{DL} that is caused by blade deformation.

The transformation between the hub-fixed non-rotating and rotating coordinate systems is defined as

$$
\left\{ \begin{array}{c} \hat{i}_R \\ \hat{j}_R \\ \hat{k}_R \end{array} \right\} = \left[\begin{array}{ccc} \cos\psi & \sin\psi & 0 \\ -\sin\psi & \cos\psi & 0 \\ 0 & 0 & 1 \end{array} \right] \left\{ \begin{array}{c} \hat{i}_H \\ \hat{j}_H \\ \hat{k}_H \end{array} \right\} = \mathbf{T}_{RH} \left\{ \begin{array}{c} \hat{i}_H \\ \hat{j}_H \\ \hat{k}_H \end{array} \right\} \tag{2.1}
$$

The transformation between the hub rotating coordinate system and the undeformed blade coordinate system is given by

$$
\left\{ \begin{array}{c} \hat{i}_U \\ \hat{j}_U \\ \hat{k}_U \end{array} \right\} = \left[\begin{array}{ccc} \cos\beta_p & 0 & \sin\beta_p \\ 0 & 1 & 0 \\ -\sin\beta_p & 0 & \cos\beta_p \end{array} \right] \left\{ \begin{array}{c} \hat{i}_R \\ \hat{j}_R \\ \hat{k}_R \end{array} \right\} = \mathbf{T}_{UR} \left\{ \begin{array}{c} \hat{i}_R \\ \hat{j}_R \\ \hat{k}_R \end{array} \right\} \tag{2.2}
$$

38

The transformation between the undeformed blade coordinate system and the local undeformed blade coordinate system is given by

$$
\left\{ \begin{array}{c} \hat{i}_L \\ \hat{j}_L \\ \hat{k}_L \end{array} \right\} = -x \cdot \hat{i}_U + \left\{ \begin{array}{c} \hat{i}_U \\ \hat{j}_U \\ \hat{k}_U \end{array} \right\} \tag{2.3}
$$

Because of the elastic blade deformation, as derived in Ref. [82, 83], the transformation between the local undeformed blade coordinate system and blade deformed coordinate system is given by

$$
\left\{ \begin{array}{c} \hat{i}_D \\ \hat{j}_D \\ \hat{k}_D \end{array} \right\} = \mathbf{T}_{DL} \left\{ \begin{array}{c} \hat{i}_L \\ \hat{j}_L \\ \hat{k}_L \end{array} \right\} \tag{2.4}
$$

$$
\mathbf{T}_{DL} =
$$

$$
\begin{bmatrix} 1 - \frac{1}{2} v'^2 - \frac{1}{2} w'^2 & v' & w' \\ -v' \cos\theta_1 - w' \sin\theta_1 & 1 - \frac{1}{2} v'^2 \cos\theta_1 - v' w' \sin\theta_1 & 1 - \frac{1}{2} w'^2 \sin\theta_1 \\ v' \sin\theta_1 - w' \cos\theta_1 & -1 - \frac{1}{2} v'^2 \sin\theta_1 - v' w' \cos\theta_1 & 1 - \frac{1}{2} w'^2 \cos\theta_1 \end{bmatrix} \tag{2.5}
$$

where u, v, w are blade elastic deformation, and $\theta_1 = \theta_0 + \phi$ is the blade total twist. Their definitions are described in section 2.3.1.

In order to define trailing-edge motion, two additional coordinate systems are introduced. They are defined below:

1. The *Hinge coordinate system*("N"), (Fig. 2.2), x_N, y_N, z_N, with unit vector, $\hat{i}_N, \hat{j}_N, \hat{k}_N$, identical to the blade deformed coordinate system except with an origin at the

trailing-edge flap hinge line with an offset d from the blade elastic axis. The flap

hinge line is assumed as a straight line parallel to the blade elastic axis. This is the

coordinate system in which the trailing-edge flap deflection is defined.

2. The *Flap coordinate system*("F"), (Fig. 2.2), x_F, y_F, z_F, with unit vector, $\hat{i}_F, \hat{j}_F, \hat{k}_F$,

   is defined as "N" system rotated about $\hat{i}_N$ by the flap deflection angle, δ. The x_F

   axis is coincident with trailing-edge flap hinge line.

The transformation between the hinge coordinate system and the blade deformed

blade coordinate system is given by

$$
\left\{ \begin{array}{c} \hat{i}_N \\ \hat{j}_N \\ \hat{k}_N \end{array} \right\} = d \cdot \hat{i}_D + \left\{ \begin{array}{c} \hat{j}_D \\ \hat{j}_D \\ \hat{k}_D \end{array} \right\} \tag{2.6}
$$

The transformation between the flap coordinate system and hinge coordinate system

is defined as

$$
\left\{ \begin{array}{c} \hat{i}_F \\ \hat{j}_F \\ \hat{k}_F \end{array} \right\} = \left[\begin{array}{ccc} 1 & 0 & 0 \\ 0 & \cos\delta & \sin\delta \\ 0 & -\sin\delta & \cos\delta \end{array} \right] \left\{ \begin{array}{c} \hat{i}_N \\ \hat{j}_N \\ \hat{k}_N \end{array} \right\} = \mathbf{T}_{FN} \left\{ \begin{array}{c} \hat{i}_N \\ \hat{j}_N \\ \hat{k}_N \end{array} \right\} \tag{2.7}
$$

2.2 Nondimensionalization and Ordering Scheme

The present formulation is developed in nondimensional form in consistent with UMARC [80]

format. The physical quantities are nondimensionalized by reference parameters associ-

ated with the rotor system as below:

Table 2.1: Parameter nondimensionalization

Physical Quantity	Reference Parameter
Length	R
Time	$1/\Omega$
Mass/Length	m_0
Velocity	ΩR
Acceleration	$\Omega^2 R$
Force	$m_0 \Omega^2 R^2$
Moment	$m_0 \Omega^2 R^3$

where m_0 is the distributed mass of a uniformed blade which has the same rotor radius and flap moment of inertia as the actual blade (which can be nonuniform). It is defined as:

$$m_0 = 3\frac{I_b}{R^3} = 3\frac{\int_0^R mr^2 dr}{R^3} \tag{2.8}$$

The present formulation of rotor equations of motion is explicit and nonlinear, and leads to very complex expressions that are unmanageable. This type of long and complex expressions is difficult to identify the physical importance of different components. Also, the implementation of this full expression is computational intensive and error prone. Therefore, an ordering scheme is adopted to retain important nonlinear terms in the formulation. It omits those terms that has little or no impact on the system response. This ordering scheme is applied in a systematic and consistent manner. By using the nondimensionalization parameters defined in Table 2.1, the order of magnitude of the non-

dimensional quantities are listed in Table 2.2.

Table 2.2: Ordering scheme

Items	Ordering
$x, \theta_0, \theta_1, \mu, \overset{\star\star}{\delta}$	$\mathcal{O}(1)$
$\frac{\partial}{\partial x}, \frac{\partial}{\partial \psi}$	$\mathcal{O}(1)$ (except when applying on δ)
$v, w, \hat{\phi}, \beta_p, d, \delta, \lambda, \beta_T$	$\mathcal{O}(\epsilon)$
$\overset{\star}{\delta}$	$\mathcal{O}(\epsilon^{1/2})$
y_F, eg	$\mathcal{O}(\epsilon^{3/2})$
u	$\mathcal{O}(\epsilon^2)$
z_F	$\mathcal{O}(\epsilon^{5/2})$
β_p, β_t	small angle

where ϵ is a small number whose quantity is equivalent to the maximum bending rotation expected in the beam model. The small angles listed in Table 2.2 are subjected to the approximation of $\sin(x) \approx x$ and $\cos(x) \approx 1$.

2.3   Structural and Inertial Modeling

The baseline rotor analysis is taken from UMARC [80] which is based on finite element discretization of blade equations of motion. This section describes the structural model in present analysis. Section 2.4 presents the aerodynamic model.

2.3.1 Elastic Blade Model

A nonlinear elastic blade model [80, 82] is used in present analysis. The blade is assumed to be an elastic beam undergoing flap bending, lag bending, elastic twist, and axial deformation. The blade is discretized into a number of beam elements. Each element consists of fifteen degrees of freedom. These degrees of freedom are distributed over five element nodes (2 boundary nodes and 3 interior nodes). There are six degrees of freedom at each element boundary node. These six degrees of freedom correspond to u, v, v', w, w', and $\hat{\phi}$. There are two internal nodes for elastic axial deflection u, and one internal node for elastic twist $\hat{\phi}$. Between elements, there is continuity of displacement and slope for flap and lag bending deflections, and continuity of displacement for elastic twist and axial deflections. This element insures physically consistent linear variations of bending moments and torsional moments, and quadratic variation of axial force within each element. The dimensional and structural properties are assumed to be uniform throughout each element with the exception of blade pretwist that may be varying in each element. Hamilton's principle is used to derive the kinematic and strain energy that results in blade elemental mass, damping, and stiffness matrices as well as force vector. Gaussian quadrature is used for the integration over each blade element. The blade elemental matrices are then assembled into global matrices which in turn results in the blade equations of motion. For computation efficiency, the governing blade finite element equations are transformed into modal space. The details of blade elemental matrices' derivation, assembly, and modalization are described in Ref [80].

2.3.2 Inertial Effects of Trailing-Edge Flap

This section describes the inertial forces and moments of the blade and hinge moment of trailing-edge flap that are originated from trailing-edge flap motion. Reference [84] details the formulation, and the results are briefly presented below. Because the blade elemental mass properties reflect the entire section including trailing-edge flaps, the inertial terms which are independent of trailing-edge flap motion are already included in the baseline UMARC analysis. The incremental inertial forces and moments acting on the blade that associated with trailing-edge flap motion are shown below. These inertial terms are then added into the force vector of blade equations of motion and the integration of hub loads calculations.

$$\Delta L_u = 0 \tag{2.9}$$

$$
\begin{aligned}
\Delta L_v = {} & -S_f \cdot (\delta_f \overset{\star}{\theta_0}{}^2 \sin\theta_0 - \hat{\phi}\cos\theta_0 \overset{\star\star}{\delta_f} - \delta_f \cos\theta_0 \overset{\star\star}{\delta_f} \\
& - \delta_f \cos\theta_0 \overset{\star\star}{\theta_0} - 2\overset{\star}{\theta_0}\overset{\star}{\delta_f}\cos\theta_0 - \overset{\star}{\delta_f}{}^2 \cos\theta_0 \\
& + \delta_f \sin\theta_0 - \sin\theta_0 \overset{\star\star}{\delta_f})
\end{aligned} \tag{2.10}
$$

$$
\begin{aligned}
\Delta L_w = {} & -S_f \cdot (-\delta_f \overset{\star}{\theta_0}{}^2 \cos\theta_0 - \hat{\phi}\sin\theta_0 \overset{\star\star}{\delta_f} \\
& - \delta_f \sin\theta_0 \overset{\star\star}{\delta_f} - \delta_f \sin\theta_0 \overset{\star\star}{\theta_0} \\
& - 2\overset{\star}{\theta_0}\overset{\star}{\delta_f}\sin\theta_0 - \overset{\star}{\delta_f}{}^2 \sin\theta_0 + \cos\theta_0 \overset{\star\star}{\delta_f})
\end{aligned} \tag{2.11}
$$

$$
\begin{aligned}
\Delta M_x = {} & S_f \cdot (x\,\delta_f \sin\theta_0\,\beta_p + 2\,d\,\delta_f \cos\theta_0^2 - d\,\delta_f \\
& + d\,\overset{\star\star}{\delta_f} + \overset{\star\star}{v}\,\delta_f \cos\theta_0 - \delta_f\,v\,\cos\theta_0 \\
& + \delta_f \sin\theta_0\,\overset{\star\star}{w}) - I_f\,\overset{\star\star}{\delta_f}
\end{aligned} \tag{2.12}
$$

$$\Delta M_y = x\, S_f\, \delta_f\, \cos\theta_0 \tag{2.13}$$

$$\Delta M_z = x\, S_f\, \delta_f\, \sin\theta_0 \tag{2.14}$$

S_f is flap first mass moment of inertia about flap hinge ($S_f = \int\int y_f dm$); I_f is flap second mass moment of inertia about flap hinge ($I_f = \int\int y_f{}^2\, dm$);

The inertial contribution to the trailing-edge flap hinge moment is shown below, and it contains terms originating from both blade deflections and trailing-edge flap motion.

$$
\begin{aligned}
M_h = \; & Sf \cdot ((-2\, d\, \overset{\star}{w}' + d\, \delta + 2\, d\, \hat{\phi})\cos\theta_0^2 \\
& + (\,(d + 2\, d\, \overset{\star}{v}')\sin\theta_0 - x\, w' - x\, \beta_p - 2\, \overset{\star}{v}\, \beta_p - 2\, w'\, \overset{\star}{v} \\
& - \hat{\phi}\, v + x\, v'\, \hat{\phi} + x\, v'\, \delta + \delta\, \overset{\star\star}{v} - \delta\, v + \hat{\phi}\, \overset{\star\star}{v} - \overset{\star\star}{w})\cos\theta_0 \\
& + (\overset{\star\star}{v} - v + x\, \delta\, \beta_p + 2\, \overset{\star}{u} + x\, \hat{\phi}\, \beta_p - 2\, \overset{\star}{w}\, \beta_p + 2\, v'\, \overset{\star}{v} + x\, w'\, \delta \\
& + x\, v' + \delta\, \overset{\star\star}{w} + x\, w'\, \hat{\phi} + \hat{\phi}\, \overset{\star\star}{w})\sin\theta_0 \\
& + d\, \overset{\star\star}{\hat{\phi}} + 2\, d\, \overset{\star}{w}' + d\, \overset{\star\star}{\theta_0} - d\, \hat{\phi} + d\, \delta\, \overset{\star}{\theta_0}{}^2\,) \\
+ \; & If \cdot ((2\, \overset{\star}{w}' - 2\, \delta - 2\, \hat{\phi})\cos\theta_0^2 + (-2\, \overset{\star}{v}' - 1)\sin\theta_0\, \cos\theta_0 + \hat{\phi} \\
& - \overset{\star\star}{\delta} - \overset{\star\star}{\theta_0} - 2\, \overset{\star}{w}' - \overset{\star\star}{\hat{\phi}} + \delta)
\end{aligned} \tag{2.15}
$$

2.4   Aerodynamic Formulation

There are several available aerodynamic models for a flapped airfoil. The Hariharan-Leishman model [55] is incorporated into UMARC for trailing edge flap studies [37].

Based on the indicial method, this model includes compressibility and unsteady effects. However, this model assumes the flap hinge located at the nose of flap, and thus lacks the capability to handle an aerodynamically balanced flap (Figure 2.3). Trailing-edge flap aerodynamic balance (nose overhang) is incorporated to change the aerodynamic characteristics of the airfoil/flap in order to reduce flap hinge moment, and hence actuation power [85]. Flap nose overhang is defined as the hinge offset from the leading-edge of the flap in terms of full chord. The baseline MD-900 flap system was designed with the flap hinge located at 10% chord behind the flap nose. This translates into an overhang of 29% of flap chord for a 30%c flap. To model the aerodynamically balanced flap, quasi-steady models adapted respectively from Theodorsen's theory [64], and table lookup based on test data are used. Theodorsen's theory does not include the compressibility effect which can be significant in transonic flow. For the second model, the blade aerodynamic section coefficients (C_l, C_d, C_m) and flap aerodynamic coefficients (C_h, C_{lf}) are obtained from the table lookup for specific angles of attack (α), Mach Number (M), and trailing-edge flap deflection (δ_f). In the chapter 3, the Theodorsen trailing-edge flap aerodynamic model (Sec. 2.4.1) is used to obtain the results of MD-900, and the Hariharan-Leishman trailing-edge flap aerodynamic model (Sec. 2.4.2) is used to obtain the results of ASI 496. The Bagai-Leishman free wake model [56] is used to obtain induced inflow distribution on the rotor disk.

2.4.1 Theodorsen Flapped Airfoil Aerodynamics Theory

Theodorsen was the first to study the unsteady aerodynamics of an airfoil with trailing-edge flap. In Ref. [74], Theodorsen presents the unsteady lift, pitching moment, and hinge moment coefficients on a thin airfoil with plain trailing-edge flap in an incompressible flow. Ref. [64] extends the work to include the effect of aerodynamic balance and the effect of a tab added to the aileron. Theodorsen theory is based on potential flow and small disturbance principles. This model considers the gap sealed; that is, no leak of fluid between the flap and the base airfoil. The contributions due to non-circulatory loadings were separated from circulatory loadings. Theodorsen theory is in the frequency domain, and uses the $C(k)$ function, which depends only on the oscillatory reduced frequency k ($k = \frac{c\omega}{2V}$), to accounts for the attenuation in magnitude of the lift and also the phase lag between the aerodynamic loads and the oscillating motion. For present analysis, quasi-steady Theodorsen theory is used. That is, $C(k) = 1$, but the non-circulatory terms are retained.

The incremental lift ΔL, pitching moment ΔM, and trailing-edge flap hinge moment H can be expressed in terms of blade and trailing-edge flap deflections, velocities, and accelerations. These incremental force and moments act in the blade deformed coordinate system, and are subsequently transformed to the blade undeformed coordinate system respectively as ΔL_w^A, $\Delta M_{\hat{\phi}}^A$, and $H_{\hat{\delta}}^A$ (Figure 2.1).

$$\Delta L = \frac{\gamma}{6a}[C_{l\delta_f} \cdot \delta_f \cdot U_t^2 + C_{l\overset{\star}{\delta_f}} \cdot \overset{\star}{\delta}_f \cdot U_t + C_{l\overset{\star\star}{\delta_f}} \cdot \overset{\star\star}{\delta}_f]$$

$$\Delta M = \frac{\gamma}{6a}[C_{m\delta_f} \cdot \delta_f \cdot U_t^2 + C_{m\overset{\star}{\delta_f}} \cdot \overset{\star}{\delta}_f \cdot U_t + C_{m\overset{\star\star}{\delta_f}} \cdot \overset{\star\star}{\delta}_f]$$

$$H = \frac{\gamma}{6a}[C_{h\delta_f} \cdot \delta_f \cdot U_t^2 + C_{h\overset{\star}{\delta_f}} \cdot \overset{\star}{\delta}_f \cdot U_t + C_{h\overset{\star\star}{\delta_f}} \cdot \overset{\star\star}{\delta}_f$$

$$+ C_{h\overset{\star}{h}} \cdot (-\overset{\star}{w}) \cdot U_t + C_{h\overset{\star\star}{h}} \cdot (-\overset{\star\star}{w}) + C_{h\alpha} \cdot (-U_t \cdot U_p)$$

$$+ C_{h\overset{\star}{\alpha}} \cdot (\overset{\star}{\theta}_0 + \overset{\star}{\hat{\phi}}) \cdot U_t + C_{h\overset{\star\star}{\alpha}} \cdot (\overset{\star\star}{\theta}_0 + \overset{\star\star}{\hat{\phi}})] \tag{2.16}$$

Using Theodorsen theory for aerodynamically balanced flaps, these coefficients are given by:

$$C_{l\delta} = 2 \cdot (T_{10} - l \cdot T_{21})$$

$$C_{l\overset{\star}{\delta}} = c \cdot l \cdot \left(-T_{10} - \sqrt{1 - e^2}\right) + \frac{1}{2}c \cdot (T_{11} - T_4)$$

$$C_{l\overset{\star\star}{\delta}} = \frac{1}{4}c^2 \cdot (l \cdot T_4 - T_1)$$

$$C_{m\delta} = (-\frac{1}{2})(l \cdot T_{22} + T_{15})$$

$$C_{m\overset{\star}{\delta}} = (-\frac{1}{4})c \cdot (l \cdot T_{23} + T_{16})$$

$$C_{m\overset{\star\star}{\delta}} = (-\frac{1}{8})c^2 \cdot (l \cdot T_{24} + 2T_{13})$$

$$C_{h\alpha} = l \cdot T_{20} - \frac{1}{2}T_{12}$$

$$C_{h\overset{\star}{\alpha}} = \frac{1}{4}c \cdot [\, l \cdot (2T_{20} - T_{25}) - T_{17} - T_{12}]$$

$$C_{h\overset{\star\star}{\alpha}} = \frac{1}{8}c^2 \cdot (-l \cdot T_{24} - 2T_{13})$$

$$C_{h\overset{\star}{h}} = l \cdot T_{20} - \frac{1}{2}T_{12}$$

$$C_{h\overset{\star\star}{h}} = \frac{1}{4}c \cdot (T_1 - l \cdot T_4)$$

$$C_{h\delta} = -\frac{1}{\pi}l^2 \cdot (\frac{1}{2}T_{28} + T_{20}T_{21}) + \frac{1}{2\pi}l \cdot (T_{12}T_{21} - T_{26} + 2T_{20}T_{10})$$

$$- \frac{1}{2\pi} \cdot (T_{18} + T_{12}T_{10})$$

$$C_{h\overset{\star}{\delta}} = \frac{1}{4\pi}c \cdot [\, l^2 \cdot (-2T_{20}T_{10} - T_{29}) + l \cdot (T_{12}T_{10} - T_{27} + T_{20}T_{11})$$

$$- T_{19} - \frac{1}{2} T_{12} T_{11} \,]$$

$$C_{h_{\delta}^{\star\star}} \quad = \quad \frac{1}{8\pi} c^2 \cdot (l^2 \cdot T_5 - l \cdot 2T_2 + T_3) \tag{2.17}$$

where $T_1 \ldots T_{29}$ are Theodorsen geometry constants of an airfoil with trailing-edge flap as defined in A.1.

2.4.2 Hariharan-Leishman Unsteady Flapped Airfoil Aerodynamics Theory

Theodorsen theory has several limitations for practical use in rotorcraft analyses. Theodorsen theory is based on incompressible flow assumption. Incompressible quasi-steady flow assumption is valid when both the local Mach number and reduced frequency are low. However, the flow around the rotor blade tip can be in the high subsonic and even transonic range, the reduced frequency is often high particular when a trailing-edge flap is used for vibration control. Furthermore, Theodorsen theory is in the frequency domain, an analysis in the time domain is more applicable to rotor analysis. Leishman and Hariharan developed a time-domain unsteady flapped airfoil aerodynamic theory by using indicial approach. This model captures the compressibility effect of the non-circulatory lift. The indicial functions for incremental lift, pitching moment and hinge moment resulting from trailing-edge flap deflection and rate are derived for both the circulatory and non-circulatory aerodynamic loads. These function are then updated during the time integration process and reflect the deficiency and phase lag of the aerodynamic response. Hariharan-Leishman model can also predict the unsteady drag of a flapped airfoil. This

model resolves the drag into normal forces, flap forces, and leading-edge suction forces:

$$C_D = \alpha C_N + \delta C_F - \eta C_S \qquad (2.18)$$

where an empirical leading edge recovery factor η is applied to account for viscous effects. In 2D steady inviscid incompressible thin-airfoil theory, where η equal to one, the airfoil drag of airfoil with plain trailing-edge flap predicted by equation 2.18 will be zero (D'Alembert's paradox). The leading edge recovery factor used in the analysis is 0.97, and aerodynamic drag coefficient of the baseline airfoil due to skin friction, C_{D0} is added to the prediction by equation 2.18.

Reference [55] describes the formulation of the unsteady aerodynamics model, and Reference [84] details the implementation in UMARC. However, this model assumes the flap hinge located at the nose of flap, and thus lacks the capability to handle an aerodynamically balanced flap.

2.4.3 Table Lookup

Table lookup method can be used to include the incremental lift, pitching moment, and hinge moment generated by the trailing-edge flap. The blade aerodynamic section coefficients (C_l, C_d, C_m) and flap aerodynamic coefficients (C_h, C_{lf}) are obtained from the table lookup for specific angles of attack (α), Mach Number (M), and trailing-edge flap deflection (δ_f). For the airfoil without a trailing-edge flap, C81 format table lookup using 2D linear interpolation algorithm may be used in UMARC to define the blade aerodynamic coefficients. For a flapped airfoil, C81 format sub-tables are prepared with different trailing-edge flap angles. Two-dimensional interpolation of aerodynamic coefficients

with regard to an arbitrary angle of attack and Mach number is performed using available data. The final aerodynamic coefficients includes the effect from a trailing-edge flap deflection as well as compressibility. The disadvantage of the table lookup method is the limited available airfoil data with trailing-edge flap. The present analysis utilizes airfoil tables for MD-900 blade airfoils; HH10 and HH06, contains a $35\%c$ plain trailing-edge flap with an $10\%c$ nose overhang. The range of trailing-edge flap deflections in the airfoil tables is $\pm 4°$.

2.4.4   Inflow and Free Wake Modeling

The rotor wake determines the inflow distribution on the rotor disk, and plays an important role in the prediction of blade response and loads. Two inflow models are used in the present analysis. Drees inflow model assumes a linear inflow variation for the steady induced inflow velocity.

The Bagai-Leishman free wake model [56] is based on the pseudo-implicit predictor-corrector relaxation scheme. The rotor wake is modeled using free tip vortices. Additional inboard trailed filaments can also be included in the analysis, either as rigid prescribed vortices or as free vortex filaments, or as combination of both. Azimuthal variations in time-varying blade loading can be accounted for by including shed circulation effects in the free wake solution. Key features in this wake model include physical vortex velocity profiles and diffusion models, a multi core vortex model, vortex elements of linearly varying strengths, centroid of vorticity adjustments, provision to superimpose arbitrary external perturbation and maneuvering velocities on the free-wake solution. Computa-

tional acceleration schemes have been developed to reduce execution times.

Although linear inflow model may be sufficient in predicting rotor trim angles, free wake model is important for vibration and loads predictions. Therefore, the free wake model is used in the prediction of trailing-edge flap angles for vibration reduction, and linear inflow model is used for primary rotor control calculations.

2.5 Trailing-Edge Flap Model

Two trailing-edge flap model are used in present analysis depending on either the trailing-edge flap motion is prescribed or calculated. The first model assumes the trailing-edge flap motion prescribed and the second model formulates the trailing-edge flap motion as a degree of freedom. Therefore, the second model includes the actuator dynamics.

2.5.1 Prescribed Trailing-Edge Flap Motion Model

Reference [84] described the implementation of prescribed trailing-edge flap motion model in UMARC. This model assumes the trailing-edge flap undergoing periodic motion at rotor harmonics. These are either prescribed to match wind tunnel test conditions or calculated using the multicyclic control algorithm (Sec. 2.8). The effects of the flap motion in term of inertial (Sec. 2.3) and aerodynamic (Sec. 2.4) forces, are included in the blade equations of motion. The contribution of trailing-edge flap deflection on blade loads and hub loads is also systematically included.

2.5.2 Coupled Blade/Flap/Actuator Model

The actuator and flap are modeled as two separate structural dynamic elements with flap hinge located at an arbitrary chordwise location. The derivation of the coupled blade/actuator/trailing-edge flap equations of motion is based on Hamilton's variational principle generalized for a nonconservative system.

$$\delta\Pi = \int_{t_1}^{t_2} (\delta U - \delta T - \delta W)\, dt = 0 \tag{2.19}$$

δU is the variation of the elastic strain energy, δT is the variation of the kinetic energy, and δW is the work done by nonconservative forces. The blade, actuator, and trailing-edge flap contribute to the energy expressions:

$$\delta U = \delta U_b + \delta U_f + \delta U_a \tag{2.20}$$

$$\delta T = \delta T_b + \delta T_f + \delta T_a \tag{2.21}$$

$$\delta W = \delta W_b + \delta W_f + \delta W_a \tag{2.22}$$

where the subscripts b, a, and f refer to the blade, actuator, and trailing-edge flap respectively. The coordinate systems for blade and flap are shown in Figure 2.1.

Strain Energy

The actuator is modeled by a torsional spring and a torsional damper, which connects the flap with the baseline blade through a hinge located at an arbitrary chordwise portion of flap. The flap motion is indirectly controlled via base motion of the torsional spring. (Figure 2.4) The actuator mass is lumped into the baseline blade mass. The flap is assumed

to be sectionally rigid, and undergoes the same flap bending, lag bending, elastic twist, and axial deformation as the baseline blade but with an additional degree of freedom, flap torsional deflection. The variation of the strain and kinematic energy of the baseline blade includes all the terms that are independent of trailing-edge flap motion. Therefore, the blade sectional structural properties must reflect the entire section, including actuator and trailing-edge flap. The variation of the strain energy of the baseline blade δU_b is not changed by the actuator and flap motion, The variation of the strain energy of actuator and flap are

$$\delta U_a \;=\; k_a \cdot (\delta_f - \delta_a) \cdot \delta(\delta_f) \tag{2.23}$$

$$\delta U_f \;=\; 0 \tag{2.24}$$

where δ_f is angular deflection of flap with respect to blade and δ_a is actuator angular deflection that is prescribed. (Figure 2.4)

Kinetic Energy

The incremental variation of the kinematic energy of the baseline blade due to the flap motion is expressed as follows

$$\begin{aligned}
\delta(\Delta T_b) \;=\; &\int_0^{l_f} (\Delta T_v \cdot \delta v + \Delta T_w \cdot \delta w + \Delta T_{\hat{\phi}} \cdot \delta \Delta \hat{\phi} \\
&+ \Delta T_{v'} \cdot \delta v' + \Delta T_{w'} \cdot \delta w') \, dx
\end{aligned} \tag{2.25}$$

where

$$\Delta T_v \;=\; -S_f \cdot (\delta_f \, \overset{\star}{\theta_0}{}^2 \sin\theta_0 - \hat{\phi} \cos\theta_0 \, \overset{\star\star}{\delta_f} - \delta_f \cos\theta_0 \, \overset{\star\star}{\delta_f}$$

54

$$-\,\delta_f \cos\theta_0\, \overset{\star\star}{\theta_0} - 2\,\overset{\star}{\theta_0}\,\overset{\star}{\delta_f}\cos\theta_0 - \overset{\star}{\delta_f}{}^{2}\cos\theta_0$$

$$+\,\delta_f\sin\theta_0 - \sin\theta_0\,\overset{\star\star}{\delta_f})$$

$$\Delta T_w = -\,S_f\cdot(-\delta_f\,\overset{\star}{\theta_0}{}^{2}\cos\theta_0 - \hat{\phi}\sin\theta_0\,\overset{\star\star}{\delta_f}$$

$$-\,\delta_f\sin\theta_0\,\overset{\star\star}{\delta_f} - \delta_f\sin\theta_0\,\overset{\star\star}{\theta_0}$$

$$-\,2\,\overset{\star}{\theta_0}\,\overset{\star}{\delta_f}\sin\theta_0 - \overset{\star}{\delta_f}{}^{2}\sin\theta_0 + \cos\theta_0\,\overset{\star\star}{\delta_f})$$

$$\Delta T_{\hat{\phi}} = S_f\cdot(x\,\delta_f\sin\theta_0\,\beta_p + 2\,d\,\delta_f\cos\theta_0^2 - d\,\delta_f$$

$$+\,d\,\overset{\star\star}{\delta_f} + \overset{\star\star}{v}\,\delta_f\cos\theta_0 - \delta_f\,v\cos\theta_0$$

$$+\,\delta_f\sin\theta_0\,\overset{\star\star}{w}) - I_f\,\overset{\star\star}{\delta_f}$$

$$\Delta T_{v'} = x\,S_f\,\delta_f\sin\theta_0$$

$$\Delta T_{w'} = x\,S_f\,\delta_f\cos\theta_0 \tag{2.26}$$

The variation of the kinematic energy of the actuator and flap are

$$\delta T_a = 0 \tag{2.27}$$

$$\delta T_f = \int_0^{l_f} T_f\cdot\delta(\delta_f)\,dx \tag{2.28}$$

where

$$T_f = Sf\cdot((-2\,d\,\overset{\star}{w}' + d\,\delta + 2\,d\,\hat{\phi})\cos\theta_0^2$$

$$+\,((d + 2\,d\,\overset{\star}{v}')\sin\theta_0 - x\,w' - x\,\beta_p - 2\,\overset{\star}{v}\,\beta_p - 2\,w'\,\overset{\star}{v}$$

$$-\,\hat{\phi}\,v + x\,v'\,\hat{\phi} + x\,v'\,\delta + \delta\,\overset{\star\star}{v} - \delta\,v + \hat{\phi}\,\overset{\star\star}{v} - \overset{\star\star}{w})\cos\theta_0$$

$$+\,(\overset{\star\star}{v} - v + x\,\delta\,\beta_p + 2\,\overset{\star}{u} + x\,\hat{\phi}\,\beta_p - 2\,\overset{\star}{w}\,\beta_p + 2\,v'\,\overset{\star}{v} + x\,w'\,\delta$$

$$+\,x\,v' + \delta\,\overset{\star\star}{w} + x\,w'\,\hat{\phi} + \hat{\phi}\,\overset{\star\star}{w})\sin\theta_0$$

55

$$+ d\, \overset{\star\star}{\hat{\phi}} + 2\, d\, \overset{\star}{w}' + d\, \overset{\star\star}{\theta_0} - d\, \hat{\phi} + d\, \delta\, \overset{\star}{\theta_0}{}^2\,)$$

$$+ \quad If \cdot ((2\, \overset{\star}{w}' - 2\, \delta - 2\, \hat{\phi})\cos\theta_0^2 + (-2\, \overset{\star}{v}' - 1)\sin\theta_0\,\cos\theta_0 + \hat{\phi}$$

$$- \overset{\star\star}{\delta} - \overset{\star\star}{\theta_0} - 2\, \overset{\star}{w}' - \overset{\star\star}{\hat{\phi}} + \delta) \tag{2.29}$$

S_f is flap first mass moment of inertia about flap hinge ($S_f = \int\int y_f dm$); I_f is flap

second mass moment of inertia about flap hinge ($I_f = \int\int y_f{}^2\, dm$); l_f is flap spanwise

length. These equations contains the same terms as derived in Sec. 2.3.2.

Virtual Work

External aerodynamic forces on the blade contribute to the virtual work of the system.

The incremental virtual work of the baseline blade due to the flap motion is expressed as

follows. For simplicity of analysis, flap drag is currently neglected in the formulation.

$$\delta(\Delta W_b) = \int_0^{l_f} (\Delta L_w^A \cdot \delta w + \Delta M_{\hat{\phi}}^A \cdot \delta\hat{\phi})\, dx$$

$$\delta W_a = -c_a \cdot (\overset{\star}{\delta_f} - \overset{\star}{\delta_a}) \cdot \delta(\delta_f)$$

$$\delta W_f = \int_0^{l_f} H_\delta^A \cdot \delta(\delta_f)\, dx \tag{2.30}$$

where c_a is smart actuator damping; ΔL_w^A, $\Delta M_{\hat{\phi}}^A$, and H_δ^A are shown in Sec. 2.4 with

using Theodorsen theory.

The air velocities (Eqs. 2.82) are functions of blade motions, therefore, many of the

aerodynamic terms in the virtual work are blade motion dependent and contribute to the

element stiffness, damping, and mass matrices.

Coupled System Equations of Motion

Blade, actuator, and trailing-edge flap equations of motion are expressed into the modal space as follows.

$$
\begin{bmatrix} \mathbf{M}_{bb} & \mathbf{M}_{bf} \\ \mathbf{M}_{fb} & \mathbf{M}_{ff} \end{bmatrix} \left\{ \begin{array}{c} \overset{\star\star}{\boldsymbol{\xi}} \\ \overset{\star\star}{\delta_{\mathbf{f}}} \end{array} \right\} + \begin{bmatrix} \mathbf{C}_{bb} & \mathbf{C}_{bf} \\ \mathbf{C}_{fb} & \mathbf{C}_{ff} \end{bmatrix} \left\{ \begin{array}{c} \overset{\star}{\boldsymbol{\xi}} \\ \overset{\star}{\delta_{\mathbf{f}}} \end{array} \right\}
$$

$$
+ \begin{bmatrix} \mathbf{K}_{bb} & \mathbf{K}_{bf} \\ \mathbf{K}_{fb} & \mathbf{K}_{ff} \end{bmatrix} \left\{ \begin{array}{c} \boldsymbol{\xi} \\ \delta_{\mathbf{f}} \end{array} \right\} = \left\{ \begin{array}{c} \mathbf{F}_{bb} \\ \mathbf{F}_{ff} \end{array} \right\} \quad (2.31)
$$

The coupled blade/actuator/trailing-edge flap equations are nonlinear and periodic, and solved using finite elements in space and time. Because the actuation force driving the flap is assumed to be periodic, the trailing-edge flap response will also be periodic. Therefore, periodic boundary conditions are applied to the temporal elements.

The element coupling matrices of mass, stiffness, damping can be partitioned to indicate contributions from axial deflection, flap bending, lag bending, and elastic torsion. They are also classified by their origination due to inertial or aerodynamic forces denoted respectively with superscript of I or A. The inertial part of blade-flap mass, stiffness,

57

damping coupling matrices and nonlinear force vector can be written as:

$$
\underbrace{\left[M_{bf}^{I}\right]}_{15\times1} = \begin{bmatrix} \underbrace{[\mathbf{0}]}_{4\times1} & \underbrace{\left[M_{bfv}^{I}\right]}_{4\times1} & \underbrace{\left[M_{bfw}^{I}\right]}_{4\times1} & \underbrace{\left[M_{bf\phi}^{I}\right]}_{3\times1} \end{bmatrix}^{T}
$$

$$
\underbrace{\left[C_{bf}^{I}\right]}_{15\times1} = \begin{bmatrix} \underbrace{[\mathbf{0}]}_{4\times1} & \underbrace{\left[C_{bfv}^{I}\right]}_{4\times1} & \underbrace{\left[C_{bfw}^{I}\right]}_{4\times1} & \underbrace{[\mathbf{0}]}_{3\times1} \end{bmatrix}^{T}
$$

$$
\underbrace{\left[K_{bf}^{I}\right]}_{15\times1} = \begin{bmatrix} \underbrace{[\mathbf{0}]}_{4\times1} & \underbrace{\left[K_{bfv}^{I}\right]}_{4\times1} & \underbrace{\left[K_{bfw}^{I}\right]}_{4\times1} & \underbrace{\left[K_{bf\phi}^{I}\right]}_{3\times1} \end{bmatrix}^{T}
$$

$$
\underbrace{\left[F_{bf}^{I}\right]}_{15\times1} = \begin{bmatrix} \underbrace{[\mathbf{0}]}_{4\times1} & \underbrace{\left[F_{bfv}^{I}\right]}_{4\times1} & \underbrace{\left[F_{bfw}^{I}\right]}_{4\times1} & \underbrace{\left[F_{bf\phi}^{I}\right]}_{3\times1} \end{bmatrix}^{T}
$$

(2.32)

where

$$
\underbrace{\left[M_{bfv}^{I}\right]}_{4\times1} = \int_{r_i}^{r_o} \underbrace{\mathbf{H}_s^{T}}_{4\times1} (-S_f\sin\theta_0)\ ds
$$

$$
\underbrace{\left[C_{bfv}^{I}\right]}_{4\times1} = \int_{r_i}^{r_o} \underbrace{\mathbf{H}_s^{T}}_{4\times1} (-2S_f\overset{\star}{\theta}_0\cos\theta_0)\ ds
$$

$$
\underbrace{\left[K_{bfv}^{I}\right]}_{4\times1} = \int_{r_i}^{r_o} \underbrace{\mathbf{H}_s^{T}}_{4\times1} S_f(\overset{\star}{\theta}_0^{\,2}\sin\theta_0 + \sin\theta_0 - \overset{\star\star}{\theta}_0\cos\theta_0)\ ds + \int_{r_i}^{r_o} \underbrace{\mathbf{H}_s'^{\,T}}_{4\times1} S_f x\sin\theta_0\ ds
$$

$$
\underbrace{\left[F_{bfv}^{I}\right]}_{4\times1} = \int_{r_i}^{r_o} \underbrace{\mathbf{H}_s^{T}}_{4\times1} S_f(\overset{\star}{\delta}^2 + \hat{\phi}\overset{\star\star}{\delta} + \delta\overset{\star\star}{\delta})\cos\theta_0\ ds
$$

$$
\underbrace{\left[M_{bfw}^{I}\right]}_{4\times1} = \int_{r_i}^{r_o} \underbrace{\mathbf{H}_s^{T}}_{4\times1} (S_f\cos\theta_0)\ ds
$$

$$
\underbrace{\left[C_{bfw}^{I}\right]}_{4\times1} = \int_{r_i}^{r_o} \underbrace{\mathbf{H}_s^{T}}_{4\times1} (-2S_f\overset{\star}{\theta}_0\sin\theta_0)\ ds
$$

$$
\underbrace{\left[K_{bfv}^{I}\right]}_{4\times1} = \int_{r_i}^{r_o} \underbrace{\mathbf{H}_s^{T}}_{4\times1} S_f(-\overset{\star}{\theta}_0^{\,2}\cos\theta_0 - \overset{\star\star}{\theta}_0\sin\theta_0)\ ds + \int_{r_i}^{r_o} \underbrace{\mathbf{H}_s'^{\,T}}_{4\times1} S_f x\cos\theta_0\ ds
$$

$$
\underbrace{\left[F_{bfv}^{I}\right]}_{4\times1} = \int_{r_i}^{r_o} \underbrace{\mathbf{H}_s^{T}}_{4\times1} S_f(\overset{\star}{\delta}^2 + \hat{\phi}\overset{\star\star}{\delta} + \delta\overset{\star\star}{\delta})\sin\theta_0\ ds
$$

$$
\underbrace{\left[M_{bf\phi}^{I}\right]}_{3\times1} = \int_{r_i}^{r_o} \underbrace{\mathbf{H}_\phi^{T}}_{3\times1} (I_f - dS_f)\ ds
$$

$$
\underbrace{\left[K_{bf\phi}^{I}\right]}_{3\times1} = \int_{r_i}^{r_o} \underbrace{\mathbf{H}_\phi^{T}}_{3\times1} (-S_f)(-d + \beta_p\sin\theta_0 x S_f + 2d\cos\theta_0^2)\ ds
$$

58

$$\underbrace{\left[F^I_{bf\phi}\right]}_{3\times1} = \int_{r_i}^{r_o} \underbrace{\mathbf{H}_\phi^T}_{3\times1} S_f(\sin\theta_0 \overset{\star\star}{w} + \cos\theta_0 \overset{\star\star}{v} - \cos\theta_0 v)\delta \ ds$$

$$\tag{2.33}$$

The inertial part of flap-blade mass, stiffness, and damping coupling matrices can

be written as:

$$\underbrace{\left[M^I_{fb}\right]}_{1\times15} = \left[\ \underbrace{[\mathbf{0}]}_{1\times4} \ \underbrace{\left[M^I_{fbv}\right]}_{1\times4} \ \underbrace{\left[M^I_{fbw}\right]}_{1\times4} \ \underbrace{\left[M^I_{fb\phi}\right]}_{1\times3} \ \right]$$

$$\underbrace{\left[C^I_{fb}\right]}_{1\times15} = \left[\ \underbrace{\left[C^I_{fbu}\right]}_{1\times4} \ \underbrace{\left[C^I_{fbv}\right]}_{1\times4} \ \underbrace{\left[C^I_{fbw}\right]}_{1\times4} \ \underbrace{[\mathbf{0}]}_{1\times3} \ \right] \tag{2.34}$$

$$\underbrace{\left[K^I_{fb}\right]}_{1\times15} = \left[\ \underbrace{[\mathbf{0}]}_{1\times4} \ \underbrace{\left[K^I_{fbv}\right]}_{1\times4} \ \underbrace{\left[K^I_{fbw}\right]}_{1\times4} \ \underbrace{\left[K^I_{fb\phi}\right]}_{1\times3} \ \right]$$

where

$$\underbrace{\left[M^I_{fbv}\right]}_{1\times4} = \int_{r_i}^{r_o} (-S_f\sin\theta_0) \underbrace{\mathbf{H}_s}_{1\times4} \ ds$$

$$\underbrace{\left[M^I_{fbw}\right]}_{1\times4} = \int_{r_i}^{r_o} (S_f\cos\theta_0) \underbrace{\mathbf{H}_s}_{1\times4} \ ds$$

$$\underbrace{\left[M^I_{fb\phi}\right]}_{1\times3} = \int_{r_i}^{r_o} (I_f - dS_f) \underbrace{\mathbf{H}_\phi}_{1\times3} \ ds$$

$$\underbrace{\left[C^I_{fbu}\right]}_{1\times4} = \int_{r_i}^{r_o} (2S_f\sin\theta_0) \underbrace{\mathbf{H}_u}_{1\times4} \ ds$$

$$\underbrace{\left[C^I_{fbv}\right]}_{1\times4} = \int_{r_i}^{r_o} (2\beta_p\cos\theta_0 S_f) \underbrace{\mathbf{H}_s}_{1\times4} \ ds + \int_{r_i}^{r_o} 2\cos\theta_0\sin\theta_0(I_f - dS_f) \underbrace{\mathbf{H}'_s}_{1\times4} \ ds$$

$$\underbrace{\left[C^I_{fbw}\right]}_{1\times4} = \int_{r_i}^{r_o} (2\beta_p\sin\theta_0 S_f) \underbrace{\mathbf{H}_s}_{1\times4} \ ds + \int_{r_i}^{r_o} 2\sin^2\theta_0(I_f - dS_f) \underbrace{\mathbf{H}'_s}_{1\times4} \ ds$$

$$\underbrace{\left[K^I_{fbv}\right]}_{1\times4} = \int_{r_i}^{r_o} (S_f\sin\theta_0) \underbrace{\mathbf{H}_s}_{1\times4} \ ds + \int_{r_i}^{r_o} (-x\sin\theta_0 S_f) \underbrace{\mathbf{H}'_s}_{1\times4} \ ds$$

$$\underbrace{\left[K^I_{fbw}\right]}_{1\times4} = \int_{r_i}^{r_o} (x\cos\theta_0 S_f) \underbrace{\mathbf{H}'_s}_{1\times4} \ ds$$

$$\underbrace{\left[K_{fb\phi}^I\right]}_{1\times 3} = \int_{r_i}^{r_o} \left((-x\beta_p\sin\theta_0 S_f + (\cos^2\theta_0 - \sin^2\theta_0)(I_f - dS_f)) \underbrace{\mathbf{H}_\phi}_{1\times 3} \right) ds \quad (2.35)$$

The inertial part of nonlinear flap-flap force, which is a scalar, can be written as:

$$
\begin{aligned}
\underbrace{F_{fb\phi}^I}_{1\times 1} = \int_{r_i}^{r_o} \Bigg(& (-\overset{\star\star}{\theta}_0 - \cos\theta_0\sin\theta_0)(I_f - dS_f) - x\beta_p\cos\theta_0 S_f \\
& + S_f\Big(\delta\big((\overset{\star\star}{v} + xv' - v)\cos\theta_0 + (xw' + \overset{\star\star}{w})\sin\theta_0\big) \\
& + (xv'\hat{\phi} + \overset{\star\star}{v}\hat{\phi} - \hat{\phi}v - 2w'\overset{\star}{v})\cos\theta_0 \\
& + (\hat{\phi}\overset{\star\star}{w} + 2v'\overset{\star}{v} + xw'\hat{\phi})\sin\theta_0\Big) \Bigg) ds
\end{aligned}
\quad (2.36)
$$

The interpolating polynomials for the shape functions, H_u, H_s, and H_ϕ, are detailed in Ref. [80].

Unlike the inertial loads, which are derived in blade undeformed frame, and do not require coordinate transformation, the aerodynamic loads are obtained in the deformed frame and these need to be transformed to the undeformed frame using the transformation matrices T_{DL}^T (Sec. 2.1).

The aerodynamic part of linear blade-flap mass, stiffness, damping coupling matrices and nonlinear force vector can be written as

$$
\begin{aligned}
\underbrace{\left[M_{bf}^A\right]}_{15\times 1} &= \left[\begin{array}{cccc} \underbrace{[\mathbf{0}]}_{4\times 1} & \underbrace{\left[M_{bfv}^A\right]}_{4\times 1} & \underbrace{\left[M_{bfw}^A\right]}_{4\times 1} & \underbrace{\left[M_{bf\phi}^A\right]}_{3\times 1} \end{array} \right]^T \\
\underbrace{\left[C_{bf}^A\right]}_{15\times 1} &= \left[\begin{array}{cccc} \underbrace{[\mathbf{0}]}_{4\times 1} & \underbrace{\left[C_{bfv}^A\right]}_{4\times 1} & \underbrace{\left[C_{bfw}^A\right]}_{4\times 1} & \underbrace{\left[C_{bf\phi}^A\right]}_{3\times 1} \end{array} \right]^T \\
\underbrace{\left[K_{bf}^A\right]}_{15\times 1} &= \left[\begin{array}{cccc} \underbrace{[\mathbf{0}]}_{4\times 1} & \underbrace{\left[K_{bfv}^A\right]}_{4\times 1} & \underbrace{\left[K_{bfw}^A\right]}_{4\times 1} & \underbrace{\left[K_{bf\phi}^A\right]}_{3\times 1} \end{array} \right]^T \\
\underbrace{\left[F_{bf}^A\right]}_{15\times 1} &= \left[\begin{array}{cccc} \underbrace{[\mathbf{0}]}_{4\times 1} & \underbrace{\left[F_{bfv}^A\right]}_{4\times 1} & \underbrace{\left[F_{bfw}^A\right]}_{4\times 1} & \underbrace{\left[F_{bf\phi}^A\right]}_{3\times 1} \end{array} \right]^T
\end{aligned}
\quad (2.37)
$$

where

$$
\underbrace{\left[M_{bfv}^{A}\right]}_{4\times1} = -\frac{\gamma}{6a} \int_{r_i}^{r_o} \underbrace{\mathbf{H}_s{}^{T}}_{4\times1} \left(-\sin\theta_0 c_{l\overset{\star\star}{\delta}}\right) ds
$$

$$
\underbrace{\left[M_{bfw}^{A}\right]}_{4\times1} = -\frac{\gamma}{6a} \int_{r_i}^{r_o} \underbrace{\mathbf{H}_s{}^{T}}_{4\times1} \left(\cos\theta_0 c_{l\overset{\star\star}{\delta}}\right) ds
$$

$$
\underbrace{\left[M_{bf\phi}^{A}\right]}_{3\times1} = -\frac{\gamma}{6a} \int_{r_i}^{r_o} \underbrace{\mathbf{H}_\phi{}^{T}}_{3\times1} \left(c_{m\overset{\star\star}{\delta}}\right) ds
$$

$$
\underbrace{\left[C_{bfv}^{A}\right]}_{4\times1} = -\frac{\gamma}{6a} \int_{r_i}^{r_o} \underbrace{\mathbf{H}_s{}^{T}}_{4\times1} \left(-\sin\theta_0\, tc\, c_{l\overset{\star}{\delta}}\right) ds
$$

$$
\underbrace{\left[C_{bfw}^{A}\right]}_{4\times1} = -\frac{\gamma}{6a} \int_{r_i}^{r_o} \underbrace{\mathbf{H}_s{}^{T}}_{4\times1} \left(\cos\theta_0\, tc\, c_{l\overset{\star}{\delta}}\right) ds
$$

$$
\underbrace{\left[C_{bf\phi}^{A}\right]}_{4\times1} = -\frac{\gamma}{6a} \int_{r_i}^{r_o} \underbrace{\mathbf{H}_\phi{}^{T}}_{4\times1} \left(tc\, c_{m\overset{\star}{\delta}}\right) ds
$$

$$
\underbrace{\left[K_{bfv}^{A}\right]}_{4\times1} = -\frac{\gamma}{6a} \int_{r_i}^{r_o} \underbrace{\mathbf{H}_s{}^{T}}_{4\times1} \left(-\sin\theta_0\, tt0\, c_{l\delta}\right) ds
$$

$$
\underbrace{\left[K_{bfw}^{A}\right]}_{4\times1} = -\frac{\gamma}{6a} \int_{r_i}^{r_o} \underbrace{\mathbf{H}_s{}^{T}}_{4\times1} \left(\cos\theta_0\, tt0\, c_{l\delta}\right) ds
$$

$$
\underbrace{\left[K_{bf\phi}^{A}\right]}_{4\times1} = -\frac{\gamma}{6a} \int_{r_i}^{r_o} \underbrace{\mathbf{H}_\phi{}^{T}}_{4\times1} \left(tt0\, c_{m\delta}\right) ds
$$

(2.38)

The aerodynamic part of linear flap-blade mass, stiffness, damping coupling matrices and nonlinear force vector can be written as

$$
\underbrace{\left[M_{fb}^{A}\right]}_{15\times1} = \left[\underbrace{[\mathbf{0}]}_{4\times1} \quad \underbrace{[\mathbf{0}]}_{4\times1} \quad \underbrace{\left[M_{fbw}^{A}\right]}_{4\times1} \quad \underbrace{\left[M_{fb\phi}^{A}\right]}_{3\times1} \right]^{T}
$$

$$
\underbrace{\left[C_{fb}^{A}\right]}_{15\times1} = \left[\underbrace{[\mathbf{0}]}_{4\times1} \quad \underbrace{\left[C_{fbv}^{A}\right]}_{4\times1} \quad \underbrace{\left[C_{fbw}^{A}\right]}_{4\times1} \quad \underbrace{\left[C_{fb\phi}^{A}\right]}_{3\times1} \right]^{T}
$$

$$
\underbrace{\left[K_{fb}^{A}\right]}_{15\times1} = \left[\underbrace{\left[K_{fbu}^{A}\right]}_{4\times1} \quad \underbrace{\left[K_{fbv}^{A}\right]}_{4\times1} \quad \underbrace{\left[K_{fbw}^{A}\right]}_{4\times1} \quad \underbrace{\left[K_{fb\phi}^{A}\right]}_{3\times1} \right]^{T}
$$

(2.39)

2.6 Vehicle Trim and Blade Response Analysis

Vehicle trim can be categorized into "free flight trim" and "wind tunnel trim", and both are used in present analysis. Free flight trim refers to an equilibrium of three forces and three moments on the aircraft, including the rotor steady forces. The wind tunnel trim procedure involves adjusting the controls to achieve zero first harmonic blade flapping, with a prescribed thrust level and shaft angles. The rotor system loads depend on the blade response, so the determination of aircraft trim and blade response is coupled together, and is solved simultaneously here. This procedure is refereed to as "coupled trim". The trim solution and blade/trailing-edge flap responses are updated iteratively until the convergence criteria is satisfied.

This section describes the formulation of vehicle trim equations, the solutions of blade response equations, and the calculations of coupled trim procedure. The trim equations are same for either conventional swashplate control system or swashplateless trailing-edge flap system. The difference is the control angles, respectively rotor pitch angles for a conventional system and trailing-edge flap angles for a swashplateless system. Section 2.9 details the coupled trim procedure of swashplateless trailing-edge flap rotor system, however, some common solution procedures are shared by both the conventional and swashplateless rotors.

2.6.1 Vehicle Trim Equations

The vehicle trim equations consist of the definitions of two vectors describing the state of trim: the residuals of vehicle trim equation, and the control angles. The residuals depends

on the control angles and the blade response, and the control angles are the quantities to be solved in the coupled trim procedure. The present analysis offers both free-flight and wind tunnel trim solutions.

Free-Flight Propulsive Trim

Free flight trim assumes steady level flight. The trim residual defines the equilibrium balance of aircraft forces and moments. Equations 2.40 defines the force residuals, consisting of the three forces (vertical, longitudinal and lateral) and three moments (pitch, roll, yaw) vehicle equilibrium equations. The trim unknowns will be rotor pitch angles, θ_0, θ_{1c}, θ_{1s}, aircraft orientation, α_s, ϕ_s, and tail rotor collective pitch, θ_{tail}.

$$
\begin{aligned}
F_1 &= D_F \cos\left(\theta_{FP}\right) + H \cos\left(\alpha_s\right) - T \sin\left(\alpha_s\right) \\[2mm]
F_2 &= Y_F + Y \cos\left(\phi_s\right) + T \sin\left(\phi_s\right) + T_{tr} \\[2mm]
F_3 &= T \cos\left(\alpha_s\right) \cos\left(\phi_s\right) - D_F \sin\left(\theta_{FP}\right) + H \sin\left(\alpha_s\right) - Y \sin\left(\phi_s\right) - W - L_{ht} \\[2mm]
F_4 &= M_{xR} + M_{xF} + Y_F \left(\bar{h} \cos\left(\phi_s\right) + \sin\left(\phi_s\right) Y_{cg}\right) \\[2mm]
&\quad + W \left(\bar{h} \sin\left(\phi_s\right) - \cos\left(\phi_s\right) Y_{cg}\right) + T_{tr} \left(\bar{h} - z_{tr}\right) \\[2mm]
F_5 &= M_{yR} + M_{yF} + W \left(\bar{h} \sin\left(\alpha_s\right) - X_{cg} \cos\left(\alpha_s\right)\right) \\[2mm]
&\quad - D_F \left(\cos(\alpha_s + \theta_{FP})\,\bar{h} + \sin(\alpha_s + \theta_{FP})\, X_{cg}\right) + L_{ht} \left(x_{ht} - X_{cg}\right) \\[2mm]
F_6 &= M_{zR} + M_{zF} + T_{tr} \left(x_{tr} - X_{cg}\right) - D_F Y_{cg} \cos\alpha_s - Y X_{cg} \cos\phi_s \qquad (2.40)
\end{aligned}
$$

Wind Tunnel Trim

A typical wind tunnel trim procedure involves adjusting the controls to achieve zero first harmonic blade flapping for a prescribed C_T/σ and shaft tilt angles (α_s and ϕ_s). This can be expressed as a system of equations:

$$F(\boldsymbol{\theta}) = \boldsymbol{\beta} - \boldsymbol{\beta}_{prescribed} = \mathbf{0} \tag{2.41}$$

where $\boldsymbol{\theta} = \{\theta_0 \ \ \theta_{1c} \ \ \theta_{1s}\}$, $\boldsymbol{\beta} = \{C_T/\sigma \ \ \beta_{1c} \ \ \beta_{1s}\}$, and in the present study $\boldsymbol{\beta}_{prescribed} = \{0.075 \ \ 0 \ \ 0\}$. Blade zero first harmonic flapping angle, β_{1c} and β_{1s} are defined as the blade tip deflection slope, w'_{1c} and w'_{1s}. Rotor shaft angles are prescribed to simulate forward flight conditions.

2.6.2   Blade Response Equations

The blade response equations are derived from the Hamilton's principle. After spatial discretization, the finite element equations can be expressed as:

$$M\overset{\star\star}{q} + C(\psi)\overset{\star}{q} + K(\psi)q = F(\psi, q) \tag{2.42}$$

These equations are in the generalized form of equations of motion in finite element discretized form. It may represent the blade response equations either in rotating or fixed frame. It can also contain additional degree of freedom such as trailing-edge flap deflection in the case of coupled blade/flap/actuator equations (Sec. 2.5.2) or rotor teetering angle in the case of teetering rotor (Sec. 2.6.6). The solution procedure of this equations is also generalized using finite element in time method.

Normal Mode Analysis

To reduce computational time, the blade finite element equations are transformed into the normal mode space by using the blade natural rotating vibration modes about its mean deflected position. The blade global displacement vector q_b is represented in terms of m modes $q_b = \Phi P_b$, and then substituting, results in the normal mode equations for the blade,

$$\bar{M}\overset{\star\star}{P_b} + \bar{C}\overset{\star}{P_b} + \bar{K}P_b - \bar{F} = 0 \tag{2.43}$$

where

$$\begin{aligned}
\bar{M} &= \Phi^T M_b \Phi \\
\bar{C} &= \Phi^T C_b \Phi \\
\bar{K} &= \Phi^T K_b \Phi \\
\bar{F} &= \Phi^T F_b
\end{aligned} \tag{2.44}$$

Finite Element Method in Time

The temporal finite element method based on the Hamilton's principle in weak form is used to solve the normal mode equations. The temporal nodal coordinates are denoted by ξ. Using Hamilton's principle, the blade normal mode equations are rewritten in the form,

$$Q^G + K_t^G \Delta \xi^G = 0 \tag{2.45}$$

where

$$Q^G = \sum_{i=1}^{N_t} \int_{\psi_i}^{\psi_{i+1}} N^T Q_i d\psi \tag{2.46}$$

and ξ^G is the global temporal nodal coordinate vector.

$$K_t^G = \sum_{i=1}^{N_t} \int_{\psi_i}^{\psi_{i+1}} N^T K_{ti} N d\psi \tag{2.47}$$

$$\Delta \xi^G = \sum_{i=1}^{N_t} \Delta \xi_i \tag{2.48}$$

$$\mathbf{Q_i} = \left\{ \begin{array}{c} \bar{F} - \bar{C}\overset{\star}{P_b} - \bar{K}P_b \\[2mm] \bar{M}\overset{\star}{P_b} \end{array} \right\} \tag{2.49}$$

$$\mathbf{K_{ti}} = \left[\begin{array}{cc} \frac{\partial \bar{F}}{\partial P_b} - \bar{K} & \frac{\partial \bar{F}}{\partial \overset{\star}{P_b}} - \bar{C} \\[3mm] 0 & \bar{M} \end{array} \right] \tag{2.50}$$

$$\mathbf{N} = \left\{ \begin{array}{c} H_t(\psi) \\[2mm] \overset{\star}{H}_t(\psi) \end{array} \right\} \tag{2.51}$$

For the ith time element, the time variation of the modal displacement vector can be expressed in terms of shape functions, $\mathbf{H_t}$, and the temporal nodal displacement vector, $\xi_\mathbf{i}$, as

$$P_{bi}(\psi) = H_t(s)\xi_i \tag{2.52}$$

where the local temporal coordinates for the ith time element is

$$s = \frac{\psi - \psi_i}{\psi_{i+1} - \psi_i} \tag{2.53}$$

$\mathbf{H_t}(s)$ is the temporal shape function matrix which has the form

$$\mathbf{H_t} = \left[H_{t1}I_m, \ldots, H_{t_{n_t}+1}Im \right] \tag{2.54}$$

66

For example, the 3rd order shape functions are as follows:

$$H_{t1}(s) = -4.50\,s^3 + 9.00\,s^2 - 5.50\,s + 1.0$$

$$H_{t2}(s) = 13.50\,s^3 - 22.50\,s^2 + 9.00\,s$$

$$H_{t3}(s) = -13.50\,s^3 + 18.00\,s^2 - 4.50\,s$$

$$H_{t4}(s) = 4.50\,s^3 - 4.50\,s^2 + s$$

$$\overset{\star}{H}_{t1}(s) = -13.50\,s^2 + 18.0\,s - 5.50$$

$$\overset{\star}{H}_{t2}(s) = 40.50\,s^2 - 45.0\,s + 9.00$$

$$\overset{\star}{H}_{t3}(s) = -40.50\,s^2 + 36.0\,s - 4.50$$

$$\overset{\star}{H}_{t4}(s) = 13.50\,s^2 - 9.0\,s + 1.00 \tag{2.55}$$

The blade global displacement vector Q_b is finally represented as

$$Q_b = \Phi H_t(s)\xi \tag{2.56}$$

Equation 2.45 is solved subject to the boundary conditions:

$$\xi(0) = \xi(2\pi)$$

$$\overset{\star}{\xi}(0) = \overset{\star}{\xi}(2\pi) \tag{2.57}$$

2.6.3   Hub Loads and Blade Sectional Loads

Rotor hub loads are calculated using a force summation method. The sum of blade and trailing-edge flap inertial and aerodynamics loads is integrated over the blade span to yield the loads reacted at the rotor hub in rotating frame. The loads in rotating frame are then transformed to the fixed system and summed through the total number of blades.

Because the present analysis assumes identical blades, the resulted hub loads only consists of integer factor of N_b/rev components whereas other harmonics are filtered out by the rotor. The steady components ($0/rev$) of hub loads are then used in the vehicle trim analysis. The N_b/rev vibratory hub loads are taken as the indication of vehicle vibration levels, and used in the multicyclic control algorithm (Sec 2.8) for vibration reduction predictions. It is recognized that different rotor configurations will be more sensitive to different component of loads, and this variability is modeled by varying the weighting matrix acting on the hub loads.

Blade sectional loads, i.e blade structural moments, are used in validation study by comparing with measurements in wind tunnel test. These moments consist of blade flapwise bending, chordwise bending, and torsional moments, and are acting on blade deformed rotating frame. All the forces and moments yielded from elements outboard of the station of interest are integrated including the contribution of trailing-edge flaps.

2.6.4   Coupled Trim Procedure

The coupled blade and trailing-edge flap responses and the trim control settings were solved simultaneously to calculate either the wind tunnel trim or free flight trim solutions. The values of trim unknowns, $\boldsymbol{\theta}$ that satisfy trim equations (2.40 and 2.41) are determined iteratively using the Newton-Raphson method:

$$\boldsymbol{\theta}_{i+1} = \boldsymbol{\theta}_i + \Delta\boldsymbol{\theta}_i \tag{2.58}$$

where $\boldsymbol{\theta} = \{\alpha_s, \phi_s, \theta_0, \theta_{1c}, \theta_{1s}, \theta_{TR}\}$ for free flight trim and $\boldsymbol{\theta} = \{\theta_0, \theta_{1c}, \theta_{1s}\}$ for wind tunnel trim. $\Delta\theta_i$ is obtained with trim equations linearized about the trim controls using

a Taylor's series expansion:

$$\boldsymbol{F}(\boldsymbol{\theta}_i + \Delta\boldsymbol{\theta}_i) = \boldsymbol{F}(\boldsymbol{\theta}_i) + \frac{\partial \boldsymbol{F}}{\partial \boldsymbol{\theta}}\Big|_{\boldsymbol{\theta}=\boldsymbol{\theta}_0}\Delta\boldsymbol{\theta}_i \tag{2.59}$$

The Jacobian matrix $\frac{\partial \boldsymbol{F}}{\partial \boldsymbol{\theta}}$ used in equation (2.59) is obtained via a forward difference method by perturbing the individual controls in $\boldsymbol{\theta}$. The initial value for the trim algorithm is provided by a reduced order rigid blade response model. The trim solution and blade responses are updated iteratively until the convergence criteria are reached.

1. Convergence of solution of equations of motion.

$$\xi_1{}^* = \frac{\|\Delta\boldsymbol{\xi}\|_2}{\|\boldsymbol{\xi}\|_2} \tag{2.60}$$

2. Convergence of trim equations.

$$\xi_2{}^* = \|\boldsymbol{F}\|_2 \tag{2.61}$$

To reduce computation time, the solutions of blade equations of motion are not fully converged in each coupled trim iteration. As shown in the coupled trim flow chart (Figure. 2.6), the solutions of blade equations of motion and trim equations are each updated once in each iteration. This procedure has been proved to be robust for conventional rotor. However, using the same procedure for swashplateless rotor is not quite successful. Because the swashplateless rotor is extremely torsional soft, there are significant nonlinear terms that contribute significantly to the blade response solution. Therefore, blade equations of motion of swashplateless rotor must be converged in each trim iteration. If free wake model is chosen in the calculation, the free wake convergence is reached in every coupled trim iteration. However, in order to reduce computation time, a loose convergence criteria of free wake geometry is used in the early stage of coupled trim procedure,

and a strict convergence criteria is used in the final stage when blade response equations are well converged to achieve an accurate wake geometry.

2.6.5   Bearingless Rotor Model

The bearingless rotor is a specialized case of hingeless rotor wherein the pitch bearing, in addition to the flap and lag hinges, is eliminated. The blade is attached to the hub by means of a dual load path flexbeam and torque tube assembly. The torsional loads are primarily carried through the torsionally stiff torque tube. The torque tube is attached to the hub by an elastomeric snubber. The torsionally soft flexbeam functions effectively as a pitch bearing. Current rotor designs tend towards bearingless rotors because they offers reduced maintenance costs (fewer parts), better hub design (simple and clean aerodynamically), and superior handling qualities. The present analysis employs a bearingless rotor model featuring multiple load paths for flexbeam/torque tube configuration, viscoelastic snubber, kinematics of control linkage, and nonlinear bending-torsion coupling within the flexbeam as described in Ref. [86].

2.6.6   Teetering Rotor Model

The present analysis implements a teetering rotor model [87] by adding an additional degree of freedom involved in teetering rotor, i.e., rotor teetering angle. The two blades of a teetering rotor are attached together, and hinged at the rotational axis, and have no independent flap and lead/lag offset hinges. The blades have a common flapping axis, however each blade has a separate pitch bearing that allows cyclic and collective pitch

change capability. The teetering design has the advantage of being mechanically simple with a lower number of parts, and is easy to maintain. The teetering head lets various forces from the blades balance themselves. Since the teetering rotor is normally stiff-in-plane, it is not subject to ground resonance instability. Precone angle is typically built into the rotor hub in order to reduce steady stresses in the blades. An undersling design is also adopted in order to reduce Coriolis forces induced by teetering motion. For articulated, hingeless, and bearingless rotors with identical blades, it is usually sufficient to trace only the motion of one blade. The motion of other blades is phase shifted with respect to the reference blade. Thus, blade equations of motion consist of the degrees of one blade and can be formulated on either hub rotating or fixed frame. In the analysis of the teetering rotor, it is necessary to treat two blades simultaneously because two blades are rigidly connected to each other and attached to the mast through a common flapping hinge. The equations of motion of teetering rotor are normally derived in hub fixed system as described in Ref. [88].

2.6.7 Main Rotor Shaft Power

The main rotor power is calculated by

$$\boldsymbol{P_r} = -M_{z0}\Omega \tag{2.62}$$

Figure of merit is calculated in hover by;

$$\boldsymbol{FM} = C_T\sqrt{C_T/2}/C_Q \tag{2.63}$$

2.6.8 Trailing-Edge Flap Actuation Power

The actuation power of the flap system is calculated by integrating the product of the hinge moment and flap deflection rate over one complete rotor revolution. Although the instantaneous power required at the flap hinge may be negative over some portions of the azimuth, it is assumed that the actuator is unable to transfer the power back to its power supply, so that the negative power is neglected. Therefore, the actuation power of the flap system is:

$$\boldsymbol{P_f} = \frac{N_b}{2\pi} \int_0^{2\pi} max(-M_h \overset{\star}{\delta}, 0) d\psi \tag{2.64}$$

where N_b is number of blades, M_h is flap hinge moment and $\overset{\star}{\delta}$ is flap velocity. The actuation power presented in equation 2.64 is "ideal" because it only includes the energy used to drive the flap system, and neglects the heat dissipation of the smart actuators (i.e., actuators' efficiency).

For actuation requirement of flap actuators, it is sometime important to take account of both the required driving force, i.e the hinge moment, and the actuation stroke, the trailing-edge flap angles. The trailing-edge flap energy is defined as below:

$$\boldsymbol{P_e} = \frac{N_b}{2\pi} \int_0^{2\pi} -M_h \delta d\psi \tag{2.65}$$

Trailing-edge flap actuation power is an indication of power consumption of the flap system while actuation energy presents the capability of smart actuators to provide the required force and stroke combinations simultaneously.

2.7 Aeroelastic Stability Analysis

This section describes the procedures implemented to predict the aeroelastic stability characteristics of trailing-edge flap helicopter rotor. The coupled blade equations of motion were linearized by using small perturbations about a steady trimmed solution. Stability was then determined from an eigenanalysis of the homogeneous equations using either Floquet method or constant coefficient approximations. The trailing-edge flap motion is included as an additional degree of freedom in this study, and the stability of the trailing-edge flap mode is properly predicted.

2.7.1 Assembly of the System Equations

System equations are again based on the application of Hamilton's Principle. The degree of freedoms or state variables (blade deflections and trailing-edge flap motion) are assumed as small perturbations about the trimmed position. The work and energies associated with the perturbation motion can be written as the sum of steady and perturbed parts:

$$\int_{t_1}^{t_2} (\delta U_0 - \delta T_0 - \delta W_0)\, dt + \int_{t_1}^{t_2} (\delta \Delta U_0 - \delta \Delta T_0 - \delta \Delta W_0)\, dt = \mathbf{0} \qquad (2.66)$$

The steady state trim equations satisfy the equations

$$\int_{t_1}^{t_2} (\delta U_0 - \delta T_0 - \delta W_0)\, dt = \mathbf{0} \qquad (2.67)$$

so the work and energy variations corresponding to the small perturbation motion become

$$\int_{t_1}^{t_2} (\delta \Delta U_0 - \delta \Delta T_0 - \delta \Delta W_0)\, dt = \mathbf{0} \qquad (2.68)$$

Therefore, the perturbation symbol may be dropped with the understanding that all the state variables represent perturbation quantities about the trim position. Rotor-flap perturbation equations are shown below. The blade equations of motions are coupled with flap motion because of aerodynamic and inertial loading on the blade is changed due to flap deflection. The trailing-edge flap equation contains the effect of blade motions because they contribute to the calculations of hinge moment which determines the flap motion. The trailing-edge flap matrices include actuator dynamics. The matrices in equation 2.69 contains the blade/flap/actuator mass, stiffness, and damping matrices and linearized force matrices ($\frac{\partial \bar{F}}{\partial P}, \frac{\partial \bar{F}}{\partial \overset{\star}{P}}$).

$$
\begin{matrix} Rotor: \\ Flap: \end{matrix}
\begin{bmatrix} \mathbf{M}_{RR} & \mathbf{M}_{RF} \\ \mathbf{M}_{FR} & \mathbf{M}_{FF} \end{bmatrix}
\left\{ \begin{matrix} \Delta \overset{\star\star}{\mathbf{Q}_R} \\ \Delta \overset{\star\star}{\mathbf{Q}_F} \end{matrix} \right\}
+
\begin{bmatrix} \mathbf{C}_{RR} & \mathbf{C}_{RF} \\ \mathbf{C}_{FR} & \mathbf{C}_{FF} \end{bmatrix}
\left\{ \begin{matrix} \Delta \overset{\star}{\mathbf{Q}_R} \\ \Delta \overset{\star}{\mathbf{Q}_F} \end{matrix} \right\}
$$

$$
+
\begin{bmatrix} \mathbf{K}_{RR} & \mathbf{K}_{RF} \\ \mathbf{K}_{FR} & \mathbf{K}_{FF} \end{bmatrix}
\left\{ \begin{matrix} \Delta \mathbf{Q}_R \\ \Delta \mathbf{Q}_F \end{matrix} \right\}
= \mathbf{0} \quad (2.69)
$$

The mass, stiffness, and damping matrices as well as the linearized force matrices are already derived in Sec 2.5.2 (The linearized force matrices are required in finite element in time method as shown in equation 2.47). The mass matrices is the same as the one in coupled blade/flap/actor equations of motion (Eq. 2.31). The stiffness and damping matrices are based on the stiffness and damping matrices in Eq. 2.31 and include the linearized force matrices ($\frac{\partial \bar{F}}{\partial P}, \frac{\partial \bar{F}}{\partial \overset{\star}{P}}$) respectively. The linearized force matrices are functions of blade response. They are evaluated at trim condition with both the blade response equations and trim equations fully converged.

2.7.2 Stability Analysis Procedure

In the stability analysis procedure, Eq. 2.69 is rewritten in the first order form as:

$$\overset{\star}{\mathbf{Y}} = \mathbf{AY} \tag{2.70}$$

with the state variable vector as:

$$\mathbf{Y} = \left\{ \begin{array}{c} \overset{\star}{Q_b} \\ \overset{\star}{\delta} \\ Q_b \\ \delta \end{array} \right\} \tag{2.71}$$

and matrix A as:

$$\mathbf{A} = - \begin{bmatrix} \mathbf{M}_{RR} & \mathbf{M}_{RF} & \mathbf{0} & \mathbf{0} \\ \mathbf{M}_{FR} & \mathbf{M}_{FF} & \mathbf{0} & \mathbf{0} \\ \mathbf{0} & \mathbf{0} & \mathbf{I} & \mathbf{0} \\ \mathbf{0} & \mathbf{0} & \mathbf{0} & \mathbf{I} \end{bmatrix}^{-1} \cdot \begin{bmatrix} \mathbf{C}_{RR} & \mathbf{C}_{RF} & \mathbf{K}_{RR} & \mathbf{K}_{RF} \\ \mathbf{C}_{FR} & \mathbf{C}_{FF} & \mathbf{K}_{FR} & \mathbf{K}_{FF} \\ \mathbf{I} & \mathbf{0} & \mathbf{0} & \mathbf{0} \\ \mathbf{0} & \mathbf{I} & \mathbf{0} & \mathbf{0} \end{bmatrix} \tag{2.72}$$

Eigenanalysis of system equations 2.70 is used to determine the aeroelastic stability of trailing-edge flap rotor. The stability matrix $\mathbf{A}$ is periodic when the helicopter is in forward flight condition because of the azimuthal changes in aerodynamic forces. Stability of linear period system can be solved using either Floquet theory or Constant Coefficient Approximation. As the blade equations of motion (Eq. 2.31), the stability equation (Eq. 2.70) is also transformed into normal mode equation before the solution procedure. The normal mode transformation is described in Sec. 2.6.2.

Floquet Theory

Floquet theory is the classic method to solve periodic coefficient equations such as Eq. 2.70. This method is used to solve Eq. 2.70 to determined the stability characteristics of helicopter rotor in forward flight. The outline of this procedure is presented below.

The solution of the linear system of equations 2.71 must be expressible as a linear combination of the state variables at time ψ_0 as:

$$\boldsymbol{Y}(\psi) = \boldsymbol{\Phi}(\psi, \psi_0)\boldsymbol{Y}(\psi_0) \tag{2.73}$$

where matrix $\boldsymbol{\Phi}(\psi, \psi_0)$ is known as state transition matrix, and by definition,

$$\boldsymbol{\Phi}(\psi_0, \psi_0) = [\mathbf{I}] \tag{2.74}$$

By substituting, the system equations is rewritten as

$$\overset{\star}{\boldsymbol{\Phi}} = \mathbf{A}\boldsymbol{\Phi} \tag{2.75}$$

By defining the discrete transition matrix as

$$\boldsymbol{Q} = \boldsymbol{\Phi}(\psi_0 + 2\pi, \psi_0) \tag{2.76}$$

The transition matrix can be written as

$$\boldsymbol{Q} = \boldsymbol{S}e^{2\pi\Lambda}\boldsymbol{S}^{-1} \tag{2.77}$$

where $\boldsymbol{S}$ is the modal matrix of $\boldsymbol{Q}$ and

$$\boldsymbol{\Theta} = e^{2\pi\Lambda} \tag{2.78}$$

is the eigenvalue matrix associated with the Floquet transition matrix $\boldsymbol{Q}$. Therefore,

$$\Lambda = \frac{1}{2\pi}ln\boldsymbol{\Theta} \tag{2.79}$$

The system is unstable if the real part of any eigenvalue, $Re(\Lambda_i) > 0$.

The Floquet transition matrix $\boldsymbol{Q}$ can be computed by integrating equation 2.75 over one rotor revolution (2π) starting with the initial conditions given by equation 2.74. In the present analysis, the integration is carried out numerically using either Gear method or Runge-Kutta method [89]. The frequency values resulted from Floquet theory are multi-valued, and their determination corresponding to the physical system requires additional effort. One approach is to compare with the predictions of constant coefficient method, and another way may be to interpret the modes associated with the Floquet transition matrix.

Constant Coefficient Approximation

If the periodicity of system equation 2.71 is only moderate, the solution may be approximately calculated with constant coefficient approximation. A key essence of periodicity is captured by averaging the system stability matrix in one rotor revolution. This results in a linear constant coefficient system equations, which can be readily solved using standard eigenvalue analysis.

$$\boldsymbol{A}_{const} = \frac{1}{2\pi} \int_0^{2\pi} \boldsymbol{A}_{periodic}\, d\psi \qquad (2.80)$$

The predictions of constant coefficient approximation is generally accurate for advance ratio below 0.3. Even for advance ratio above 0.3, where the predictions may be poor, this method can be used to help in the identification of frequencies predicted with Floquet theory. Constant coefficient method also uses less computation time comparing with the Floquet theory.

2.8 Multicyclic Controller

A multicyclic controller [90, 91] is used to determine the flap control inputs for an active vibration control. The goal is to minimize N_b/rev rotor hub loads. This algorithm is based on minimization of an objective function,

$$J \equiv z_n{}^T W_z z_n + \theta_n{}^T W_\theta \theta_n + \Delta\theta_n{}^T W_{\Delta\theta} \Delta\theta_n \tag{2.81}$$

where z_n is a hub loads vector at time step n. θ_n and $\Delta\theta_n$ represent the harmonics of the control inputs and control rates, respectively. The diagonal matrices W contain weights for different harmonics of the vibration (W_z), the control inputs (W_θ) and the control rates ($W_{\Delta\theta}$).

The hub loads vector containing the cosine and sine coefficients of the N_b/rev fixed system hub longitudinal, lateral and vertical forces (F_x, F_y, F_z,) and rolling and pitching moments (M_x and M_y). It is expressed as

$$\mathbf{z} = \begin{bmatrix} F_x{}^{cos} & F_x{}^{sin} & F_y{}^{cos} & F_y{}^{sin} & F_z{}^{cos} & F_z{}^{sin} & M_x{}^{cos} & M_x{}^{sin} & M_y{}^{cos} & M_y{}^{sin} \end{bmatrix}^T$$

For a 5-bladed rotor, the trailing-edge flap inputs used in the present study are 4/rev, 5/rev, 6/rev. The flap motion input is written as

$$\theta_{\mathbf{n}} = \begin{bmatrix} \delta_{4/rev}^{cos} & \delta_{4/rev}^{sin} & \delta_{5/rev}^{cos} & \delta_{5/rev}^{sin} & \delta_{6/rev}^{cos} & \delta_{6/rev}^{sin} \end{bmatrix}^T$$

The weighting matrix of hub loads, W_z, is selected to give a compromised consideration on the vibration levels at the pilot seat, copilot seat, CG, and Notar fan based on a

NASTRAN simulation for MD-900 helicopter. W_z used in the present study is:

$$\mathbf{W_z} = \begin{bmatrix} 0.040 & & & & \\ & 0.023 & & & \\ & & 1.0 & & \\ & & & 0.440 & \\ & & & & 0.136 \end{bmatrix}$$

The flap motion and rate weighting matrices, W_θ and $W_{\Delta\theta}$, are used to establish relative importance of hub loads versus flap deflections and rates in the objective function J. The present analysis does not restrain the flap motions, and thus does not put weighting of flap motions on the objective function ($\mathbf{W_\theta} = 0$ and $\mathbf{\Delta W_\theta} = 0$). In this case, the controller will attempt to minimize hub loads without regards to the trailing-edge flap motion and rate.

The flow chart shown in Figure 2.7 presents the solution procedure of the multi-cyclic controller.

2.9 Swashplateless Trailing-Edge Flap Rotor Analysis

For a conventional rotor with a swashplate control system, lifting or lowering of the swashplate disks changes blade collective pitch, while forward or side tilting of the swash-plate disks governs the cyclic pitch. The trim variables for a conventional helicopter are blade collective pitch, θ_0, and cyclic pitch, θ_{1c} and θ_{1s}. The present swashplateless rotor design modifies the baseline rotor by replacing the pitch link assembly with a simple lin-

ear root spring. A soft root spring reduces the effective torsional frequency of the blade. For the bearingless rotor, the torque tube is unaltered in the swashplateless rotor design, and serves as an aerodynamic fairing, as well as providing inplane blade damping together with the snubber. For a swashplateless rotor with trailing-edge flap concept, the flaps produce pitching moment changes, which impel the main blades to pitch against the root spring to achieve aerodynamic equilibrium, thereby producing the desired collective and cyclic blade twist. The trim variables for a swashplateless rotor are flap collective deflection, δ_0, and cyclic deflections, δ_{1c} and δ_{1s} (Figure 2.9).

Two unique characteristics of swashplateless rotor, compared with a conventional rotor, are torsionally soft blades and pre-collective angles. Torsionally soft blades, which can be achieved using soft root springs, are required to increase the flap effectiveness (the ratio of blade pitch to trailing-edge flap deflection angle). Pre-collective pitch angle or indexing (Figure 2.8) is used to reduce the amount of blade pitch travel excited by the trailing-edge flap, and hence decrease the required flap deflections.

2.9.1 Blade Pitch Indexing

The blade pitch index angle defines the three-quarter radius blade pitch value relative to the hub plane. Pitch index angle is normally selected to be higher than collective pitch required to trim the helicopter at a selected forward speed, i.e., the cruising speed. As the rotor is accelerated to its normal rotational speed, the nose-down pitching moment generated by trailing-edge flaps will twist the blade nose-down to the desired pitch position. Higher index angle requires downward deflected flap, which generates upward lift on the

blade. This upload moves the blade airload distribution inboard, and improves the rotor performance in hover and forward flight conditions [42, 76].

2.9.2 Large Twist Displacement

The swashplateless rotor pitch control is achieved through blade twist displacement at the root spring. This large twist displacement has two contributions to the formulation and solution of blade equations of motion. Firstly, the initial assumption of the blade elastic twist, ϕ, is a small angle, and thus $sin(\phi) \approx \phi$, $cos(\phi) \approx 1$ is no longer valid. Secondly, the convergence of blade response equations becomes difficult. Convergence is more sensitive to twist than to other blade deformations because twist has a dominating influence on the blade angle of attack and thus the aerodynamic loads. The first problem is solved by including higher order expansion in the Taylor's series , i.e., $sin(\phi) \approx \phi - \phi^3/6$, $cos(\phi) \approx 1 - \phi^2/2$. A major advantage of this approach is that required modifications to the basic formulations of blade response equations are minimum. It is required to include a few additional higher order terms. Convergence problem is also alleviated with this refined approximation of triangular functions of blade twist. The convergence problem can be further minimized by including proper numerical damping in the solution procedure of blade equations of motion.

The air velocities, which defines the blade angle of attach as $\alpha = -tan^{-1}(U_p/U_t)$, are rewritten with additional terms underlined:

$$
\begin{aligned}
U_r &= (-\overset{\star}{v'} - 1)\, \eta_r\, cos\theta_0 + (-\overset{\star}{w'} + \hat{\phi})\, \eta_r\, sin\theta_0 \\
&\quad + (\frac{1}{2}\, v'^2 + \beta_p\, w' - 1 + \frac{1}{2}\, w'^2)\, \mu\, cos\psi + \lambda\, \beta_p + \lambda\, w' + v'\, \overset{\star}{v}
\end{aligned}
$$

$$+ \sin\psi\, v'\, \mu - v + w'\, \overset{\star}{w} + x\, v' + \overset{\star}{\hat{u}}$$

$$
\begin{aligned}
U_t =\ & ((\hat{\phi}\, w' + \beta_p\, \hat{\phi} + v')\, \mu \cos\psi + (1 - \frac{\underline{\underline{\hat{\phi}^2}}}{2} - \frac{v'^2}{2})\, \mu \sin\psi + \hat{\phi}\, \overset{\star}{w} \\
& - w\, \beta_p + \overset{\star}{\hat{v}} - \frac{x\, v'^2}{2} + u + v\, v' + x - \frac{x\, \underline{\underline{\hat{\phi}^2}}}{2} + \lambda\, \hat{\phi})\cos\theta_0 \\
& + ((\beta_p + w' - \hat{\phi}\, v')\, \mu \cos\psi + (-\hat{\phi} - v'\, w')\, \mu \sin\psi - x\, \hat{\phi} + v\, w' \\
& - x\, v'\, w' - \hat{\phi}\, \overset{\star}{\hat{v}} + v\, \beta_p + \lambda + \overset{\star}{w})\sin\theta_0 \\[6pt]
U_p =\ & ((\beta_p + w' - \hat{\phi}\, v')\, \mu \cos\psi + (-\hat{\phi} - v'\, w')\, \mu \sin\psi - x\, \hat{\phi} + v\, w' \\
& - x\, v'\, w' - \hat{\phi}\, \overset{\star}{\hat{v}} + v\, \beta_p + \lambda + \overset{\star}{w})\cos\theta_0 \\
& + ((-v' - \hat{\phi}\, w' - \beta_p\, \hat{\phi})\, \mu \cos\psi + (\frac{\underline{\underline{\hat{\phi}^2}}}{2} - 1 + \frac{v'^2}{2})\, \mu \sin\psi - u \\
& - \hat{\phi}\, \overset{\star}{w} + w\, \beta_p - \overset{\star}{\hat{v}} - v\, v' + \frac{x\, v'^2}{2} - \lambda\, \hat{\phi} - x + \frac{x\, \underline{\underline{\hat{\phi}^2}}}{2})\sin\theta_0 \\
& + (\beta_p + w' + \overset{\star}{\hat{\phi}} + \overset{\star}{\theta_0})\, \eta_r
\end{aligned}
$$

$$\text{(2.82)}$$

The blade twist displacement is also involved in the blade coordinate transformation matrix T_{DL}, which transforms the blade loads from blade undeformed to deformed frame. The extra terms are included in the nonlinear part of T_{DL} matrix, which is written as:

$$\mathbf{T}_{DLq2} =$$

$$
\begin{bmatrix}
-\frac{1}{2}\, v'^2 - \frac{1}{2}\, w'^2 & 0 & 0 \\[8pt]
\hat{\phi}\, v' \sin\theta_0 - \hat{\phi}\, w' \cos\theta_0 & -\frac{1}{2}\cos\theta_0(\underline{\underline{\hat{\phi}^2}} + v'^2) - v'\, w'\sin\theta_0 & -\frac{1}{2}\sin\theta_0(\underline{\underline{\hat{\phi}^2}} + w'^2) \\[8pt]
\hat{\phi} v' \cos\theta_0 + \hat{\phi} w' \sin\theta_0 & \frac{1}{2}\sin\theta_0(\underline{\underline{\hat{\phi}^2}} + v'^2) - v'w'\cos\theta_0 & -\frac{1}{2}\cos\theta_0(\underline{\underline{\hat{\phi}^2}} + w'^2)
\end{bmatrix}
\quad \text{(2.83)}
$$

The extra terms involved with large blade twist displacement are nonlinear terms, and

systematically included in the nonlinear force vectors in blade equations of motion fol-

lowing the finite element discretization procedure described in Sec. 2.5.2. These terms

also contribute in the calculation of the blade and hub loads.

2.9.3   Coupled Trim Procedure of Swashplateless Rotor

For a swashplateless rotor with flaps, the control angle input to the blade is given by:

$$\delta(\psi) = \delta_0 + \delta_{1c}\cos(\psi) + \delta_{1s}\sin(\psi) \tag{2.84}$$

and the blade pitch angle consists of the blade index angle and the elastic twist induced

by flap control inputs;

$$\theta(\psi) = \theta_{index} + \phi_{twist}(\psi) \tag{2.85}$$

The flap control angles are obtained from the coupled trim procedure. Given a set

of controls, shaft orientation, and inflow distribution, the coupled analysis determines the

blade response, and provides the blade loads together with the fixed system hub loads.

In turn, these loads and responses are used in a separate set of equations representing ei-

ther the vehicle free-flight equilibrium, or a prescribed wind tunnel operating condition.

These equations govern the rotor control settings. The coupled trim procedure of a swash-

plateless rotor with trailing-edge flaps is similar to that of conventional rotor described in

Sec. 2.6. The difference is that swashplateless rotor trim requires a fully converged so-

lution of blade equations of motion before an update is made to the control angles of

the trim equations. However, the coupled trim procedure of conventional rotor can toler-

ate a loose converged solution of blade equations at each trim iteration, and thus having

the blade equations and trim equations converging simultaneously to save computational

time. This is because the swashplateless rotor is inherent torsionally soft, and therefore results in large blade displacements. The nonlinear effect must be properly included in iterations. The Jacobian matrix $\frac{\partial F}{\partial \theta}$ used in equation (2.59) is again obtained via a forward difference method by perturbing the individual controls in θ. The initial value for the trim algorithm is provided by a reduced order rigid blade response model that includes trailing-edge flap. The trim solution and blade responses are updated iteratively until the convergence criteria are reached. The incremental lift and pitching moment of an active trailing-edge flap, consisting of both inertial and aerodynamic contributions, are included in this coupled trim procedure (Figure 2.10).

2.9.4 Trailing-Edge Flaps Performing Multiple Functions

It is attractive to use the trailing-edge flaps for both primary control and active vibration control in order to reduce overall system weight and cost. The trailing-edge flap required to minimize N_b/rev fixed system hub loads are actuated at higher harmonics of rotational speed, typically at $(N_b-1, N_b, N_b+1)/rev$. For active vibration control, the trailing-edge flap input to the blade is

$$\delta(\psi) = \sum_p (\delta_{pc}\cos(p\psi) + \delta_{ps}\sin(p\psi)) \tag{2.86}$$

where $p = N_b - 1, N_b, N_b + 1$. For a 5-bladed rotor, the trailing-edge flap inputs used in the present study are 4, 5, and 6/rev. The multicyclic controller described in Sec. 2.8 is used to determine the flap active control inputs (δ_{pc}, δ_{ps}). By adding the input for primary control, the control input to the blade is:

$$\delta(\psi) = \delta_0 + \delta_{1c}cos(\psi) + \delta_{1s}sin(\psi) + \sum_p (\delta_{pc}\cos(p\psi) + \delta_{ps}\sin(p\psi)) \tag{2.87}$$

In summary, this section describes the coupled trim procedure of swashplateless rotor with trailing-edge flaps which may be used for both free flight and wind tunnel trim conditions. The trim variables for a swashplateless rotor are flap collective deflection, δ_0, and cyclic deflections, δ_{1c} and δ_{1s}. Two unique characteristics of swashplateless rotors, torsionally soft blades and pre-collective angles, are properly modeled in the analysis. A multicyclic controller was implemented with the swashplateless rotor analysis to calculate the flap control inputs for minimization of vibratory rotor hub loads. The feasibility of trailing-edge flap performing both primary control and active vibration control is then be examined.
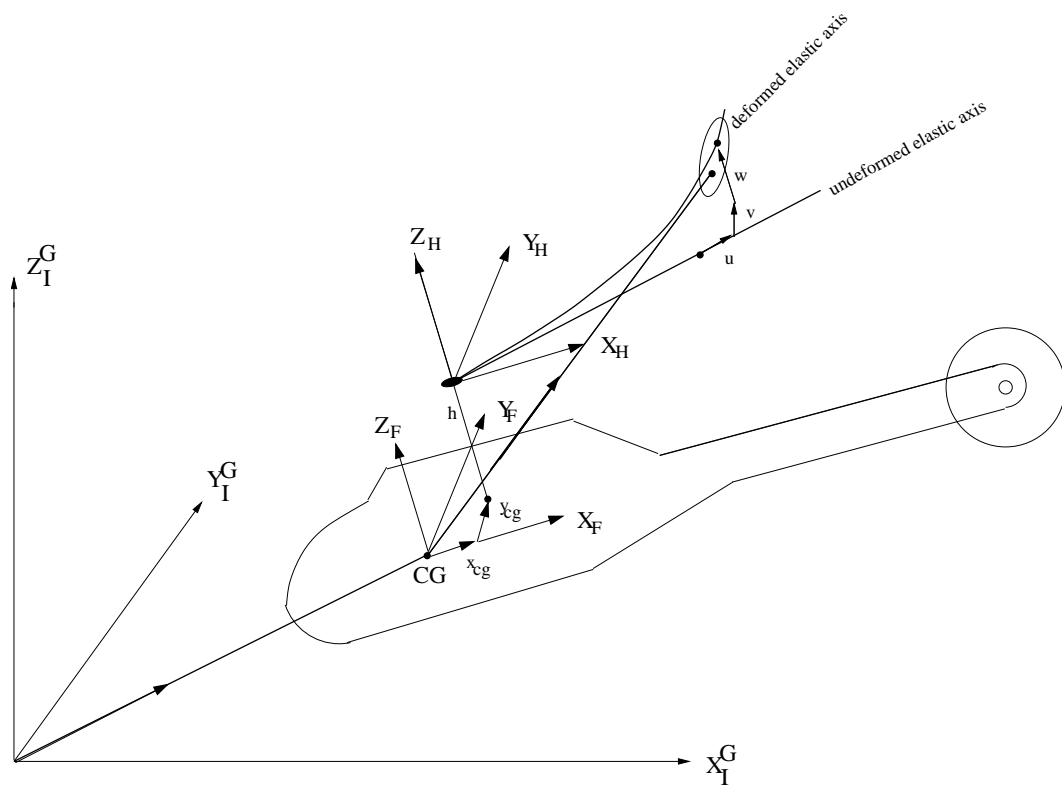
Figure 2.1: Coordinate System

86
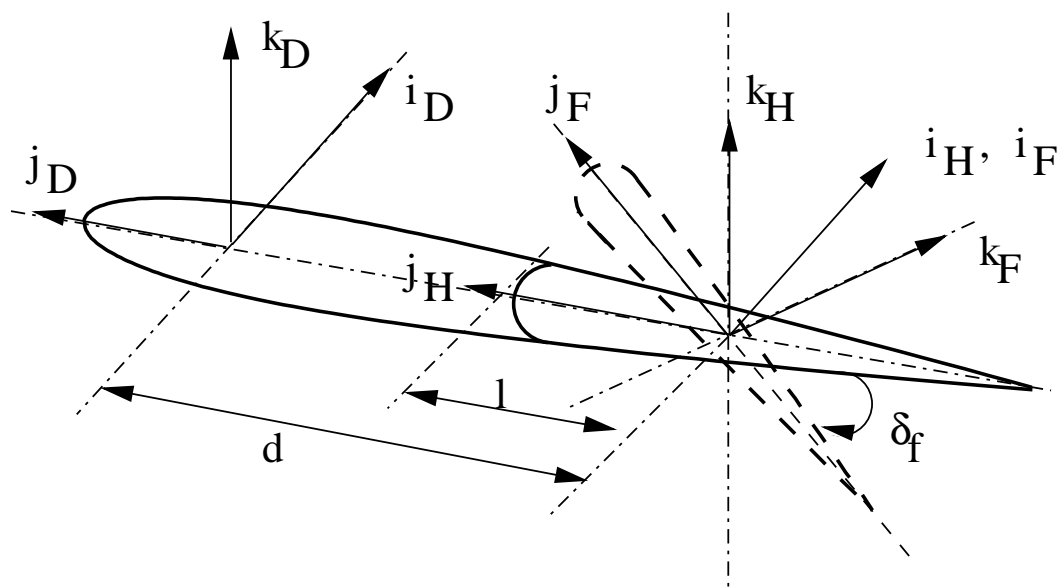
Figure 2.2: Flap Coordinate System
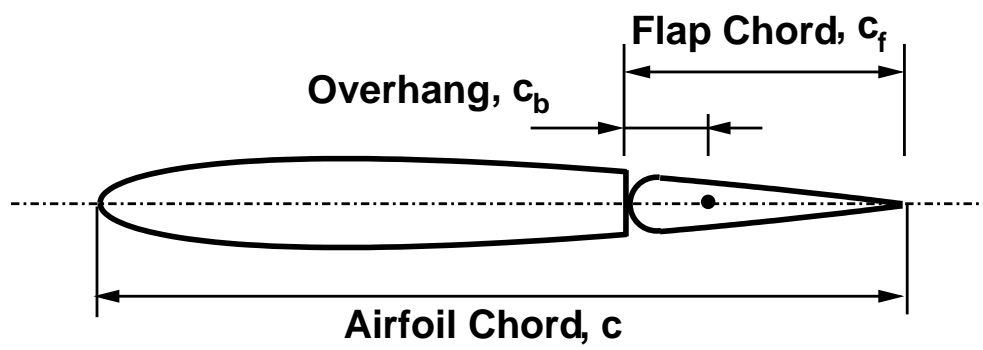
Figure 2.3: Trailing-edge flap with aerodynamic balance (nose overhang)
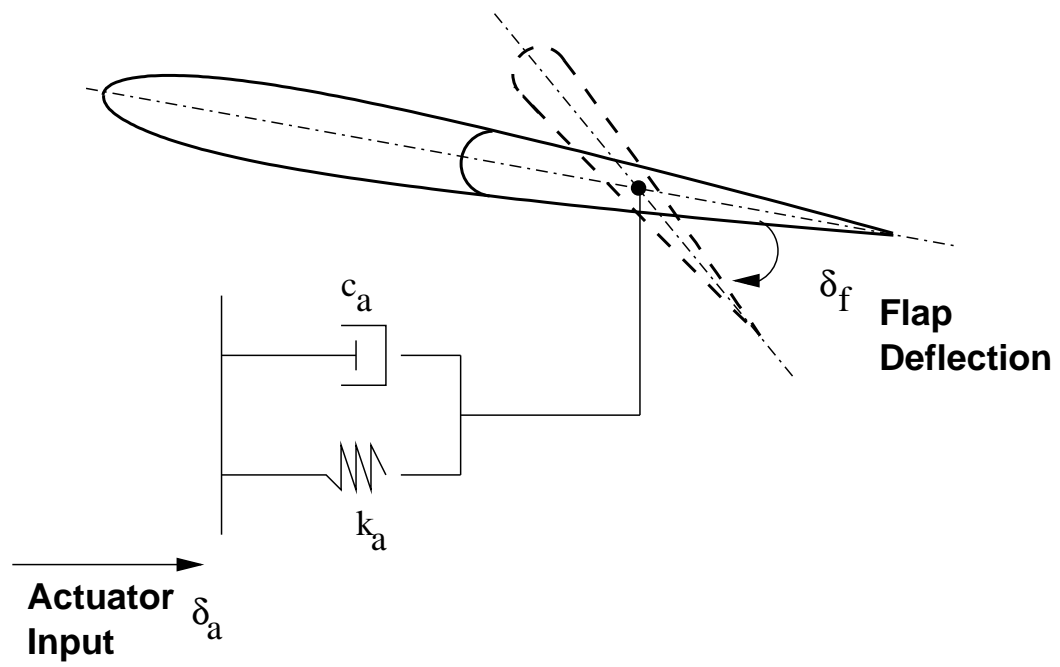
Figure 2.4: Actuator and Flap System

Blade Segment
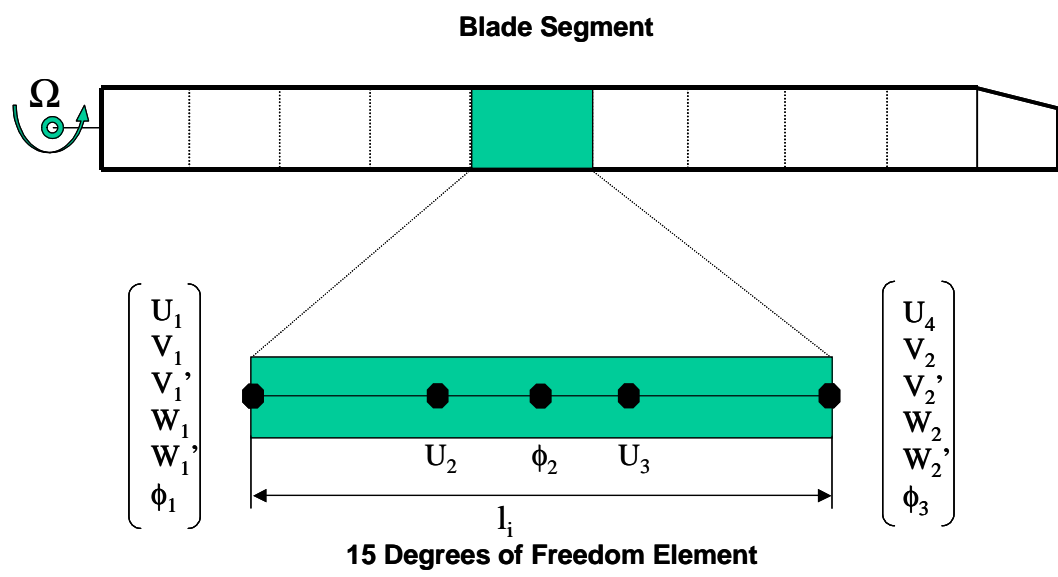
Figure 2.5: Finite element method
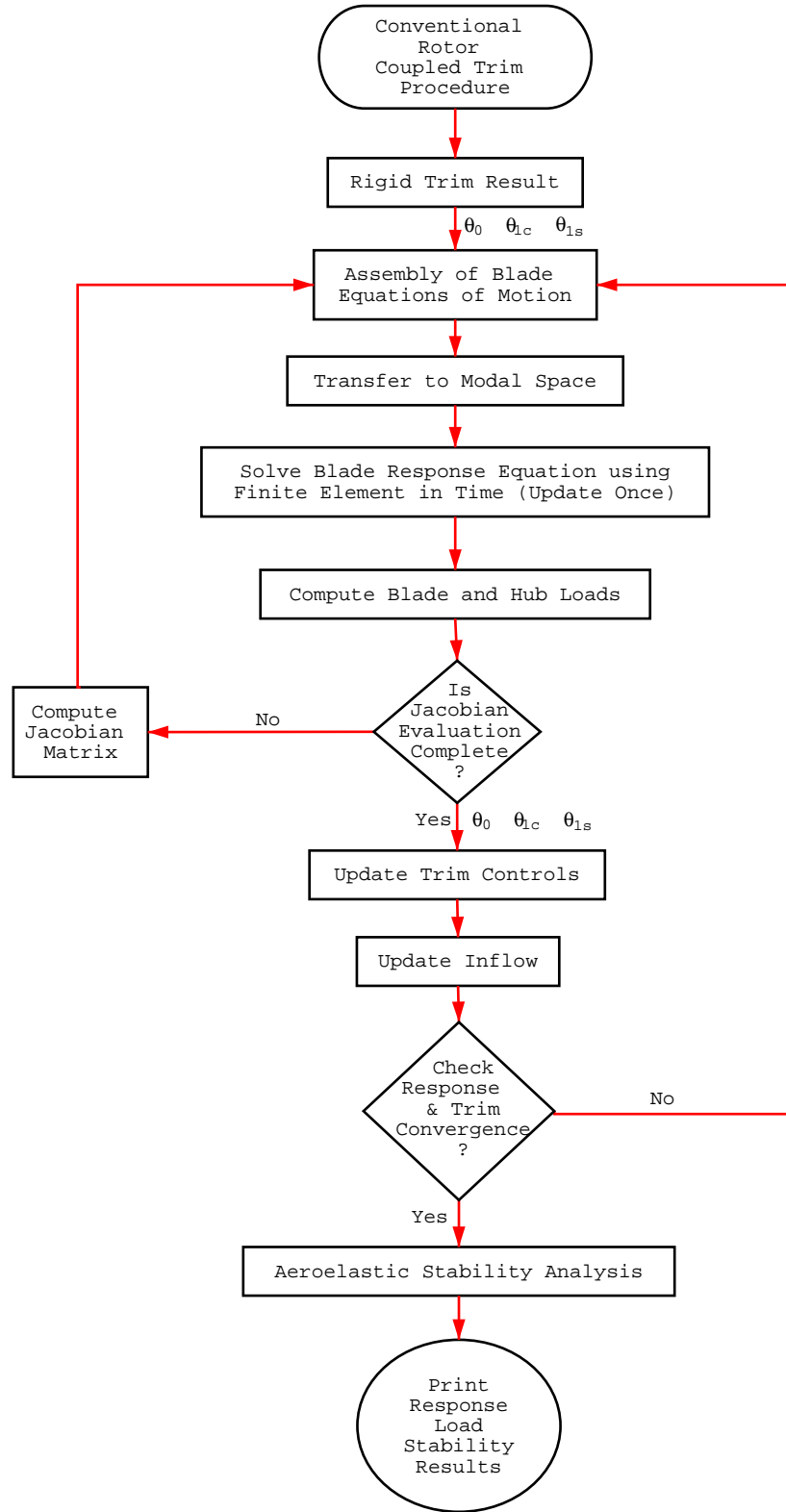
Figure 2.6: Flow chart of conventional rotor coupled trim procedure
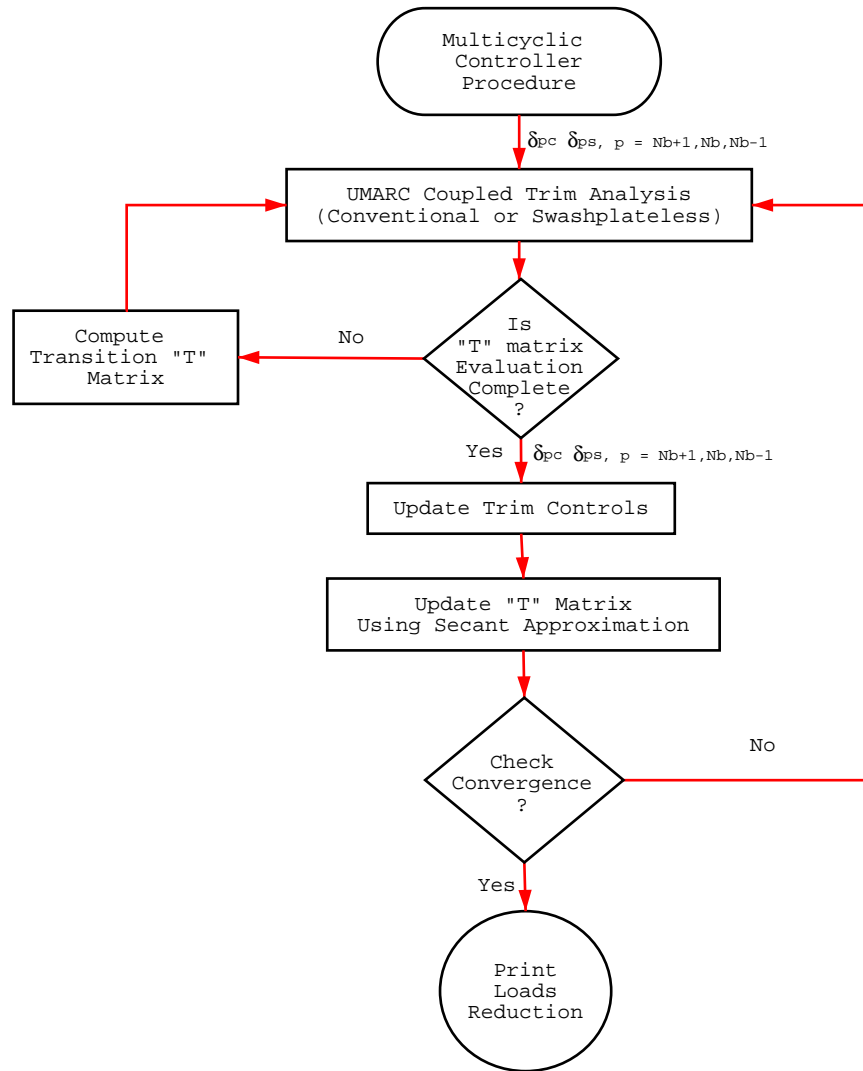
Figure 2.7: Flow chart of multicyclic controller

Non–Indexed

Indexed

Blade Pitch

Smart Flap Deflections

$+\Delta M$

$-\Delta L$

$+\Delta L$

$-\Delta M$
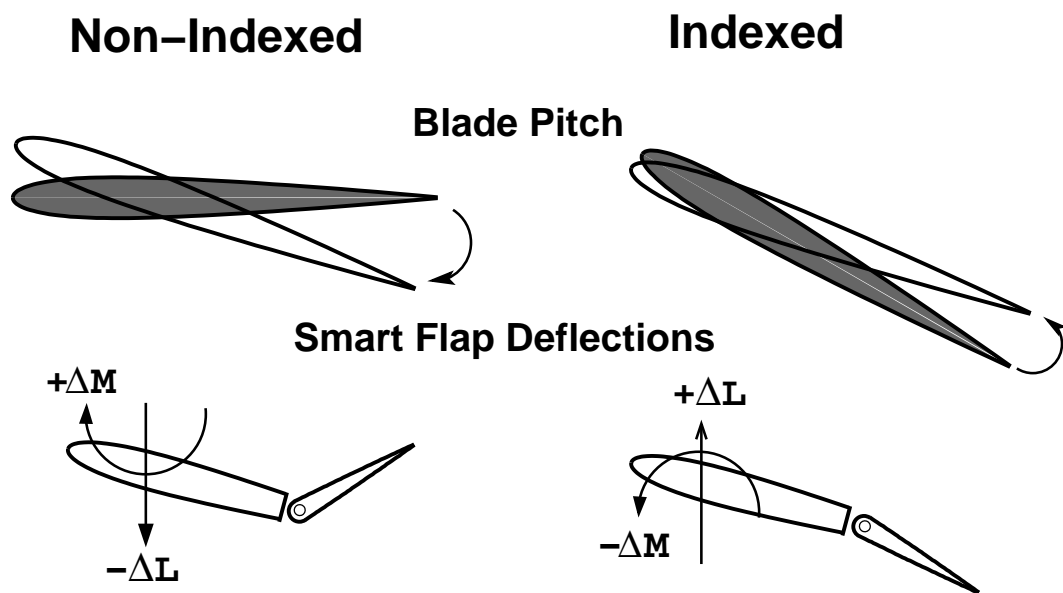
Figure 2.8: Blade Pitch Indexing
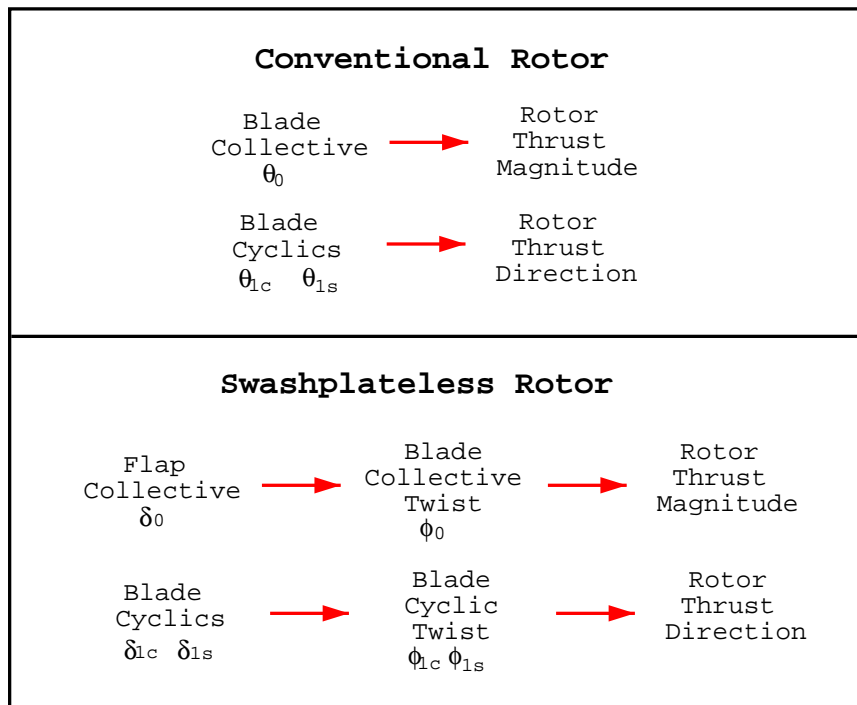
Figure 2.9: Comparison of conventional rotor and swashplateless trailing-edge flap rotor trim

Swashplateless Rotor Coupled Trim Procedure

Rigid Trim Result

δ_0 δ_{1c} δ_{1s}

Assembly of Blade Equations of Motion

Transfer to Modal Space

Solve Blade Response Equation using Finite Element in Time (Converged)

Compute Blade and Hub Loads

Is Jacobian Evaluation Complete ?

No

Compute Jacobian Matrix

Yes δ_0 δ_{1c} δ_{1s}

Update Trim Controls

Update Inflow

Check Response & Trim Convergence ?

No

Yes

Aeroelastic Stability Analysis

Print Response Load Stability Results

Figure 2.10: Flow chart of swashplateless rotor coupled trim procedure

Chapter 3

Results and Discussion

This chapter presents the results obtained using the analytical model developed in Chapter 2. This chapter can be divided into five major sections. The first section addresses the validation study focused on predicted blade responses and loads. Both the results of a baseline rotor (without trailing-edge flaps) and a flapped rotor are correlated either with wind tunnel test data or with the predictions of another comprehensive code (CAMRAD II). The second section presents the results with trailing-edge flaps for vibration reduction using the coupled blade/flap/actuator model developed in Sec 2.5.2. Parametric study using both "prescribed trailing-edge flap motion model" and "coupled blade/flap/actuator model" are carried out to investigate the effect of actuator dynamics on the flap effectiveness and actuation requirements. The third section presents the aeroelastic stability characteristics of helicopter trailing-edge flap rotor using the model developed in Sec 2.7. The fourth section addresses the results of using trailing-edge flaps as the primary control device to enable a swashplateless rotor configuration. Parametric study was carried out to investigate the effect of key design variables on flap control effectiveness and actuation requirements. The stability characteristics of swashplateless rotors were studied, and the

capability of using trailing-edge flaps for both primary control and vibration reduction was investigated. The baseline rotor used in the first four sections is the MD-900 bearingless rotor, and the trim procedure adopted is the wind tunnel trim. The final section presents the results of a swashplateless 2-bladed teetering rotor of an ultralight helicopter (ASI 496) with trailing-edge flaps as primary control device. Free flight trim procedure is used. Correlation study of the baseline rotor (without trailing-edge flaps) was carried out by comparing calculated results with CAMRAD II predictions. Parametric study was conducted to investigate the rotor performance of a swashplateless rotor configuration. Theodorsen trailing-edge flap aerodynamic model (Sec. 2.4.1) is used to obtain the results of MD-900, and the Hariharan-Leishman trailing-edge flap aerodynamic model (Sec. 2.4.2) is used to obtain the results of ASI 496.

3.1 Validation Study of Baseline Bearingless Rotor (MD-900)

The analytical model of a bearingless rotor is quite involved as described in Sec 2.6.5. Therefore, a validation study of the baseline rotor (without trailing-edge flaps) is carried out by comparing calculated results with wind tunnel test data.

3.1.1 Description of Baseline Rotor

The MDART rotor is a preproduction version of the MD-900 Explorer (Fig. 3.1), a 5-bladed bearingless rotor. A schematic of the rotor is shown in Fig. 3.2, and the rotor

97

design parameters are given in Table 3.1. The nominal "1g" thrust for the rotor was taken to be 5800 lbs for the MDART test, and the design cruise speed was 150 kts (an advance ratio of 0.364). The blade is attached to the hub by means of a dual load path flexbeam and torque tube assembly. The torsional loads are primarily carried through the torque tube, which is attached to the hub by an elastomeric snubber and to the control system by the pitch horn. The blades and flexbeams are made of fiberglass whereas the torque tube, for which high stiffness is essential, is made of graphite. The snubber damper assembly consists of upper and lower elastomeric dampers, each of which attaches to the torque tube and to the metal snubber. The snubber is attached to the hub via an elastomeric bearing. This bearing allows pitch and flap angular motions of the torque tube about the hub. The snubber restricts the vertical displacement of the torque tube root. This, with the high torque tube flapping stiffness, forces the virtual flapping hinge to be very close to the snubber location for any flight condition. The high torque tube chordwise stiffness, the carefully tailored chordwise stiffness of the flexbeam, and the relative softness of the elastomeric damper combine to yield a large amount of damper shearing motion per degree of blade lead-lag deflection. The damping force that results from shearing the high-loss-factor elastomer effectively stabilizes the rotor. The modern HH10 airfoil extends from the blade attachment to the 74% blade radial station, from which the blade cross section undergoes a region of airfoil transition covering 10% of the blade radius. The HH06 airfoil forms the remaining part of the blade tip region. The blade chord is constant 10 inches that is swept into a parabolic leading edge shape at the tip for performance and acoustic benefits.

The difference between the MDART rotor and MD-900 rotor is the control system

Table 3.1: MDART rotor properties

Property	Value
Rotor Type	bearingless
Number of Blades	5
Rotor Diameter	34 ft.
Rotor Speed	392 RPM
Chord	$0.0492R$
Twist Angle	$-10°$ (nominal; actual value by table lookup)
Solidity	0.078

stiffness. The control system stiffness of the MD-900 rotor is 316 lb/in, which results in a blade fundamental torsional frequency of 3.03/rev. The wind tunnel test stand gives a control system stiffness of 4900 lb/in, which results in a torsional frequency around 6.0/rev (Table 3.2). Detailed rotor design data used in present analysis were provided by the aircraft manufacturer (Boeing-Mesa). Table 3.2 compares calculated natural frequencies of the MDART rotor between the present analysis and CAMRAD II. Overall good agreement is seen. The small discrepancy may be a result of different structural properties used in the analyses. For example, the present analysis assumes a snubber stiffness consistent with Ref. [92] while CAMRAD II results in Table 3.2 are based on a lower value.

Table 3.2: MD-900 blade natural frequencies

	UMARC (/rev)	CAMRAD II (/rev)
flap	1.03	1.05
	2.63	2.78
	4.56	4.57
lag	0.68	0.61
	4.33	4.43
torsion	6.00	5.95

3.1.2 Description of Wind Tunnel Tests

The experimental data used in this validation study were obtained in a wind tunnel test of McDonnell-Douglas Advanced Rotor Technology (MDART) in 1994. The test procedures and results are documented in detail in Refs. [92–94].

The wind tunnel test was intended to obtain performance, loads, stability, and acoustic data for a state-of-the-art bearingless rotor system over a wide range of operating conditions, and also to measure the effects of open-loop HHC inputs on these parameters. The tests covered speeds more than 200 knots (an advance ratio of 0.49) and thrusts of more than 10,000 lbs (a C_T/σ of 0.13). The wind tunnel test results are retrieved from the Rotor Data Reduction System (RDRS) database at NASA Ames.

The full-scale MDART rotor was installed on the McDonnell Douglas Large Scale Dynamic Rig (LSDR) in the NASA Ames 40- by 80-foot wind tunnel (Fig. 3.3). The

LSDR lower housing contained a 1500 hp electric motor and transmission system. The upper housing contained the rotor balance and the hydraulic servo-actuators for the control system.

The full-scale MDART rotor was fully instrumented, including blade strain gauges for flapwise and chordwise bending and torsional moments. The blade flapwise bending moments were measured at six radial stations, the chordwise bending moments at four stations, and the torsion moment at three stations. The torque tube flapwise and chordwise bending moments and torsional moment were measured at one location. The flexbeam had one flapwise bending moment, one chordwise bending moment, and two torsional moment measurements. Both steady and vibratory hub loads, which includes the longitudinal, lateral, and vertical forces, and the rolling and pitching moments, were measured by the five-component rotor balance.

Both static and dynamic data were acquired during the test program. A slip ring was used to transmit the forty-four analog channels of rotating instrumentation into the fixed frame. The raw dynamic data were sampled at 64 per rotor revolution and were passed through a four-pole Bessel filter with a bandwidth of 100 Hz. Eight revolutions of data were harmonically analyzed, and ten harmonics of the reduced data were saved in the RDRS database. The data used in the present validation study were directly retrieved from the database.

Aeroelastic stability tests on the MDART rotor were also carried out for an extensive set of simulated flight conditions. Standard techniques were used to acquire the stability data. Once the desired steady state operating condition was achieved, the swashplate was excited at the fixed system regressive lag mode frequency. This resulted in

blade pitch oscillations at the fundamental chordwise frequency in the rotating frame. The resulting oscillating airloads caused the blade to flap, and the blade inplane motions were excited through the Coriolis coupling with the flapping motions. Then the excitation was cut off and subsequent transient response signals were analyzed using both a moving block method and a time domain transient analysis.

3.1.3   CAMRAD II Analysis

The results of present analysis were correlated with the calculations of CAMRAD II analysis [62, 63, 95], especially for cases where the test data were not available. The CAMRAD II results of the MDART rotor were obtained by the rotor manufacturer (Boeing-Mesa), and the results of ASI 496 were provided by the developer of CAMRAD II (Wayne Johnson). CAMRAD (Comprehensive analytical Model of Rotorcraft Aerodynamics and Dynamics) II is an aeromechanical analysis of helicopters and it incorporates multibody dynamics methodology and nonlinear finite elements. The trim solution calculates the equilibrium solution (constant or periodic) for a steady state operating condition. The operating condition can be free flight (including level flight, steady climb or descent, and steady turns), or constrained (such as a rotor in a wind tunnel, with typically the thrust and flapping trimmed to target values). It is usually necessary to identify the control positions and aircraft orientation required to achieve the specified operating condition. The transient procedure numerically integrates the equations in time (from the trim solution), for a prescribed excitation. The flutter solution is obtained from an eigenanalysis of the linearized differential equations.

Table 3.3: Prescribed thrust level and shaft angles in different forward speeds. (Positive is shaft tilt forward)

Advance Ratio μ	Airspeed (kts)	Thrust Level C_T/σ	Shaft Angle α_s (deg.)
0.080	33.2	0.07499	1.1
0.151	62.5	0.07560	2.6
0.200	82.6	0.07372	4.9
0.248	102.8	0.07514	6.9
0.299	123.2	0.07771	8.8
0.349	144.3	0.07515	10.9
0.373	154.8	0.07455	11.8

3.1.4 Wind Tunnel Trim and Performance

The typical wind tunnel procedure is to adjust blade collective pitch, θ_0 to obtain a prescribed thrust level, C_T/σ, and the cyclic pitch, θ_{1c}, θ_{1s} to achieve zero first harmonic flapping. The blade flapping is derived from the flexbeam bending moment measurement. For a known forward speed, the rotor shaft angles are prescribed to simulate free flight condition. Table 3.3 shows the rotor thrust level and shaft tilt angles used in the wind tunnel tests.

Figure 3.4 shows the predicted and measured values for blade collective pitch, longitudinal and lateral cyclic pitches for different advance ratios. Figure 3.4(a) shows good agreement between predicted and measured collective control angles except a slightly overprediction at low advance ratios. Figure 3.4(b) illustrates that the longitudinal control

angle agrees well with the test data for the complete range of advance ratios. Figure 3.4(c) shows a fair agreement on lateral cyclic pitch θ_{1c} at low advance ratios. Lateral cyclic is, in general, sensitive to inflow modeling and blade flapping dynamics.

Figure 3.5 presents the predicted and measured main rotor power in different flight speeds. UMARC predictions agree well with test data except of a slight underprediction. It is not unusual that the analysis underpredicts the main rotor power. There are secondary aerodynamics phenomena such as the interactions of rotor and wind tunnel setup are normally difficult to include in the analysis. These factors tend to reduce the rotor aerodynamic efficiency, and thus increase the actual main rotor power.

3.1.5 Blade Loads Correlation

This section presents the comparison of blade structural moments, i.e., flap bending moments, chordwise bending moments, and torsional moments of UMARC predictions and measured data. Both the mean and oscillatory components are compared. The mean test data were corrected for a gravity tare computed for a nonrotating blade, while the effects of rotation on the strain gauge signals were not addressed. The UMARC predictions are obtained using force summation method.

Figure 3.6 compares the measured and predicted flap bending moments at an advance ratio of 0.20. Figure 3.6(a) shows the mean flap bending moments agreeing well between the measurement and prediction except the small overpredictions at some stations. Figure 3.6(b) compares the oscillatory flap bending moments between measurement and predictions. UMARC calculations show good agreement with the test data at

the two ends of the blade, but small underpredictions in the blade middle segment.

Figure 3.7 compares the measured and predicted chordwise bending moments at an advance ratio of 0.20. Figure 3.7(a) shows the mean chordwise bending moments comparing poorly between the measurement and prediction. There are only four chordwise bending moment measurement points on the blades besides the one on the blade root attachment location. It may not be enough to provide the trend when the test data varies largely such as this case. The test data also show a significant forward chordwise bending moment at the blade radial location of $r/R = 0.8$, and this is normally unexpected because the large drag at the blade tip generates backward chordwise bending moments. In contrast, the predictions present a more reasonable trend of blade chordwise bending moments with a monotonic increase from the blade tip to root. On the other hand, the oscillatory chordwise bending moments were compared well between measurements and predictions as shown in Fig. 3.6(b).

Figure 3.8 compares the measured and predicted torsional moments at an advance ratio of 0.20. Figure 3.8(a) shows mixed comparison results of the mean torsional moments between the measurement and prediction. There are three torsional moment measurement points on the blade and one on blade attachment position. The predictions show good agreement with the measurement near the blade tip, and poor comparison close to the root. The test shows a large positive mean pitching moment (nose-up) near blade station of $r/R = 0.35$. Normally, this is unexpected because the aerodynamic pitching moments generated by the airfoil HH10 and HH06 used on the MDART blades are nose-down in the normal operating conditions. Figure 3.8(b) shows a good agreement between measurements and predictions of oscillatory torsional moments.

Figure 3.9 compares the measured and predicted flap bending moments at an advance ratio of 0.373. Figure 3.9(a) shows the mean flap bending moments agreeing fairly between the measurements and predictions. The predictions capture the general trend near the blade tip, but show a large overprediction at the root. Figure 3.9(b) compares the oscillatory flap bending moments between measurements and predictions. UMARC calculations show good agreement with the test data.

Figure 3.10 compares the measured and predicted chordwise bending moments at an advance ratio of 0.373. Similar to the comparison at the advance ratio of 0.20, Figure 3.10(a) shows a poor correlation of the mean flap bending moments between the measurements and predictions. Again, the oscillatory chordwise bending moments were compared well between measurements and predictions as shown in Fig. 3.9(b).

Figure 3.11 compares the measured and predicted torsional moments at an advance ratio of 0.373. Figure 3.11(a) shows again a mixed comparison of the mean torsional moments between the measurements and predictions (similarly as the case of advance ratio 0.20). Figure 3.11(b) shows good agreement between measurements and predictions of oscillatory torsional moments.

Figures 3.12, 3.13, and 3.14 compare the measured and calculated time history of blade structural moments at an advance ratio of 0.2. Figure 3.12 shows the blade flapwise bending moment at r/R = 0.21. The flapwise bending moments are well captured except the high frequency content. Figure 3.13 shows the blade chordwise bending moment at r/R = 0.59, and good agreement is observed. Figure 3.14 illustrates the blade torsional moment at r/R = 0.75. Although overall trend is captured, the high frequency components are not predicted well. This requires an improved representation for pitching moment

including three-dimensional effects (through detailed CFD modeling).

3.1.6 Vibratory Hub Loads Correlation

This section compared the measured and predicted vibratory hub loads, i.e., longitudinal, lateral, and vertical forces and rolling and pitching moments. A well-balanced rotor generates vibratory hub loads at discrete frequencies that are multiple of number of blades. The components of other harmonics are canceled at the hub. The 5-bladed MDART rotor should generate $5, 10, \ldots$ per revolution vibratory loads with the 5/rev being the dominant component. This 5/rev vibratory hub loads in the hub fixed system are a result of the 4, 5, 6/rev blade loads in the rotating frame, and accurate 5/rev hub load predictions can only be achieved when these higher harmonics of blade loads are calculated correctly. It is, however, a challenging task to predict the high harmonic components of blade loads accurately.

The test data of 5/rev vibratory hub loads are dynamically corrected and represent the nonrotating hub loads in the fixed system. Reference [96] documented the dynamic calibration procedure. Only the magnitudes of the vibratory hub loads are shown, and the results are nondimensionalized as described in Sec. 2.2.

Figure 3.15 shows the magnitude of the 5/rev hub longitudinal force at different flight speeds. The longitudinal force is high in the transition flight condition ($\mu = 0.08$), and this is captured well by the predictions. It then reduces as the forward speed increases to an advance ratio of 0.15, and this is also well predicted by UMARC. UMARC predictions underpredicted the 5/rev hub longitudinal force in the advance ratio range from 0.20

to 0.373 although the large increase at high advance ratios is predicted well.

Figure 3.16 shows the 5/rev hub lateral force magnitude versus advance ratios. UMARC prediction shows a variation and magnitude of the 5/rev lateral force similar to the longitudinal force shown in Fig. 3.15. However, the test data of 5/rev hub lateral force presents small magnitude and less variation comparing with the predictions. Reference [96] shows the 5/rev hub lateral force is scaled down over the speed range in the dynamically correcting procedure. The correction factor is moderate at the low speeds and becomes significant at the higher speed range. The largest correction occurs at the advance ratio of 0.20 with a reduction of two-thirds in magnitude.

Figure 3.17 presents the variation of 5/rev vertical force with forward speed. The high 5/rev vertical force at transition flight condition is again well predicted. The relative constant variation at high forward speeds is well captured by the predictions. UMARC overall underpredicted the test data except at a low advance ratio ($\mu = 0.08$).

Figures 3.18 and 3.19 shows the variations of 5/rev vibratory hub rolling and pitching moments with advance ratios. UMARC predictions compare fairly at low advance ratios, but largely underpredicts the data at high forward speed, and shows the different trend. Compared with vibratory hub force, the hub moments are more difficult to obtain accurate predictions [97]. The difficulties shown in here may be due to the lack of high harmonic contents in the inflow distributions obtained by the free wake model.

3.1.7 Aeroelastic Stability

This section compares measurement and prediction of the stability characteristics of the baseline MDART bearingless rotor. The test obtains the stability data using the flexbeam chordwise bending moments and the damper displacement measurements. These signals were analyzed to provide first blade lag mode damping ratios using both a moving block method and a time domain transient analysis [94]. The blade lag mode is normally the least damped among the blade flap, lag, and torsion modes. The behavior of blade lag mode dominates the aeroelastic stability characteristics of the rotor system. The coupling of this mode with the inplane hub motions can cause dynamic instabilities known as ground and air resonance. The lag mode damping level must be sufficient to prevent such instabilities. In the discussion to follow, the first blade lag damping ratio is compared between UMARC predictions and wind tunnel measurements.

Figure 3.20 compares measurements and predictions of variation of lag damping ratios with blade collective pitch angles in hover. The test data scatter is small except at 10 degree collective pitch, and the scatter is attributed to the nonlinear behavior of the elastomeric damper [94]. UMARC results overall agree well with the test data with a small overprediction at small collectives and underpredictions at a high collective, i.e., larger than 10 degrees.

Figure 3.21 shows variation of lag mode damping with flight speed. The thrust level and shaft tilt angle are prescribed to simulate steady level flight conditions (Table 3.3). The MDART rotor shows sufficient damping level in the complete range of advance ratios. UMARC prediction using Floquet theory compares well with the test data except some

small overpredictions in advance ratio range from 0.15 to 0.25.

Figure 3.22 illustrates variation of lag damping with collective pitch angle for an advance ratio of 0.20 and forward shaft tilt of 5.5 degrees. The test data shows the lag damping ratio increases almost linearly with the collective angle. This linear increase is captured by UMARC predictions using both the Floquet theory and Constant Coefficient Approximation although the results obtained by Floquet method are more close to the test data.

Figure 3.23 illustrates lag damping variation of the MDART rotor with collective pitch angle for an advance ratio of 0.25 and forward shaft tilt of 7.3 degrees. The test data shows approximately a quadratic increase of lag damping ratios with collective angles. This increase is attributed to the favorable flap-lag and pitch-lag couplings of the rotor blade at high collective pitch angles [94]. UMARC predictions using Floquet theory compare well with the test data except the underpredictions at high collective angles.

3.2   Validation Study of Helicopter Rotor with Active Trailing-Edge Flaps

This section describes the validation study of helicopter rotors with active trailing-edge flaps. UMARC prediction capability of a flapped helicopter rotor was evaluated in [84] by comparing the analytical results with wind tunnel test data for the McDonnell-Douglas Active Flap Rotor (AFR) [98]. The AFR was a four-bladed fully articulated rotor model with 12 ft. diameter, and featured plain trailing edge flaps of 25%c extending from 0.79-

0.97R. The flaps were driven via a cam and pulley arrangement. The experimental data reflect both flap-fixed and active flap cases. Overall, the UMARC results showed adequate correlation with the experiment data.

The results of present analysis are obtained using the MD-900 active trailing-edge flap rotor, an advanced bearingless rotor system. The full-scale active flap rotor test is not completed yet, hence test data are not available. The correlation study is carried out by comparing the predictions of present analysis with CAMRAD II. The results of CAMRAD II were provided by the rotor manufacturer (Boeing-Mesa). The aerodynamic model used in this section is Theodorsen flap aerodynamics described in Sec. 2.4.1.

3.2.1 Description of MD-900 Active Flap Rotor

The MD-900 active flap rotor is based on the MDART bearingless rotor. The structural properties of the active flap rotor are assumed to be same as the MDART rotor. Figure 3.24 shows the full scale MD-900 active flap rotor system. The trailing-edge flap has a 35%c chord, a radial span of 18%R, an aerodynamic balance of 29% flap chord, and located at 83%R (Table 3.4).

3.2.2 Trailing-Edge Flap Airfoil Aerodynamics

This section presents the validation study of trailing-edge flap airfoil aerodynamics model by comparing the predictions with wind tunnel test data. The test data are from a two-dimensional wind tunnel test conducted in the NASA Langley 0.3-m Transonic Cryogenic Tunnel (TCT) [85]. The goal is to identify a suitable trailing-edge flap geometry for

Table 3.4: MD-900 active trailing-edge flap properties

Property	Value
Flap Type	Plain Flap
Spanwise Length	36 inch (0.18R)
Chordwise Size	35 % (Blade Chord)
Flap Midspan Location	0.83R
Flap Hinge Overhang	10% (Airfoil Chord)

helicopter rotor aerodynamic/dynamic applications. Two pressure-instrumented models of the HH-06 (9.5% thick), HH-10 (12% thick) airfoils having 35% chord integral plain trailing-edge flaps and different overhang lengths were tested.

The aerodynamic coefficient predictions using the analytical model described in Secs. 2.4.1 and 2.4.2 are compared with wind tunnel test data for the HH06 and HH10 airfoils in Figures 3.25 - 3.28. The two-dimensional airfoil aerodynamic coefficients of lift, drag, and pitching moment are compared with three trailing-edge flap deflections, namely neutral, and four degrees upward and downward, at different angles of attack. Because the test data are for trailing-edge flaps with aerodynamic balance, the Theodorsen flap aerodynamic theory (Sec. 2.4.1) is used to predict the lift and pitching moment coefficient. However, Theodorsen flap aerodynamic theory has no drag model, therefore Hariharan-Leishman model (Sec. 2.4.2) is used to predict the drag coefficient although this model does not include the effect of flap nose overhang. The leading edge recovery factor used in the analysis is 0.97, and aerodynamic drag coefficient of the baseline airfoil due to skin

friction, C_{D0} is added on the prediction by Eq. 2.18. Good agreement is seen for the lift coefficient, and fair agreement for pitching moment coefficient. Drag predictions only qualitatively agree with the test data. Most of the difference between predictions and test data are a result of viscous effects at the hinge gap and flow separation effects.

3.2.3   Validation of Active Flap Blade Loads and Response

The predictions of responses and loads of active trailing-edge flap rotor blade are compared with CAMRAD II calculations. The comparisons were completed for a simulated descent flight condition at an advance ratio of 0.2 with a 3.5 degree aft shaft tilt angle and a thrust coefficient C_t/σ of 0.0774. Both analyses utilized the wind tunnel trim procedure: trimming to the prescribed thrust level with zero first harmonic blade flapping.

The correlation of the flap analysis was based on data for a trailing-edge flap control schedule $\delta_f = 2^o\cos(4\psi - 240^o)$, which is a simple 2 degree harmonic input at a $4/rev$ frequency phased to give a maximum trailing-edge down flap angle at 60 degree azimuth. The study presents two sets of UMARC results using two flap aerodynamics models. The first uses the flap coefficients defined by data table lookup, and the second by analytical expressions. The CAMRAD II results used the table lookup for the flap coefficients. Furthermore, the results presented in the correlation section were obtained using flap analysis excluding actuator dynamics in order to compare with the CAMRAD II and CAMRAD/JA predictions. The prescribed flap motion essentially assumes a rigid actuator.

Blade Torsional Moments

Figure 3.29 shows the blade torsion moment variation for one complete revolution at 60% radial station. The present predictions show good agreement with CAMRAD II results, with some small differences between predictions obtained by present analysis using table lookup and analytical expressions.

Blade Tip Pitch

Figure 3.30 illustrates the blade tip pitch response (control inputs and blade elastic torsion, excluding the built-in twist) for the baseline case (zero flap input), and with the flap control activated. The pitch motions for the baseline case agree well except a roughly $2°$ offset between the two analyses. In the active flap case, it is observed that approximately the same amount of pitch motion was induced by the trailing-edge flap on the advancing blades.

Blade Section Angle of Attack

Figure 3.31 illustrates the spanwise distributions of the section angle of attack at 60 degree azimuth where the flap has its maximum 2 degree down deflection. UMARC results agree well with CAMRAD II predictions. The larger differences near the root are believed to be wake related.

    Figures 3.29 and 3.31 show that there are only small differences between UMARC predictions obtained using table lookup and analytical expression for aerodynamic coefficients.

3.2.4 Trailing-Edge Flap Hinge Moment and Shear

The predictions of flap hinge moment is very important for the calculations of aeroelastic stability of a trailing-edge flap rotor because it directly determines the flap motion given the actuator input and couples the blade motion with the flap deflections. Figure 3.32 compares flap hinge moment predictions from UMARC using table lookup as well as using analytical expressions with CAMRAD II predictions [40]. UMARC hinge moment predictions utilizing table lookup agree fairly with CAMRAD II results that are also calculated using table lookup. The predictions using Theodorsen flap model qualitatively agree with the results using table lookup, however, there are considerable underpredictions of the magnitude in the first quadrant. The hinge shear variation shows a fair agreement between results of UMARC and CAMRAD II (Figure 3.33).

3.3 Validation Study of Multicyclic Controller

This section examines the capability of the multicyclic controller (Sec 2.8) of predicting optimal trailing-edge flap input for minimizing hub vibratory loads. Open loop simulations were carried out with the trailing-edge flap motion actuated at a single frequency (sequentially 4, 5 and 6/rev) and varying in amplitude and phase. The results are shown as a contour plot in Figures[3.34- 3.36]. Figures 3.34 illustrates the variation of fixed system hub vertical forces with different amplitude and phase inputs of the trailing-edge flap at 4/rev. The vertical force is in nondimensional form, as a ratio of the baseline vertical force (zero flap inputs). The optimal amplitude and phase of 4/rev flap input to minimize the 5/rev vibratory hub vertical force can be visually identified in the contour

plot. Figure 3.34 shows that the prediction of the multicyclic controller, plotted as the dot, is indeed the optimal 4/rev flap input to minimize 5/rev vibratory vertical hub force. Similarly, Figures 3.35 and 3.36 show respectively that the multicyclic controller predicts the optimal 5/rev and 6/rev flap inputs to minimize vertical force as well. Although a trailing-edge flap system would certainly include active control inputs at multiple rotor harmonics, it is of interest to examine the open loop simulations. Open loop results can also provide a general understanding of the sensitivities of the flap input on various components of the fixed system vibratory loads.

3.4 Trailing-Edge Flap for Vibration Reduction

This section describes the analytical results of using trailing-edge flaps as a vibration reduction device. The UMARC predictions including actuator dynamics are included in two parts:

1. Investigation of coupling effect among blade, smart actuator and flap.

2. Parametric study on flap spanwise location that includes actuator dynamics.

The baseline rotor is the MDART active flap rotor with its properties shown in Table 3.4.

3.4.1 Trailing-Edge Flap Analysis including Actuator Dynamics

The following sections discuss calculated results from the UMARC analysis using analytical expressions for aerodynamic coefficients, and with the inclusion of actuator dynamics using the fully coupled blade/actuator/flap analysis.

Figure 3.37 compares the flap response prediction with UMARC and CAMRAD II for an actuator input $\delta_a = 2^o\cos(4\psi - 240^o)$. While larger flap response is shown with CAMRAD II result especially in the first quadrant, a slight reduction in flap angle is seen with UMARC results. The difference is because of the discrepancy in the flap hinge moment calculation, which is critical for the prediction of flap response. Figure 3.38 illustrates the coupling effect of actuator dynamics on resultant flap angle variation for one complete revolution for two different values of actuator stiffness. Two actuator stiffnesses were considered: 1) 10% of the baseline 2) ten times of the baseline. The soft actuator generates the flap deflection largely diverting from the actuator input especially in the last two quadrants while the flap deflection using the rigid actuator is almost the same with the actuator input.

3.4.2   Parameter Study

Parametric studies have been conducted to investigate the impact of flap and actuator design on control authority and power consumption. Key flap design parameters, such as flap spanwise length and chord, spanwise location, have been examined [36,99]. The goal of the present study is to investigate the coupling effect of actuator and flap dynamics on the selection of flap design parameters. The predictions of the present UMARC model, incorporating actuator dynamics, are compared with that of UMARC using prescribed flap motion. The multicyclic controller described earlier is used to provide the optimum flap control schedule. For the prescribed flap, the controller output is the flap deflection schedule. In contrast, for the coupled blade/actuator/flap model, the controller output is

the actuator input. The actual flap control schedule is calculated by solving the coupled blade/flap/actuator equations.

The spanwise location of the trailing-edge flap is believed to be an important factor for the active control system [36, 99]. To obtain an optimum flap spanwise location, the simulations are performed with different flap locations. The following results are calculated at an advance ratio 0.30 (123 knots), and for a selected C_T/σ of 0.0774.

The objective function reduction ratio is shown in Figure 3.39. The objective function is reduced to less than 4.5 percent. The coupled model is more sensitive to the spanwise location than the prescribed model. Figure 3.40 illustrates the peak-to-peak values of control inputs for both models. The coupled model requires about 10% larger peak-to-peak control input. The actuation power required is presented in Figure 3.41. It shows that with the inclusion of actuation dynamics, about 30% more actuation power is needed to control vibration actively. The optimum location of trailing-edge flap midspan for this rotor is at 78 percent of blade radius. There is an unexpected reduction of control input and power requirement for the coupled flap model with the trailing-edge flap located at 87% radius. A similar result was also observed in another case study by the authors using the prescribed model. Examining the transfer matrix used in the multicyclic controller revealed that the complex aerodynamic environment near the blade tip resulted in this optimum solution for the multicyclic controller. However, this optimum flap location was disregarded because it is not true for all trim conditions.

The current MD-900 flap design parameters are shown in Table 3.4. With this flap system, simulations are performed using both the coupled flap/actuator model and the prescribed flap motion model at several advance ratios. The objective function is shown

in Figure 3.42. Both models show the objective function reduces below 25% for advance ratios from 0.1 to 0.3. Figure 3.43 and Figure 3.44 respectively illustrate the effect of actuation dynamics on the peak-to-peak control input and actuation power required. At low advance ratios, the prescribed model shows a larger flap control input as well as a higher actuation power than that of the coupled model. These differences decrease with higher advance ratios. The predicted 5/rev vibratory hub loads with both models are shown in Figures 3.45 to 3.49. The 5/rev vibratory longitudinal force and lateral force were either not reduced or reduced slightly because of their small weight in the objective function. The 5/rev vibratory vertical force is almost reduced to zero due to its significant weighting parameters in the objective functions. The difference between the two models becomes more pronounced for the rolling and pitching moments. The coupled model including actuator dynamics calculated the 5/rev vibratory pitching and rolling moment reduce almost to zero while the prescribed model shows mixed results. There is a reduction of rolling moment ranging from 41% to 17%, whereas for pitching moment there is an increase of 25% from its baseline value at low advance ratios for the prescribed flap motion model.

3.5   Aeroelastic Stability of Trailing-Edge Flap Helicopter Rotor

Before stability results for the trailing-edge flap rotor are presented, the predictive capabilities of UMARC for a bearingless rotor without trailing-edge flaps are evaluated by

correlating with wind tunnel experimental data. The trailing-edge flap hinge moments of UMARC are compared with CAMRAD II predictions. Then the UMARC predictions of stability results for the trailing-edge flap rotor are carried out, and the flap aerodynamic and mass balance effects are investigated. The stability results are carried out at trimmed state with non-zero flap deflection. The flap deflections are calculated by the coupled blade/flap/actuator equations. The actuator input, δ_0, is set to zero, however, the flap deflection may not be zero. This is because a nonzero hinge moment exists even in the absence of a flap motion.

3.5.1 Effect of Trailing-Edge Flap Aerodynamic Balance

The effect of trailing-edge flap aerodynamic balance (nose overhang) is studied in this section, and the flap is assumed mass-balanced (flap mass CG is coincident with the hinge). The purpose of using flap overhang is to reduce flap actuation requirements. Figure 3.50(a) shows that the actuation power was reduced by 60% with an overhang length of 29% flap chord (hinge at 29% flap chord) compared with the no overhang case (hinge at leading-edge of the flap). Figure 3.50(b) shows that half peak-to-peak flap response increases with increasing overhang length, and more dramatically above 40% flap chord. Figure 3.51 illustrates the effect of flap overhang length on blade and trailing-edge flap stability characteristics. The trailing-edge flap mode damping decreases with increasing flap overhang, and becomes unstable with overhang length larger than 50% flap chord. This is because the flap becomes aerodynamically over-balanced with large flap overhangs, and the flap mode diverges. The effects of flap overhangs on blade stability result

stem from the coupling among trailing-edge flap motion and blade modes. The trailing-edge flap is static mass-balanced in this case so that the coupling between flap and blade are primarily through aerodynamic forces. The aerodynamic coupling between blade flap mode and trailing-edge flap motion is in phase, which positive trailing-edge flap deflection produces positive blade flap bending motion. This positive coupling results in a decrease in blade flap mode damping with increasing flap overhangs. The aerodynamic coupling between blade torsion mode and trailing-edge flap mode is out of phase, which positive trailing-edge flap motion decreases blade torsion motion. This negative coupling leads to an increase in blade torsion mode damping with increasing flap overhangs. Blade lag mode virtually stays constant with flap overhangs. It is shown that although aerodynamic balance of trailing-edge flaps is the key to minimizing actuation requirements, excessive overhangs may lead to blade/trailing-edge flap instability.

3.5.2   Effect of Trailing-Edge Flap Mass Balance

The effect of trailing-edge flap mass-balance on blade and trailing-edge flap stability is investigated in this section. The simulations were carried out with various flap CG offsets from the flap hinge, and this variation will change the inertia forces on the blade and trailing-edge flap. The flap CG offsets in this study are varied to show its sensitivity on stability. The baseline MD-900 trailing-edge flap system is designed to be mass-balanced.

Figure 3.52(a) shows the variation of trailing-edge flap frequency with flap CG offset. The hinge is located at 29% of flap chord and positive CG offset is behind flap hinge. The trailing-edge flap frequency is shown to decrease with increasing flap CG

offset. This is because the moment of inertia of flap increases with flap CG offset and the actuator stiffness is kept the same here. Figure 3.52(b) reveals the effect of flap CG offset on blade and trailing-edge flap stability characteristics. The trailing-edge flap mode is shown to become unstable after a flap CG offset of 0.26 flap chord. This instability is typical trailing-edge flap-blade torsion flutter. That instability results from the energy transfer between the trailing-edge flap mode and blade torsion mode. Blade flap mode damping is shown to decrease with flap CG offset and flap CG offset has a negligible effect on blade lag mode stability.

3.5.3   Parameter Study for Aeroelastic Stability

The study of various important blade and trailing-edge flap structural properties, such as rotor control stiffness, blade torsional stiffness, actuator stiffness, and trailing-edge flap size and locations are carried out in combination with a mass-imbalanced flap (CG offset of 0.33 flap chord and flap overhang length of 0.29 flap chord). The simulations are conducted at an advance ratio of 0.30 except where noted. Figure 3.53 shows the effect of rotor control system stiffness (designated as pitch link stiffness) on blade and trailing-edge flap stability characteristics. Figure 3.53(a) presents the variation of blade flap, lag, and torsion mode natural frequencies with pitch link stiffness. It shows that the blade torsion frequency increases from 2.3/rev for a pitch link stiffness of 158 lb/in to 4.2/rev for a pitch link stiffness of 800 lb/in. The blade fundamental flap and lag frequencies are essentially unchanged with pitch link stiffness. Figure 3.53(b) shows effect of pitch link stiffness on blade and trailing-edge flap stability characteristics. The flap overhang is 29%

flap chord and the flap CG offset is 33% flap chord behind the hinge. The trailing-edge flap mode becomes gradually more unstable with increasing pitch link stiffness. Blade flap mode damping increases largely with pitch link stiffness whereas blade torsion mode damping slightly decreases. Blade lag mode damping shows small variation.

Figure 3.54 shows the effect of blade torsional stiffness (GJ factor over baseline value) on blade and trailing-edge flap stability. Figure 3.54(a) presents the variation of blade natural frequencies with blade GJ factors. The frequencies of blade flap and lag mode reveal virtually no variation with GJ factors while torsion frequency increases from 2.96/rev with 75% of the baseline GJ to 3.18/rev with twice the baseline GJ. Figure 3.54(b) presents the variation of blade and trailing-edge flap damping with GJ factor. Trailing-edge flap mode is unstable in the range from 75% to 200% baseline GJ, and shows small variation. Blade torsion mode damping is shown to be slightly decreasing with increasing GJ factor whereas flap mode damping increases with GJ factor.

Figure 3.55 presents the effect of trailing-edge flap actuator stiffness on blade and trailing-edge flap stability characteristics. Figure 3.55(a) shows the variation of trailing-edge flap frequency with actuator stiffness for a mass-balanced flap (no flap CG offset) and a mass-imbalanced flap (flap CG offset of 33% flap chord). The frequencies of both types of flap increase largely with increasing actuator stiffness, however, the mass-imbalanced flap shows smaller variation slope than the mass-balanced flap because of its larger moment of inertia. Figure 3.55(b) illustrates the trailing-edge flap mode is unstable for the mass-imbalanced flap with a soft actuator, and becomes stable with actuator stiffness above 1.5 times the baseline actuator. Blade flap mode damping increases gradually with increasing actuator stiffness whereas torsional mode damping decreases. The effect

of actuator stiffness on blade lag mode is negligible.

Figures 3.56, 3.57, and 3.58 examine the effect of trailing-edge flap size (length and chord ratio) and spanwise location on blade and trailing-edge flap stability characteristics. Figure 3.56 illustrates that trailing-edge flap mode becomes unstable when flap is positioned toward blade tip. Blade flap mode damping is shown to decrease slightly with flap moving to blade tip, and torsion mode damping increases with flap placed toward the tip. Blade lag mode damping shows no variation with trailing-edge flap location. Figure 3.57 shows that trailing-edge flap mode becomes unstable with flap length above 14% blade radius. Blade flap mode damping is shown to decrease with increasing flap length whereas torsion mode increases with flap length. However, both modes are quite stable. Comparing figures 3.56 and 3.57, the flap length parameter is shown to have the similar effect as the flap location, though it is more effective at changing the blade and trailing-edge flap stability characteristics. Figure 3.58 shows trailing-edge flap mode is unstable with the flap chord in the range of 0.15 to 0.40 airfoil chord, and stable otherwise. This may be because of the aerodynamic characteristics of the trailing-edge flap changing dramatically with flap chord ratio. The flap pitching moment reaches a maximum around a flap chord ratio of 0.26, while the flap lift coefficients increase monotonically with flap chord ratio [100]. Again, because of the positive aerodynamic coupling between blade flap mode and trailing-edge flap motion, blade flap mode damping shows the same trends of variations as the trailing-edge flap mode with flap chord ratio. Conversely, the blade torsion mode damping presents the opposite pattern of variation with flap chord ratio comparing with trailing-edge flap mode because of the negative aerodynamic coupling between blade torsion mode and trailing-edge flap mode.

Figures 3.59 and 3.60 examine the variation of blade and trailing-edge flap stability characteristics in different flight conditions. Figure 3.59(a) shows the effect of blade collective pitch in hover. The trailing-edge flap mode is shown to become unstable with large collective pitch, though the variation is very small. Figure 3.59(b) shows the effect of blade collective pitch on blade and trailing-edge flap stabilities in forward flight condition with an advance ratio of 0.3. The trailing-edge flap mode is unstable in the range of collective pitch from four to twelve degrees, and is increasingly unstable with larger collective pitch. Figure 3.60 examines the effect of variation of forward speed. The trailing-edge flap mode is weakly unstable in hover and becomes more unstable with forward speed.

3.6 Swashplateless Trailing-Edge Flap Helicopter Rotor in Wind Tunnel Trim

This section describes the analytical results of helicopter rotors with trailing-edge flaps for primary control. The analytical mode of swashplateless rotors is described in Sec. 2.9.

3.6.1 Description of Baseline Rotor

The active trailing-edge flap rotor and swashplateless rotor have the same blade structural properties and rotor configuration as the MDART rotor (Table 3.1) with the exception that the swashplateless rotor uses a softer root spring. A typical root spring stiffness used in the present study is 119 lb/in, resulting in a blade fundamental torsional frequency of

2.1/rev. The torque tube is unaltered in the swashplateless rotor design, and serves as an aerodynamic fairing, as well as providing inplane blade damping through the snubber. For comparison purposes, the conventional rotor used in this section exhibits the same torsional frequency as the swashplateless rotor configuration. This is achieved by adjusting the control system stiffness of the conventional rotor.

The baseline trailing-edge flap characteristics are given in Table 3.1. Trailing-edge motion is positive for downward deflection, and hinge moment is positive when its direction is "nose-up" (and "tail-down").

3.6.2   Blade Elastic Pitch and Twist

The mechanism of primary control with trailing-edge flaps involves the entire blade pitch motion about the root spring and blade sectional elastic twist about the elastic axis. It is apparent that the root spring stiffness and blade torsional stiffness distribution are important design parameters.

Figure 3.61 presents the variation of blade fundamental torsional frequency with root spring stiffness and blade torsional stiffness distribution. The blade torsional stiffness is changed as a percentage of baseline blade value. As expected, the blade torsion frequency exhibits an increase with root spring stiffness as well as with torsional stiffness, though it shows a greater sensitivity to root spring stiffness.

Figure 3.62 illustrates the effects of root spring and blade torsional stiffness on blade pitch and elastic twist. The predictions for a conventional MD-900 are shown for reference. Three swashplateless rotor configurations are shown: first, the baseline rotor

with a torsion frequency of 2.1/rev, second, a swashplateless rotor with soft root spring (69 lb/in) with a torsional frequency of 1.8/rev, and last, a swashplateless rotor with 50% reduced blade torsional stiffness with a torsion frequency of 2.04/rev. Figure 3.62(a) illustrates the variation of blade elastic twist with blade station at an azimuth angle of zero degree. The blade segments extend from approximately $21\%R$ to the tip and the flexbeam and torque tube connect the root of the blade to the hub. As expected, the blade with soft torsional stiffness exhibits a larger twist variation than the baseline blade. Figure 3.62(b) presents the variation of blade tip pitch for one complete rotor revolution at an advance ratio of 0.3. The tip pitch of the swashplateless rotors exhibit the 1/rev characteristics of primary control function, and shows small difference between the baseline swashplateless configuration and soft root spring case or soft torsional stiffness case. The difference is primarily a result of the required trim setting that slightly changes as the blade properties vary.

3.6.3 Comparison of Conventional and Swashplateless Rotor Trimming Angles

Figure 3.63 compares conventional and swashplateless rotor pitch angles for the complete range of advance ratios ($\mu = 0$ to 0.35). The blade pitch angles are obtained at 75% blade station. The swashplateless rotor has a pitch index angle of $16°$. The figure shows that the swashplateless rotor is successfully trimmed with the trailing-edge flap control in the complete range of advance ratios. Figure 3.63(a) shows collective blade pitch of the swashplateless rotor exhibiting smaller θ_0 than the conventional rotor at advance ratios

below 0.30. This is because the collective angle of the flap is downward at advance ratios below 0.30 (Figure 3.63(d)), and this results in favorably additional lift from the trailing-edge flaps, which in turn reduces the required blade pitch angles. At an advance ratio of 0.35, the trailing-edge flap is collectively deflected $4°$ upward, which generates adverse negative lift. This is compensated by a half degree increase of main blade pitch as shown in Figure 3.63(a). Figures 3.63(b) and 3.63(c) compare the blade cyclic pitch of the conventional rotor with the swashplateless configuration. As expected, similar trends are observed between the two rotor configurations. The difference is attributed to the additional lift generated by the flap cyclic deflections.

Figure 3.63(d) presents the trailing-edge flap deflection required to trim the swashplateless rotor. The blade index angle of the swashplateless rotor, 16°, is larger than the required blade pitch at advance ratios below 0.30. Trailing-edge flap collective angle, δ_0, is deflected downward for μ below 0.30 to bring the blade pitch down, while δ_0 is deflected upward at an advance ratio of 0.35 to twist the blade nose-up to the desired position further. The longitudinal cyclic, δ_{1s}, presents small variation at advance ratios below 0.25, and increases largely above an advance ratio of 0.25. This is because of the cyclic twist effect of rotor blades from the flap collective angle, δ_0, under the lateral asymmetric aerodynamic environment in forward flight conditions. A downward deflected δ_0 twists the blade nose-down more in the advancing side of the rotor than the retreating side because of difference of tangential velocities, and this results in a desirable blade longitudinal cyclic twist used to trim the rotor. As shown at advance ratios of 0.1 and 0.25, this blade cyclic twist resulted from trailing-edge flap collective deflection, δ_0, is sufficient to trim the rotor as the required trailing-edge longitudinal cyclic, δ_{1s}, is almost zero. Similar

effect is seen for the blade lateral cyclic twist because of the flap collective deflections. However, trailing-edge flap lateral cyclic, δ_{1c}, is generally small because of the small required values of blade lateral cyclic pitch. Overall, the required half peak-to-peak values of trailing-edge flap deflections are shown below $6°$ while the mean values are below $5°$ in the complete range of advance ratios.

Figure 3.63(e) illustrates the mean and half peak-to-peak values of the flap hinge moments at several advance ratios. Due to the use of aerodynamic balance overhang, the hinge moments are relatively small in the complete range of advance ratios. Amplitude of mean hinge moments generally reduces with increasing advance ratio because the flap collective, δ_0, is decreasing with respect to advance ratio. Half peak-to peak values of hinge moments increase with respect to advance ratio primarily because of the increment of trailing-edge flap travel range and the aggravation of unsteady aerodynamic environment.

Figure 3.63(f) presents the actuation power for the swashplateless rotor at several advance ratios. The actuation power is the mean value of the positive product of the hinge moment and flap input rate, and is essentially dominated by the flap deflection amplitude and rate. At an advance ratio of 0.25, the actuation power is at minimum because the half peak-to-peak trailing-edge flap deflections are at minimum (Figure 3.63(d)).

Figure 3.64 compares conventional and swashplateless rotor control settings for the complete range of advance ratios ($\mu = 0$ to 0.35). For comparison purposes, the conventional rotor used in this section has the same torsional frequency as the swashplateless rotor configuration. Figure 3.64(a) presents the trailing-edge flap deflection required to trim the swashplateless rotor. The blade index angle used in the simulation is 18°, which yields

small collective flap angle at an advance ratio of 0.3. The required half peak-to-peak values of trailing-edge flap deflections are shown to be below 4°, and the mean values are smaller than 6° in the complete range of advance ratios. The trailing-edge flap collective angle, δ_0, is deflected downward (positive) at advance ratios below 0.30 to bring the blade pitch down, whereas δ_0 is deflected upward (negative) at an advance ratio of 0.35 to twist the blade nose-up to the desired position further. The longitudinal cyclic, δ_{1s}, shows small variation at advance ratios below 0.30, and increases rapidly at advance ratios above 0.30. This is because of the cyclic twist effect from the flap collective angle, δ_0, in forward flight; that is, flap collective generates a cyclically varying pitching moment because of the laterally asymmetric air velocities. This results in a cyclic blade pitch variation from flap collective deflection. The cyclic blade pitch of a downward deflected flap collective, δ_0, benefits flap longitudinal cyclic, δ_{1s} whereas, upward, δ_0 is against δ_{1s}. Trailing-edge flap lateral cyclic, δ_{1c}, is generally small because of the small blade lateral cyclic pitch. Figure 3.64(b) compares the 75%R pitch angles of a conventional and swashplateless rotor. The pitch angle is relative to the hub plane; that is, the pitch index angle is included for the swashplateless rotor. The collective blade pitch of the swashplateless rotor exhibits smaller θ_0 than the conventional rotor at advance ratios below 0.30. This is because of the favorable additional lift generated from the downward deflected trailing-edge flaps. The blade longitudinal and lateral cyclic pitch of the swashplateless rotor exhibits similar trends to those of the conventional rotor, with the small difference attributable to the additional lift generated by the flap cyclic deflections, δ_{1s} and δ_{1c}. Figure 3.64(c) illustrates flap actuation requirements at several advance ratios. By using flap aerodynamic balance overhang, the hinge moments are relatively small in the complete range of advance ratios.

The actuation power is dominated by the flap deflection amplitude and hinge moment. At an advance ratio of 0.30, the actuation power is a minimum, because the trailing-edge flap cyclic angles are small (as shown in Fig. 3.64(a)).

3.6.4   Parameter Study

This section presents the result of parametric study of key design variables on the control effectiveness and actuation requirement of trailing-edge flap as primary control devices. These variables are blade pitch index angle, blade root spring stiffness, blade torsional stiffness distribution, and flap location, length, chord ratio, and overhang length.

Blade Pitch Indexing

Blade pitch index angle is a key design parameter as described in Sec. 2.9.1. The optimal pitch index angle is varying with advance ratios because of the variation of required blade pitch, and as a result, a compromise is required. The effect of blade pitch indexing on the flap actuation requirements is examined at both a mediate and high speed forward flights in Figures 3.65 and 3.66, respectively, with advance ratios of 0.2 and 0.3.

Figure 3.65(a) presents the flap deflections as a function of blade pitch index angles at an advance ratio of 0.2. Both the mean and half peak-to-peak amplitude of the flap deflection are shown decreasing initially with increasing index angles. The mean and half peak-to-peak values reach a minimal value for index angles of $10°$ and $14°$ respectively, and increase thereafter with higher index angles. The decreasing of mean values of flap deflection, δ_0, is because of the required blade collective pitch is reduced with higher index angles. The half peak-to-peak values of flap deflection are reduced because of the

favorable blade cyclic twist effect induced by flap collective deflection δ_0 in the asymmetric aerodynamic environment. Figure 3.65(b) illustrates the hinge moment changes with respect to the blade pitch index angle. The half peak-to-peak component of the hinge moment shows small variations with the blade index angle. The mean values turns from a nose-up hinge moment at zero index angle to nose-down moment for index angles below $4°$ because of the required flap collective deflection is gradually changes from upward deflections, $-6°$ at zero index angle, to a downward deflection, $6°$ at an index angle of $22°$ (Figure 3.65(a)). Figure 3.65(c) presents the actuation power shows small variation with index angles before $14°$ and increases largely after that because of the increasing of both mean and half peak-to-peak components of trailing-edge flap deflections as shown in Figure 3.65(a).

Figure 3.66(a) shows that the mean values of flap deflection, δ_0, are decreased, because the required blade collective pitch motion is reduced with higher index angles. The flap collective deflection reaches almost zero with a pitch index angle of 16° at an advance ratio of 0.3, and increases thereafter, because the index angle provides more pitch than is needed for steady flight trim (i.e., downward flap deflections would be required). The flap cyclic deflections reduce because of the favorable blade cyclic twist effect induced by downward flap collective deflection, δ_0, in the asymmetric aerodynamic environment. Figure 3.66(b) shows that blade collective pitch decreases with blade index angle because of the additional lift generated by a downward deflected flap. Similarly, the lift obtained by cyclic flap inputs alters the blade longitudinal cyclic pitch. Figure 3.66(c) shows the half peak-to-peak value of flap hinge moment changes less because of small variation of cyclic components of blade pitch angle and flap deflections. The mean values vary from a

nose-up hinge moment at zero index angle, to a nose-down moment for index angles be-low 8°. The actuation power decreases with larger index angles because of the reduction of flap cyclic deflections and hinge moments. Figure 3.66 suggests an optimal blade pitch index angle of 18° for an advance ratio of 0.3 with the baseline root spring. However, the optimal pitch index angle is varying with advance ratios because of the variation of required blade pitch, and as a result, a compromise is required.

Blade Root Spring Stiffness

Figure 3.67 investigates the effect of root spring stiffness on flap deflection, blade pitch, and actuation requirement. Figure 3.67(a) shows the flap collective deflection increases dramatically with increasing blade root spring. Flap collective deflection also changes from upward deflection for root spring stiffness at 69 lb/in to downward deflection for the rest cases. This is because the pitching down aerodynamic moment generated by the baseline blade is also more effective in driving the blade pitch nose-down with a softer root spring. This results in the flap deflecting upward to pitch up the blade, to achieve the required trim position. Flap cyclic deflections increase after root spring stiffness of 150 lb/in, and it also shows the cyclic effects of flap collective. When flap collective is upward, larger cyclic is required. Figure 3.67(b) compares blade pitch angles of swash-plateless and conventional rotor with different root spring stiffness. For the conventional rotor, the root spring stiffness represents the value of rotor control system stiffness. The blade collective pitch of the swashplateless rotor reduces with increasing spring stiffness because of the favorable lift generated by the flap downward deflections. The blade cyclic pitch also exhibits a variation with root spring stiffness because of the lift generated by

the cyclic flap deflections. Figure 3.67(c) shows mean of the hinge moment is directly related to the corresponding components of the flap collective, increasing with increasing root spring stiffness. The actuation power shows a minimum at root spring of 119 lb/in, which has small cyclic flap deflection, and increases thereafter. Figure 3.67 shows that flap deflections, both collective and cyclic, are small using a root spring around 119 lb/in, which results in a blade torsional frequency of 2.1/rev. However, the selection of low root spring stiffness should be considered along with targeted forward speed and selection of index angles. The selection of soft root spring can be of concern to aeroelastic stability and has been examined carefully.

Blade Torsional Stiffness Distribution

Figure 3.68(a) shows that flap collective increases with increasing blade torsional stiffness. This increase is attributable to the reduction in twist motion along the blade segment. The blade torsion stiffness parameter was found less effective at raising the flap effectiveness, because the trailing-edge flap achieves primary control mainly through blade pitch at the root spring, rather than blade sectional twist motion. Figure 3.68(b) shows a small variation of blade pitch angle with torsional stiffness. This is because the small changes in flap angle result in a minimal increment of lift through the plain flap motion. Figure 3.68(c) shows a relatively small change in both hinge moment and actuation power with blade torsional stiffness. Figure 3.68 shows the torsionally soft blade as the optimum design. However, the selection of blade torsional stiffness can have significant influence on rotor performance and dynamics.

Flap Spanwise Location

Flap spanwise location was identified as an important parameter in several studies of flaps used for active vibration control [36, 37, 39]. Figure 3.69(a) shows a reduction in both collective and cyclic flap deflection being achieved by moving the flap spanwise location toward the blade tip. This is because the flap effectiveness increases when the flap is located near the blade tip, where high dynamic pressure exists. Figure. 3.69(b) shows that the mean and half peak-to-peak components of hinge moment exhibit a very small variation with the flap location because of two counteracting effects when moving flaps outboard: the raising of dynamic pressure, and the reduction of flap deflections. For a given baseline flap length of $18\%R$, Figure 3.69 suggests the optimum flap location at $83\%R$ because moving flaps further outboard achieves small reduction on flap deflections and actuation requirements.

Flap Length

Both flap collective and cyclic reduce with increasing flap length, as shown in Figure 3.70(a), because flap effectiveness increases. Figure 3.70(b) shows the effect of flap length on actuation requirements. Although both cyclic and collective flap deflections become small with increasing flap length, the mean and half peak-to-peak components of the hinge moment increase. Overall, actuation power decreases slightly with increasing flap length. Considering both the flap effectiveness and actuation requirement, Figure 3.70 suggests an optimal flap length of $22\%R$. Further increasing the flap length achieves only small reductions in flap deflections and actuation requirements.

Flap Chord Ratio

The flap chord ratio is a key design parameter, because it plays an important role in determining the dominant flap effect (i.e., incremental lift or pitching moment). Previous test data and theoretical predictions related to fixed-wing trailing-edge flaps [64, 100] show that the flap pitching moment coefficient reaches a maximum around a flap chord ratio of 0.26 without overhang, or 0.36 with an overhang of 29% flap chord (Figure 3.71). Figure 3.72(a) shows that flap collective presents the minimum at 30% airfoil chord although the variation of flap collective and cyclic with flap chord ratio is small. This is because of the small changes of $dc_m/d\delta$ in the range of 0.1 to 0.5c for a flap with overhang length of 29% flap chord (Fig. 3.71). Figure 3.72(b) shows both the mean and half peak-to-peak values of flap hinge moment increase with increasing flap chord ratio, which mainly results from flap hinge moment coefficient increase. The actuation power increases with flap chord ratio. Figure 3.72 suggests a flap chord ratio of 0.30 or smaller, when considering both flap effectiveness and actuation requirements.

Flap Overhang

Figure 3.73(a) shows both collective and cyclic flap deflections reduce with increasing flap overhang because of the increased sensitivities to pitching moment, $dc_m/d\delta$ (Fig. 3.71). Figure 3.73(b) shows both the mean and half peak-to-peak components of hinge moment reduce with increasing flap overhang, reaching minimum around 15% chord, and then increase thereafter. Actuation power has a minimum at a flap overhang of 15% chord. The use of flap overhang can be of concern to aeroelastic stability if flap

overhang becomes too large [70].

3.6.5   Trailing-Edge Flap Performing Multiple Functions

Predictions with a trailing-edge flap performing both primary control and active vibration control are shown in Figures 3.74 and 3.75. Figure 3.74(a) illustrates the flap input requirements to provide primary control and active vibration control for a complete rotor revolution at an advance ratio of 0.2. The total flap inputs required for both primary control and active control are between 2 to 6 degrees. Figure 3.74(b) compares the 5/rev vibratory hub loads of the swashplateless rotor with and without active flap inputs for vibration reduction. The weighting parameters on the hub loads are $\{0.04, 2.3, 1.0, 0.44, 0.136\}$, acting on hub longitudinal, lateral, and vertical forces, and rolling and pitching moments respectively. Maximum reduction is shown with hub rolling moments that has a 78% reduction whereas minimum reductions with hub longitudinal force with 27% reduction. Overall, the objective function J (Eq. 2.8) is reduced by 83%. Similarly, Figure 3.75 shows the flap input requirements and vibration reductions at an advance ratio of 0.3. The total flap inputs required for both primary control and active control are between -5 to 4 degrees. Maximum reduction is shown with hub lateral forces that has a 85%. Hub pitching moment has a 15% increase with the active vibration control, and this may indicate that it require a larger weighting in the objective function J. Overall, the objective function J is reduced by 56%.

3.6.6 Aeroelastic Stability of Swashplateless Rotor

Figure 3.76 presents the variation of blade stability with airspeed for both a swashplateless rotor and conventional rotor. The stability results presented are damping ratios in the rotating frame. For comparison purposes, the conventional rotor used in this section, again, has the same torsional frequency as the swashplateless rotor, i.e., 2.1/rev. Figure 3.76(a) compares the blade lag mode damping ratio. The behavior of the blade lag mode is important for the aeroelastic stability of the rotor system, because the coupling of this mode with the inplane hub motions, which can cause dynamic instabilities known as ground and air resonance. The swashplateless concept has higher lag damping than the conventional rotor at advance ratios below 0.325. Figure 3.76(b) illustrates the variation of the blade flap mode damping with airspeed, for both the swashplateless and conventional rotor. The blade flap mode is generally a less important mode in rotor aeroelastic stability, because this mode is always adequately damped by the aerodynamic forces. Figure 3.76(c) compares the torsion mode damping of swashplateless and conventional rotors. Both have a well damped torsion mode, with the swashplateless rotor having a higher damping ratio than the conventional rotor at advance ratios above 0.15.

Low blade torsional frequency, which is inherent in the swashplateless design, has been known to be the cause of aeroelastic instability and flutter of the rotor blades [28]. Figure 3.77 presents the variation of blade aeroelastic stability with blade fundamental torsional frequency at an advance ratio of 0.3. This sweep of blade torsional frequencies was carried out by altering the blade root spring stiffness for the swashplateless concept and changing the pitch link stiffness for the conventional case. Figure 3.77(a) shows

that blade lag mode damping of the swashplateless rotor exhibits small variation with torsional frequency, whereas the conventional rotor lag damping reduces slightly with increasing blade torsional frequency. Figure 3.77(b) shows that for the swashplateless rotor, flap damping is higher than for conventional rotor. Figure 3.77(c) shows that both the swashplateless and conventional rotors have moderately well damped torsional modes. The swashplateless concept has a larger torsional damping value than the conventional rotor.

3.7 Swashplateless Trailing-Edge Flap Helicopter Rotor in Free Flight Trim

This section describes the analytical result of a swashplateless ultralight helicopter rotor with trailing-edge flaps for primary flight control in free flight trim.

3.7.1 Correlation Study of Baseline Teetering Rotor (ASI 496)

Before the results of a rotor with trailing-edge flaps are investigated, the predictive capability of present comprehensive analysis is evaluated for a baseline teetering rotor (without trailing-edge flaps). Since there is no measured data available, the predictions of present analysis are compared with calculations from CAMRAD II [62, 63]. The calculated results of blade natural frequencies, trim angles, blade flapping angle, and main rotor power are correlated. Following this, the predicted results of the flapped rotor with the embedded flaps are presented, and the effects of various important design variables are investigated.

Description of Baseline Rotor

The baseline rotor used in this section is of ASI 496, an ultralight 2-bladed teetering rotor (Figure 3.78). This helicopter has a cruise speed of 61 knots, corresponding to an advance ratio of 0.16 at the nominal rotor speed. The rotor characteristics are given in Table 3.5. The blades are attached together, and hinged at the rotational axis, and have no independent flap and lead/lag offset hinges. The blades have a common flapping axis, however each blade has a separate pitch bearing which allows cyclic and collective pitch change capability. The teetering design has the advantage of being mechanically simple with fewer arts, and is easy to maintain. The teetering head lets various forces from the blades balance themselves. Since the teetering rotor is inherently stiff-in-plane, it is not subject to ground resonance instability. ASI 496 rotor has a precone of three degrees built into the rotor hub in order to reduce the stresses in the blades. An undersling design is also adopted in order to reduce Coriolis forces induced by teetering motion. The rotor system is torsionally soft with the fundamental torsional frequency of 2.2/rev (Table 3.6). This torsionally soft design is also appropriate for implementation of trailing-edge flaps for primary controls. The fuselage has a forward longitudinal CG offset from the rotor hub of 0.75 inches, and the vertical fuselage CG position is located below the hub of 50.6 inches. The main shaft has a built in forward tilt of 2 degrees.

Blade Natural Frequencies

Figure 3.79 compares computed natural blade frequencies from the present analysis with results obtained using CAMRAD II. Good agreement is seen for the first and second

Table 3.5: ASI 496 rotor properties

Property	Value
Rotor Type	Teetering
Number of Blades	2
Rotor Diameter	23 ft.
Rotor Speed	525 RPM
Chord	6.7 inch
Linear Twist Angle	-8°
Lock Number	5.01
Solidity	0.0309
C_T/σ	0.075
Undersling	3.45 inch
Weight	912 lb
Cruise Speed	61 knots
CG position	0.75 in forward
Parasite Drag Area Ratio ($\frac{f}{A}$)	0.0315

flapwise bending modes, the first chordwise mode, and the first torsion mode. Some discrepancy exists in the fourth flapwise bending mode and second inplane mode predictions. It may be due to differences in modeling assumptions since these higher order coupled modes are expected to be sensitive to them. Natural frequencies for the baseline rotor are summarized in Table 3.6 for the nominal rotating speed.

Table 3.6: Calculated normal mode frequencies for ASI 496 rotor at rotating speed of 525 RPM

Mode	Frequency (per rev)
1st flap	1.11
1st inplane	1.23
1st torsion	2.20
2nd flap	3.09
3rd flap	5.78
2nd inplane	7.42
4th flap	8.72

Forward Flight Trim

Figure 3.80 compares blade pitch, shaft tilt, flapping angles and main shaft power for the basic teetering rotor. Figure 3.80(a) shows the predicted values for blade collective pitch, longitudinal cyclic pitch and lateral cyclic pitch for different advance ratios. Good agreement is seen between two sets of results.

Figure 3.80(b) shows the prediction of rotor shaft angles for different advance ra-

tios. Good agreement is seen for the longitudinal shaft angles except UMARC predictions show a slightly higher value at high advance ratios. Lateral shaft tilt angles are shown to have the same trend between the calculations of UMARC and CAMRAD II with a deviation of half degree. This may be due to the difference of inflow modeling used.

Figure 3.80(c) presents the calculation of blade flapping angle (or teetering angle) for various advance ratios. The longitudinal flapping angle is shown to agree well between the predictions of UMARC and CAMRAD II. The lateral blade flapping angle shows some discrepancies between the two predictions. Again, this may be attributed to the differences in inflow modeling.

Rotor Power

Figure 3.80(d) illustrates the computation of main rotor power for different advance ratios. Good agreement is seen for high advance ratios. For low advance ratios, UMARC predictions are lower than CAMRAD II predictions. This discrepancy may be due to different empirical factors used in the computation of main rotor shaft power between the two analyses.

3.7.2 Description of Swashplateless Rotor

The present swashplateless rotor design modifies the baseline rotor by replacing the pitch link assembly with a linear root spring, and keeping the torsional frequency the same as the conventional rotor. The parasite drag area of the swashplateless configuration is selected at 0.02678, 15% smaller than that of the conventional, a benefit of removing swashplate system. The selected weight for both configurations is 912 lbs that gives a

Table 3.7: ASI 496 rotor trailing-edge flap properties

Property	Value
Flap Type	Plain Flap
Spanwise Length	25 inch (0.18R)
Chordwise Size	25 % (Blade Chord)
Flap Midspan Location	0.82R

C_W/σ of 0.075 except where noted. The baseline trailing-edge flap characteristics are given in Table 3.7, and the flap has no aerodynamic balance [85] in this study. Trailing-edge flap motion is positive for downward deflection, and hinge moment is positive when its direction is "nose-up" (and "tail-down").

The analysis of swashplateless rotors is described in Sec. 2.9. Fifteen elements are used to model the main blade. The coupled blade response and the trim control settings are solved simultaneously for the propulsive trim condition. Eight time elements with fifth order shape functions are used to calculate the coupled trim solution. The trailing-edge flap motion is prescribed, and as such dynamics of smart actuators is neglected for this study [39]. A quasi-steady model adapted from Theodorsen's theory [64] is used to model the aerodynamic forces of the trailing-edge flap. The Drees linear inflow is used to obtain the induced inflow distribution over the rotor disk.

3.7.3 Comparison of Conventional and Swashplateless Rotor Performance

Figure 3.81 compares conventional and swashplateless rotor control settings for the complete range of advance ratios (μ = 0 to 0.17). The swashplateless rotor has a pitch index angle of 18°, which yields small collective flap at the cruise speed 61 knots ($\mu = 0.16$).

Figure 3.81(a) presents the trailing-edge flap deflection required to trim the swashplateless rotor. The required flap collective and cyclic angles are shown to be below 4° in the complete range of advance ratios. The trailing-edge flap collective angle, δ_0, is deflected downward for the complete advance ratio range to bring the blade pitch down. The flap collective angle also generates a cyclically varying pitching moments in forward flight conditions, which produces blade cyclic pitch motion. A downward deflected flap collective and nose-down pitching moments of the baseline airfoil are beneficial for reducing required flap cyclic deflections. The cyclic flap deflections (half peak-to-peak), show small variation for advance ratios below 0.13, and increases rapidly for higher advance ratios.

Figure 3.81(b) compares the 75%R pitch angles of a conventional and swashplateless rotor. The pitch angle is relative to the hub plane, that is, the pitch index angle is included for the swashplateless rotor. As expected, blade pitch angles, both collective and cyclic, are similar for the two configurations. The collective blade pitch of the swashplateless rotor is slightly smaller than the conventional rotor in forward flight conditions. This is because of the smaller parasite drag of the swashplateless configuration and the favorable additional lift generated from the downward deflected trailing-edge flaps. The

blade longitudinal and lateral cyclic pitch angles of the swashplateless rotor show small variations compared with the conventional, because of the parasite drag difference and the additional lift generated by the flap cyclic deflections, δ_{1s} and δ_{1c}.

Figure 3.81(c) compares main rotor power of the swashplateless and conventional rotors. In high speed forward flight conditions, the swashplateless rotor consumes moderately less power than the conventional, because of the reduced parasite drag of the swashplateless design. In hover and low speed flight conditions, the swashplateless rotor consumes the same or slightly less power.

Figure 3.81(d) illustrates main rotor shaft tilt angles of both configurations. The swashplateless rotor exhibits smaller forward tilt because of reduction of parasite drag in high speed forward flight. Lateral shaft tilts exhibit only slight difference between the two configurations.

Figure 3.81(e) shows the flap actuation requirements in different flight speeds. The mean values of the hinge moments are generally decided by the flap collective, δ_0. The half peak-to peak values of the hinge moments show small variations at hover and low speed forward flights, and increase largely for advance ratios higher than 0.13, primarily because of an increment of the trailing-edge flap cyclic, and the aggravation of the unsteady aerodynamic environment.

Figure 3.81(f) shows the flap actuation power, both the absolute value and as a fraction of main rotor power. This power is essentially zero, because it does not account for the thermodynamic losses of the actuator.

3.7.4 Hover Performance

Figure 3.82 evaluates the performance of swashplateless and conventional rotors at hover for different weight configurations. The ratio of thrust coefficient to rotor solidity, C_T/σ, are from 0.055 to 0.095 corresponding to weight from 670 to 1155 lbs.

Figure 3.82(a) shows the flap collective decreases with higher C_T/σ because of the correspondingly large blade pitch collective requirement as shown in figure 3.82(b). Flap cyclic was shown with virtually no difference at different C_T/σ. Unlike in forward flight conditions, the flap collective has no effect on blade cyclic pitch, and hence no effect on flap cyclic at hover.

Figure 3.82(b) compares the blade pitch of swashplateless and conventional rotors, and the differences are very small. As expected, the blade collective pitch angles are increasing with C_T/σ, and the blade cyclic pitch angles are virtually constant versus C_T/σ.

Figure 3.82(c) evaluates the performance of swashplateless and conventional rotors with the main shaft power and figure of merit illustrated. The swashplateless rotor consumes slightly less power than the conventional, and has a slightly higher figure of merit in the ranges of C_T/σ. The advantage of the swashplateless rotor is possibly because of upload generated by flap collective moves the lift inboard, and results in more uniform blade airloads distribution [42].

Figure 3.82(d) presents the magnitudes of mean hinge moments reduce with C_T/σ because of the decreasing of flap collective angles. Half peak-to-peak hinge moments show virtually no variation with C_T/σ because the constant flap cyclic and steady aero-

dynamic environment at hover.

3.7.5   Parametric Study on Rotor Performance

The objective of the parametric study is to evaluate the performance of the teetering rotor of an ultralight helicopter with plain trailing-edge flap system for primary control, and investigate effect of various key design variables such as pitch index angle, flap location and size on rotor performance, trailing-edge flap deflections and actuation requirements.

Blade Pitch Index Angle

Figure 3.83 examines the effect of blade pitch index angle on the flap angle, blade pitch, main rotor power, and flap actuation requirements at an advance ratio of 0.16.

Figure 3.83(a) shows that the mean values of flap deflection, δ_0, are decreased, because the required blade collective pitch motion is reduced with higher index angles. The flap collective deflection reaches almost zero with a pitch index angle of 17° at an advance ratio of 0.16, and increases thereafter, because the index angle provides more pitch than is needed for steady flight trim (i.e., downward flap deflections would be required). The flap longitudinal cyclic deflection reduces because of the favorable blade cyclic pitch induced by downward flap collective deflection, δ_0, in high forward flight conditions. The effect is smaller on lateral flap cyclic than longitudinal cyclic. The half peak-to-peak of flap deflections decreases with increasing of pitch index angles.

Figure 3.83(b) illustrates that blade collective pitch decreases slightly with blade index angle because of the additional lift generated by a downward deflected flap collective. Similarly, the lift obtained by cyclic flap inputs alters the blade longitudinal cyclic

pitch, and again more on the longitudinal component.

Figure 3.83(c) presents the main rotor power showing virtually no variation in different blade index angles. This contradicts the expectation because large drag should have been generated with large flap deflections with small blade index angles. In order to give better power prediction, it requires a more accurate aerodynamic drag model.

Figure 3.83(d) shows the half peak-to-peak value of flap hinge moment changes less because of small variation of cyclic components of blade pitch angle and flap deflections. The mean values vary from a nose-up hinge moment at zero index angle, to a nose-down moment for an index angle below 14°.

Figure 3.83 suggests an optimal blade pitch index angle of 18° for an advance ratio of 0.16. However, the optimal pitch index angle is varying with advance ratios because of the variation of required blade pitch, and as a result, a compromise is required.

Flap Spanwise Location

Figure 3.84 examines the effect of flap location on the flap angle and main rotor power at an advance ratio of 0.16. Figure 3.84(a) shows a reduction in flap collective deflection is achieved by moving the flap spanwise location toward the blade tip. This is because the flap effectiveness increases when the flap is located near the blade tip, where high dynamic pressure exists. Similarly, flap cyclic reduces. Figure. 3.84(b) presents main rotor power showing no variation with trailing-edge flap locations.

Flap Length

Figure. 3.85(a) shows both flap collective and cyclic reduce with increasing flap length, because of the increasing of flap effectiveness. Again, main rotor power presents no variation with different trailing-edge flap length (figure 3.85(b)).

Flap Chord Ratio

Figure 3.86 examines the effect of flap chord ratio on the flap angle and main rotor power at an advance ratio of 0.16. The flap chord ratio is a key design parameter, because it plays an important role in determining the dominant flap effect; i.e., incremental lift or pitching moment. Previous test data and theoretical predictions related to fixed-wing trailing-edge flaps [64, 100] show that the flap pitching moment coefficient reaches a maximum around a flap chord ratio of 0.26 for a plain trailing-edge flap (Figure 3.71). As shown in Figure 3.86(a), both flap collective and cyclic deflections are minimized with a 20% airfoil chord. The main rotor power (Figure 3.86(b)) exhibits no variation with regard to trailing-edge flap chord ratio.
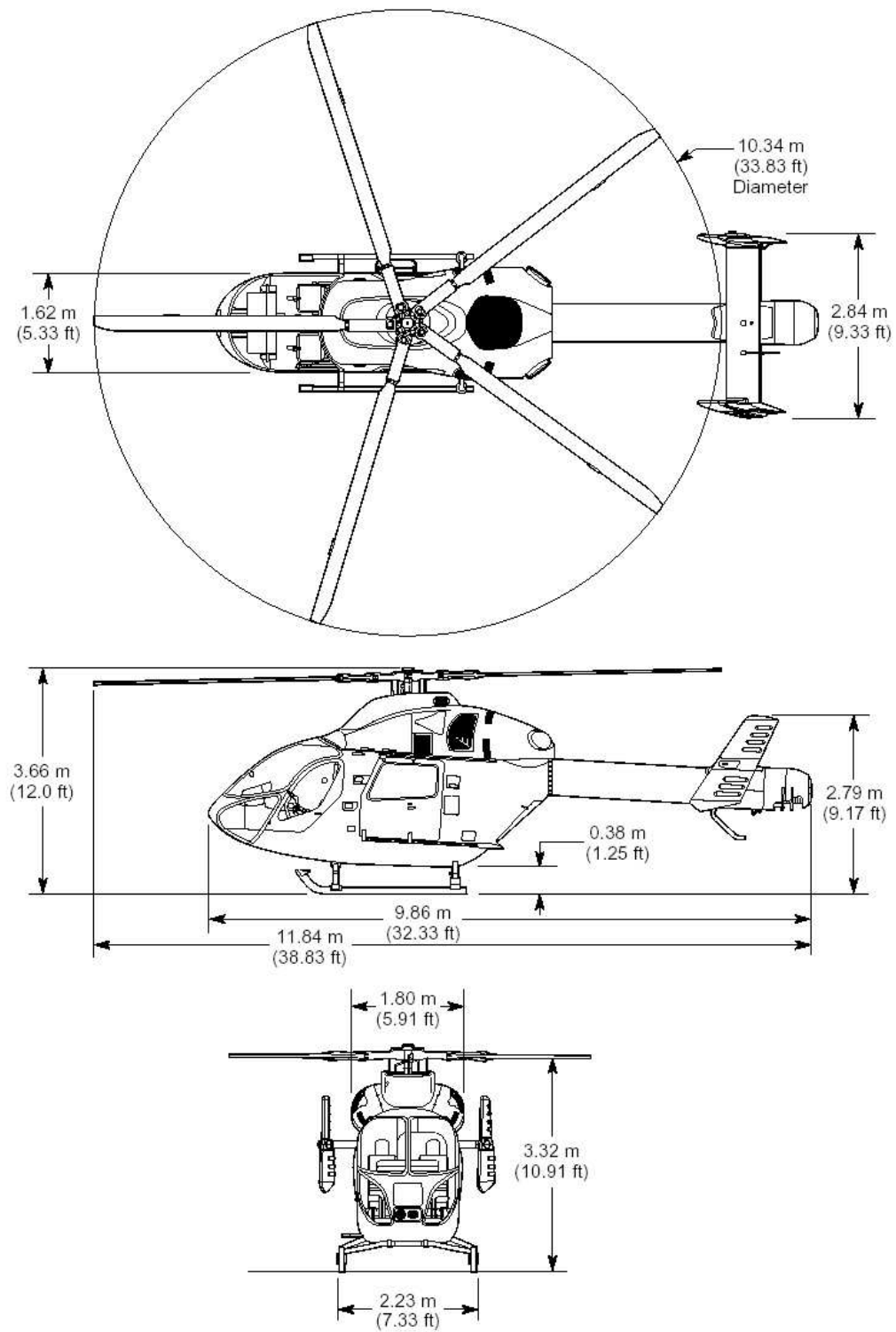
Figure 3.1: MD900 explorer [78]
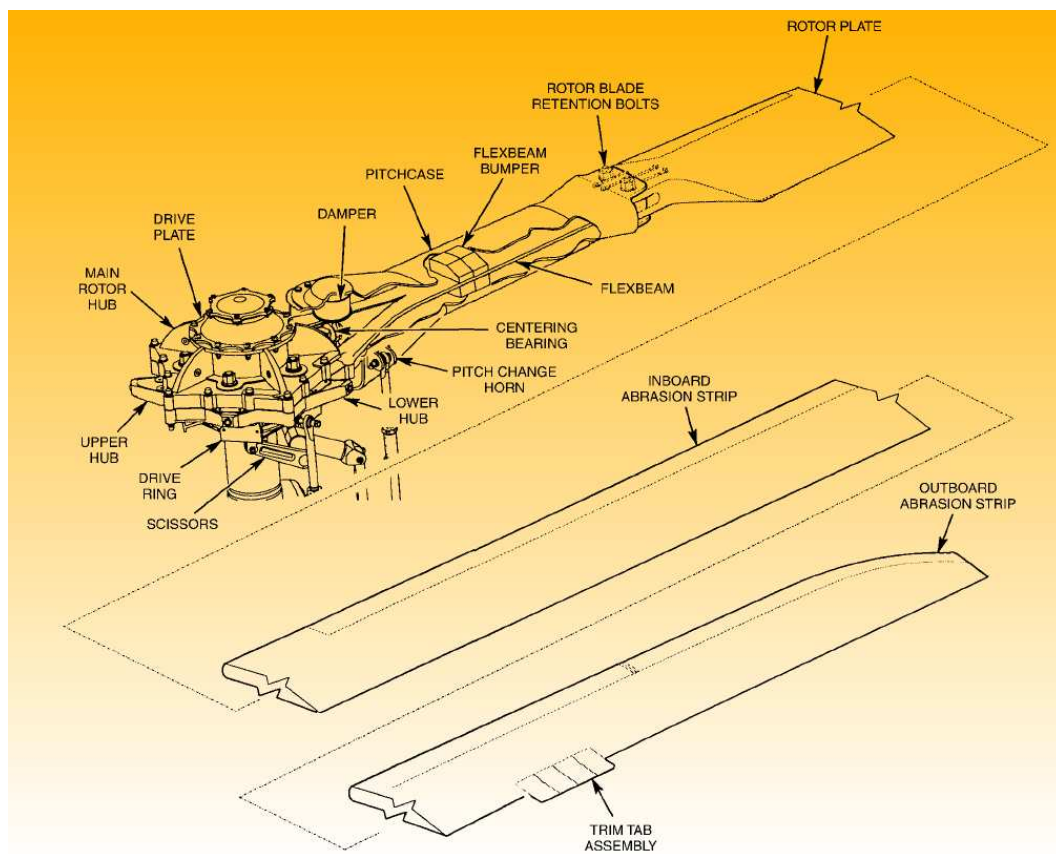
Figure 3.2: MD900 main rotor blades [78]

Figure 3.3: MDART wind tunnel test [93]
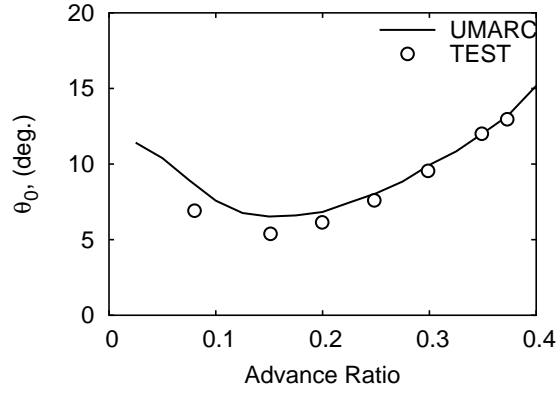
(a) Collective pitch, θ_0
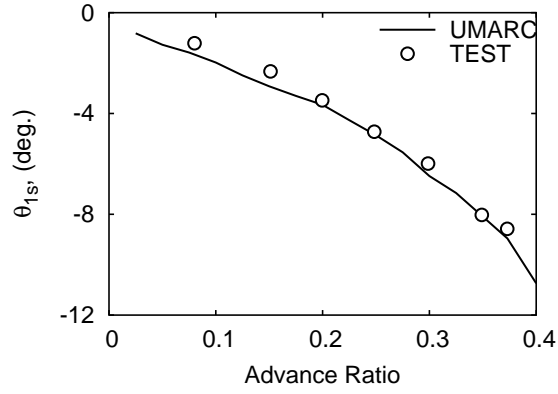
(b) Longitudinal cyclic, θ_{1s}
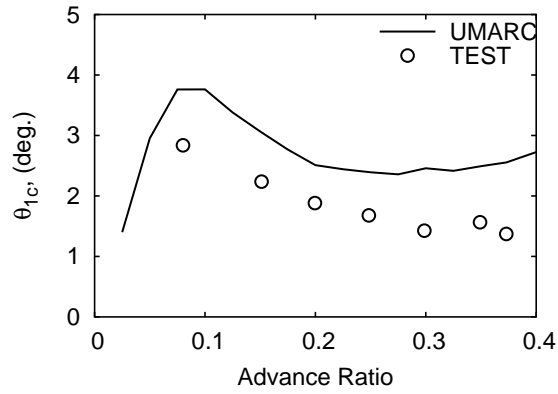
(c) Lateral cyclic, θ_{1c}

Figure 3.4: Measured and predicted control settings $\theta_0, \theta_{1c}, \theta_{1s}$ vs. advance ratio, μ (conventional swashplate control system).
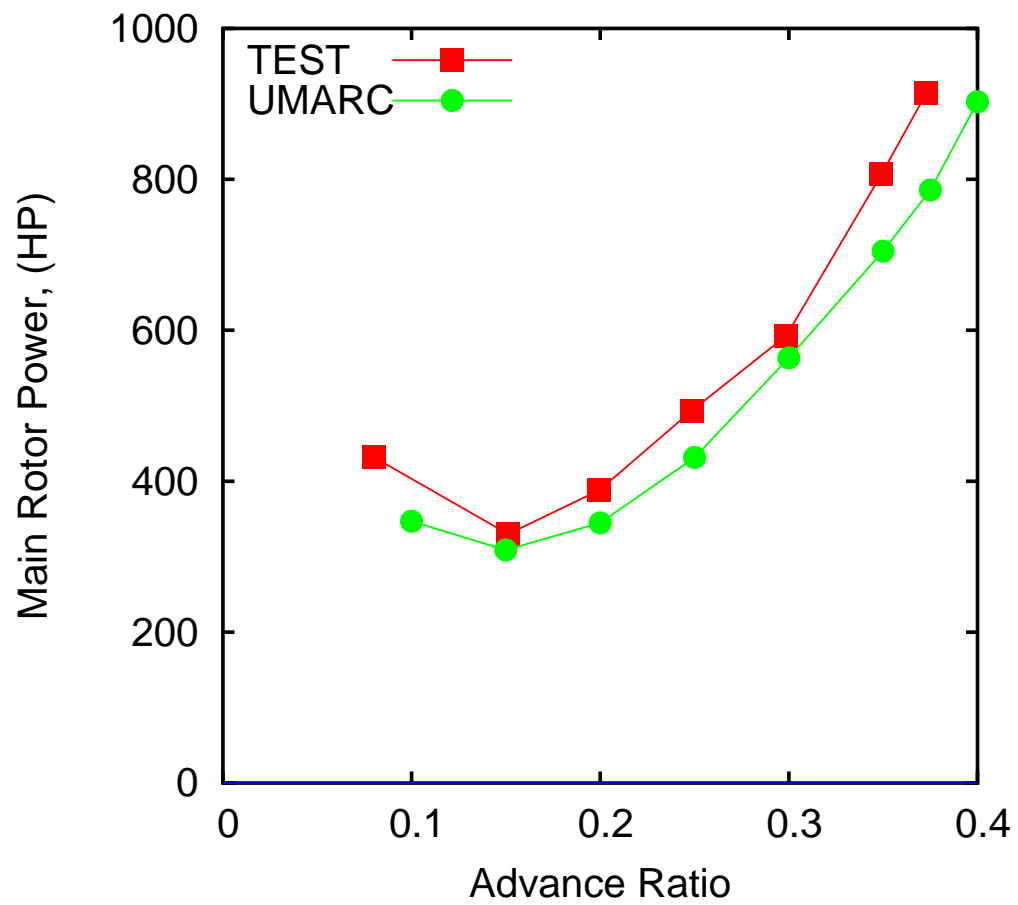
Figure 3.5: Measured and predicted main rotor power vs. advance ratio
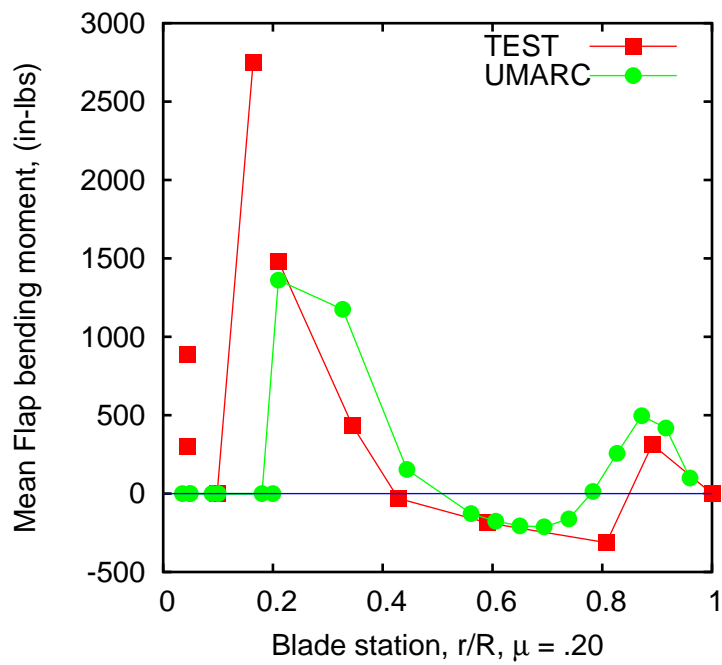
(a) Flap bending moment, mean
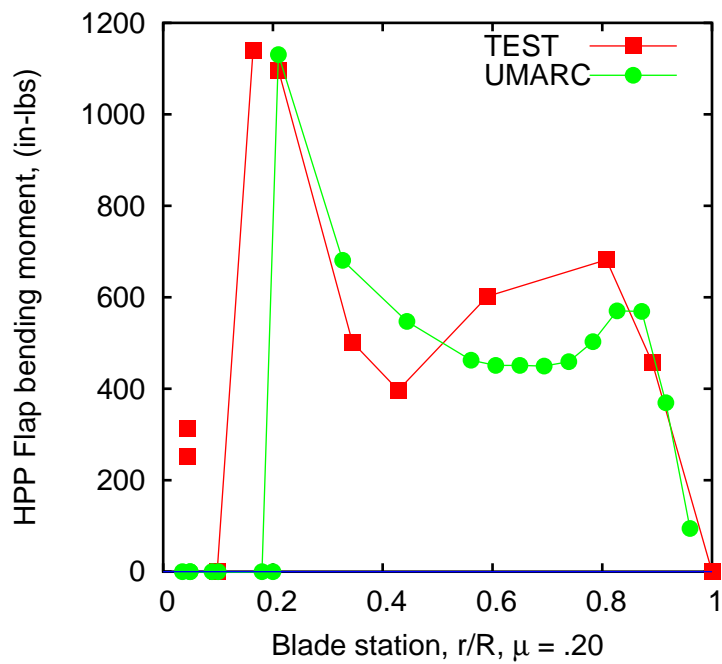
(b) Flap bending moment, half peak-to-peak

Figure 3.6: Measured and predicted flap bending moment, $\mu = 0.2$, $C_T/\sigma = 0.074$.
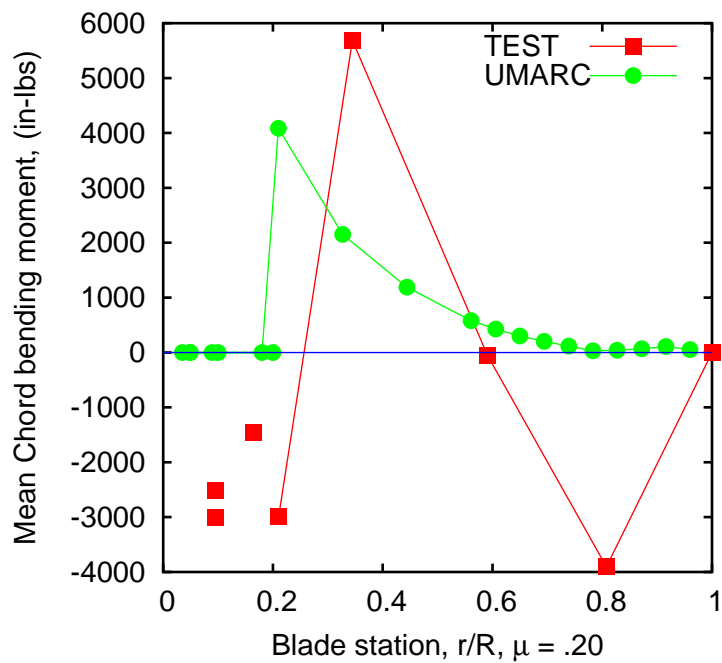
(a) Chordwise bending moment, mean
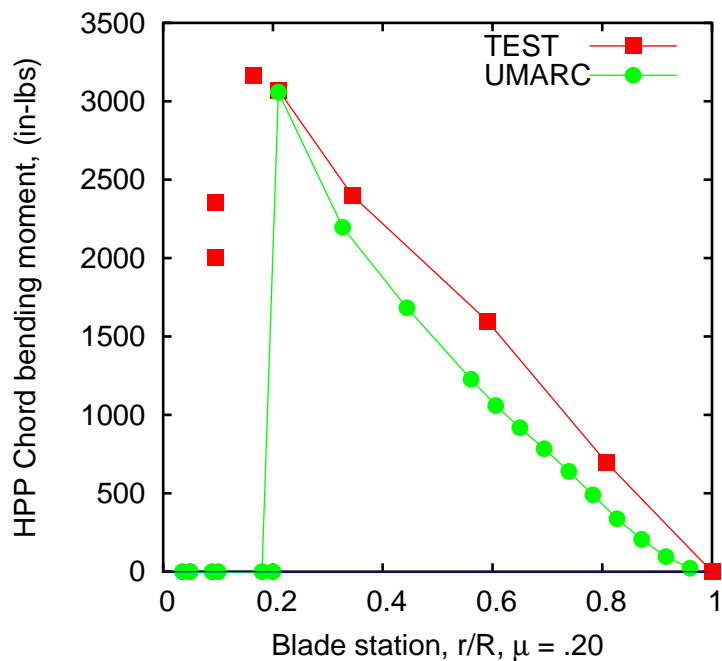
(b) Chordwise bending moment, half peak-to-peak

Figure 3.7: Measured and predicted chordwise bending moment, $\mu = 0.2, C_T/\sigma = 0.074$.
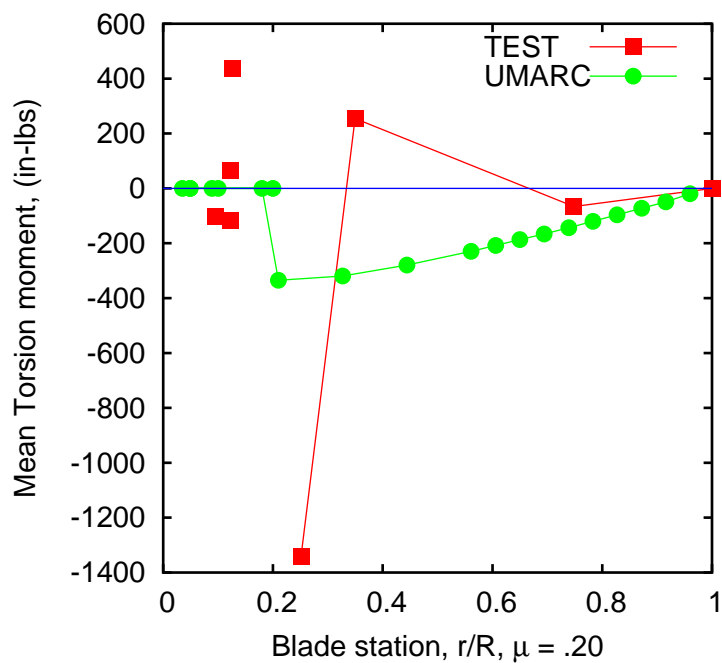
(a) Torsional moment, mean
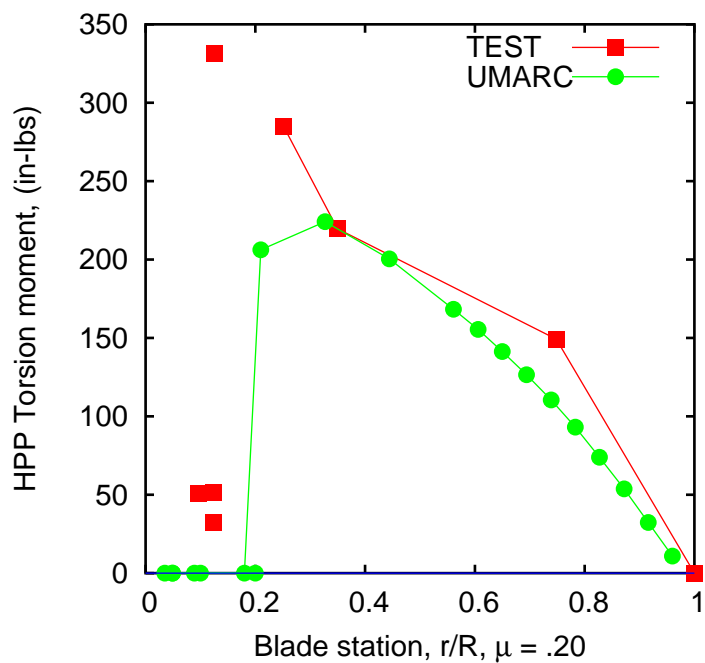
(b) Torsional moment, half peak-to-peak

Figure 3.8: Measured and predicted torsional moment, $\mu = 0.2$, $C_T/\sigma = 0.074$.
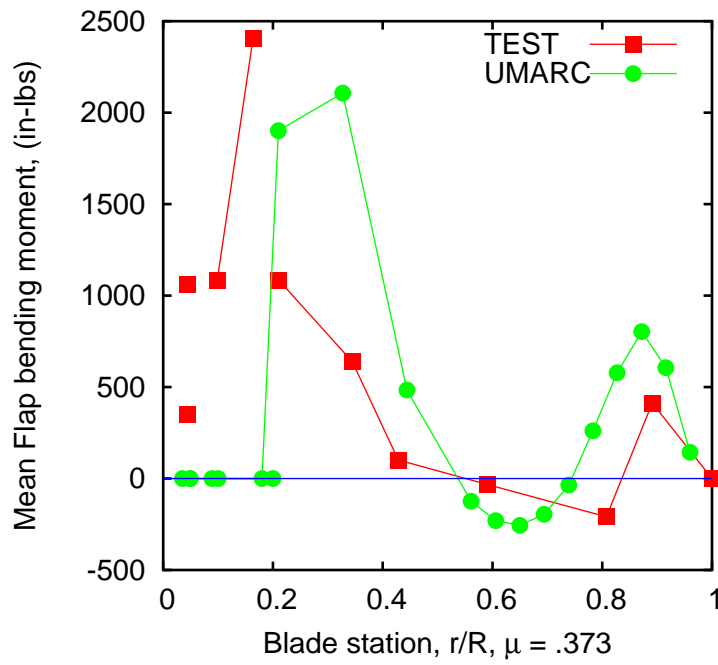
(a) Flap bending moment, mean
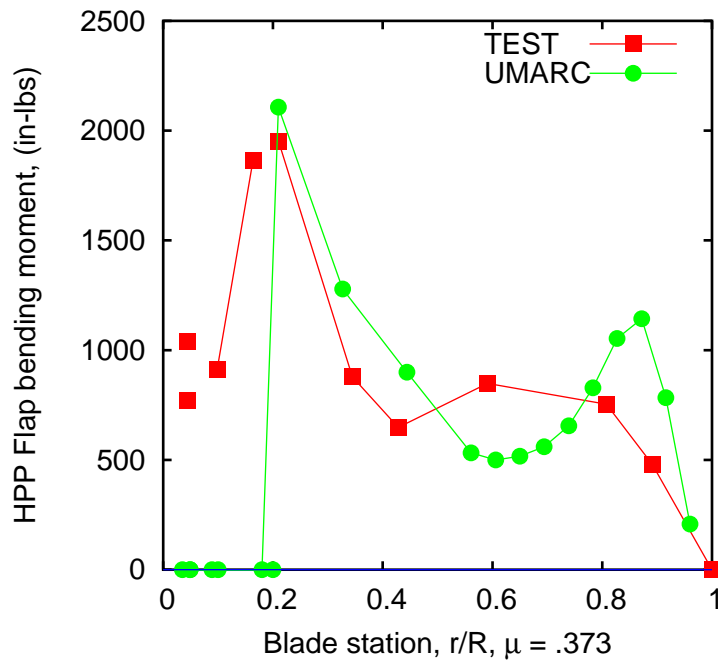
(b) Flap bending moment, half peak-to-peak

Figure 3.9: Measured and predicted flap bending moment, $\mu = 0.373$, $C_T/\sigma = 0.075$.
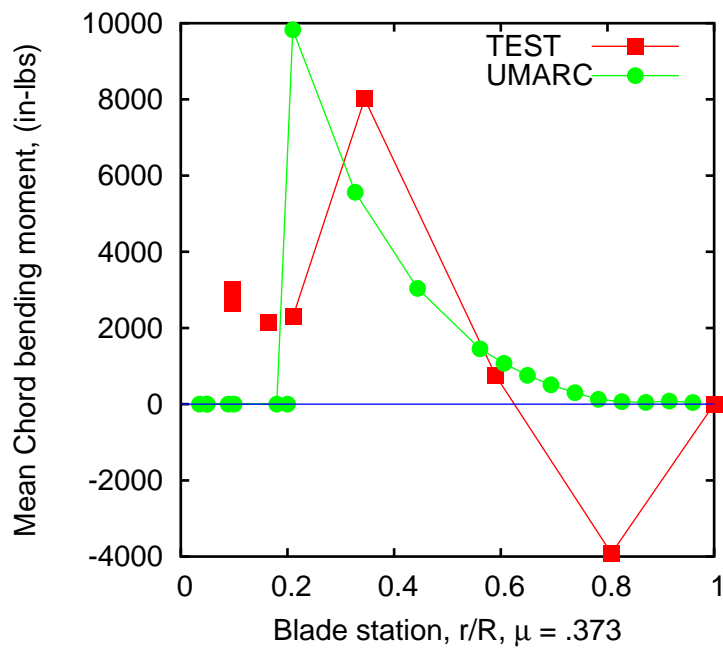
(a) Chordwise bending moment, mean
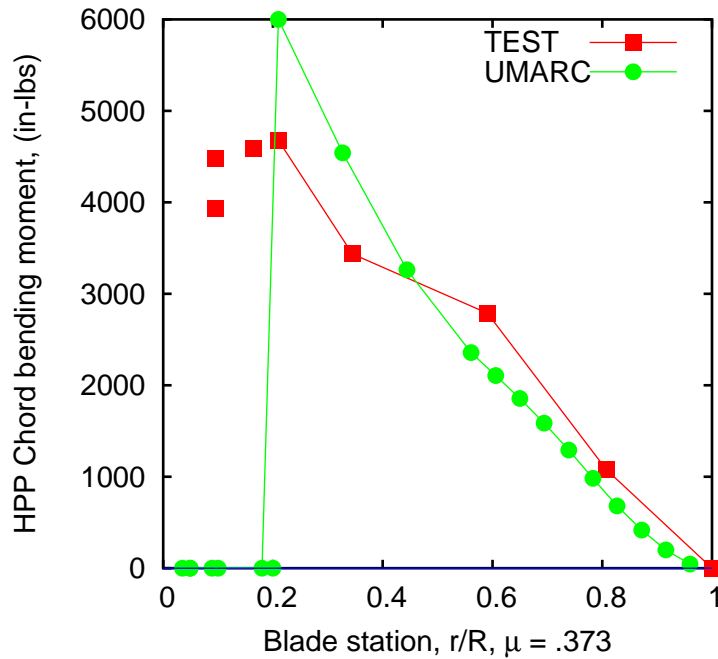
(b) Chordwise bending moment, half peak-to-peak

Figure 3.10: Measured and predicted chordwise bending moment, $\mu = 0.373$, $C_T/\sigma = 0.075$.
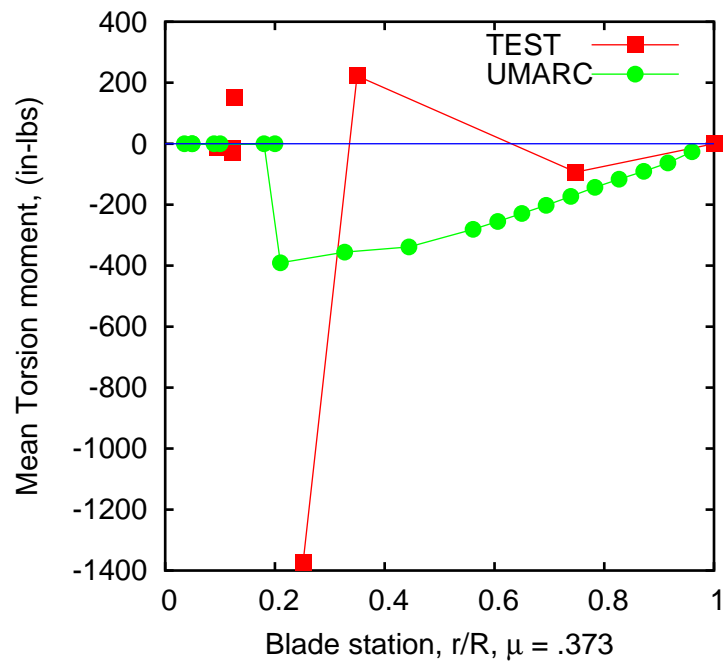
(a) Torsional moment, mean
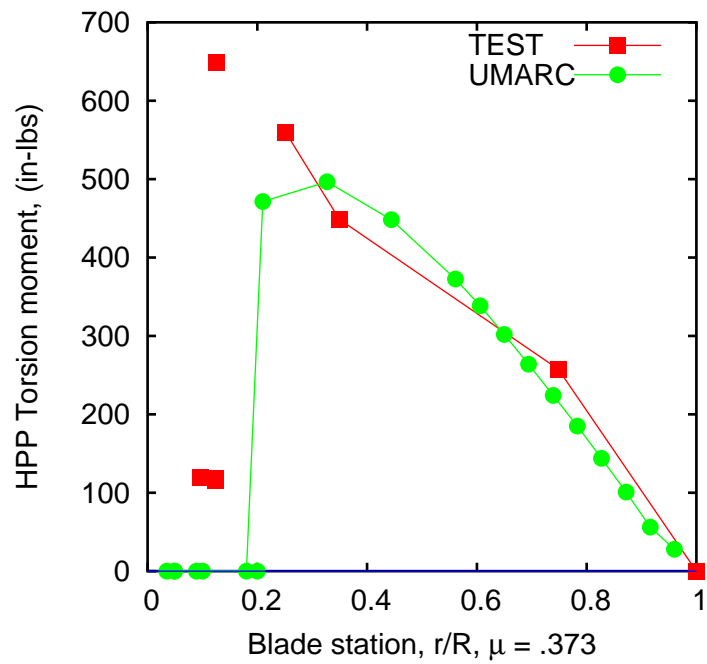
(b) Torsional moment, half peak-to-peak

Figure 3.11: Measured and predicted torsional moment, $\mu = 0.373$, $C_T/\sigma = 0.075$.
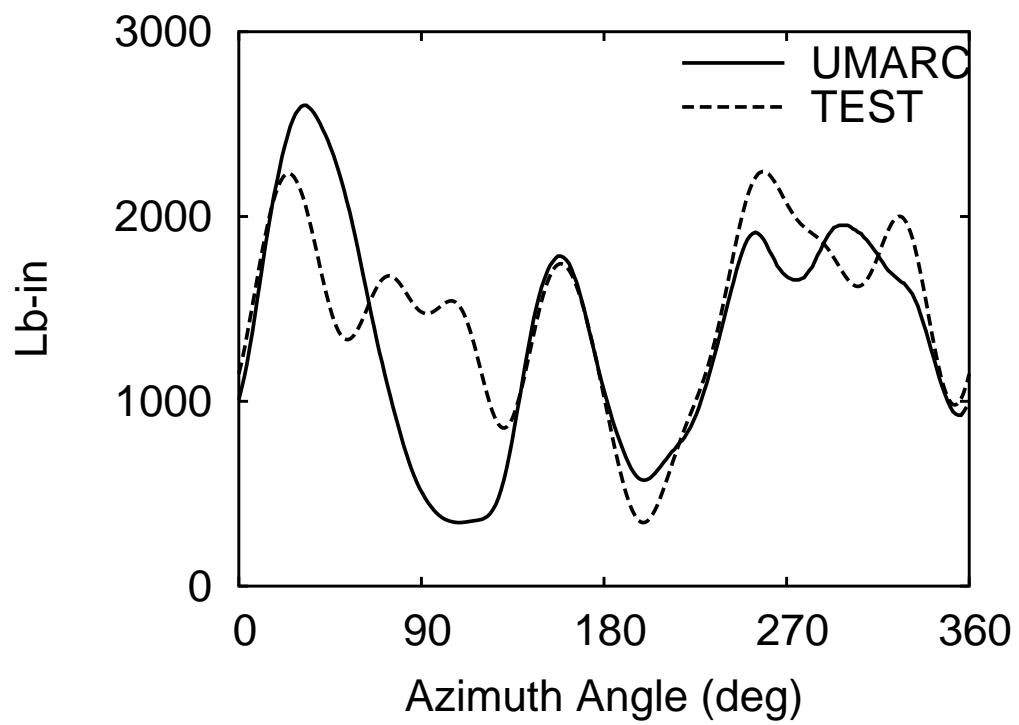
Figure 3.12: Measured and predicted flap bending moment, at $r/R = 0.21$, $\mu = 0.2$
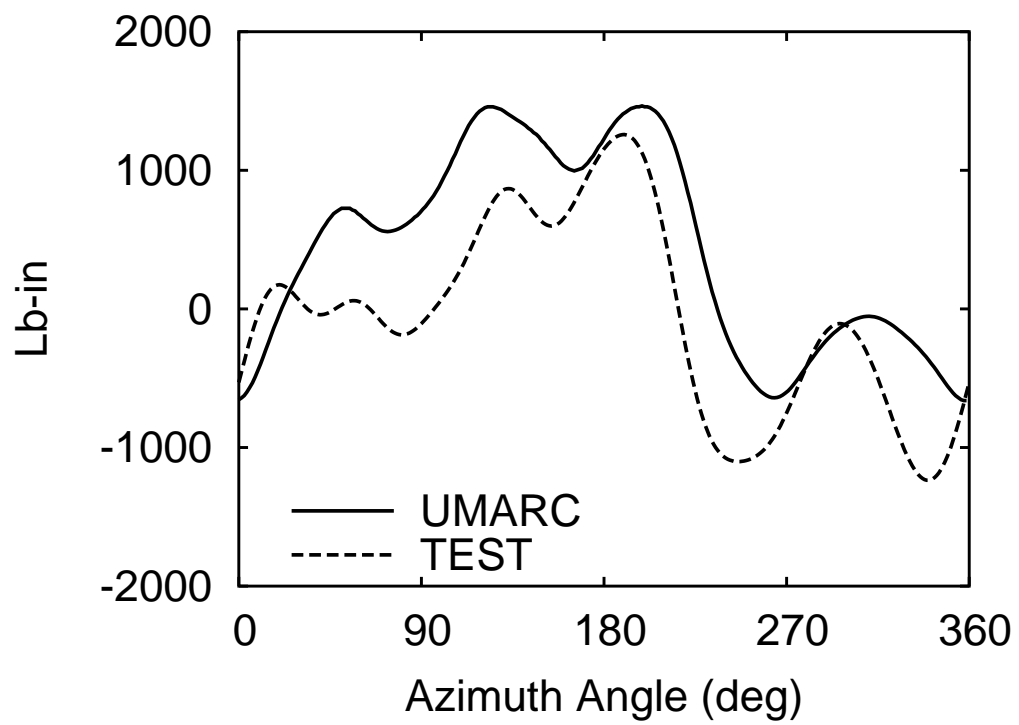
Figure 3.13: Measured and predicted chordwise bending moment, at $r/R = 0.59, \mu = 0.2$
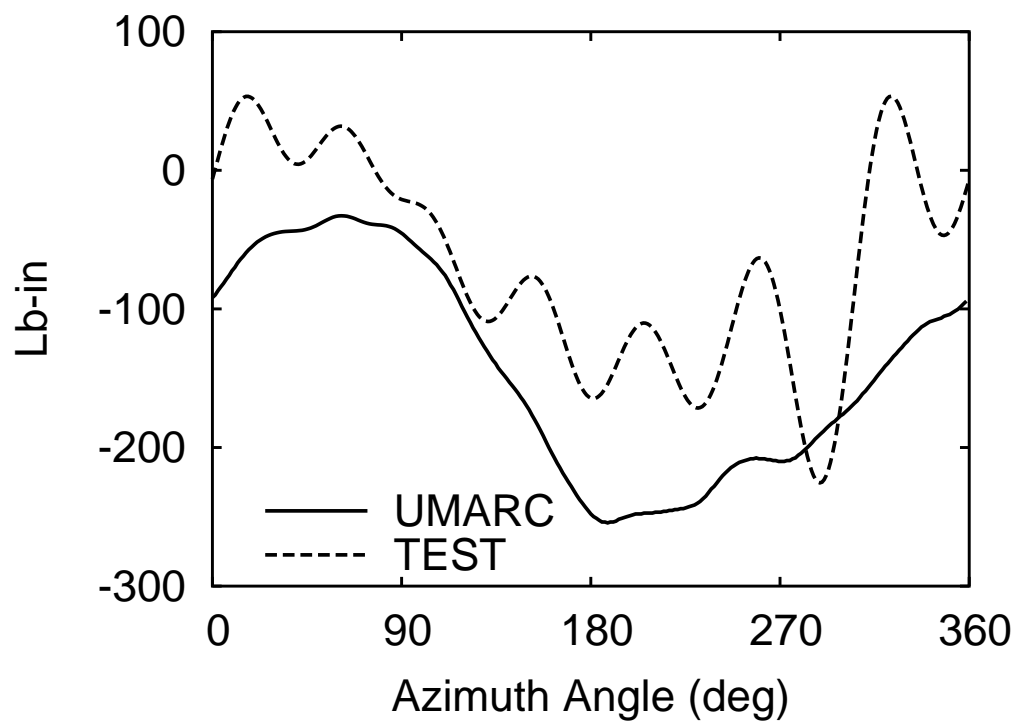
Figure 3.14: Measured and predicted torsional moment, at $r/R = 0.75, \mu = 0.2$
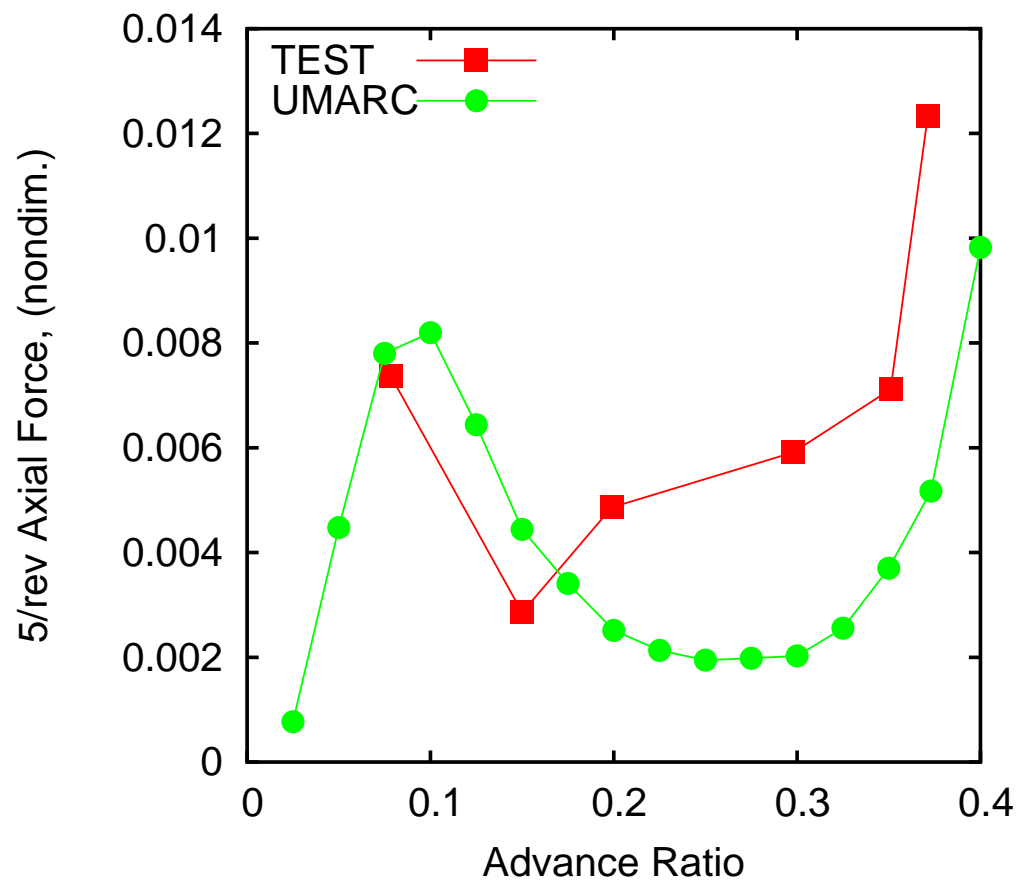
Figure 3.15: Measured and predicted 5/rev hub axial force
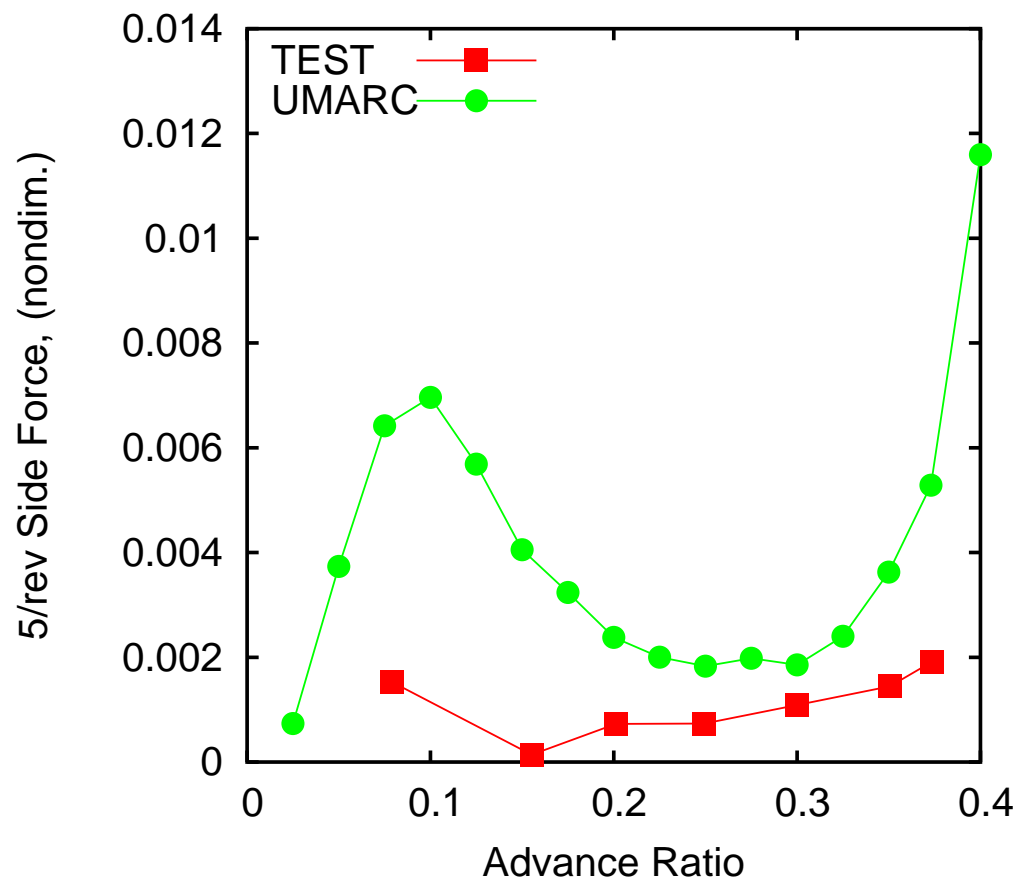
Figure 3.16: Measured and predicted 5/rev hub side force
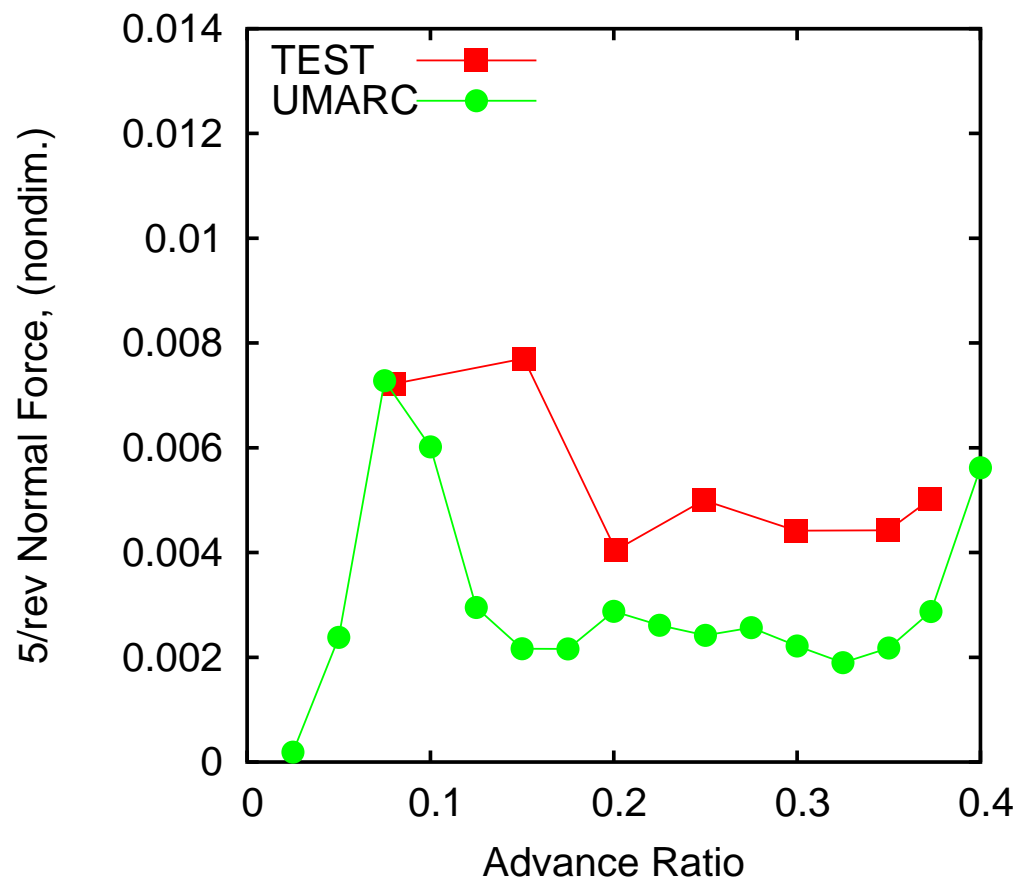
Figure 3.17: Measured and predicted 5/rev hub normal force
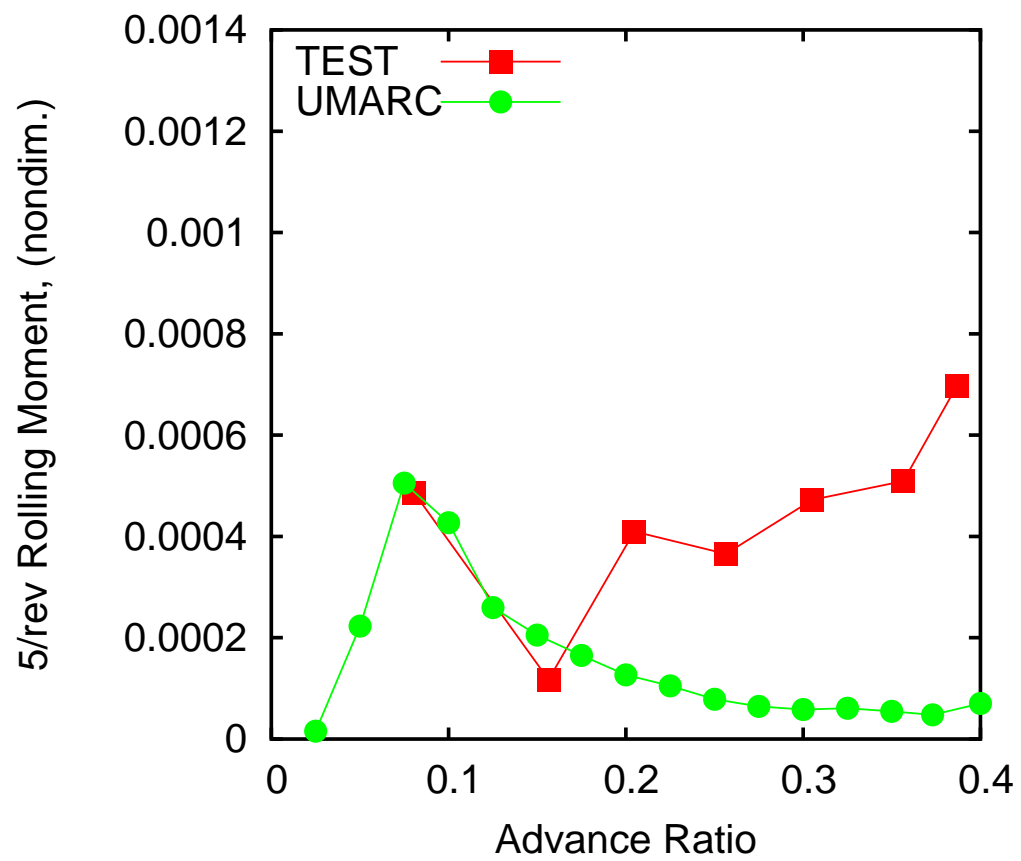
Figure 3.18: Measured and predicted 5/rev hub rolling moment
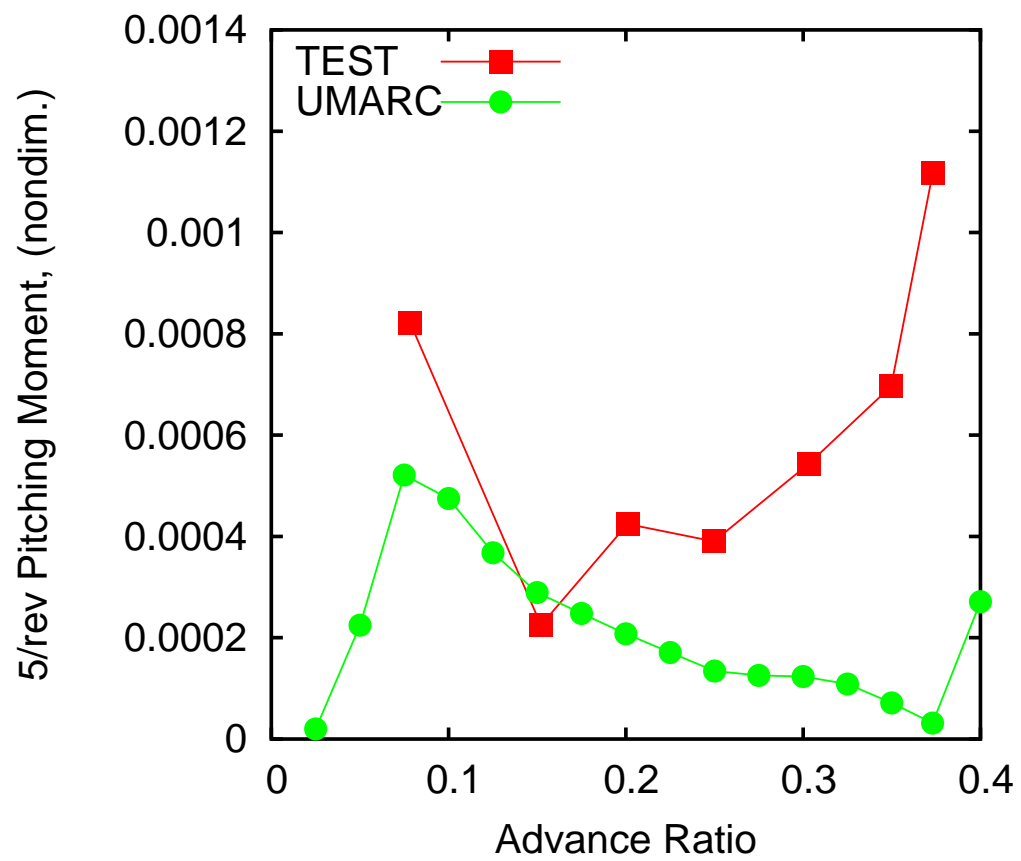
Figure 3.19: Measured and predicted 5/rev hub pitching moment
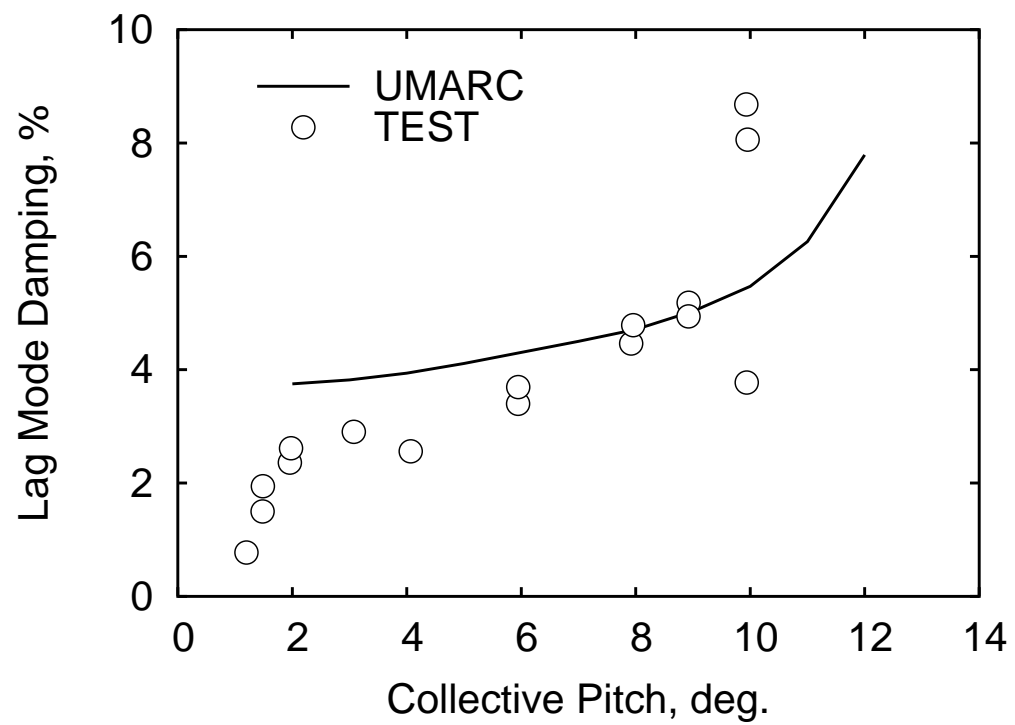
Figure 3.20: Measured and predicted blade inplane stability vs. blade collective pitch in hover
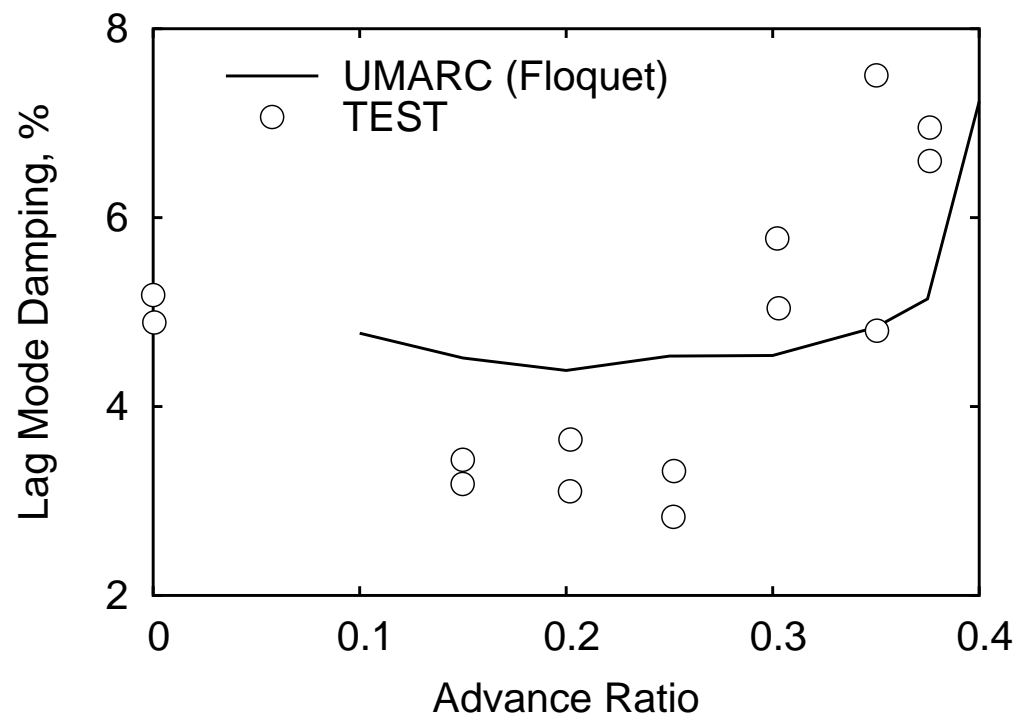
Figure 3.21: Measured and predicted blade inplane stability at different flight speeds
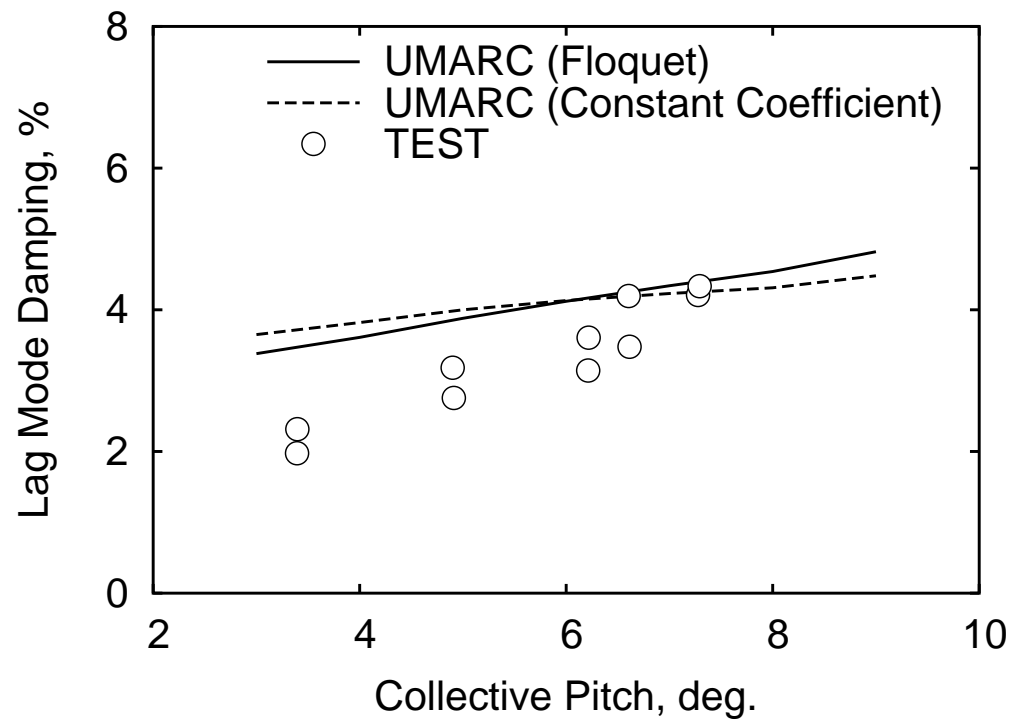
Figure 3.22: Measured and predicted blade inplane stability vs. blade collective pitch in forward flight, $\mu = 0.20$, forward shaft tilt of 5.5 degree
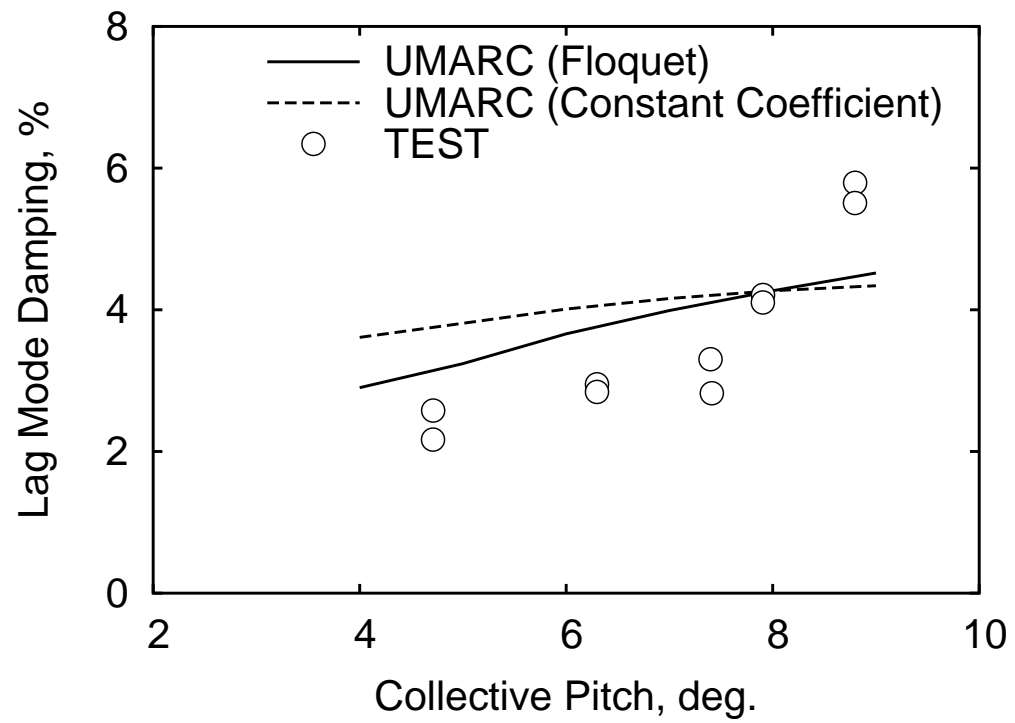
Figure 3.23: Measured and predicted blade inplane stability vs. blade collective pitch in forward flight, $\mu = 0.25$, forward shaft tilt of 7.3 degree
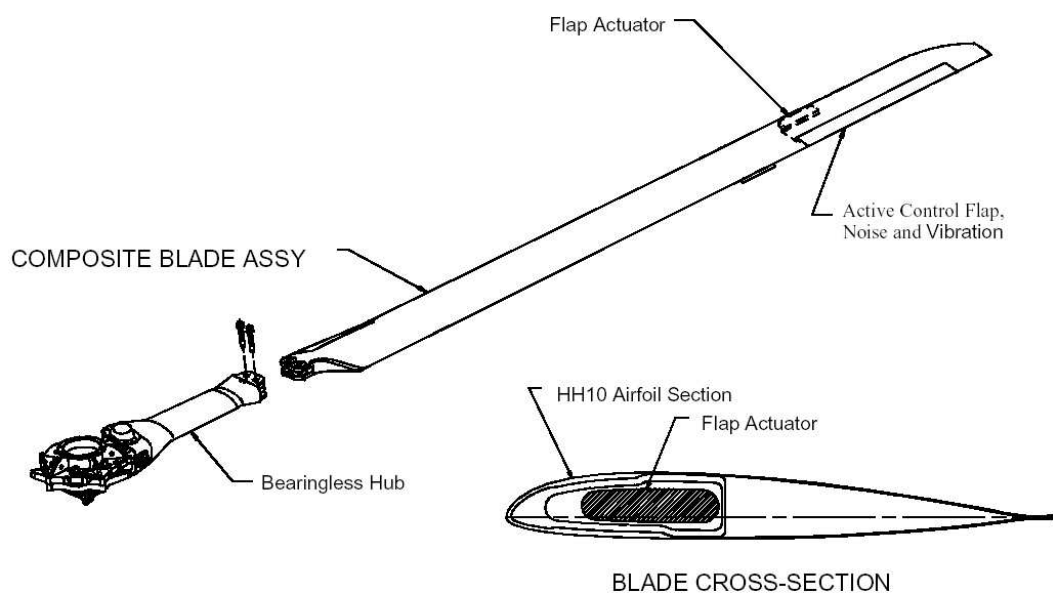
Figure 3.24: MD-900 and blade with active control flap [40]
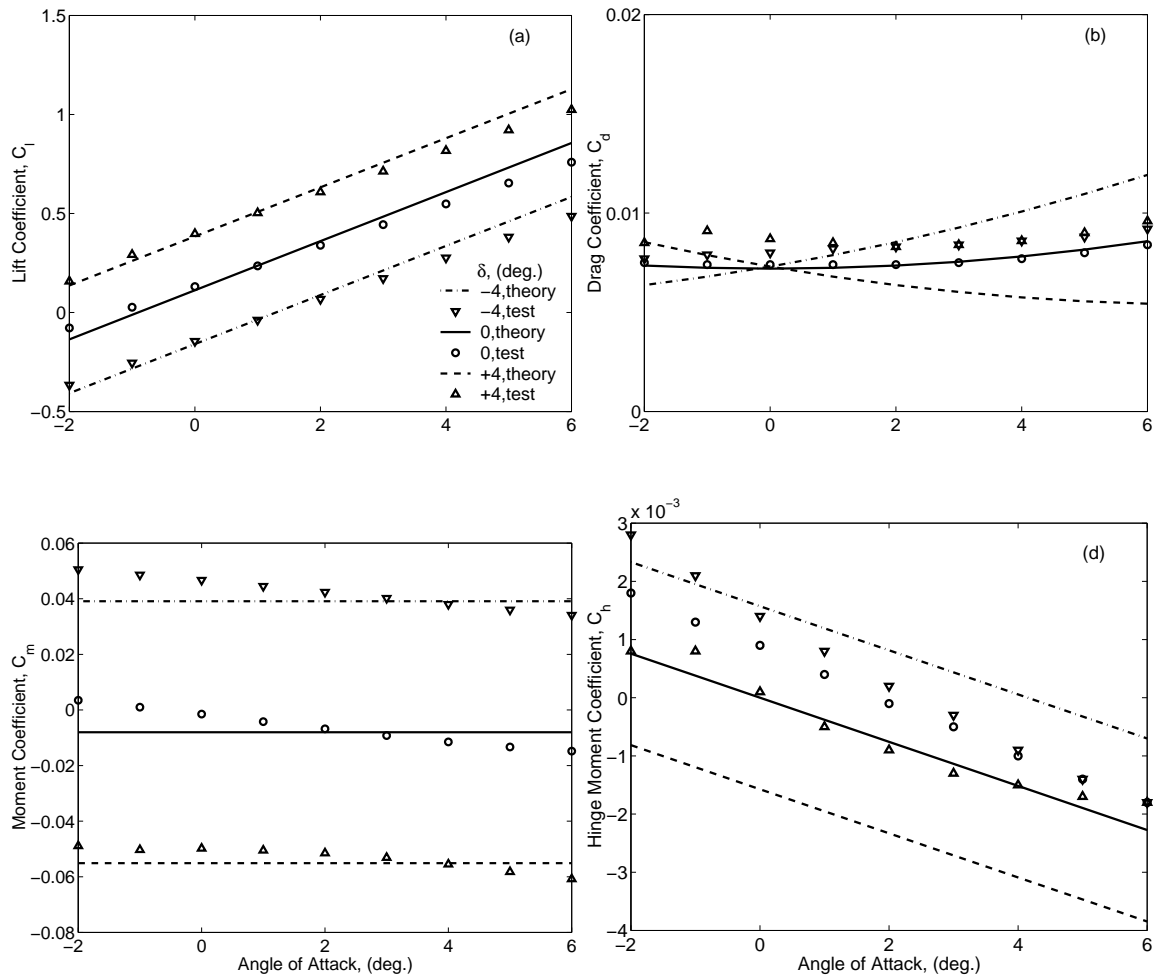
Figure 3.25: Measured and predicted aerodynamic coefficients of 2D HH-06 airfoil with 0.35 plain trailing-edge flap (10%c overhang, Mach = 0.20); (a) lift (b) drag (c) pitching moment and (d) hinge moment
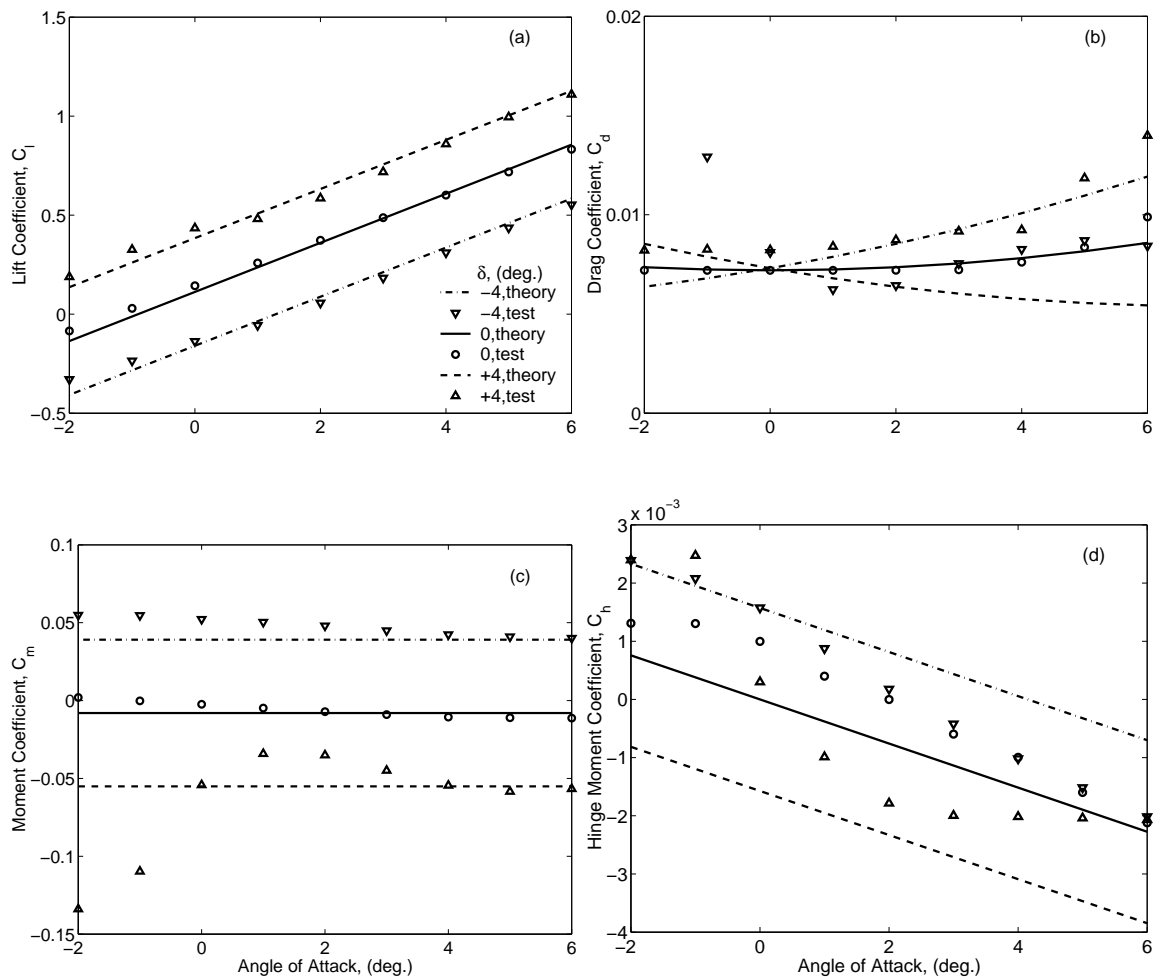
Figure 3.26: Measured and predicted aerodynamic coefficients of 2D HH-06 airfoil with
0.35 plain trailing-edge flap (10%c overhang, Mach = 0.45); (a) lift (b) drag (c) pitching
moment and (d) hinge moment
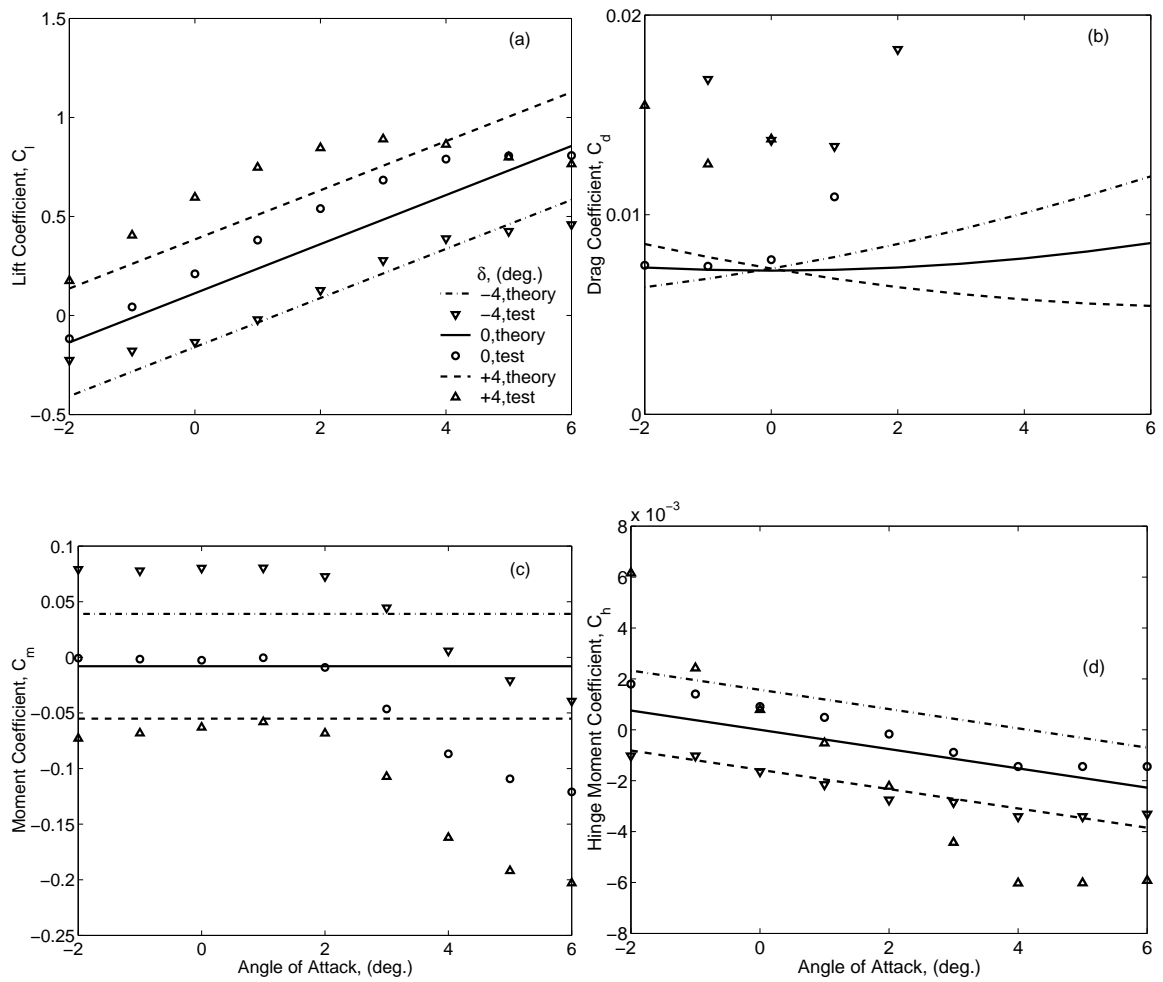
Figure 3.27: Measured and predicted aerodynamic coefficients of 2D HH-06 airfoil with 0.35 plain trailing-edge flap (10%c overhang, Mach = 0.70); (a) lift (b) drag (c) pitching moment and (d) hinge moment
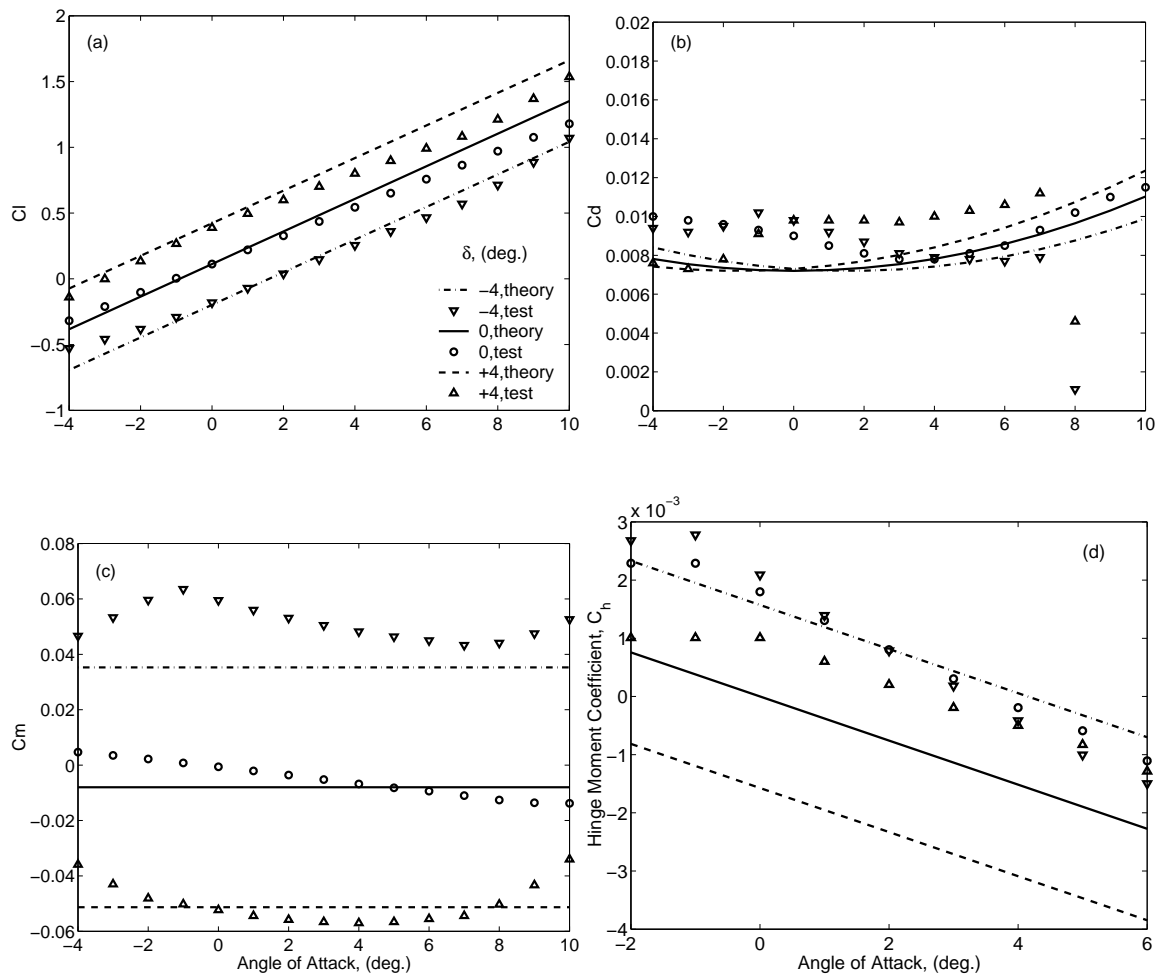
Figure 3.28: Measured and predicted aerodynamic coefficients of 2D HH-10 airfoil with 0.35 plain trailing-edge flap (10%c overhang, Mach = 0.45); (a) lift (b) drag (c) pitching moment and (d) hinge moment
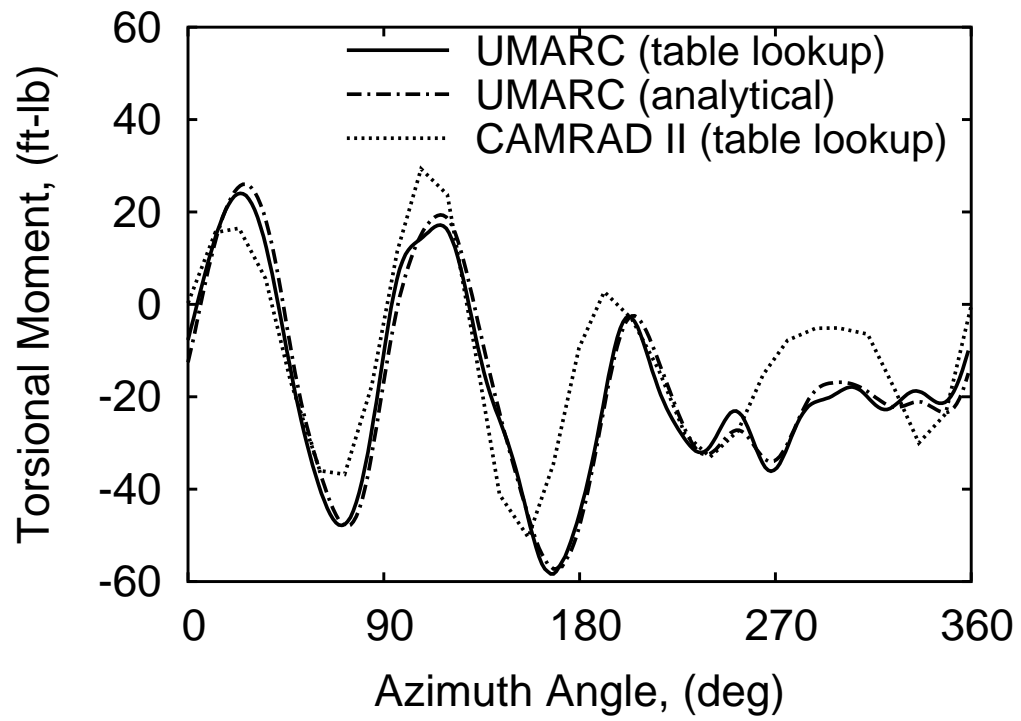
Figure 3.29: Comparison of torsional moment predictions of UMARC and CAMRAD II at $r/R = 0.6$ with prescribed flap motion $\delta_f = 2^o cos(4\psi - 240^o)$, $\mu = 0.2$, $C_T/\sigma = 0.0774$
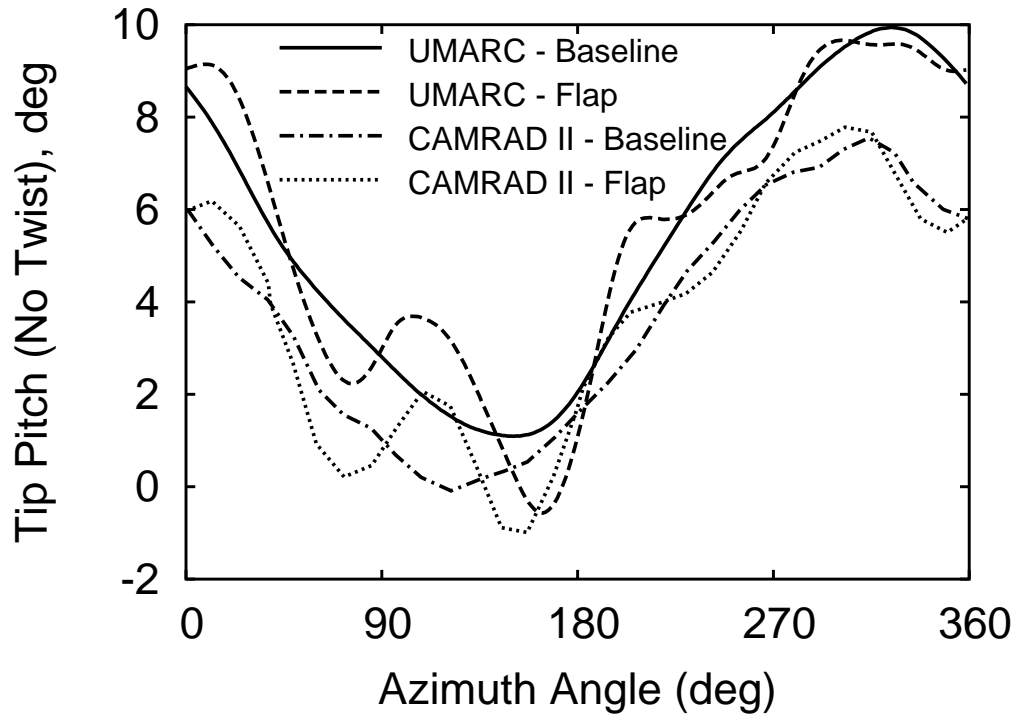
Figure 3.30: Comparison of UMARC and CAMRAD II predictions of blade tip pitch (excluding built-in twist) with and without trailing-edge flap control, prescribed flap motion $\delta_f = 2^o cos(4\psi - 240^o)$, $\mu = 0.2$, $C_T/\sigma = 0.0774$
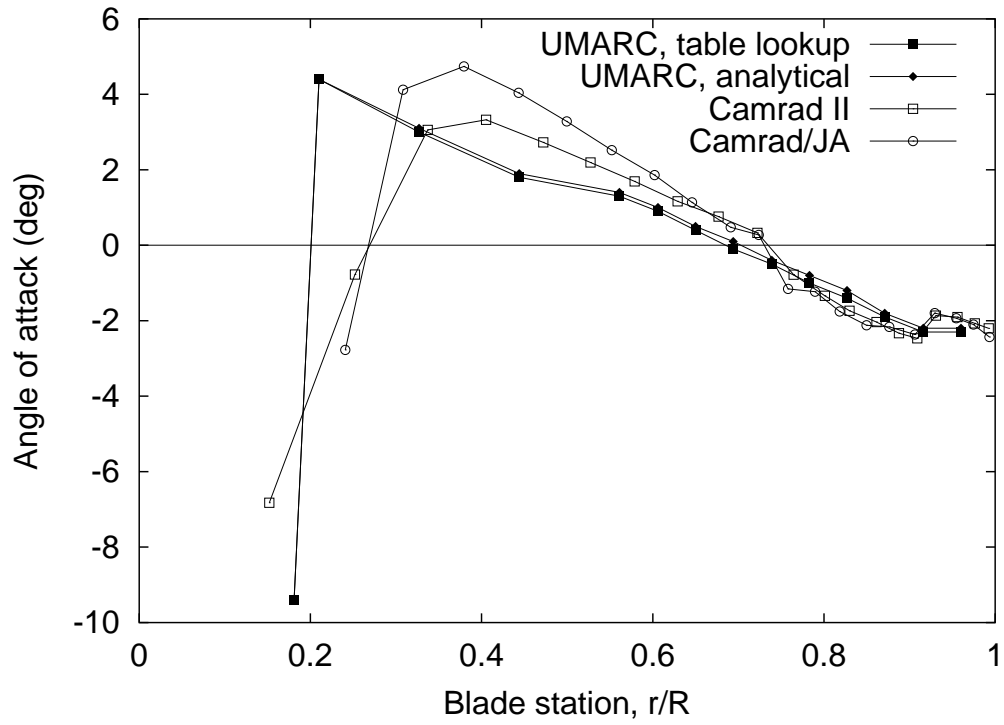
Figure 3.31: Comparison of UMARC and CAMRAD II predictions of angle of attack at $r/R = 0.6$ with prescribed flap motion $\delta_f = 2^o cos(4\psi - 240^o)$, $\mu = 0.2$, $C_T/\sigma = 0.0774$
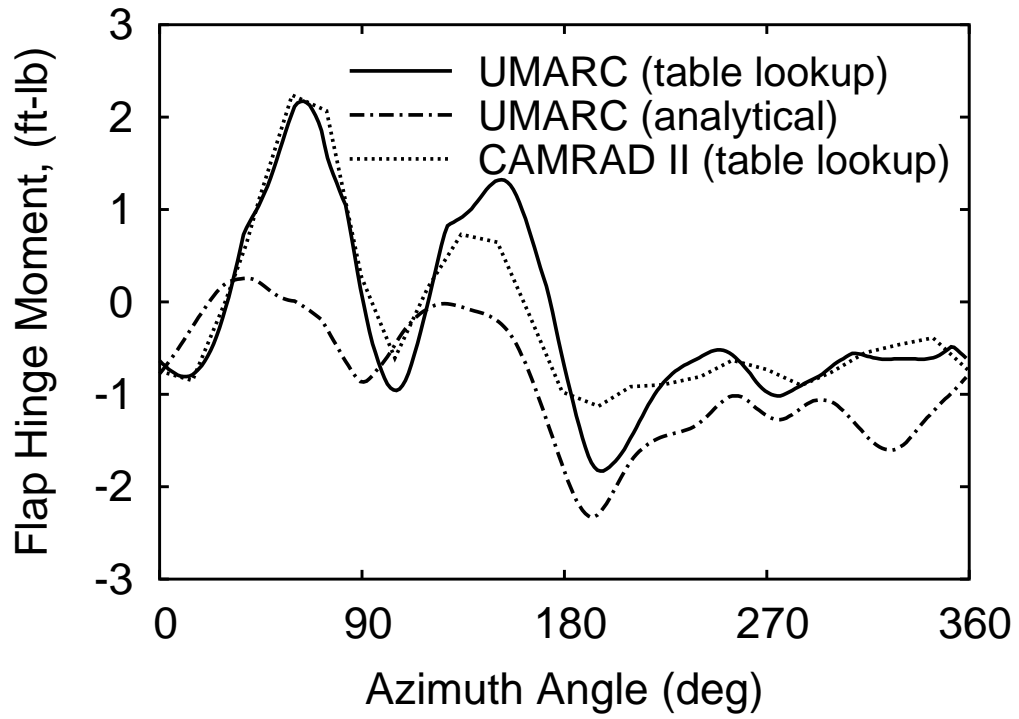
Figure 3.32: Comparison of flap hinge moment predictions of UMARC and CAMRAD II with prescribed flap motion $\delta_f = 2^o cos(4\psi - 240^o)$, $\mu = 0.2$, $C_T/\sigma = 0.0774$, $c_b/c_f = 0.29$, $c_{cg}/c_f = 0$
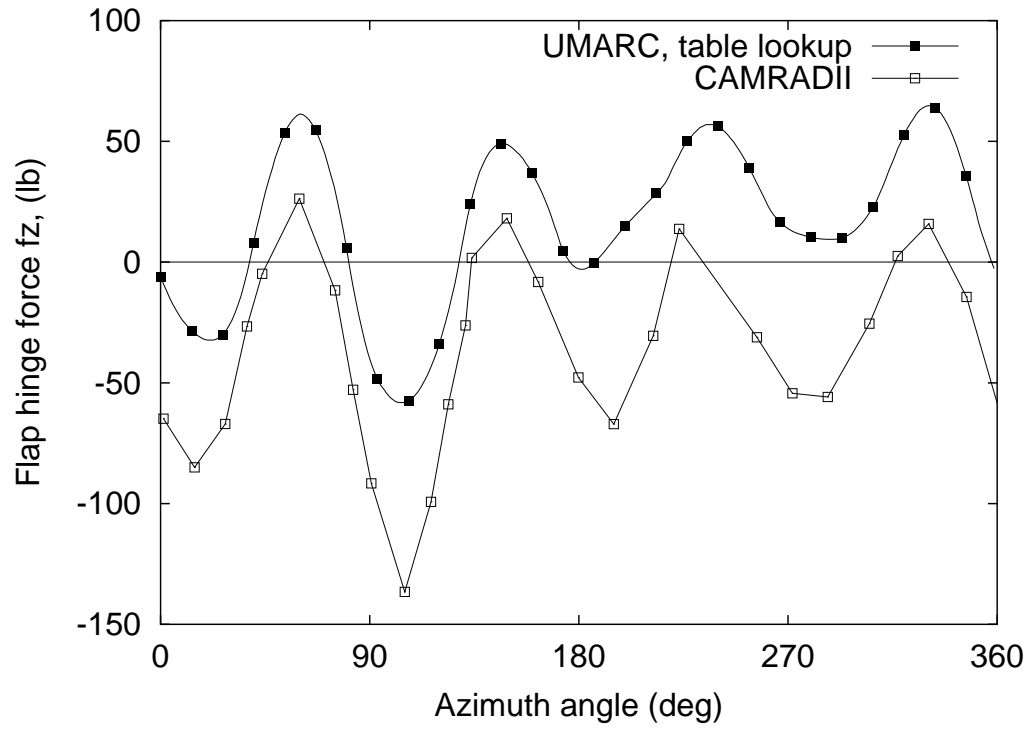
Figure 3.33: Comparison of flap hinge shear predictions of UMARC and CAMRAD II with prescribed flap motion $\delta_f = 2^o cos(4\psi - 240^o)$, $\mu = 0.2$, $C_T/\sigma = 0.0774$, $c_b/c_f = 0.29$, $c_{cg}/c_f = 0$
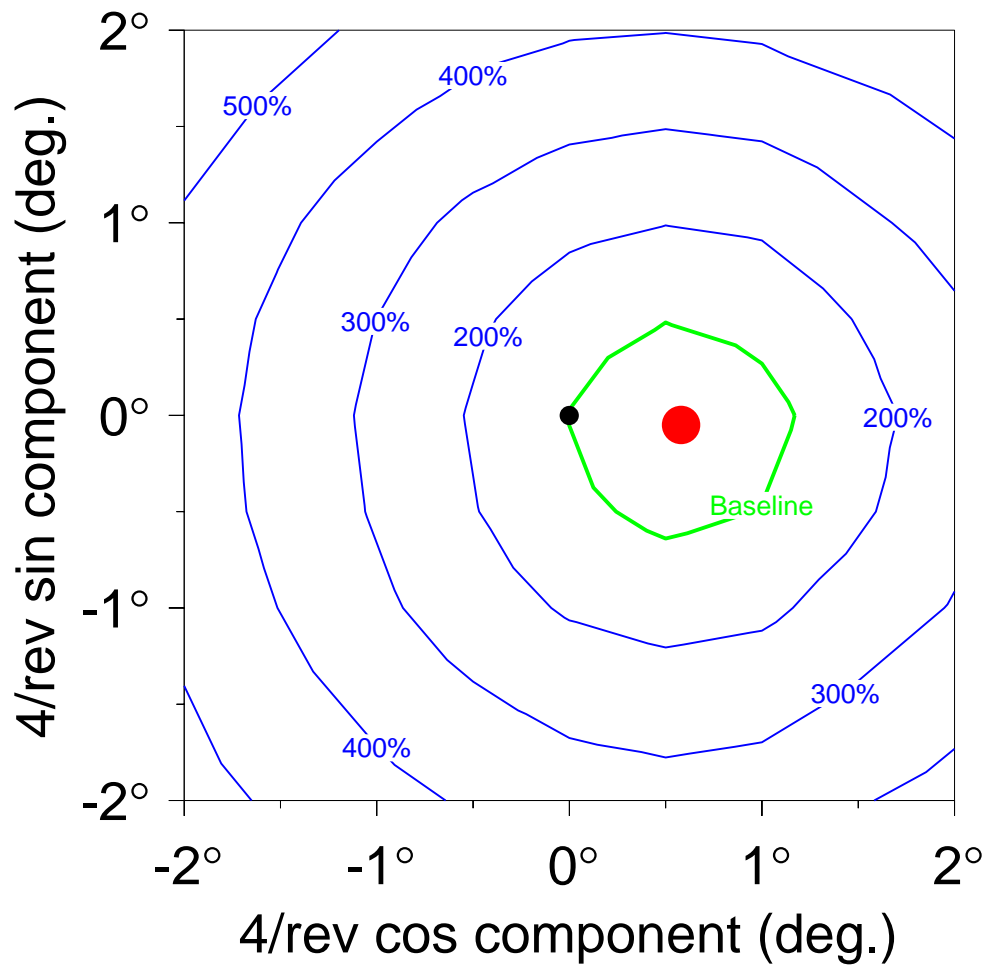
Figure 3.34: 5/rev fixed system hub normal force with 4/rev open loop trailing-edge flap input
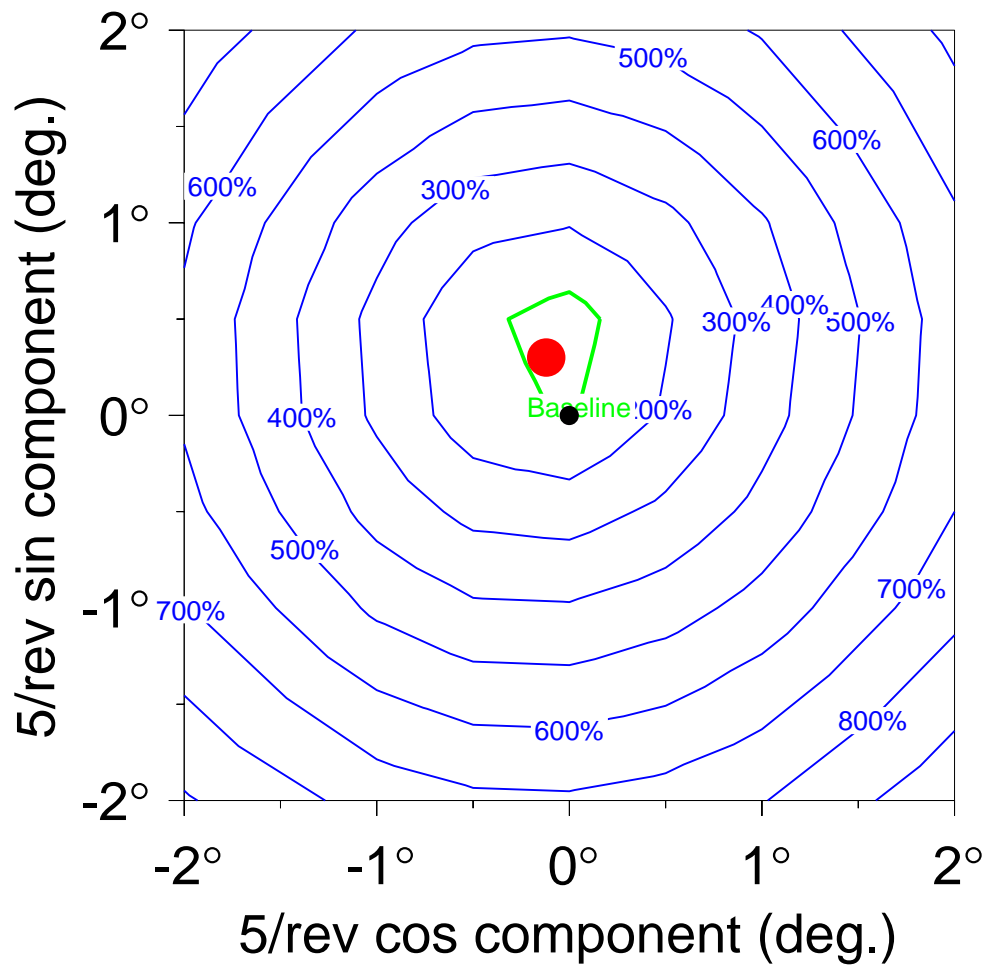
Figure 3.35: 5/rev fixed system hub normal force with 5/rev open loop trailing-edge flap input
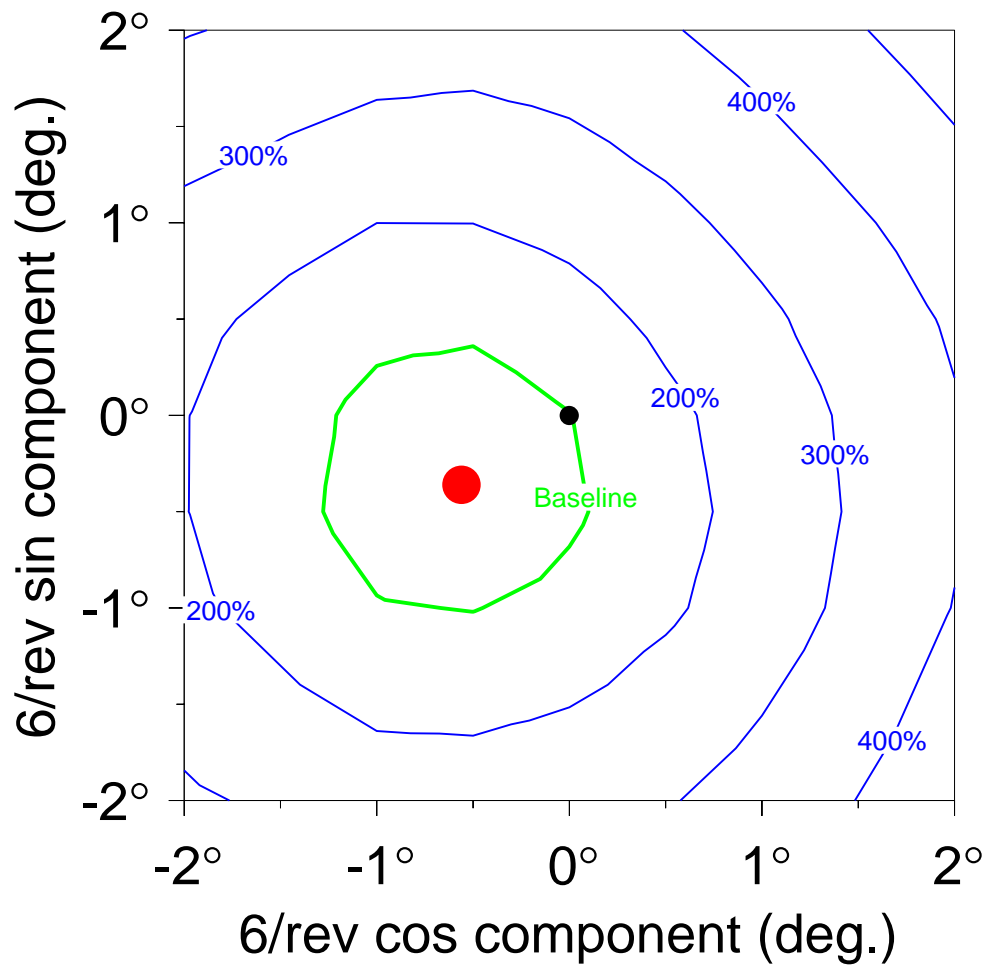
Figure 3.36: 5/rev fixed system hub normal force with 6/rev open loop trailing-edge flap input
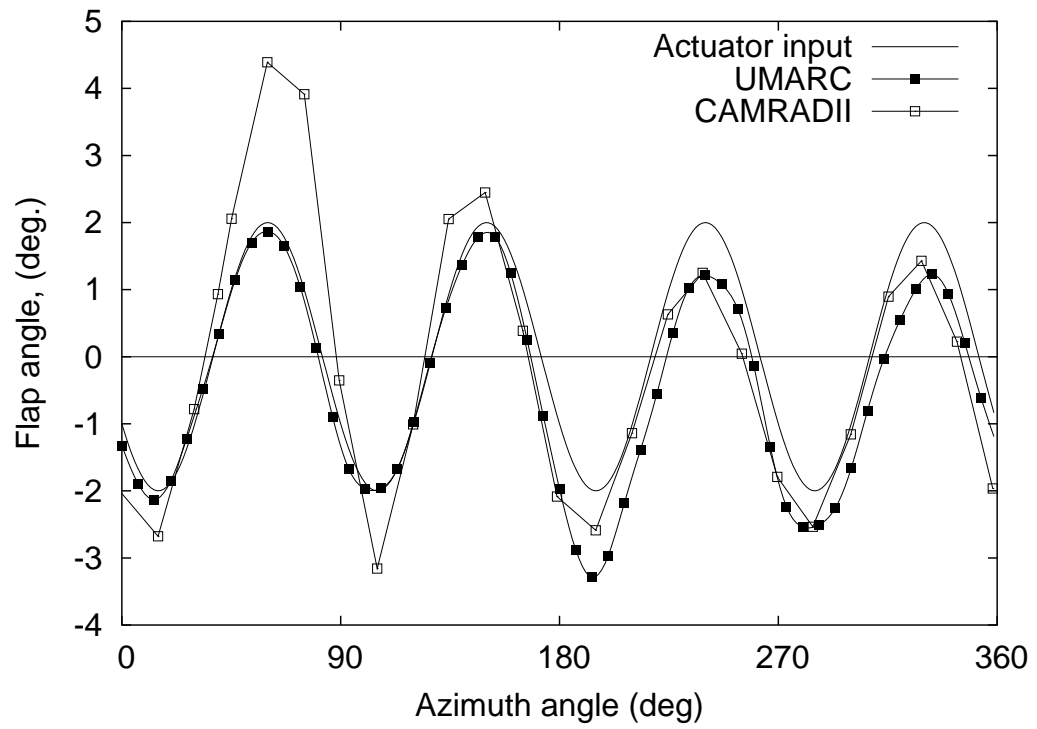
Figure 3.37: Flap angle for baseline actuator, 82 knots, with actuator input $\delta_a = 2°Cos(4\psi - 240°)$
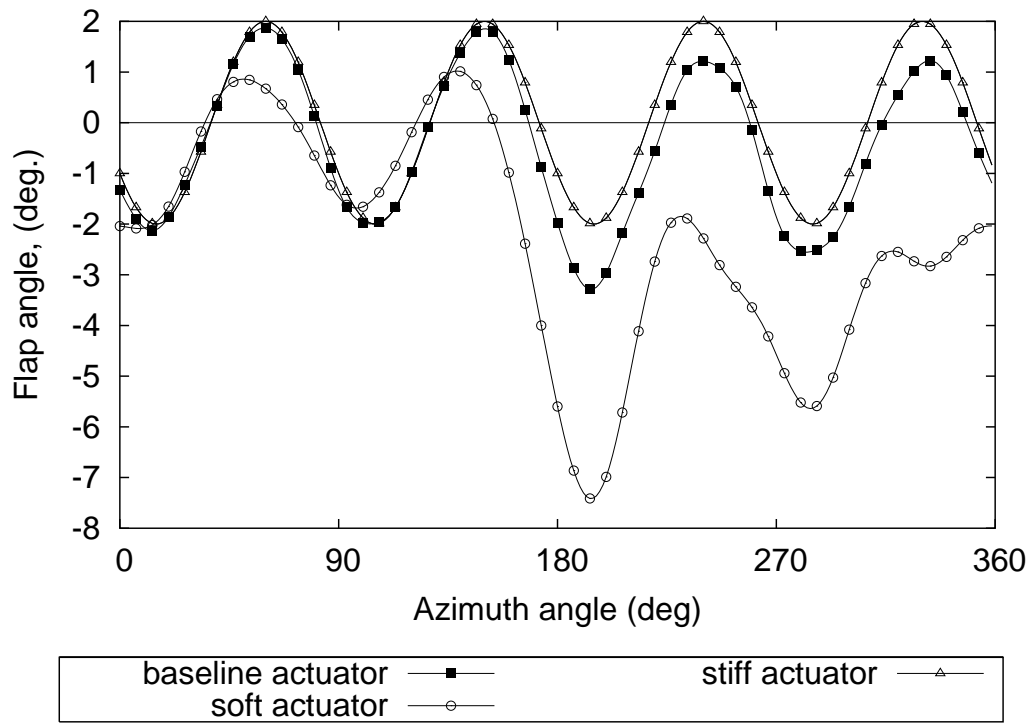
Figure 3.38: Flap angle for soft and rigid actuator, 82 knots, with actuator input $\delta_a = 2°Cos(4\psi - 240°)$
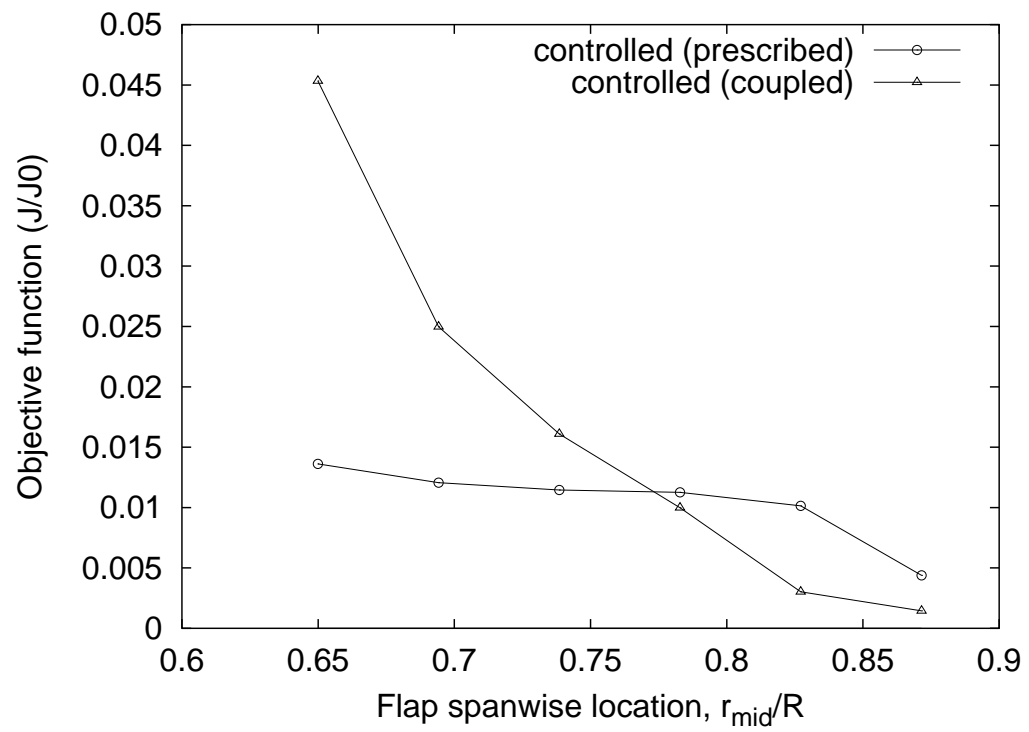
Figure 3.39: Objective function vs flap location, $\mu = 0.3$ (123knots), $C_T/\sigma = 0.0774$
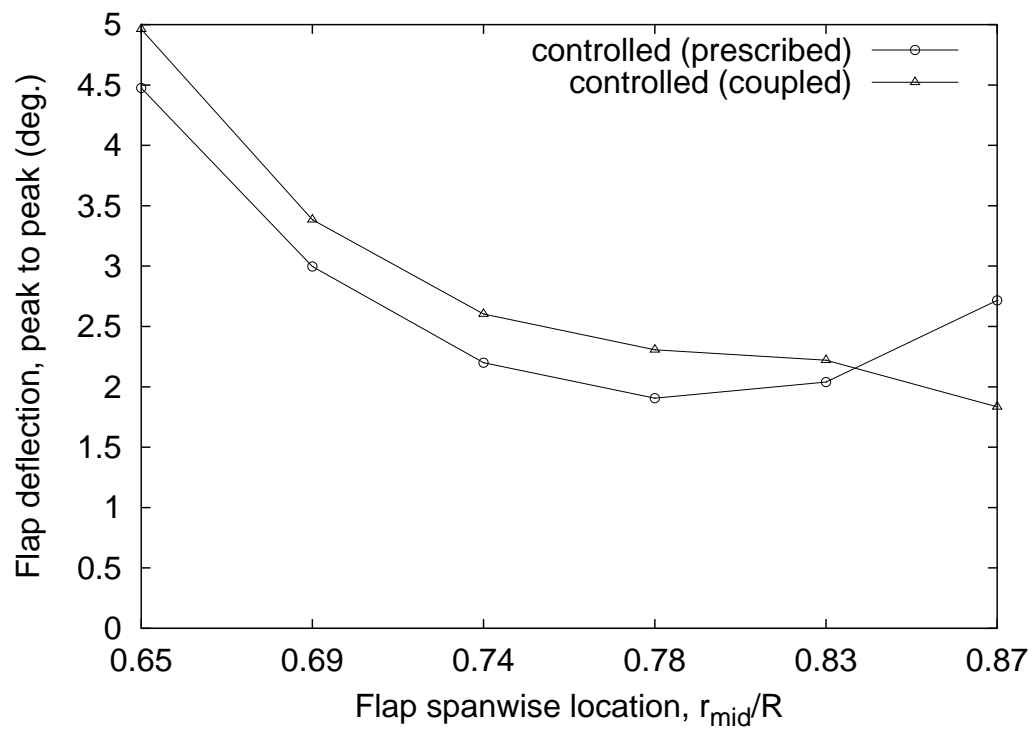
Figure 3.40: Flap deflection vs flap location, $\mu = 0.3$ (123knots), $C_T/\sigma = 0.0774$
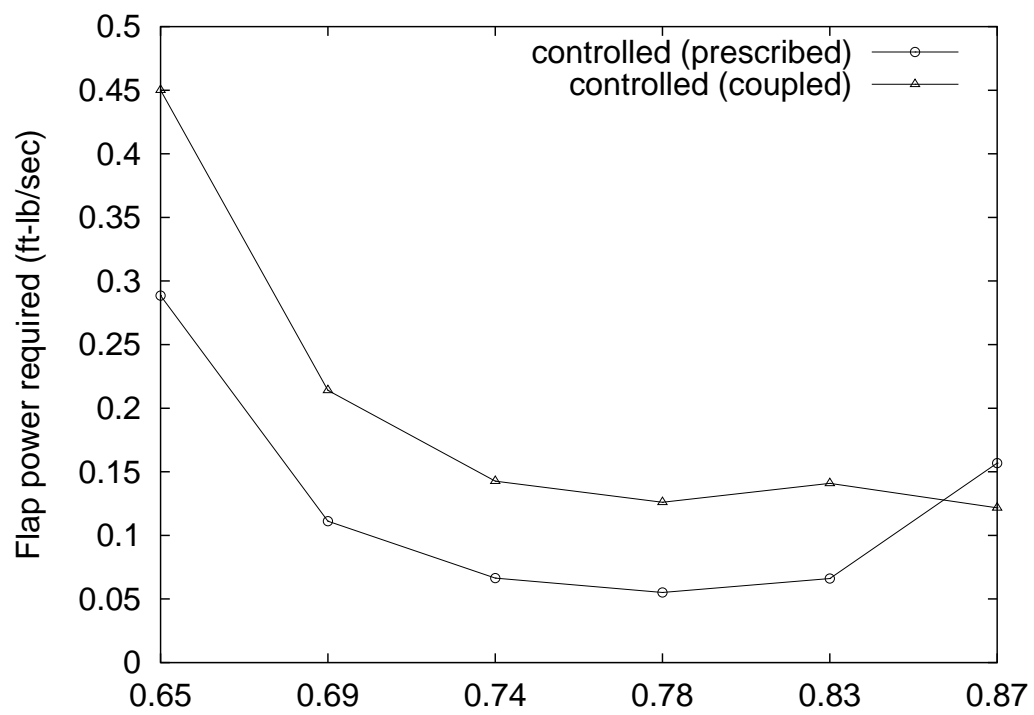
Figure 3.41: Actuation power vs flap location, $\mu = 0.3$ (123knots), $C_T/\sigma = 0.0774$
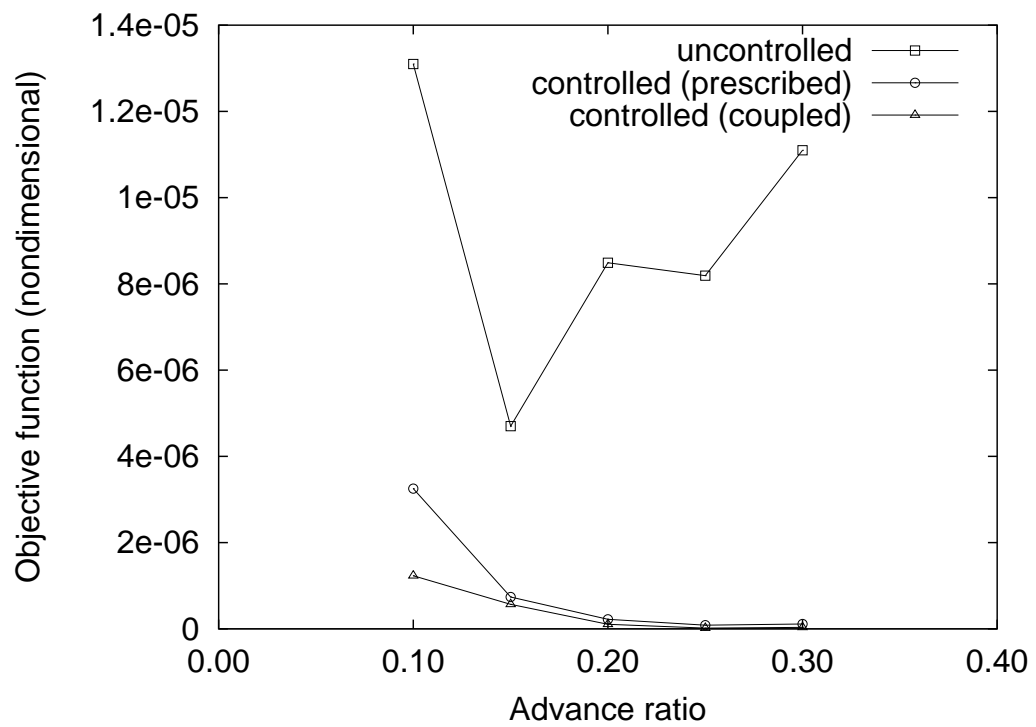
Figure 3.42: Objective function vs advancing ratio with flap midspan location at 83% radius
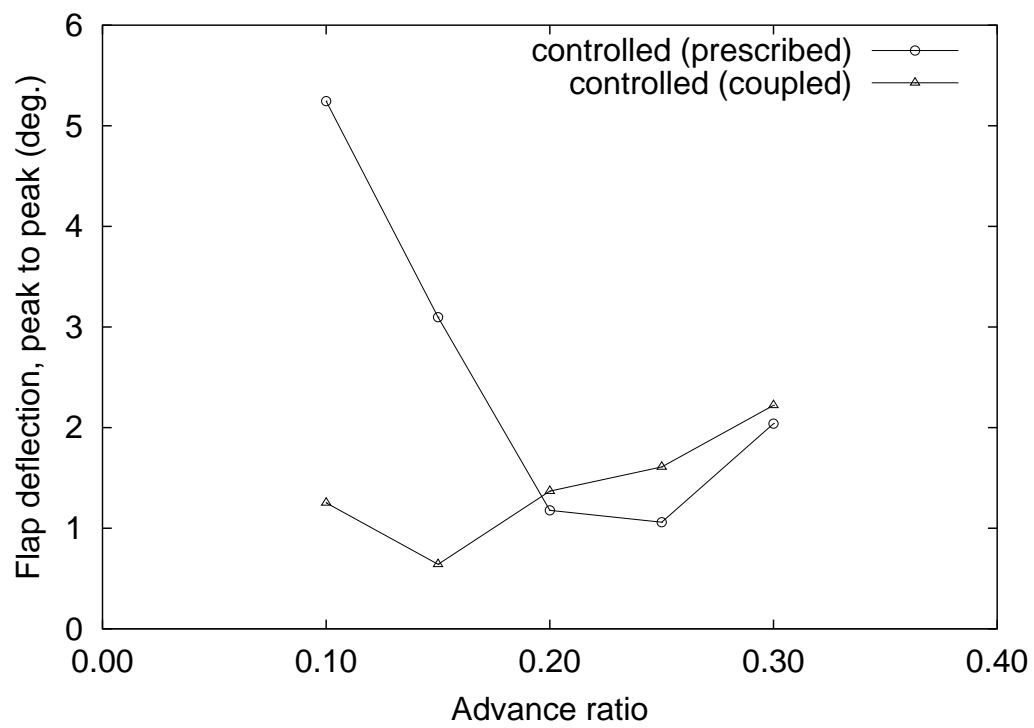
Figure 3.43: Flap deflection vs advancing ratio with flap midspan location at 83% radius
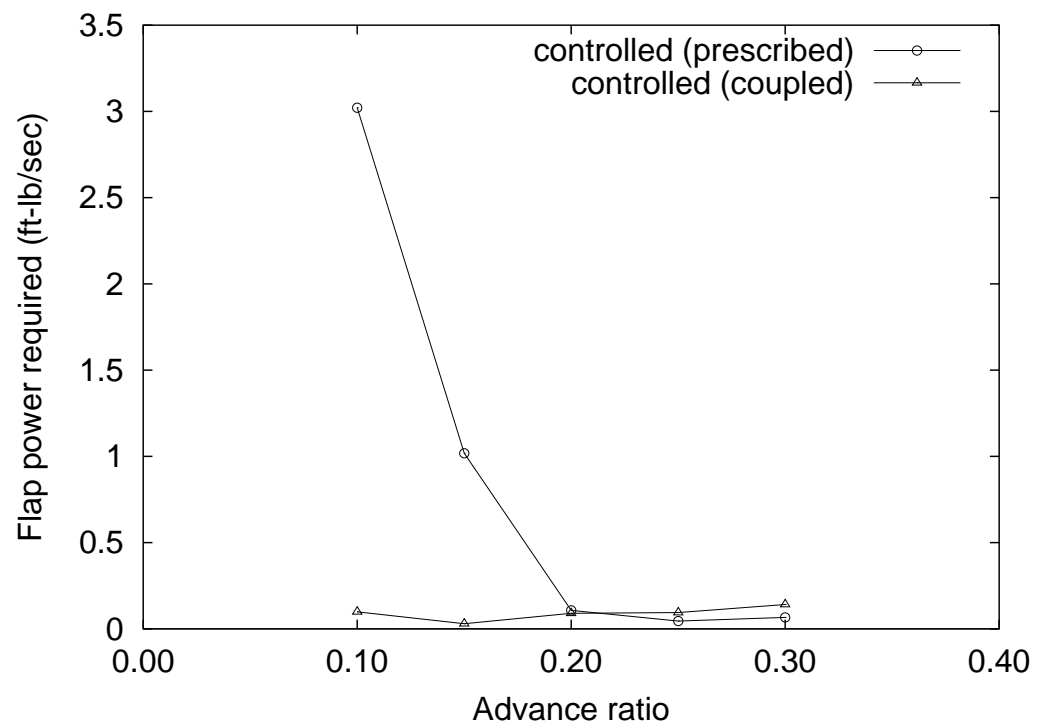
Figure 3.44: Actuation power vs advancing ratio with flap midspan location at 83% radius
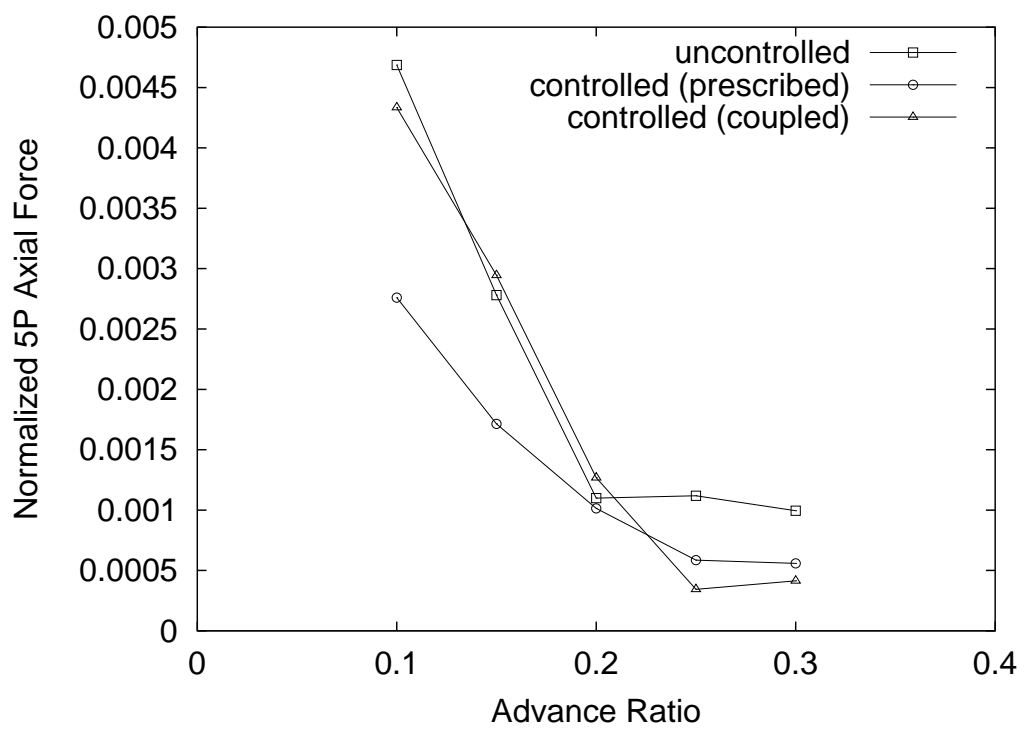
Figure 3.45: 5/rev hub axial force
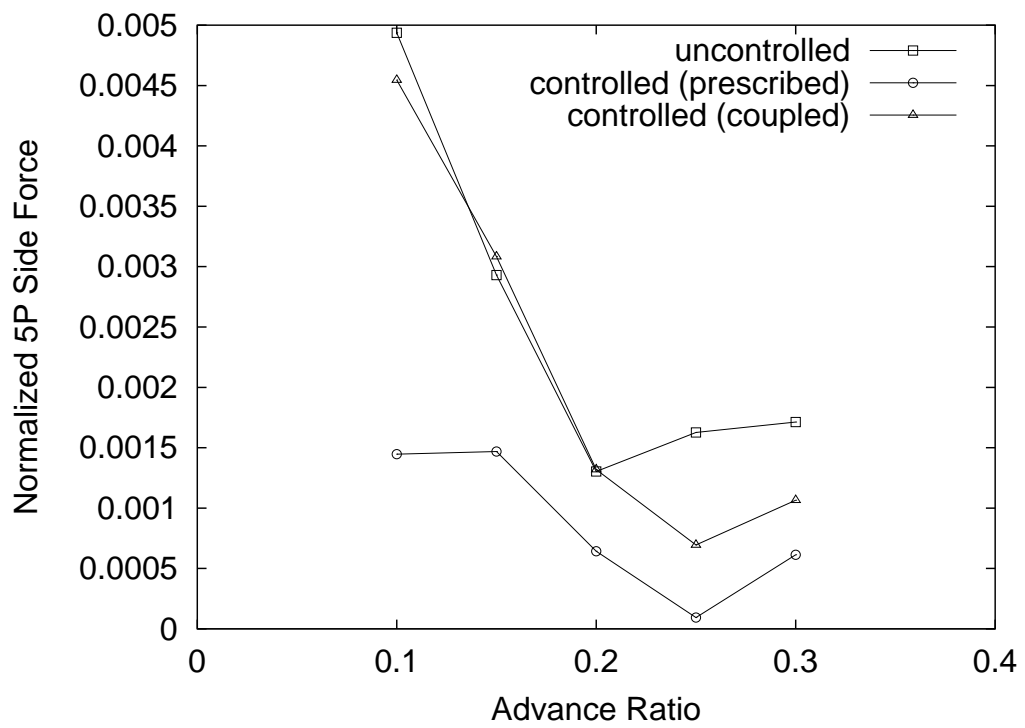
Figure 3.46: 5/rev hub side force
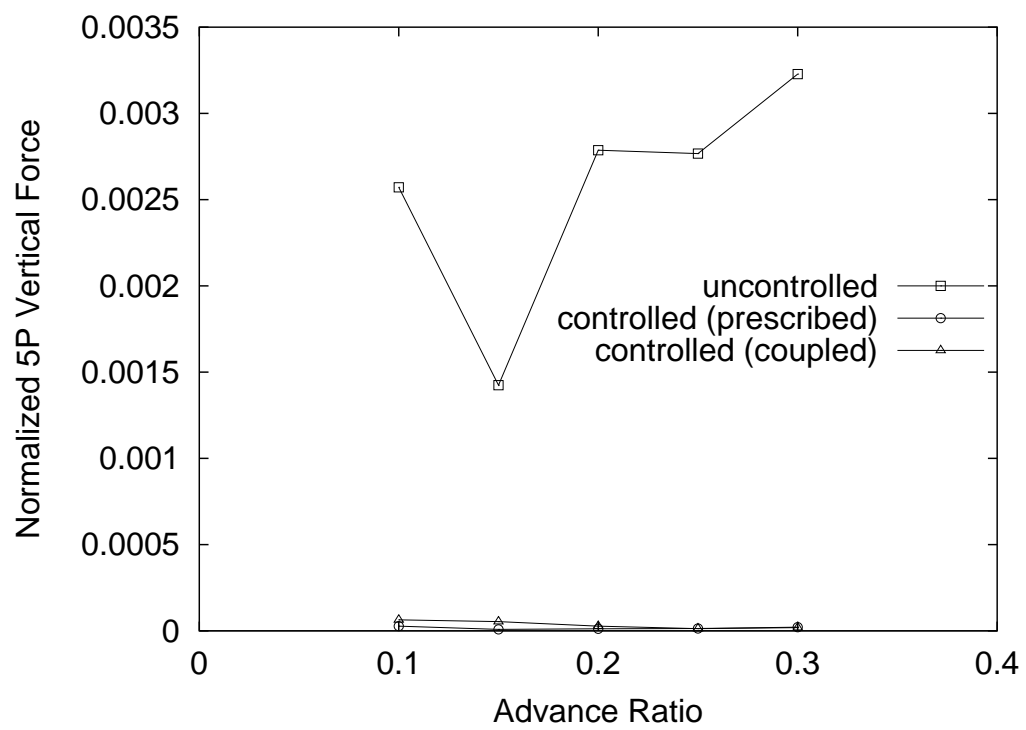
Figure 3.47: 5/rev hub vertical force
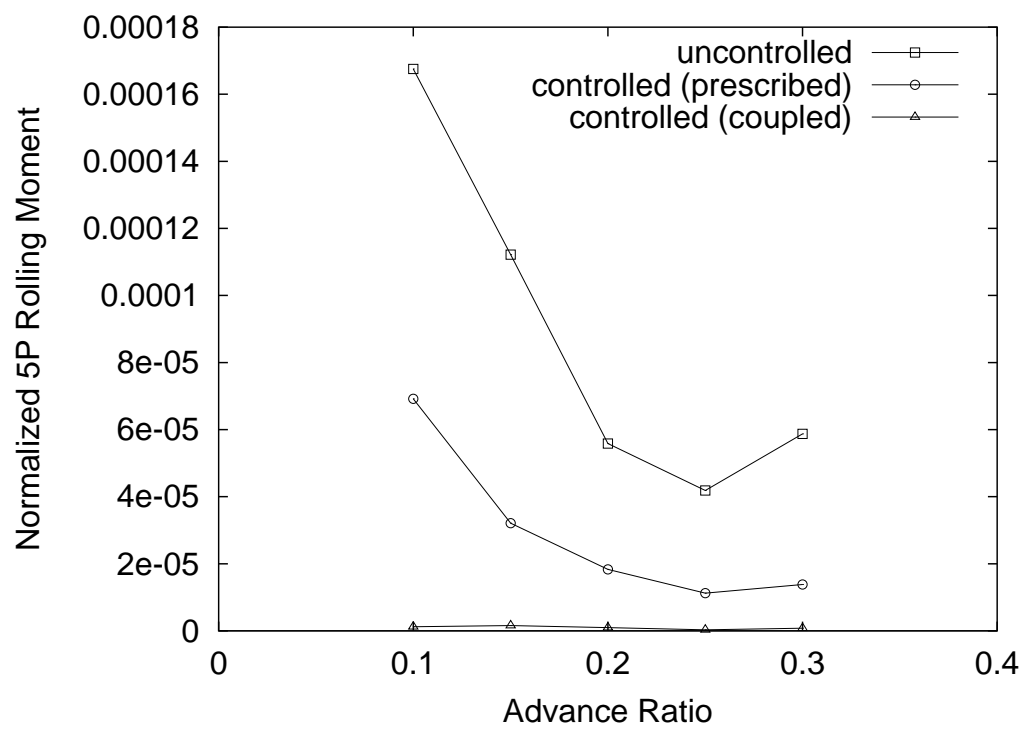
Figure 3.48: 5/rev hub rolling moment
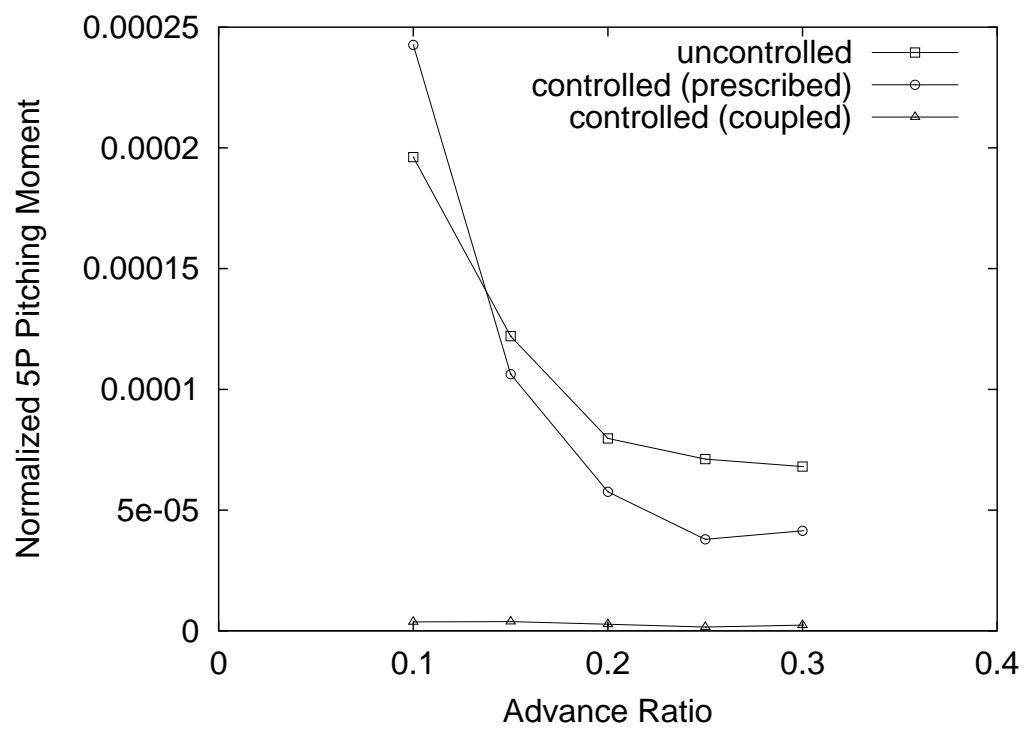
Figure 3.49: 5/rev hub pitching moment
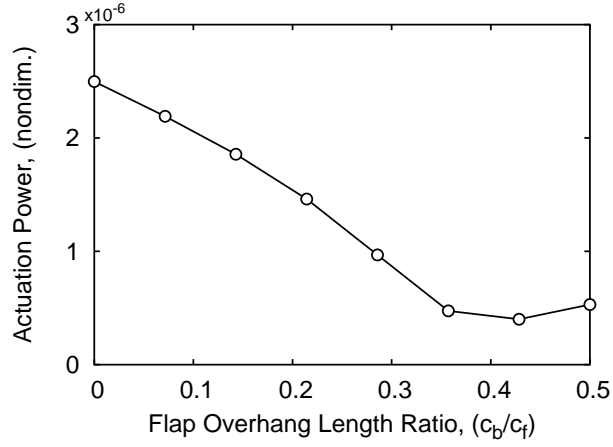
(a) Actuation requirement
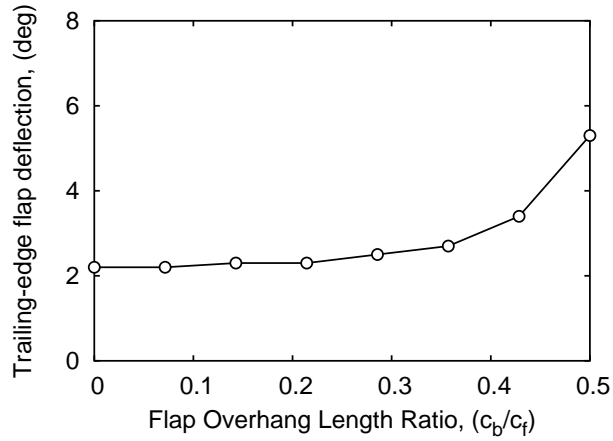
(b) Trailing-edge flap response

Figure 3.50: Trailing-edge flap actuation power and response (half peak-to-peak) versus trailing-edge flap overhang length, $\mu = 0.2$, $C_T/\sigma = 0.0774$, $c_{cg}/c_f = 0$, $\delta_a = 2^o cos(4\psi - 240^o)$
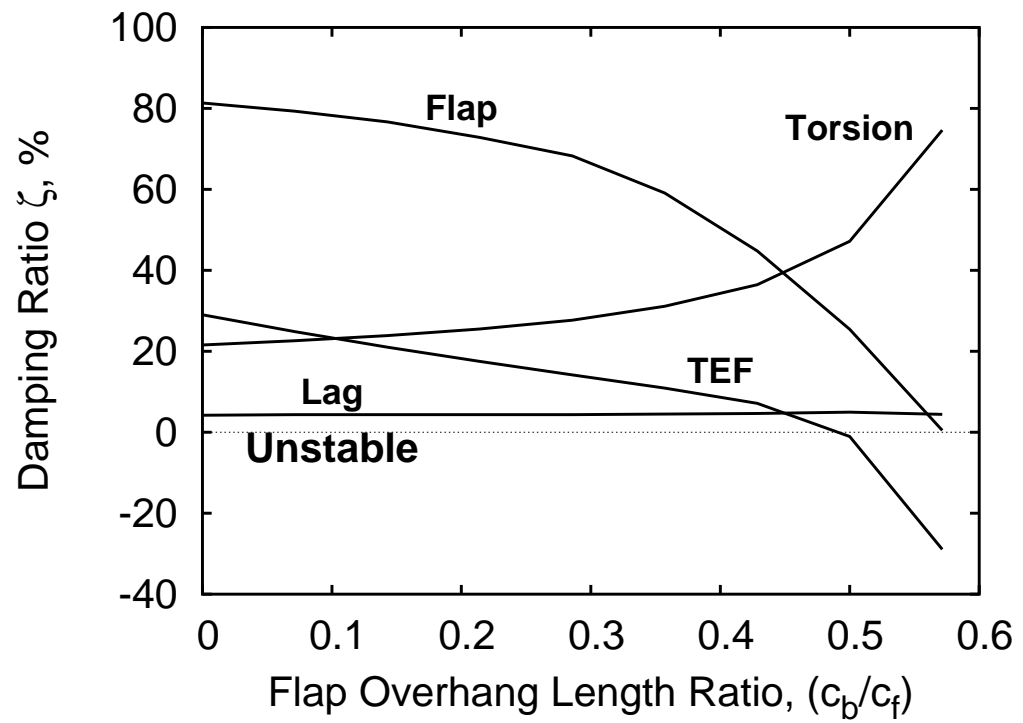
Figure 3.51: Effect of overhang length on blade and trailing-edge flap (TEF) stability in hover, $c_{cg}/c_f = 0$
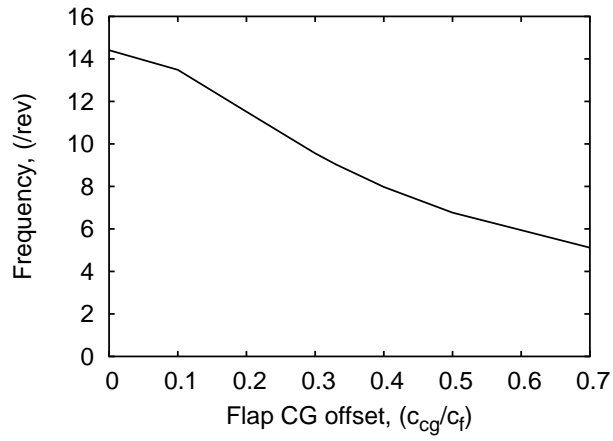
(a) Trailing-edge flap frequency
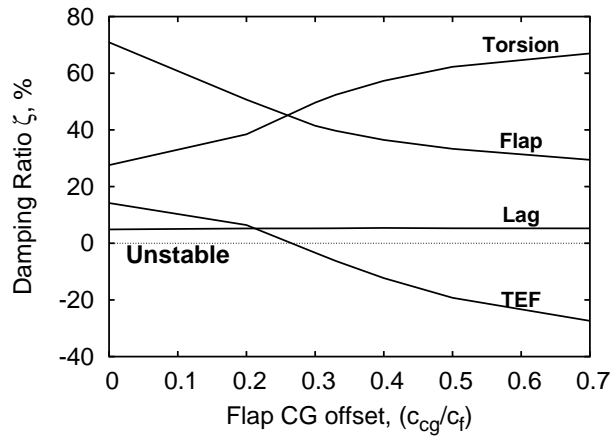
(b) Blade and trailing-edge flap damping

Figure 3.52: Effect of flap CG offset on blade and trailing-edge flap (TEF) stability in forward flight, $c_b/c_f = 0.29$, $\mu = 0.30$
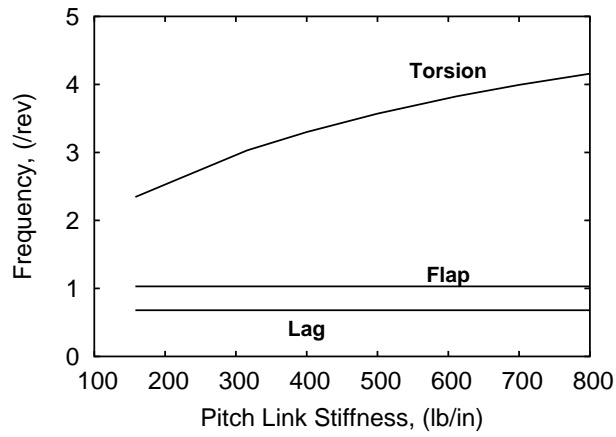
(a) Blade frequency
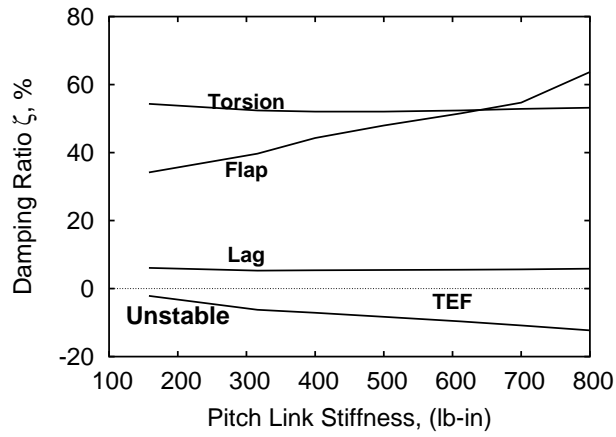
(b) Blade and trailing-edge flap damping

Figure 3.53: Effect of pitch link stiffness on blade and trailing-edge flap (TEF) stability in forward flight, $\mu = 0.30$, $c_b/c_f = 0.29$, $c_{cg}/c_f = 0.33$
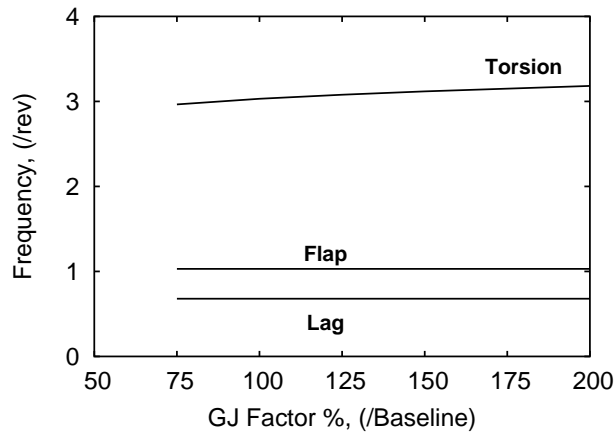
(a) Blade frequency
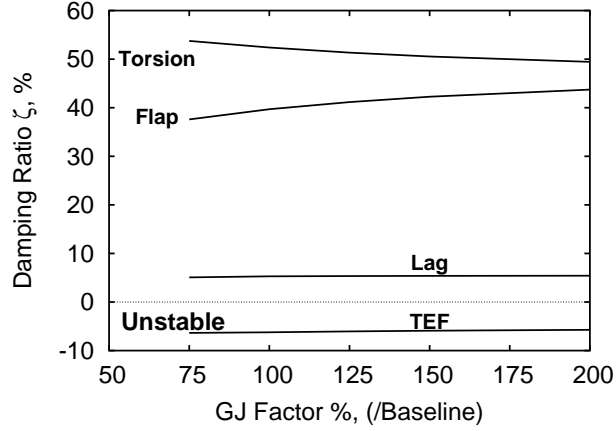
(b) Blade and trailing-edge flap damping

Figure 3.54: Effect of blade torsional stiffness on blade and trailing-edge flap (TEF) stability in forward flight, $\mu = 0.30$, $c_b/c_f = 0.29$, $c_{cg}/c_f = 0.33$
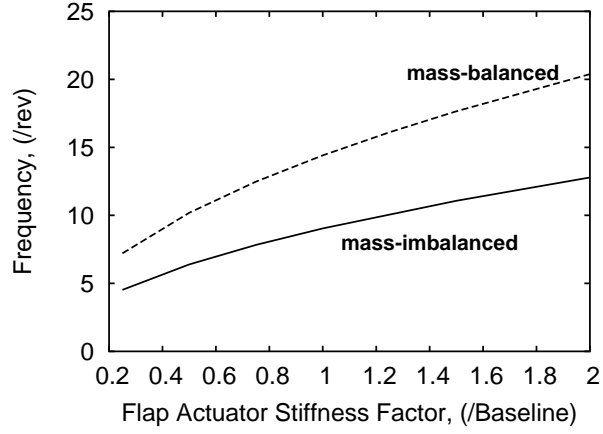
(a) Trailing-edge flap frequency
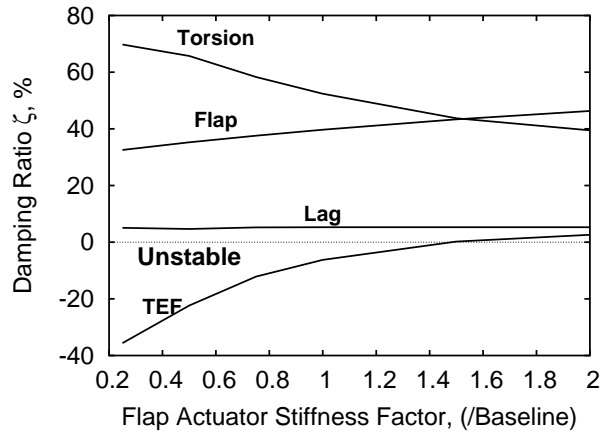
(b) Blade and trailing-edge flap damping, $c_{cg}/c_f = 0.33$

Figure 3.55: Effect of actuator stiffness on blade and trailing-edge flap (TEF) stability in forward flight, $\mu = 0.30$, $c_b/c_f = 0.29$
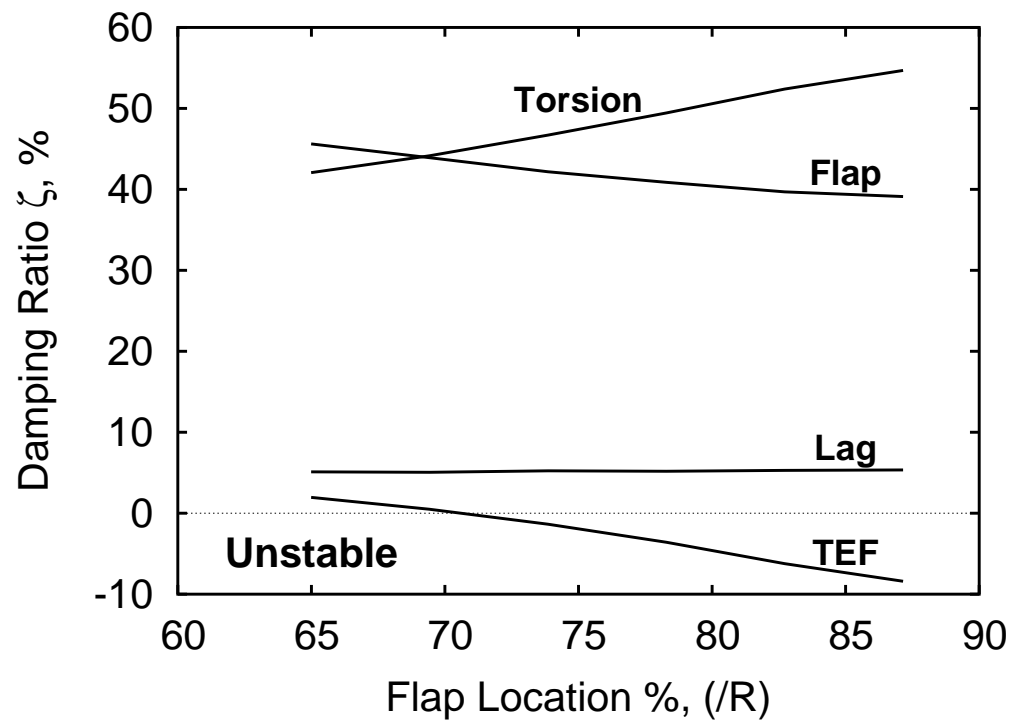
Figure 3.56: Effect of flap spanwise location on blade and trailing-edge flap (TEF) stability in forward flight, $\mu = 0.30$, $c_b/c_f = 0.29$, $c_{cg}/c_f = 0.33$
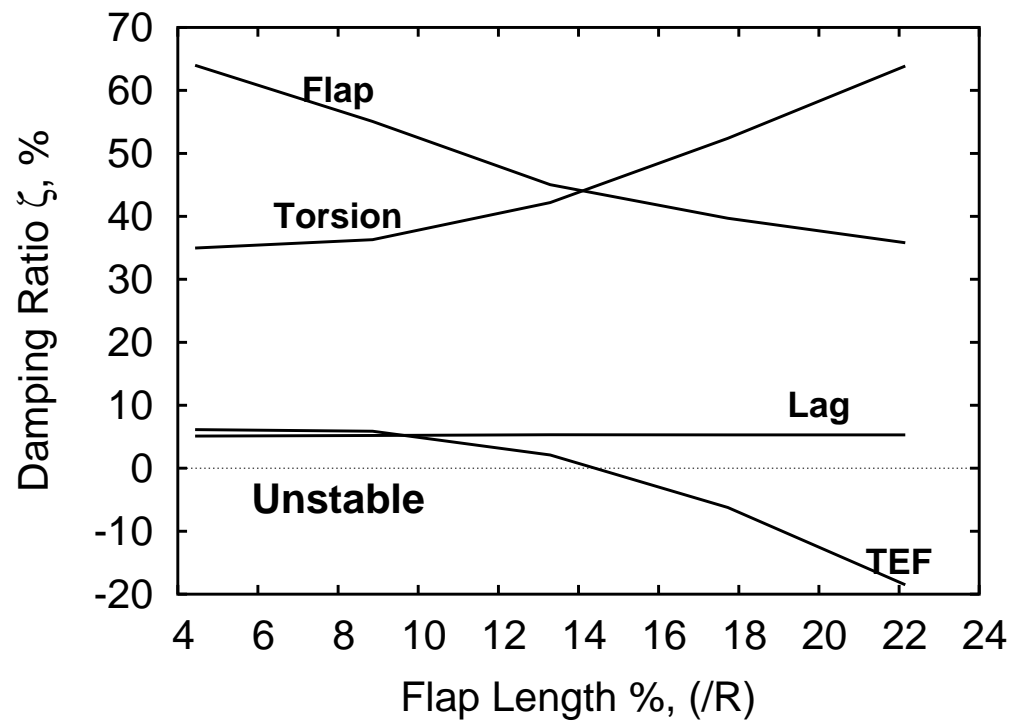
Figure 3.57: Effect of flap length on blade and trailing-edge flap (TEF) stability in forward flight, $\mu = 0.30$, $c_b/c_f = 0.29$, $c_{cg}/c_f = 0.33$
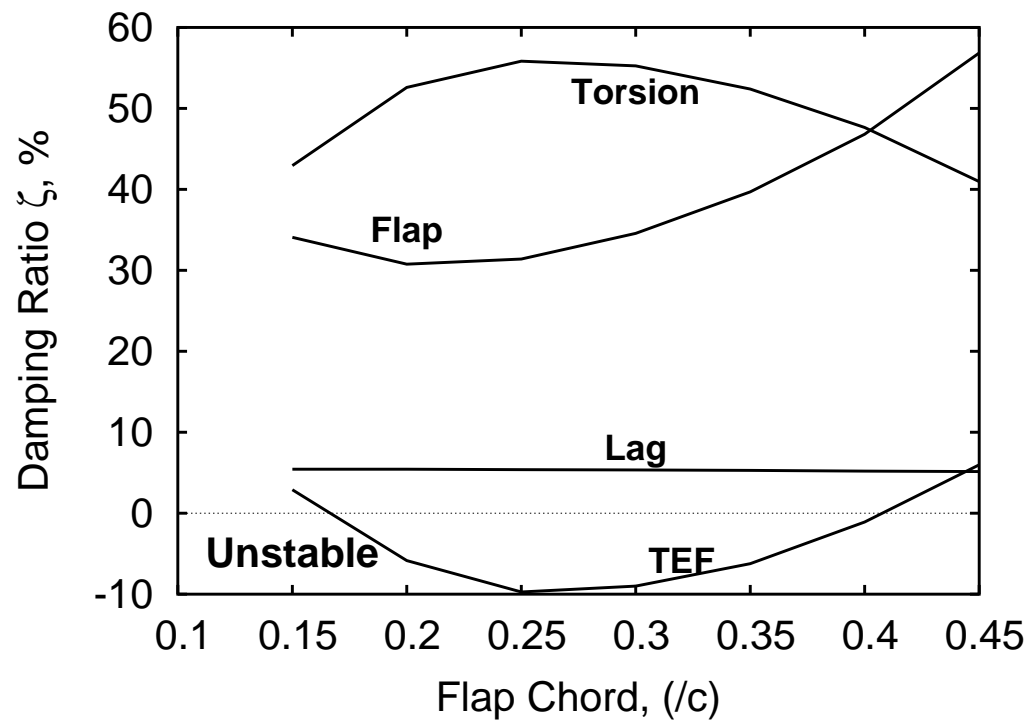
Figure 3.58: Effect of flap chord size on blade and trailing-edge flap (TEF) stability in forward flight, $\mu = 0.30$, $c_b/c_f = 0.29$, $c_{cg}/c_f = 0.33$
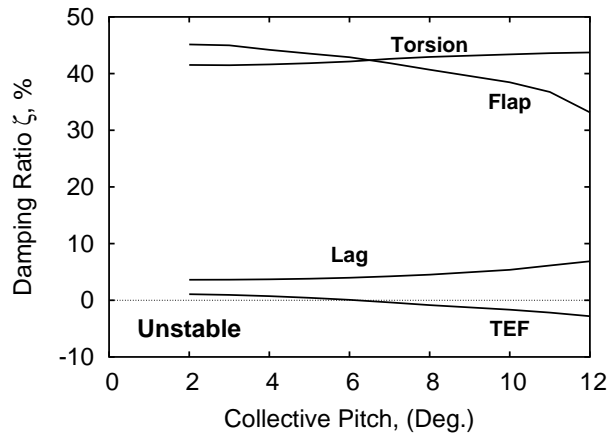
(a) Hover
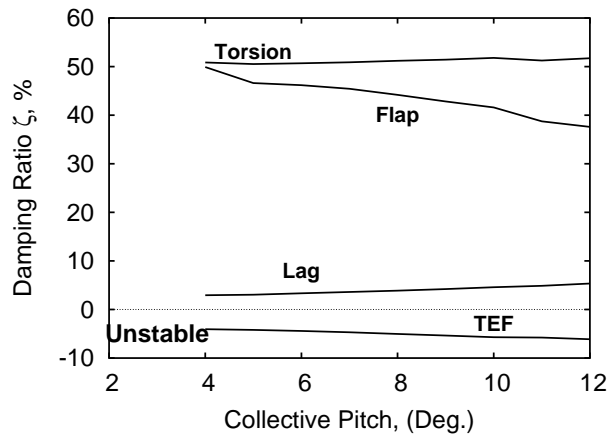
(b) Forward flight, $\mu = 0.30$

Figure 3.59: Effect of collective pitch on blade and trailing-edge flap (TEF) stability, $c_b/c_f = 0.29$, $c_{cg}/c_f = 0.33$
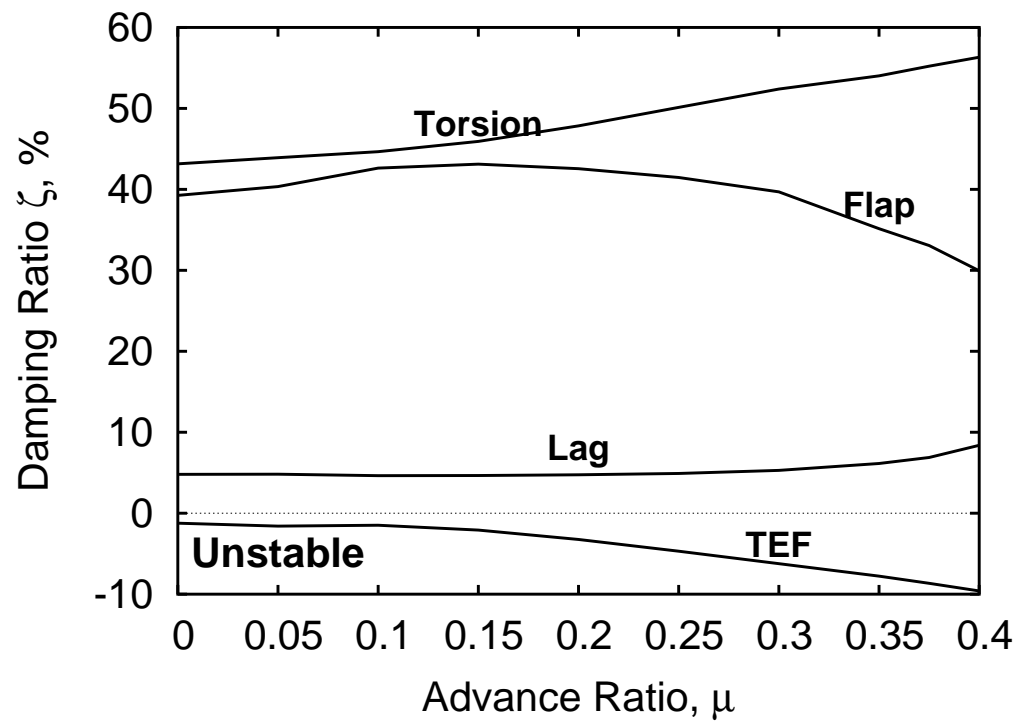
Figure 3.60: Effect of forward speed on blade and trailing-edge flap (TEF) stability, $c_b/c_f = 0.29$, $c_{cg}/c_f = 0.33$
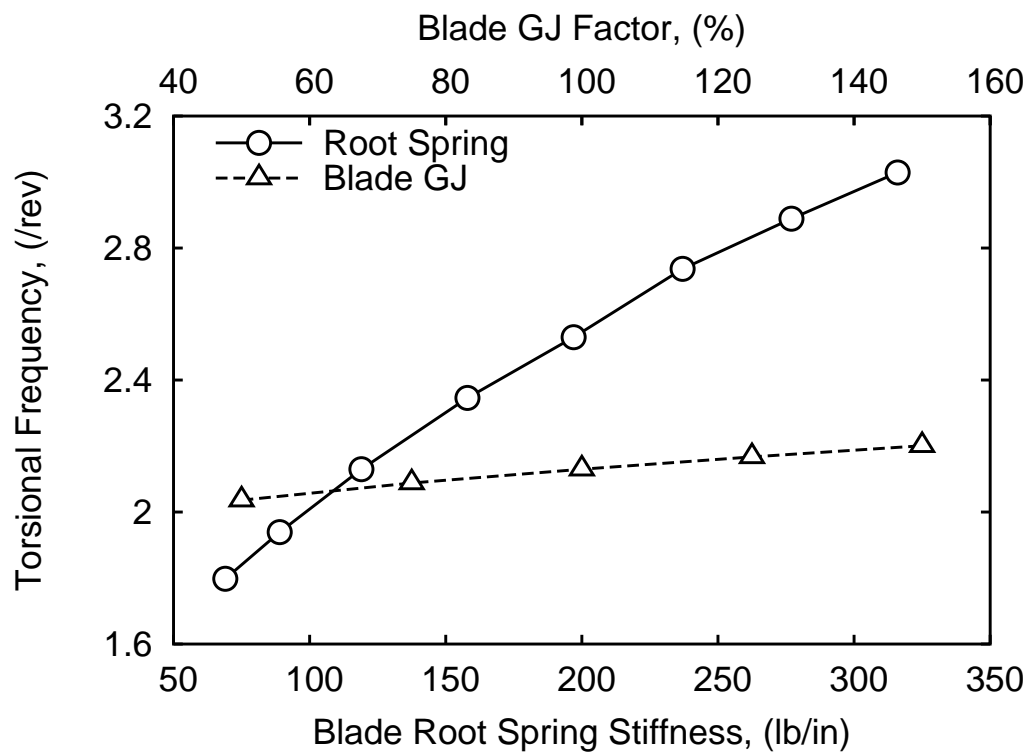
Figure 3.61: Variation of blade torsion frequency with root spring stiffness and blade torsional stiffness distribution.
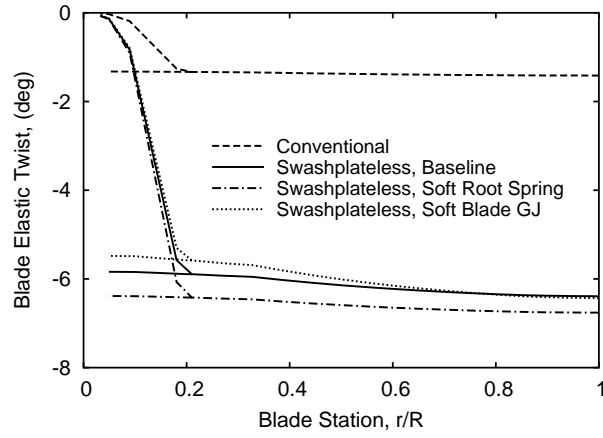
(a) Variation of blade elastic twist with blade station ($\psi = 0^o$).
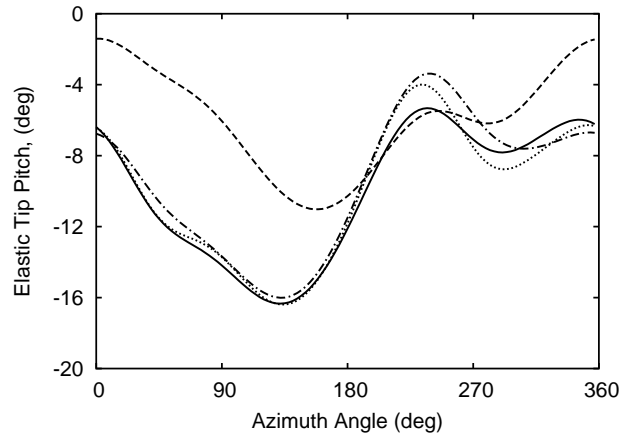
(b) Variation of blade tip pitch with azimuth angle.

Figure 3.62: Effect of blade root spring stiffness and blade torsional stiffness on blade pitch and twist ($\mu = 0.30$).
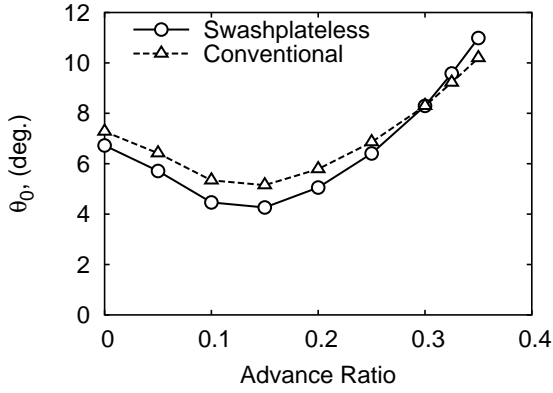
(a) Collective pitch at 75%R, θ_0
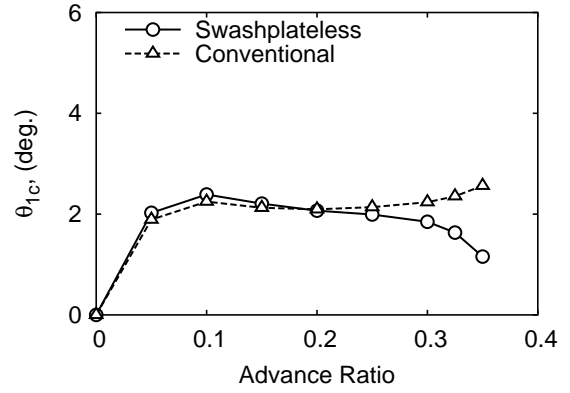
(b) Lateral cyclic at 75%R, θ_{1c}
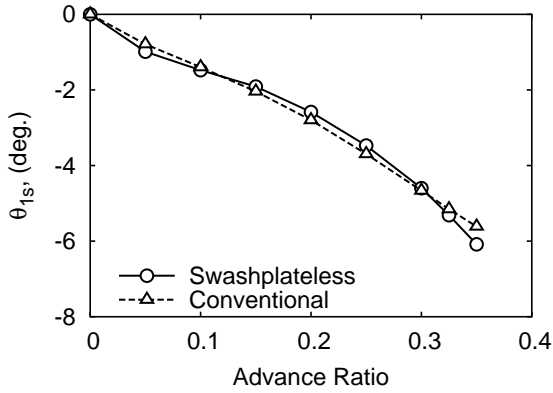
(c) Longitudinal cyclic at 75%R, θ_{1s}
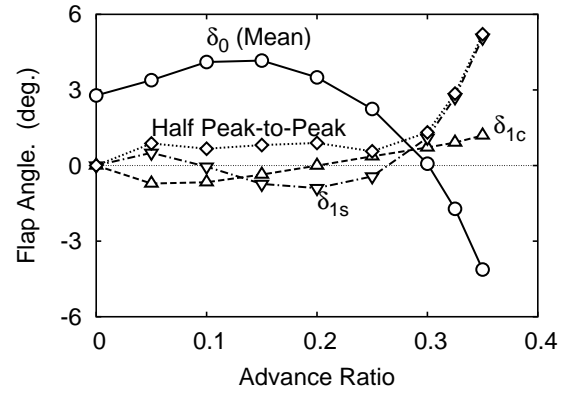
(d) Trailing-edge flap deflections
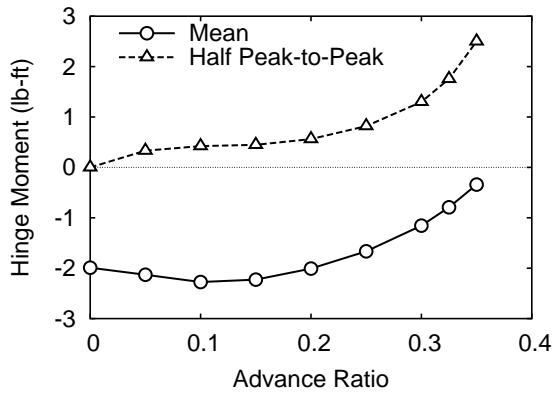
(e) Trailing-edge flap hinge moment
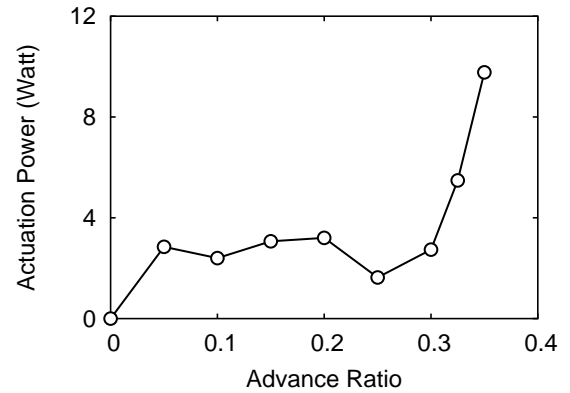
(f) Trailing-edge flap actuation power

Figure 3.63: Comparison of conventional and swashplateless rotor at different forward speeds, blade pitch index angle of $16°$, $C_T/\sigma = 0.075$.
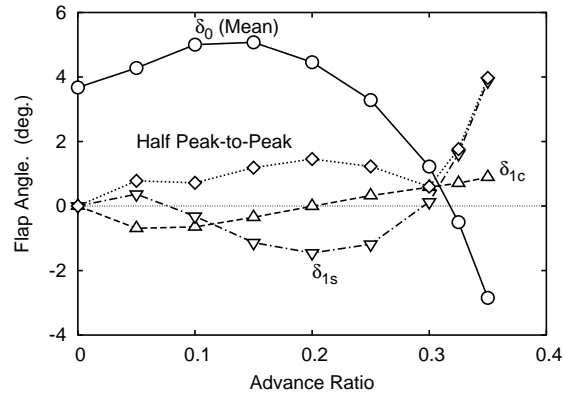
(a) Trailing-edge flap angle
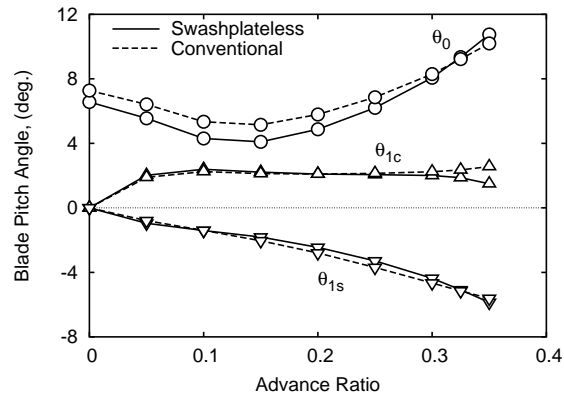
(b) Blade pitch angle at 75%R
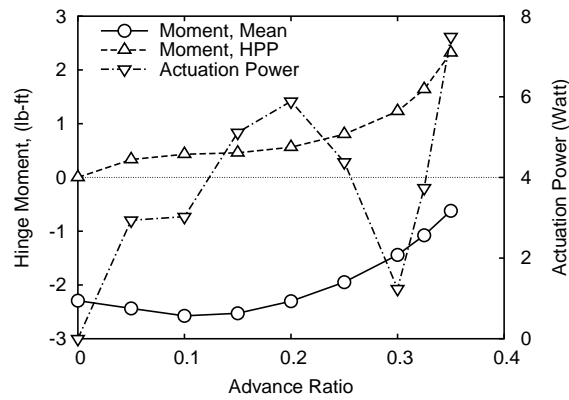
(c) Flap hinge moment and actuation power

Figure 3.64: Trailing-edge flap deflection, blade pitch angle, and actuation requirement of swashplateless rotor at different forward speeds (blade pitch index angle of 18°, $C_T/\sigma = 0.075$, $\nu_\theta = 2.1/rev$). HPP: Half Peak-to-Peak
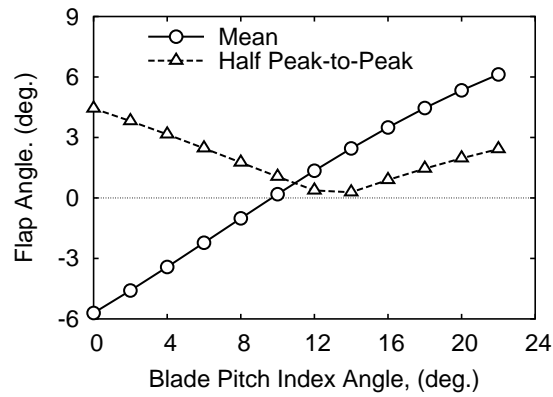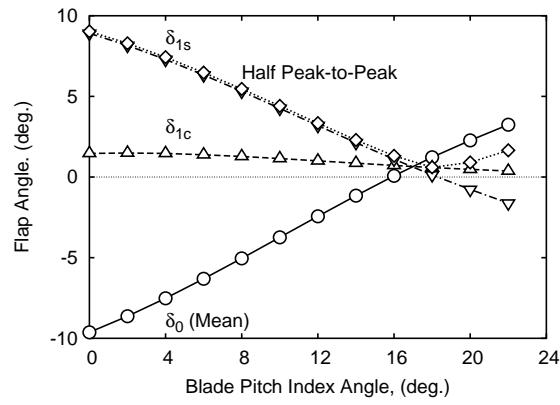
(a) Trailing-edge flap angle
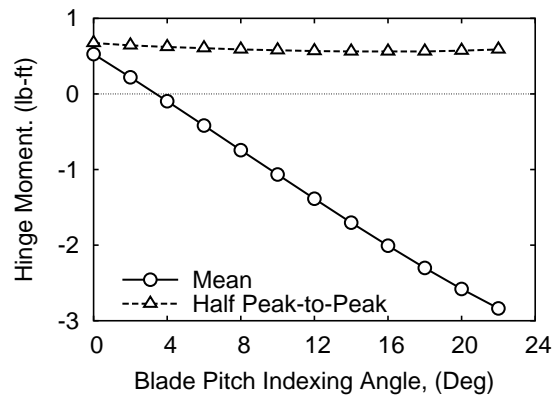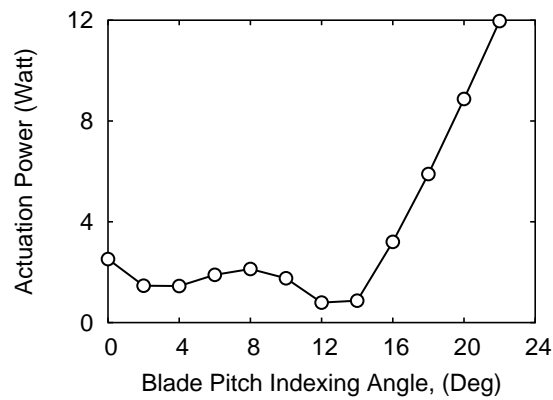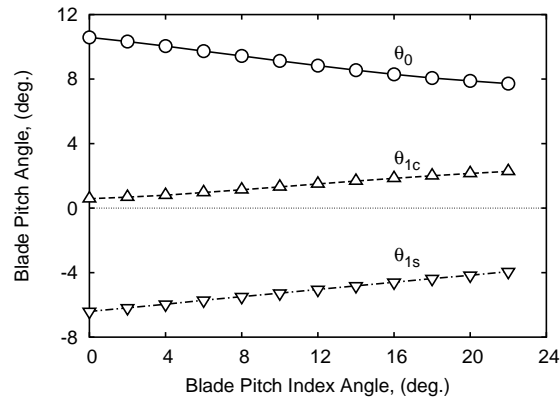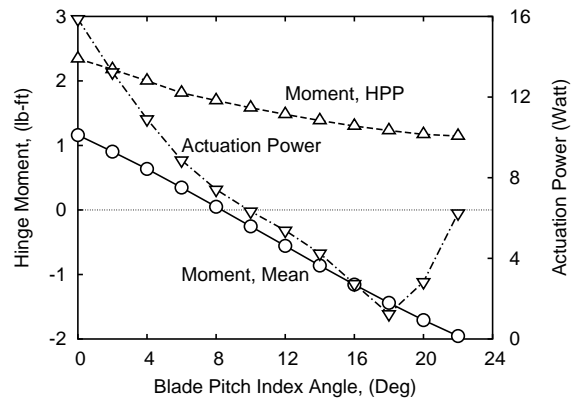

(b) Flap hinge moment

(c) Flap actuation power

Figure 3.65: Effect of blade pitch index angle on trailing-edge flap deflections and actuation requirement, advance ratio of 0.2, $C_T/\sigma = 0.075$.
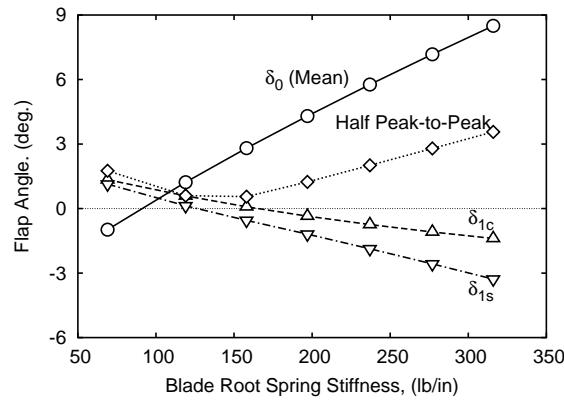
(a) Trailing-edge flap angle
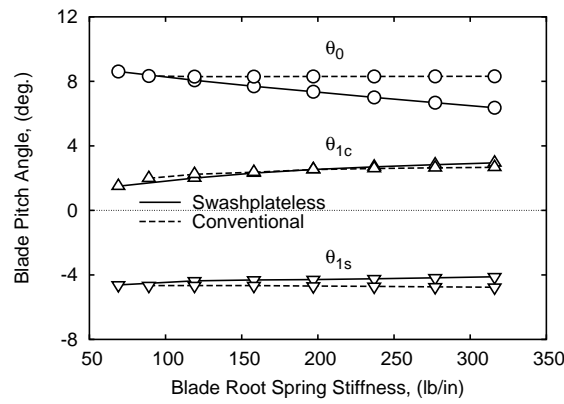

(b) Blade pitch angle at 75%R
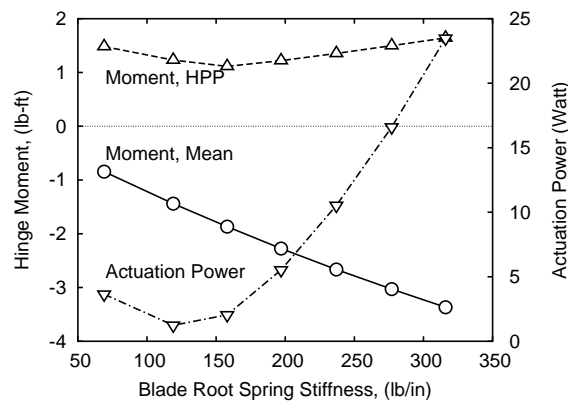

(c) Flap hinge moment and actuation power

Figure 3.66: Effect of blade index angle on flap deflection, blade pitch angle, and flap actuation requirement ($\nu_\theta = 2.1/rev$, $\mu = 0.30$). HPP: Half Peak-to-Peak
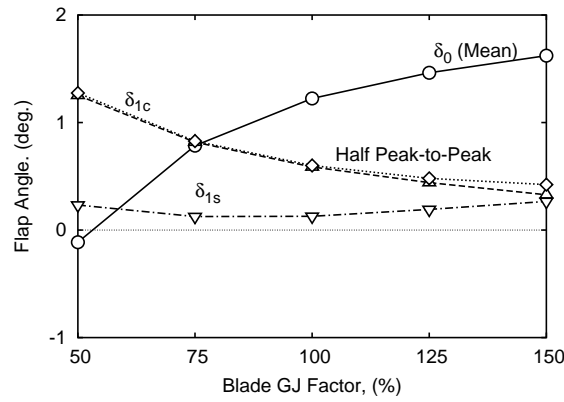
216

(a) Trailing-edge flap angle
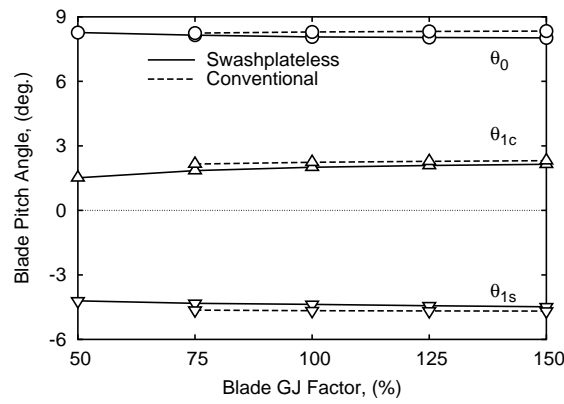

(b) Blade pitch angle at 75%R

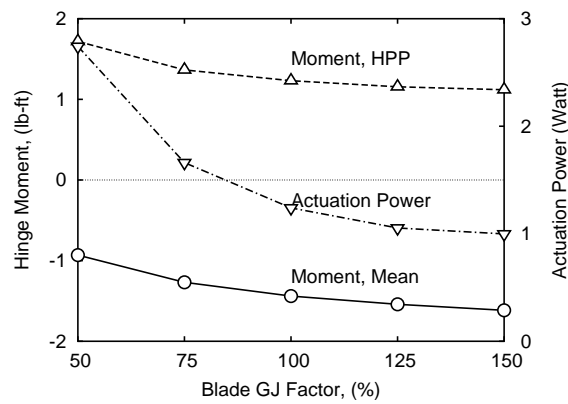(c) Flap hinge moment and actuation power

Figure 3.67: Effect of blade root spring stiffness on flap deflection, blade pitch angle, and flap actuation requirement (baseline blade torsional stiffness distribution, blade index angle of 18°, $\mu = 0.30$).
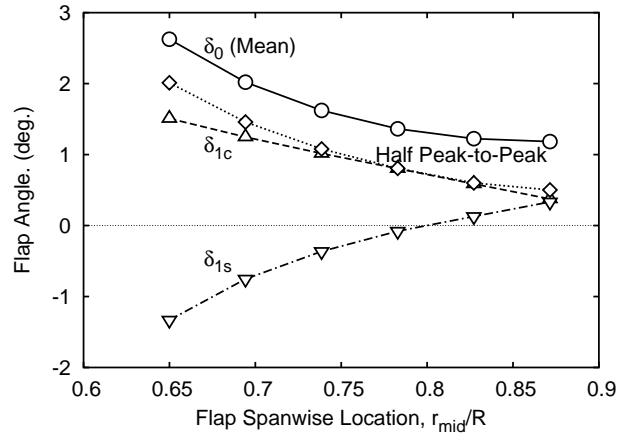
(a) Trailing-edge flap angle

(b) Blade pitch angle at 75%R

(c) Flap hinge moment and actuation power

Figure 3.68: Effect of blade torsional stiffness distribution on flap deflection, blade pitch angle, and flap actuation requirement (blade root spring stiffness of 119 lb/in, blade pitch index angle of 18°, $\mu = 0.30$).

(a) Trailing-edge flap angle
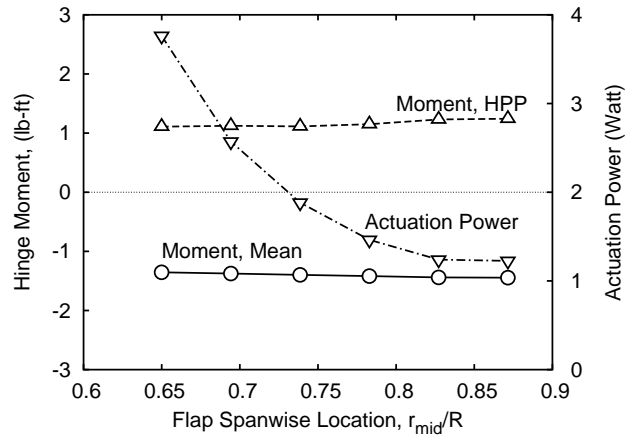
(b) Flap hinge moment and actuation power

Figure 3.69: Effect of flap spanwise location on flap deflection and actuation requirement (blade pitch index angle of 18°, flap length of $18\%R$, $\nu_\theta = 2.1/rev$, $\mu = 0.30$).

(a) Trailing-edge flap angle

(b) Flap hinge moment and actuation power

Figure 3.70: Effect of flap length on flap deflection and actuation requirement (blade pitch index angle of 18°, flap middle section located at $83\%R$, $\nu_\theta = 2.1/rev$, $\mu = 0.30$).
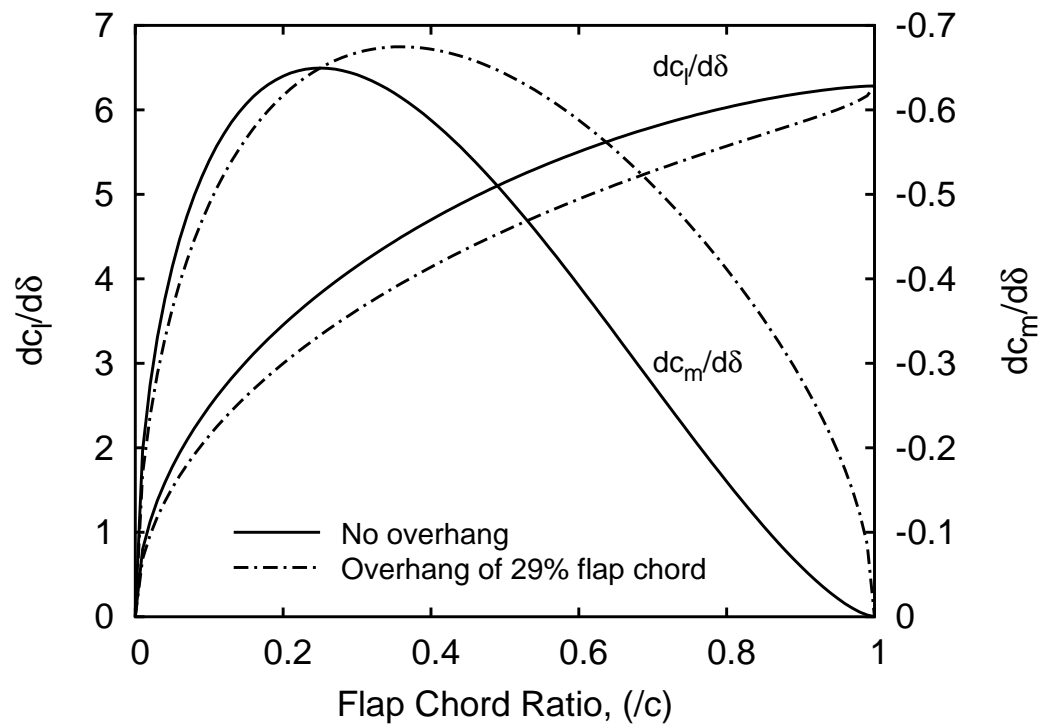
Figure 3.71: Theoretical lift and pitching moment characteristics of plain trailing-edge flaps
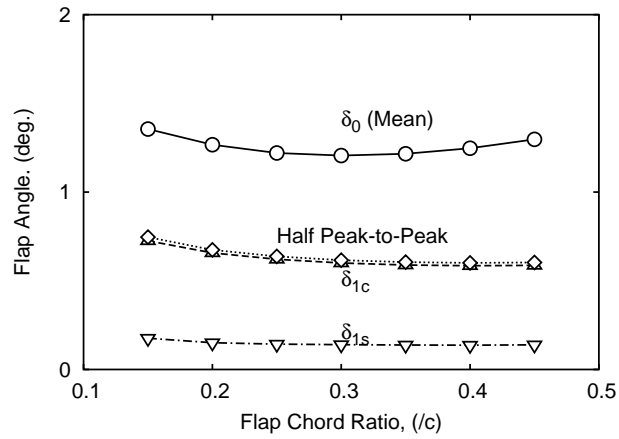
(a) Trailing-edge flap angle
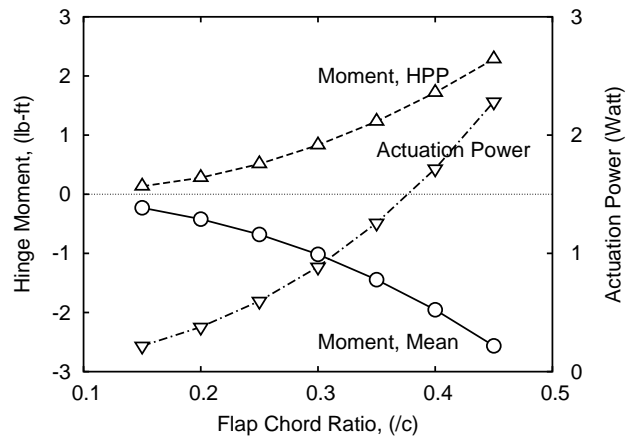
(b) Flap hinge moment and actuation power

Figure 3.72: Effect of flap chord ratio on flap deflection and actuation requirement (blade pitch index angle of 18°, flap overhang of 29% flap chord, $\nu_\theta = 2.1/rev$, $\mu = 0.30$).
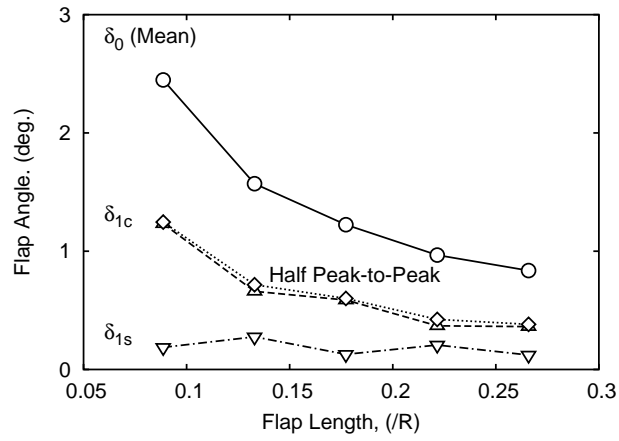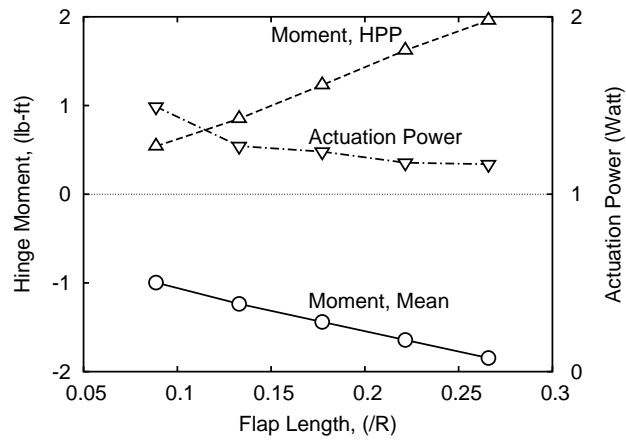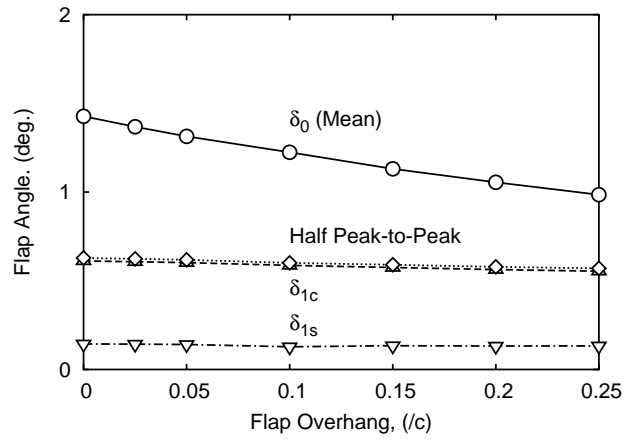
(a) Trailing-edge flap angle
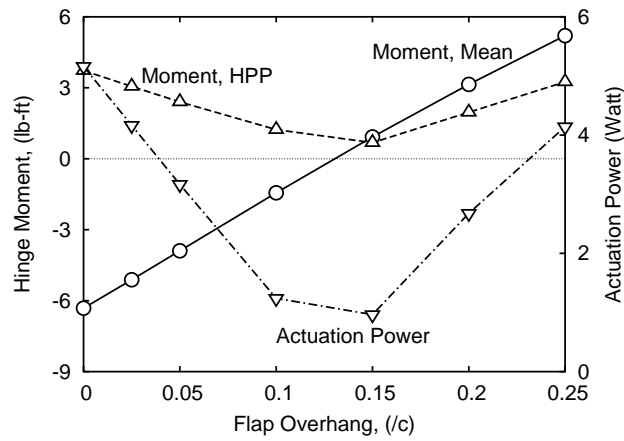
(b) Flap hinge moment and actuation power

Figure 3.73: Effect of flap overhang on flap deflection and actuation requirement (blade pitch index angle of 18°, flap chord of 0.35c, $\nu_\theta = 2.1/rev$, $\mu = 0.30$).
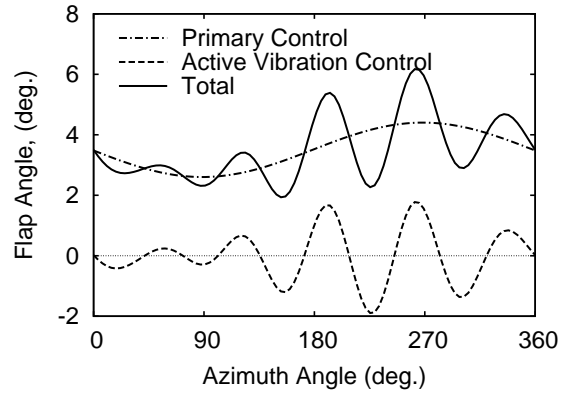
(a) Trailing-edge flap input
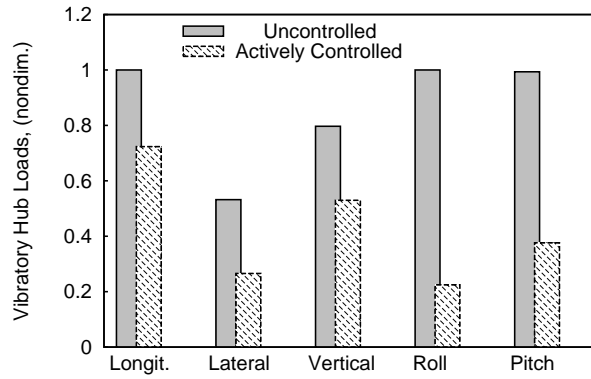

(b) 5/rev vibratory hub loads minimization

Figure 3.74: Trailing-edge flap performing both functions of primary control and active vibration control, advance ratio of 0.2, $C_T/\sigma = 0.075$, blade pitch index angle of $16°$.
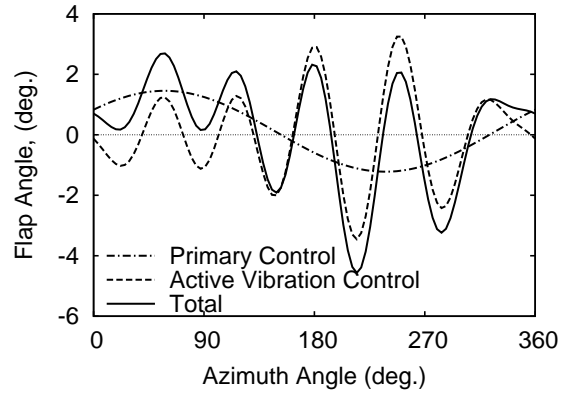
(a) Trailing-edge flap input
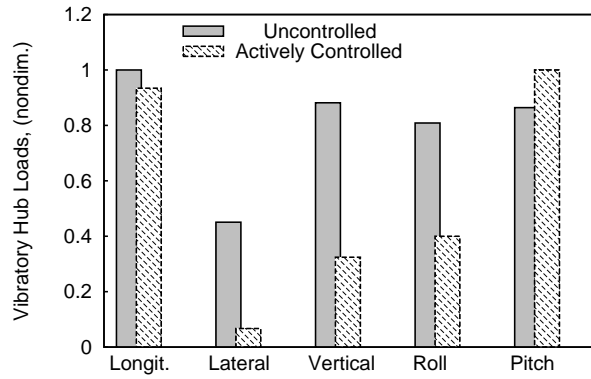
(b) 5/rev vibratory hub loads minimization

Figure 3.75: Trailing-edge flap performing both functions of primary control and active vibration control, advance ratio of 0.3, $C_T/\sigma = 0.075$, blade pitch index angle of $16°$.
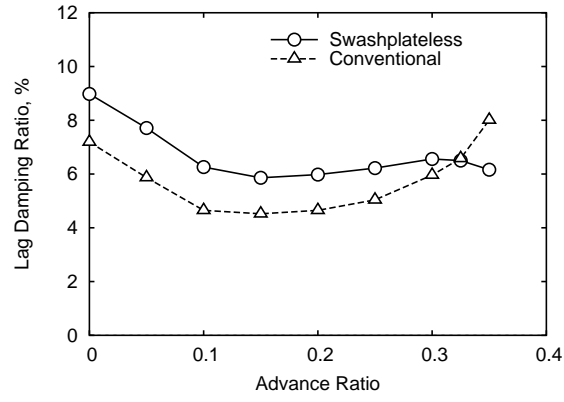
(a) Blade lag damping
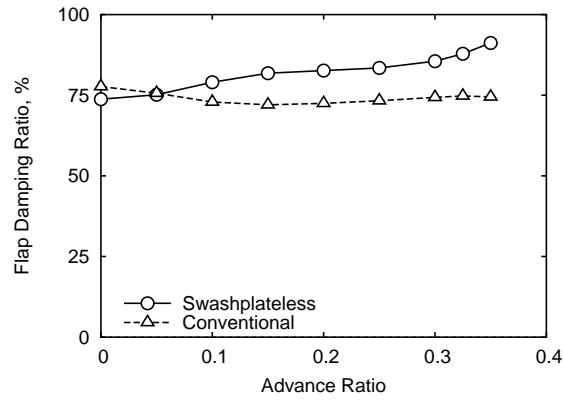
(b) Blade flap damping
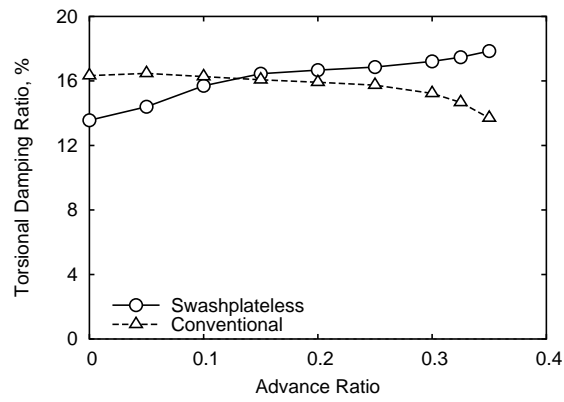
(c) Blade torsional damping

Figure 3.76: Comparison of blade stability for a swashplateless and conventional rotor at different forward speeds (blade pitch index angle of 18°, $\nu_\theta = 2.1/rev$).
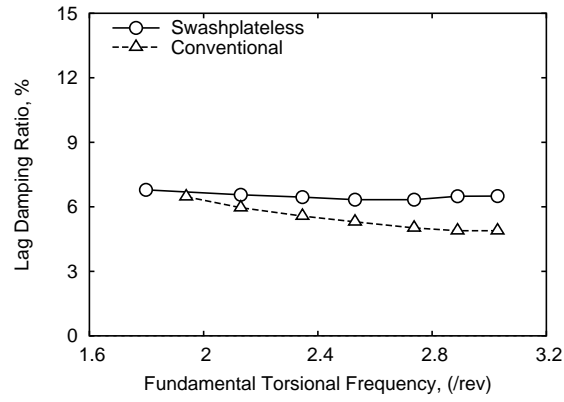
(a) Blade lag damping
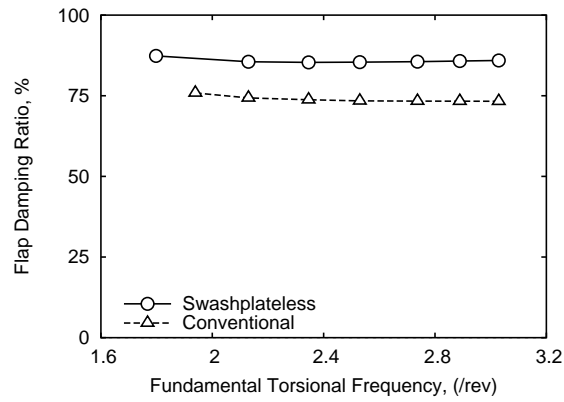
(b) Blade flap damping
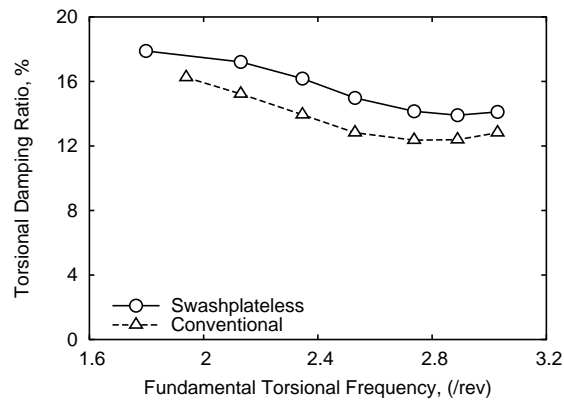
(c) Blade torsional damping

Figure 3.77: Comparison of blade stability for a swashplateless and conventional rotor with various blade torsional frequencies (blade pitch index angle of 18°, $\mu = 0.30$).
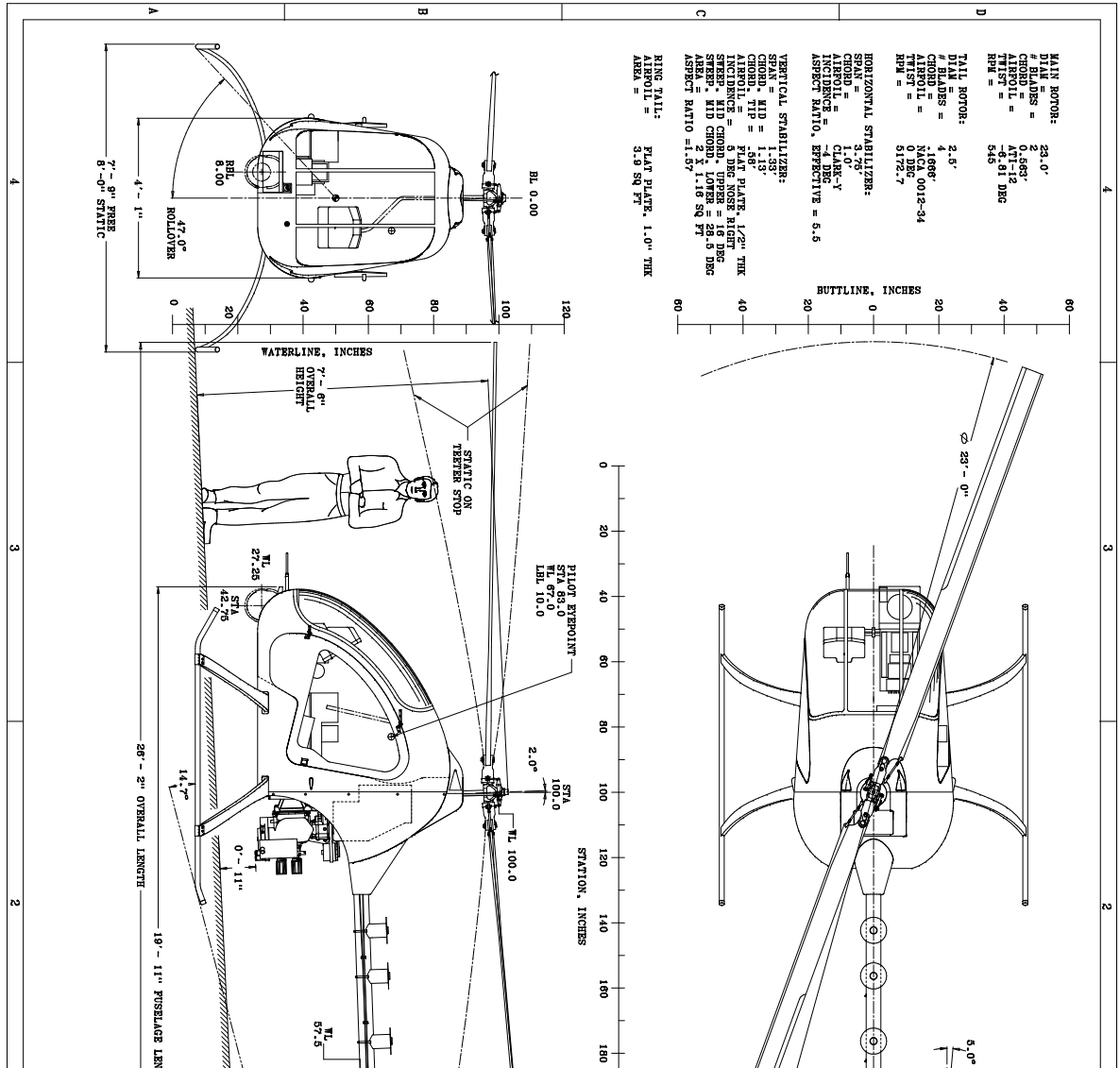
Figure 3.78: ASI 496 teetering rotor
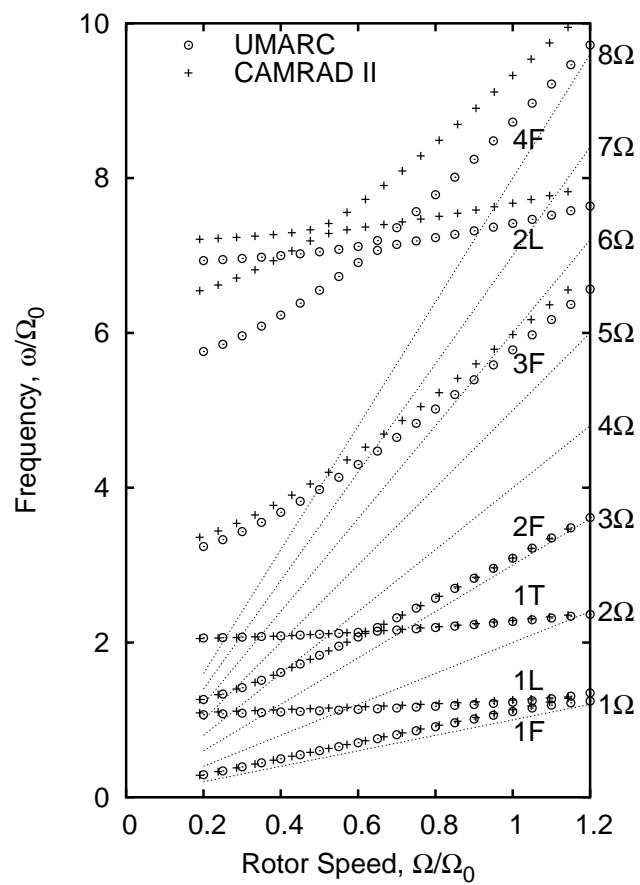
Figure 3.79: Comparison of blade normal mode frequency for ASI 496 teetering main rotor
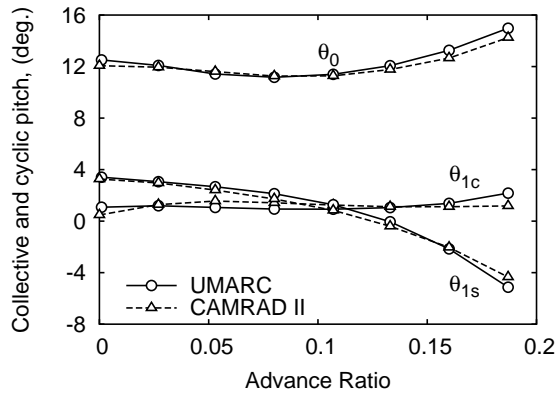
(a) Blade pitch angles
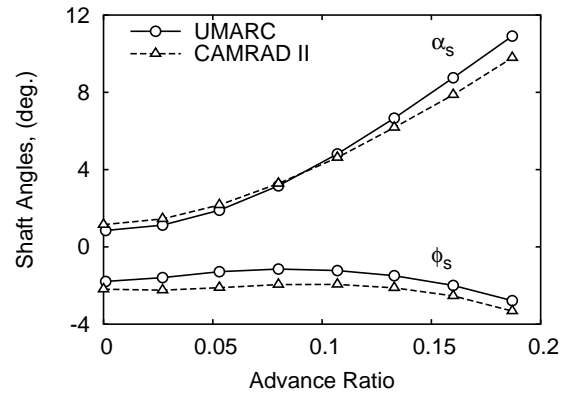
(b) Shaft tilt angles
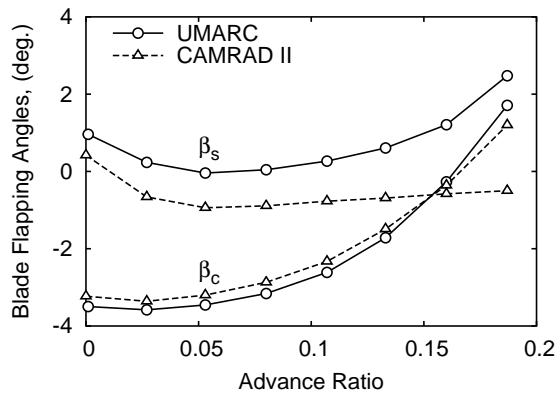
(c) Blade flapping angles
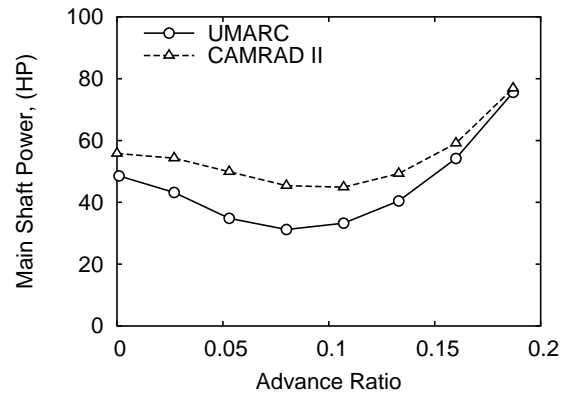
(d) Main shaft power

Figure 3.80: Comparison of blade pitch, shaft tilt, flapping angles, and main shaft power for the basic teetering rotor.
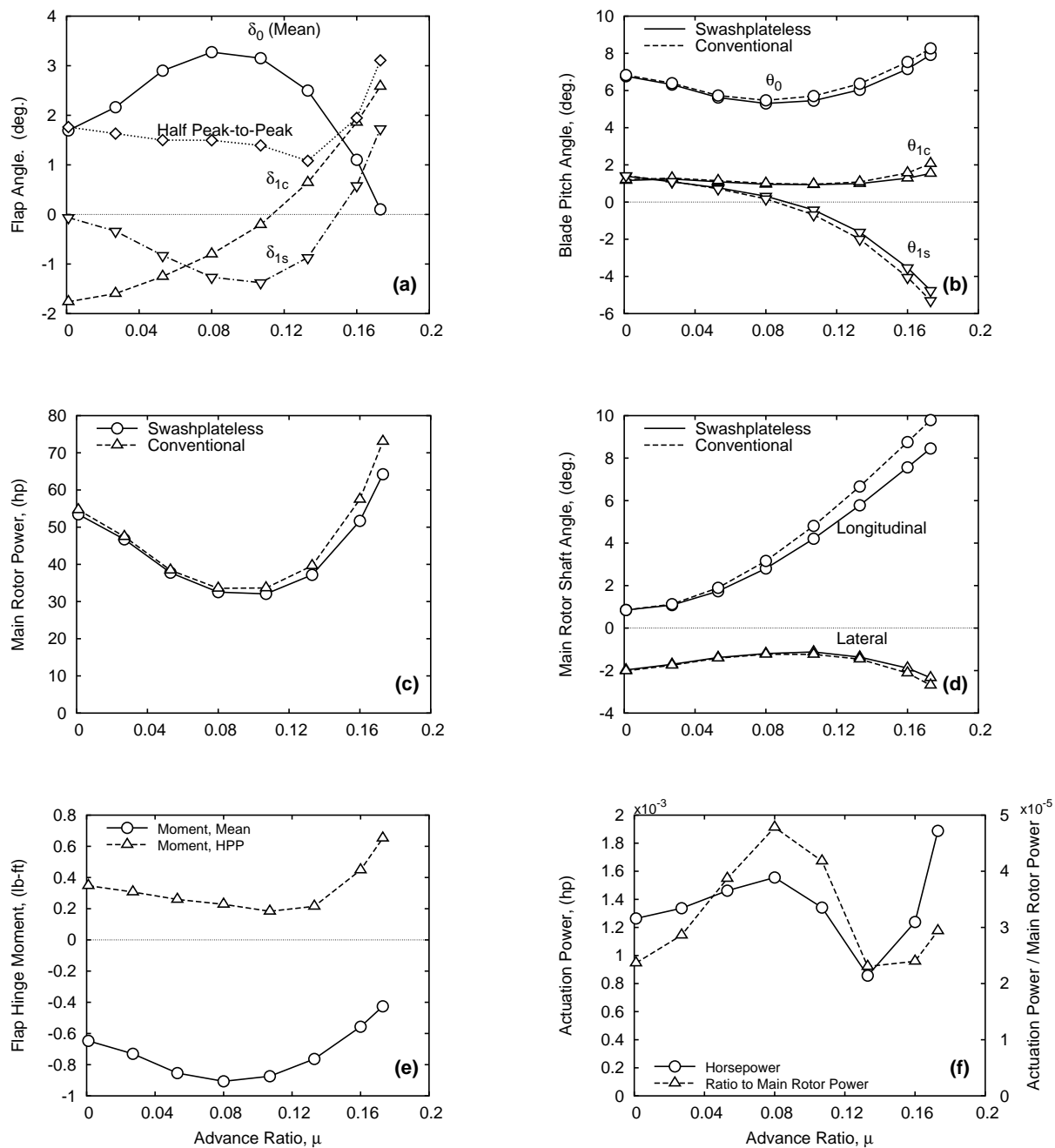
Figure 3.81: Comparisons of conventional and swashplateless rotor at different forward speeds with pitch index angle of $18°$
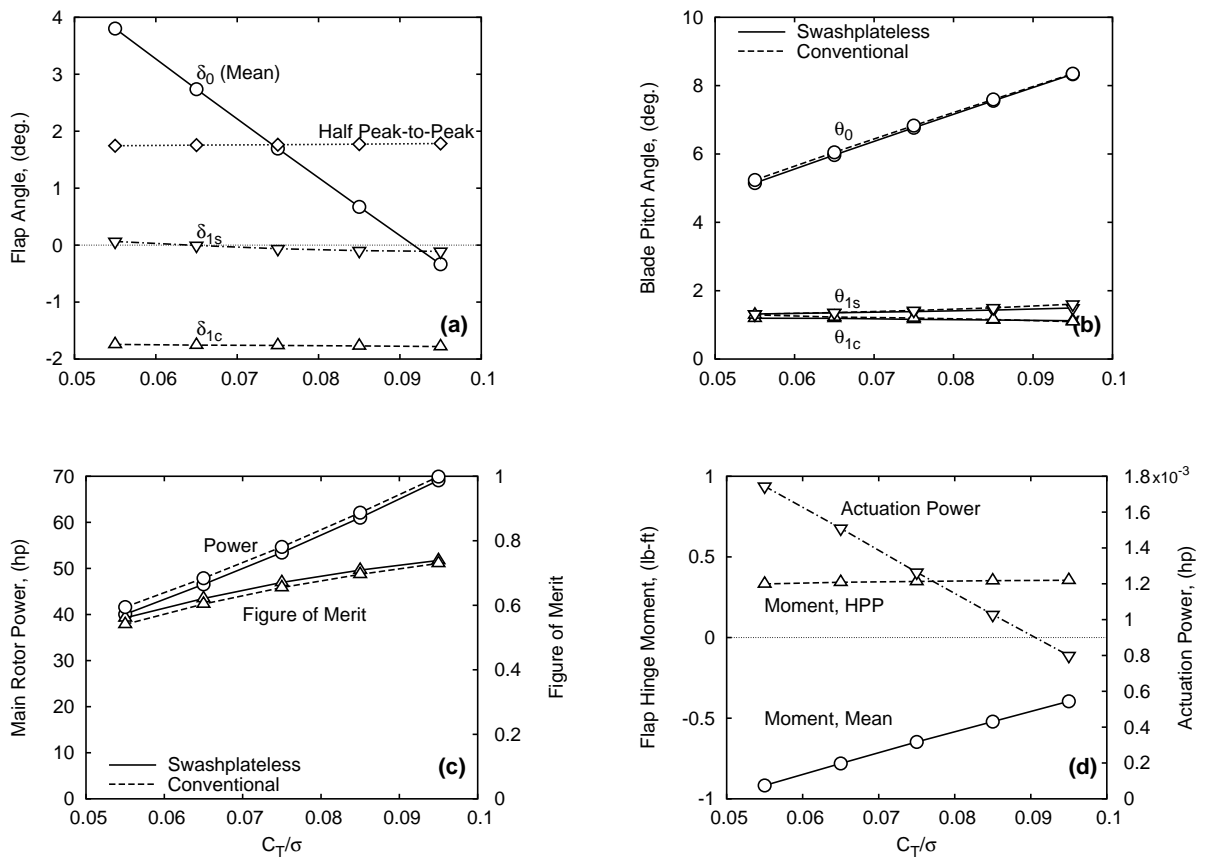
Figure 3.82: Comparisons of conventional and swashplateless rotors for different thrust levels at hover
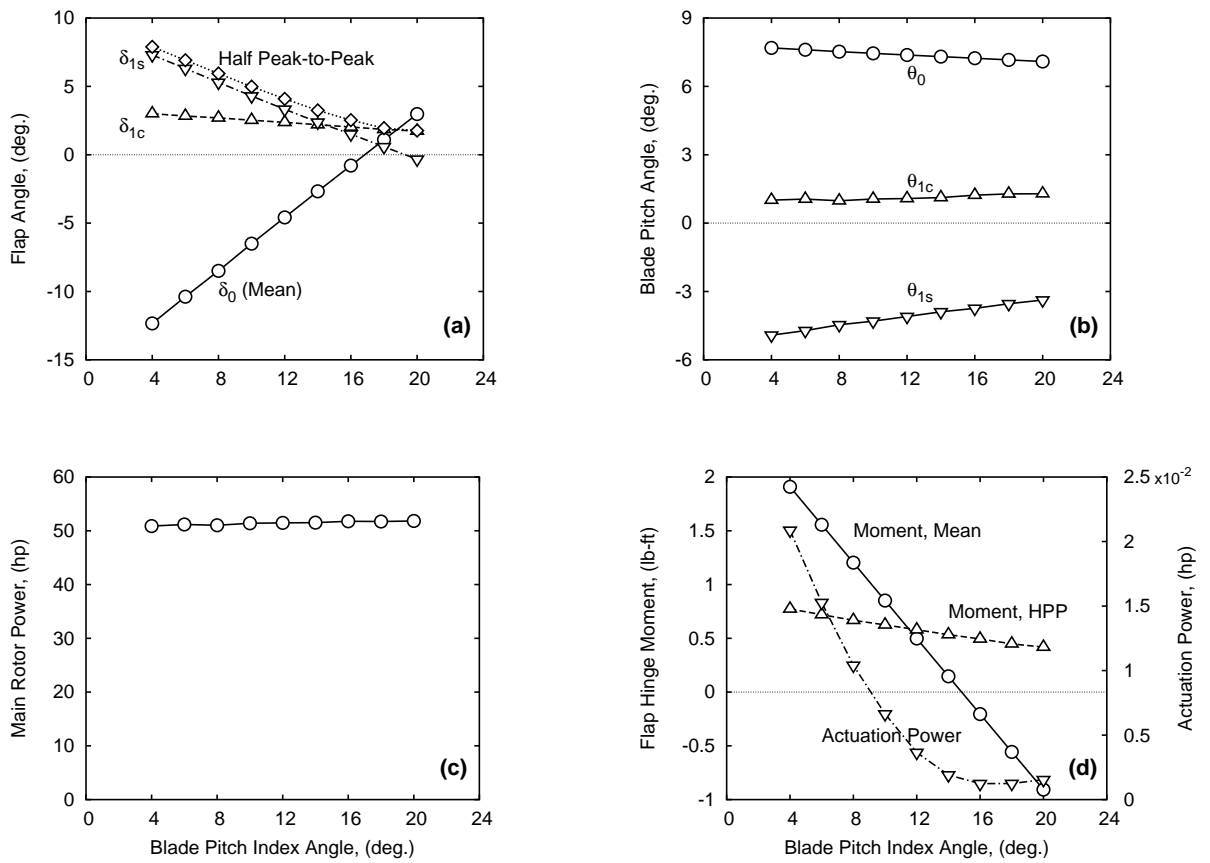
Figure 3.83: Effect of pitch index angle on trailing-edge flap angles, main rotor power, and and actuation requirements at forward speed of 60 knots ($\mu = 0.16$)
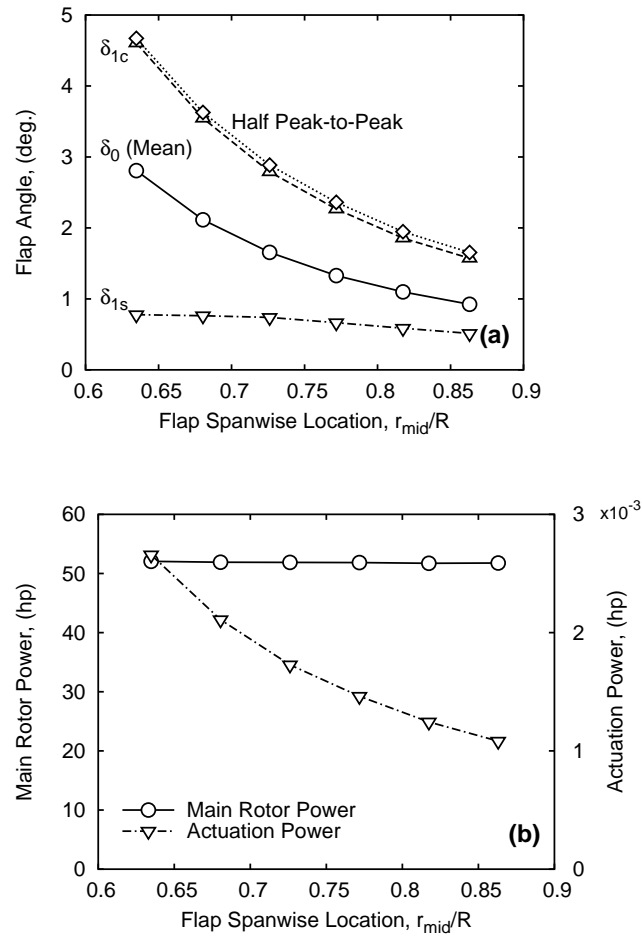
Figure 3.84: Effect of trailing-edge flap location on flap angles, main rotor power, and and actuation requirements at forward speed of 60 knots ($\mu = 0.16$)
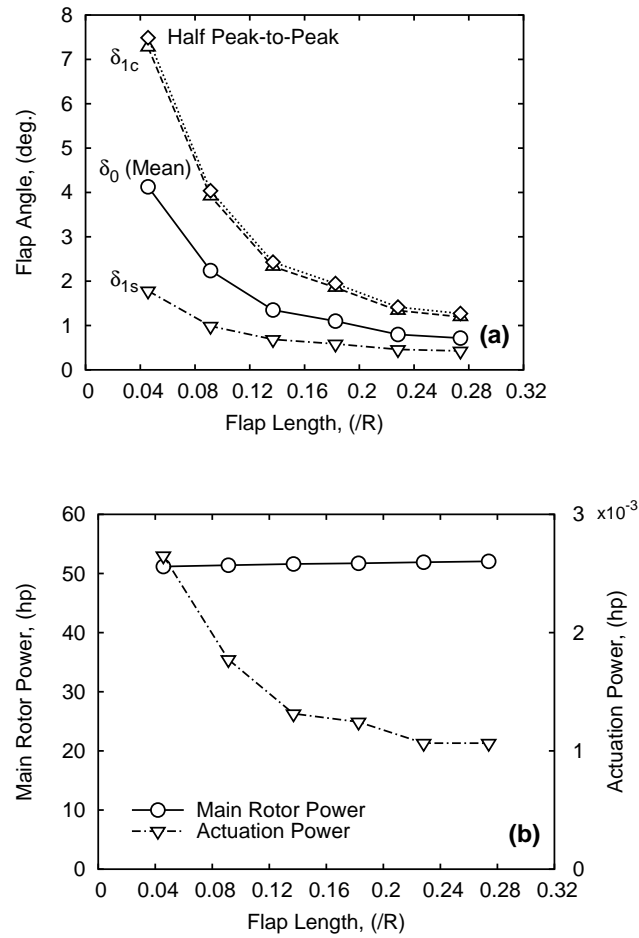
Figure 3.85: Effect of trailing-edge flap length on flap angles, main rotor power, and and actuation requirements at forward speed of 60 knots ($\mu = 0.16$)
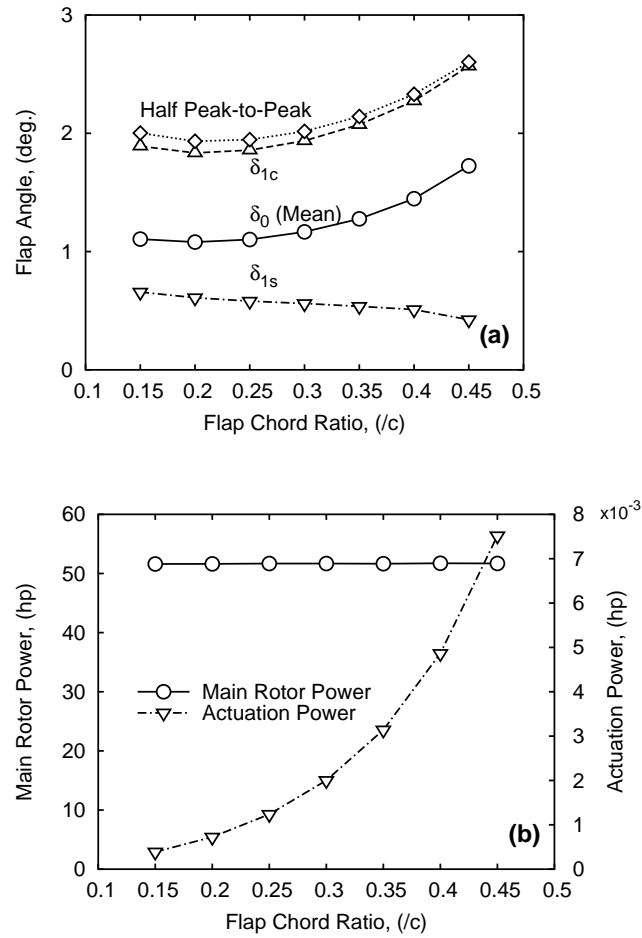
Figure 3.86: Effect of trailing-edge flap chord ratio on flap angles, main rotor power, and and actuation requirements at forward speed of 60 knots ($\mu = 0.16$)

Chapter 4

Summary and Conclusions

The present analysis evaluates the advantages of plain trailing-edge flaps actuated by compact, light weight smart material actuators on helicopter rotors. The aeroelasticity of trailing-edge flap helicopter rotor was investigated systematically. The feasibility of using trailing-edge flap for helicopter vibration reductions and primary control was studied systematically.

The research effort presented in this dissertation may be divided into four main parts. First, a fully coupled blade/flap/actuator analysis was developed to investigate the effects of actuator dynamics on aeroelastic response of blade and trailing-edge flap system, and furthermore on the actuation requirements of using trailing-edge flap for vibration control. Second, perturbation equations of the coupled blade/flap/actuator system were derived to study the aeroelastic stability characteristics of a trailing-edge flap helicopter rotor. Third, an aeroelastic analysis of swashplateless bearingless helicopter rotors in wind tunnel trim was developed to study the feasibility of using trailing-edge flap for primary control. Fourth, the analysis was modified to model a swashplateless ultralight teetering helicopter rotor in free flight conditions. The rotor performance of

the swashplateless rotor was compared with the conventional configuration. This chapter summarizes the development of analytical model of trailing-edge flap rotors for primary and vibration controls, and then presents the major conclusions reached for each of these four parts of present analysis, and includes recommendations for future research in the final section.

4.1   Development of Analytic Model

A comprehensive aeroelastic analytical model of helicopter rotors with trailing-edge flaps for primary and vibration controls has been developed. The derivation of system equations is based on Hamilton principles, and implemented with finite element method in space and time. The blade element consists of fifteen degrees of freedom representing blade flap, lag, torsional, and axial deformations. Three aerodynamic models of flapped airfoils were implemented in the present analysis, an advanced unsteady Leishman- Hariharan model for flaps without aerodynamic balance, a quasi-steady Theodorsen theory for an aerodynamic balanced flap, and table lookup based on wind tunnel test data. Bagai-Leishman free wake model based on pseudo-implicit predictor-corrector relaxation scheme is used to provide inflow distribution on the rotor disk. Drees linear inflow is also implemented. Nonlinear inertial effects of the flap and blade are fully captured. The trailing-edge flap deflections may be modeled as a degree of freedom so that the actuator dynamics can be captured properly. The coupled trim procedures are solved in either wind tunnel trim or free flight conditions. The aeroelastic stability characteristics of trailing-edge flap rotors can also be predicted.

The system equations of the fully coupled blade/flap/actuator system are formulated using Hamilton's variational principle. The actuator and flap are modeled as two separate structural dynamic elements with the flap hinge located at an arbitrary chordwise portion of the flap. The flap motion is indirectly controlled via base motion of the torsional spring. The blade/actuator/flap aerodynamic and inertial coupling effects were explicitly derived. The coupled blade/flap/actuator equations are nonlinear and periodic, and solved using finite elements in space and time.

Rotor hub loads and blade sectional loads are calculated using a force summation method. The sum of blade and incremental trailing-edge flap inertia and aerodynamics loads is integrated over the blade span to yield the loads reacted at the rotor hub in the rotating frame. The loads in the rotating frame are then transformed to the fixed system and summed up for all the blades.

The coupled blade equations of motion were linearized by using small perturbations about a steady trimmed solution. Stability was then determined from an eigenanalysis of the homogeneous equations using either Floquet method or Constant Coefficient Approximations. The trailing-edge flap motion is included as an additional degree of freedom in this study, and the stability of the trailing-edge flap mode is properly predicted.

The coupled trim procedure was modified to model a swashplateless bearingless helicopter rotor with trailing-edge flaps in wind tunnel trim conditions. The flaps produce pitching moment changes, which impel the main blades to pitch against the root spring to achieve aerodynamic equilibrium, thereby producing the desired collective and cyclic blade twist. The trim variables for a swashplateless rotor are flap collective deflection, δ_0, and cyclic deflections, δ_{1c} and δ_{1s}. Two unique characteristics of swashplateless rotors,

compared with conventional rotors, are torsionally soft blades and pre-collective angles, and both are properly modeled in the analysis.

The swashplateless rotor model was further enhanced to model an ultralight teetering helicopter rotor with trailing-edge flaps in free flight conditions. An additional degree of freedom involved in teetering rotors, the rotor teetering angle, was added in the system equations. Teetering angle, consists of only the odd harmonics, which are determined by the summation of the flap moments of the two blades at the teetering hinge. The blade equations of motion have to be transformed into hub-fixed system to treat the blades of teetering rotors simultaneously. This is because the two blades are rigidly connected to each other and attached to the mast through a common flapping hinge.

A multicyclic controller is also implemented to calculate the flap control inputs for minimization of vibratory rotor hub loads. This controller may be used in vibration control of both the conventional and swashplateless rotors.

This comprehensive trailing-edge flap helicopter model provides a design tools to investigate the effect of flap configurations of arbitrary locations, length, chord ratio, overhang length and mass properties on the effectiveness of primary and vibration controls, actuation requirements, and aeroelastic stability characteristics of trailing-edge flap rotors.

4.2 Validation Study

The prediction capability of present analysis is validated by comparing with MDART wind tunnel test data as well as correlating with the predictions of another comprehensive

analysis (CAMRAD II). The loads and stability prediction of MDART bearingless rotor is first compared with MDART test data. Then, predictions of trailing-edge flap rotor are correlated with the calculations of CAMRAD II.

4.2.1   Validation with MDART Loads Data

A correlation study for the baseline bearingless rotor (without trailing-edge flaps) was performed using wind tunnel experimental data. The experimental data used in this validation study was obtained in a wind tunnel test of the MDART rotor conducted in NASA Ames 40- by 80-foot wind tunnel in 1994. The wind tunnel test obtained trim, performance, loads, and stability, for the state-of-the-art MDART bearingless rotor system over a wide range of operating conditions. The UMARC predictions of rotor trim angles, rotor performance, blade sectional loads, vibratory hub loads, and aeroelastic stability characteristics were compared with wind tunnel measurement in different flight conditions.

The predicted rotor trim angles of the baseline rotor show good agreement with the experiment data. The UMARC predictions of main rotor power agree well with the test data except of a slight underprediction.

The comparison of blade sectional loads between predictions and measurements is overall successful. Good agreement is seen for the vibratory components of blade flap bending, chord bending, and torsion moments. The comparison of mean components of blade flap bending, chord bending, and torsion moments shows mixed results. Good agreement is seen on the mean flap bending moments, and poor comparison on the chord bending and torsional moments probably because of measurement error in the test data.

The measured and calculated time history of blade structural moments were compared at an advance ratio of 0.2. The flapwise bending moments are well captured except the high frequency content, and good agreement is observed for the chord bending moments. The overall trend of torsional moment is captured, however, the high frequency components are not predicted well.

The predicted 5/rev vibratory hub loads of the MDART rotor in forward flights show mixed result comparing with the measurements. The trend of longitudinal force, and vertical force are well captured by the predictions though somewhat underpredicted. UMARC largely overpredicted the vibratory side force, and this discrepancy may be attributed to wind tunnel test data was not properly dynamically calibrated. Predicted 5/rev pitching moments and rolling moments are overall underpredicted, and this may be due to the lack of high harmonics contents in the inflow distributions calculated by the free wake model.

4.2.2   Validation with MDART Stability Data

The accuracy of aeroelastic stability predictions was evaluated by comparing the calculated lag damping ratio of the MDART bearingless rotor with the test data in several flight conditions. In hover, UMARC results overall agree well with the test data with a small overprediction at small collectives and underpredictions at a high collective, i.e., larger than 10 degrees. In simulated forward flight conditions, the UMARC predictions using Floquet theory compare well with test data except small overpredictions in advance ratio range from 0.15 to 0.25. Variation of lag damping with collective pitch angle is compared

with test data for advance ratios of 0.20 and 0.25, good agreement is seen.

4.2.3   Correlation with CAMRAD II

The correlation study of trailing-edge flap analysis is carried out by comparing the predictions of the active flap MD-900 rotor between present analysis and CAMRAD II. The results of CAMRAD II are provided by the rotor manufacturer (Boeing-Mesa). The comparison shows good agreement of the blade tip response and torsion moments. The UMARC Predictions obtained using data table lookup and analytical expressions for aerodynamic coefficients show only small differences, and also correlate well with the CAMRAD predictions. Flap hinge shear and hinge moment predictions of UMARC using table lookup show good agreement with the CAMRAD II predictions that are also calculated using table lookup. However, the flap hinge moment results of UMARC utilizing analytical expressions only qualitatively agree with the other two models.

4.3   Parametric Study: Vibration Reduction

The impact of actuator dynamics on the flap effectiveness on vibration reductions and actuation requirements was investigated. A large coupling effect due to actuator dynamics is seen with a soft actuator.

The parametric study conducted to examine flap location using both coupled and prescribed flap motion models showed the trailing-edge flap was very effective in reducing 5/rev vibratory hub loads. Spanwise placement of the flap has a significant impact on actuation power. Both coupled and prescribed flap models indicate that the placement

of flap midspan at 78% radius resulted in minimum actuation power for this rotor. The coupled model requires a 10% larger flap control input and a 30% higher actuation power requirement for different flap placements. Both models showed the objective function can be reduced to less than 25% of the baseline value.

The key conclusions from this study are:

1. The coupling effect of actuator dynamics cannot be neglected, especially for a torsionally soft actuator.

2. The coupled flap model requires larger actuation effort than that of the prescribed model for most spanwise flap locations.

3. Blade/actuator/flap coupling has a more significant effect at low advance ratios than at high advance ratios.

4.4   Aeroelastic Stability

The present analysis examined the effects of various key design variables such as flap overhang length, flap CG offset, rotor control system stiffness, blade torsional stiffness, actuator stiffness, and trailing-edge flap size and location on the aeroelastic stability characteristics of a trailing-edge flap rotor system. Simulations for several advance ratios and various collective pitches were performed. The following conclusions are reached through numerical simulations:

1. Although flap aerodynamic balance (nose overhang) is a key to minimizing actuation requirements, excessive overhangs may lead to blade/trailing-edge flap insta-

bility.

2. Large trailing-edge flap CG offsets cause torsion-flap flutter, especially at high advance ratios.

3. Increasing rotor control stiffness for a rotor with a mass-imbalanced flap may have a destabilizing effect on trailing-edge flap mode stability.

4. Increasing flap actuator stiffness for a rotor with a mass-imbalanced flap has a stabilizing effect on trailing-edge flap mode stability.

5. With a mass-imbalanced flap, increasing the flap length or moving flap toward the blade tip has a destabilizing effect on the trailing-edge flap mode stability.

6. Increasing collective pitch results in more instability of the trailing-edge flap mode.

4.5 Swashplateless Rotor in Wind Tunnel Trim

The actuation requirements of a primary control system were evaluated, and the feasibility of trailing-edge flap performing both primary control and active vibration control was examined.

The swashplateless rotor was shown to be trimmed successfully with trailing-edge flap control system in the complete range of advance ratio ($\mu = 0$ to 0.35). With a blade pitch index angle of $16°$, the required half peak-to-peak values of trailing-edge flap deflections are below $6°$ while the mean values are below $5°$. Trailing-edge flap hinge moments are small because of the use of aerodynamic balance overhang in the trailing-

edge flap design, and this in turn resulted in small actuation power requirements in the complete range of advance ratios.

The blade pitch index angle was found to be a key design parameter for a feasible swashplateless rotor system. An optimally selected pitch index angle was shown to decrease substantially the actuation requirement. The advantages of using blade pitch indexing are: (i) reduces the trailing-edge flap collective deflection, δ_0. (ii) decreases the trailing-edge flap cyclic deflection, δ_{1c} and δ_{1s}, through the desirable blade cyclic twist induced by downward deflected δ_0 in the asymmetric rotor aerodynamic condition of a forward flying helicopter.

Trailing-edge flaps were shown to be able to perform both primary control and active vibration control functions. It was observed that the rotor was trimmed and the objective function consisting of vibratory hub loads was reduced approximately 83%. The required trailing-edge flap deflections at an advance ratio of 0.2 are only moderate with using a blade pitch index angle of $16°$. Noting that the requirements of the swashplateless rotor in maneuvering and autorotation flights are not investigated in this study although it must be met in the swashplateless rotor design.

A parametric design study was numerically conducted for a helicopter primary control system utilizing trailing-edge flaps. The swashplateless rotor design is based on a typical production helicopter rotor, with plain trailing-edge flaps as primary control devices. The primary design parameters are summarized below:

1. Blade root spring stiffness is another important parameter that can be used to increase the trailing-edge flap control effectiveness. It is shown that increasing blade

246

root spring stiffness results in an increase in the magnitude of both the mean and cyclic components of the required flap deflections, and hence the actuation requirement. The present study suggests low root spring stiffness that results in a blade torsional frequency of 2.1/rev as the optimum value at an advance ratio of 0.30 and index angle of 18°.

2. Low blade torsional stiffness increases flap effectiveness. However, the blade torsion stiffness is less effective than blade root stiffness because the trailing-edge flap achieves primary control mainly through blade pitch at the root spring, rather than blade sectional twist motion.

3. Locating trailing-edge flaps close to the blade tip where high dynamic pressure exists, will decrease flap deflection and actuation requirements.

4. Increasing the spanwise length of the flap will increase the flap effectiveness in providing primary control. It will also reduce actuation power by lowering the required flap deflection.

5. The flap chord ratio is a key parameter in plain flap design, because it plays an important role in determining the dominant flap effect. The study suggests a flap chord ratio of around 0.30 for a flap with an overhang of 29% flap chord.

6. Implementation of flap aerodynamic balance (nose overhang) is important to reduce actuation requirements. The study suggests a flap overhang of 15% chord that for a 35% chord flap translates into an overhang of approximately 43% of the flap chord.

7. The swashplateless rotor exhibits larger damping in the blade flap and torsion modes

than a conventional rotor at advance ratios above 0.15. The swashplateless rotor shows larger lag damping than the conventional at advance ratios below 0.325. A similar result was observed with the variation of blade stability with torsion frequency. Overall, the swashplateless rotor was more damped than the conventional rotor.

4.6   Swashplateless Rotor in Free Flight Trim

A comprehensive rotorcraft analysis for an ultralight helicopter with trailing-edge flaps for primary control was developed, and actuation requirements for a range of forward speeds were evaluated. The baseline rotor is a teetering rotor, and the prediction capability of present analysis is correlated with the predictions of another comprehensive analysis (CAMRAD II). The correlation is carried out for the baseline rotor without trailing-edge flaps embedded. The predicted blade natural frequencies at different rotor rotating speeds were compared, and good agreement is generally seen except the two higher frequency modes (second inplane, fourth flap bending). The calculated blade pitch angles, main shaft tilt angles and blade flapping angles are compared at different advance ratios between the two analyses. Blade pitch, longitudinal shaft tilt, and longitudinal flapping angle compare well between two predictions while lateral shaft tilt and lateral flapping angles show some level of discrepancy, and this may attribute to the different inflow models used in the two analyses. Main shaft power compares well between the two analyses at high advance ratios while displays some difference at low advance ratios possibly due to different empirical factors used.

The present analysis evaluated the performance of an ultralight helicopter rotor with trailing-edge flaps as primary flight control devices, and examined effects of various key design variables such as pitch index angle, flap location and geometry on rotor performance and trailing-edge flap deflections. The following conclusions are subject to the limitations of the analysis and the scope of the study:

1. With the design of baseline trailing-edge flap system, which consists of an $18\%R$ plain flap with 25% chord ratio located at $82\%R$, the trailing-edge flap deflections required to trim the rotor are moderate in the complete range of flight speed. Both flap collective and cyclic deflections are below 4°. Accordingly, actuation requirements are also small.

2. Compared with a conventional swashplate-controlled rotor, the swashplateless configuration consumes moderately less power in high speed forward, because of the 15% reduction in parasite drag assumed for the swashplateless design. In hover and low speed flight conditions, the swashplateless rotor consumes same or slightly less power.

3. Compared with the conventional rotor at various gross weights in hover, the swashplateless rotor consumes slightly less power, and hence shows higher figures of merit.

4. Optimal selection of pitch index angle, flap location, length and chord ratio is key to reduce trailing-edge flap angles and actuation requirements, with virtually no effect on rotor performance.

4.7   Recommendations for Future Work

The research presented in this dissertation carried out an exhaustive study of trailing-edge helicopter rotors. The analytical model provides a design tool of trailing-edge flap system. Nevertheless, there are areas where the investigation was limited by the capabilities of present analysis. The following section suggests enhancements for the present analysis as well as recommendations for future research in the trailing-edge flap helicopter rotor analysis.

1. The present analysis uses a quasi-steady aerodynamic model for trailing-edge flaps with aerodynamic balance. The Leishman-Hariharan time-domain unsteady aerodynamic model for a flapped airfoil can be extended to model a flap with a nose overhang. Once the model is available, it can be readily incorporated into the present analysis.

2. Experimental demonstration of swashplateless trailing-edge flap rotors is required. The present analysis of using trailing-edge flap for primary control has not been validated because of lack of test data. It is necessary to carry out a validation study using a Mach-Scaled rotor test data in a wind tunnel.

3. The present analysis of swashplateless rotor study is carried out in steady level flight conditions. The required flap angles and actuation requirement in maneuvering flight and auto-rotation conditions may be more severe especially for the flap collective deflection. A detailed study in these flight conditions is mandated in the flap sizing study.

4. The present analysis uses hub vibratory loads as the indication of helicopter vibration level. However, a more precise representation will be acceleration levels at key locations in the fuselage, such as the pilot seat, copilot seat, CG, and tail rotor. In order to achieve this, a fully coupled rotor/fuselage model is required. The UMARC comprehensive rotorcraft code, on which the present analysis is based on, already has the capability of modeling coupled rotor/fuselage system [88]. It is anticipated these modifications can be incorporated into a coupled analysis.

5. With the inclusion of coupled rotor/fuselage analysis, the aeromechanical stability characteristics of helicopter rotor/fuselage/trailing-edge flap system can be investigated. The possibilities of ground resonance and air resonance of the rotor system may then be studied.

6. The present analysis investigates using trailing-edge flap for primary and vibration control. Another area where active trailing-edge flap system can be used is helicopter noise control [41]. In order to predict the helicopter noise level, an acoustic code such as WOPWOP [101] need to be coupled with trailing-edge flap analysis.

7. The present analysis assumes identical rotor blades. However, there are always dissimilarities existing among the manufactured rotor blades. A dissimilar rotor analysis [14] is also available in UMARC code that can be incorporated to study the capability of using trailing-edge flaps to auto-track the rotor and minimize the vibration of a dissimilar rotor with the improved adaptive controller [102].

8. Extensive wind tunnel testing of airfoils with trailing-edge flaps is required to vali-

date and improve the aerodynamic model. The tests need to be carried out systematically for different trailing-edge flap configurations, and effects of chord ratio and overhang length need to be tested. Trailing-edge flap angles of the order of ten degrees are needed in the swashplateless rotor analysis. Trailing-edge flap deflections at high harmonics, covering of $N_b - 1, N_b, N_b + 1$/rev harmonics, are required for vibration reductions.

Appendix A

Equations

A.1 Theodorsen Geometry Constants of Trailing-Edge Flap

$$T_1 = -\frac{1}{3}\sqrt{1-e^2}\,(2+e^2) + e\,\mathrm{acos}(e)$$

$$T_2 = e\,(1-e^2) - \sqrt{1-e^2}\,(1+e^2)\,\mathrm{acos}(e) + e\,\mathrm{acos}(e)^2$$

$$T_3 = (-\frac{1}{8}-e^2)\,\mathrm{acos}(e)^2 + \frac{1}{4}\,e\,\sqrt{1-e^2}\,\mathrm{acos}(e)\,(7+2\,e^2)$$
$$\quad - \frac{(1-e^2)\,(5\,e^2+4)}{8}$$

$$T_4 = -\mathrm{acos}(e) + e\,\sqrt{1-e^2}$$

$$T_5 = -1 + e^2 - \mathrm{acos}(e)^2 + 2\,e\,\sqrt{1-e^2}\,\mathrm{acos}(e)$$

$$T_6 = e\,(1-e^2) - \sqrt{1-e^2}\,(1+e^2)\,\mathrm{acos}(e) + e\,\mathrm{acos}(e)^2$$

$$T_7 = (-\frac{1}{8}-e^2)\,\mathrm{acos}(e) + \frac{1}{8}\,e\,\sqrt{1-e^2}\,(7+2\,e^2)$$

$$T_8 = -\frac{1}{3}\sqrt{1-e^2}\,(2\,e^2+1) + e\,\mathrm{acos}(e)$$

$$T_9 = \frac{1}{6}\sqrt{1-e^2}^3 + \frac{1}{2}\,a\,(-\mathrm{acos}(e) + e\,\sqrt{1-e^2})$$

$$T_{10} = \sqrt{1-e^2} + \mathrm{acos}(e)$$

$$T_{11} = \text{acos}(e)\,(1 - 2\,e) + \sqrt{1 - e^2}\,(2 - e)$$

$$T_{12} = \sqrt{1 - e^2}\,(2 + e) - \text{acos}(e)\,(2\,e + 1)$$

$$T_{13} = -\frac{1}{2}\left(-\frac{1}{8} - e^2\right)\text{acos}(e) - \frac{1}{16}\,e\,\sqrt{1 - e^2}\,(7 + 2\,e^2)$$
$$- \frac{1}{2}\,(e - a)\left(-\frac{1}{3}\,\sqrt{1 - e^2}\,(2 + e^2) + e\,\text{acos}(e)\right)$$

$$T_{14} = \frac{1}{16} + \frac{a\,e}{2}$$

$$T_{15} = e\,\sqrt{1 - e^2} + \sqrt{1 - e^2}$$

$$T_{16} = -\frac{1}{3}\,\sqrt{1 - e^2}\,(2 + e^2) + \frac{1}{3}\,\sqrt{1 - e^2}\,(2\,e^2 + 1)$$
$$- (e - a)\left(-\text{acos}(e) + e\,\sqrt{1 - e^2}\right) + \frac{1}{2}\,\text{acos}(e)\,(1 - 2\,e)$$
$$+ \frac{1}{2}\,\sqrt{1 - e^2}\,(2 - e)$$

$$T_{17} = -\frac{1}{3}\,\sqrt{1 - e^2}^3 - a\left(-\text{acos}(e) + e\,\sqrt{1 - e^2}\right) + \frac{1}{3}\,\sqrt{1 - e^2}\,(2 + e^2)$$
$$- e\,\text{acos}(e) + \left(a - \frac{1}{2}\right)\left(-\text{acos}(e) + e\,\sqrt{1 - e^2}\right)$$

$$T_{18} = -1 + e^2 - \text{acos}(e)^2 + 2\,e\,\sqrt{1 - e^2}\,\text{acos}(e)$$
$$- \left(-\text{acos}(e) + e\,\sqrt{1 - e^2}\right)\left(\sqrt{1 - e^2} + \text{acos}(e)\right)$$

$$T_{19} = -\frac{1}{2}\left(-\text{acos}(e) + e\,\sqrt{1 - e^2}\right)\left(\text{acos}(e)\,(1 - 2\,e) + \sqrt{1 - e^2}\,(2 - e)\right)$$

$$T_{20} = -\sqrt{1 - e^2} + \text{acos}(e)$$

$$T_{21} = \sqrt{\frac{1 + e}{1 - e}}$$

$$T_{22} = 2\sqrt{1 - e^2} - \sqrt{\frac{1 + e}{1 - e}}$$

$$T_{23} = (-1 - 2e + 2a)\sqrt{1 - e^2}$$

$$T_{24} = T_8 + (e - a)\,T_4$$

$$T_{25} = T_4 - (1 - e)\,\sqrt{1 - e^2}$$

$$
\begin{aligned}
T_{26} &= 2\sqrt{1-e^2}\,T_{20} + T_4\sqrt{\frac{1+e}{1-e}} \\[2ex]
T_{27} &= T_4\,T_{10} - \sqrt{1-e^2}\,T_1 \\[2ex]
T_{28} &= 2\left(1 + e + \log N(e, e')\right) \\[2ex]
T_{29} &= 2\sqrt{1-e^2}\,T_{10}
\end{aligned}
\tag{A.1}
$$

BIBLIOGRAPHY

[1] John Fay. *The Helicopter*, pages 125–126. London, 3rd edition, 1976.

[2] J. Gordon Leishman. *Principles of Helicopter Aerodynamics*, chapter 1, Introduction: A History of Helicopter Flight. Cambridge University Press, 2000.

[3] Jay P. Spenser. *Whirlybirds: A history of the U.S. Helicopter Pioneers*. University of Washington Press, 1997.

[4] R.E. Hansford and J Vorward. Dynamic workshop on rotorcraft vibratory loads predictions. *Journal of the American Helicopter Society*, 43(1):76–87, January 1998.

[5] Anubhav Datta and Inderjit Chopra. Validation of structural and aerodynamic modeling using UH-60 flight test data. In *American Helicopter Society 59th Annual Forum Proceedings*, page 15, Phoenix, AZ, May 6-8 2003.

[6] Jayanarayanan Sitaraman, James Baeder, and Inderjit Chopra. Validation of UH-60 rotor blade aerodynamic characteristics using CFD. In *American Helicopter Society 59th Annual Forum Proceedings*, Phoenix, AZ, May 6-8 2003.

[7] S. P. Viswanathan and A. W. Myers. Reduction of helicopter vibration through control of hub-impedance. *Journal of the American Helicopter Society*, 25(4):3–12, October 1980.

[8] C. W. Ellis and R. Jones. Application of an absorber to reduce helicopter vibration levels. *Journal of the American Helicopter Society*, 8(3):30–42, July 1963.

[9] A. E. Staple. An evaluation of active control of structural response as a means of reduction helicopter vibration. In *Proceedings of the 15th European Rotorcraft Forum*, Amsterdam, Netherlands, September 1989.

[10] W. Welsh, C. Fredrickson, C. Rauch, and I. Lyndon. Flight test of an active vibration control system on the UH-60 black hawk helicopter. In *American Helicopter Society 51st Annual Forum Proceedings*, Fort Worth, TX, May 9-11 1995.

[11] L. E. Smollen, P. Marshall, and R. Gabel. Active vibration isolation of helicopter rotors. *Journal of the American Helicopter Society*, 7(2):42–55, April 1962.

[12] E. Schuett. Application of passive rotor isolation for alleviation of rotor induced vibration. *Journal of the American Helicopter Society*, 14(2):34–48, April 1969.

[13] O. A. Bauchau, J. Rodriguez, and S-Y Chen. Modeling the bifilar pendulum using nonlinear, flexible multibody dynamics. *Journal of the American Helicopter Society*, 48(1):53–62, January 2003.

[14] Mao Yang. *A Coupled Rotor-Fuselage Vibration Analysis for Helicopter Rotor System Fault Detection*. PhD thesis, University of Maryland, College Park, MD, 2002.

[15] Fu-Shang (John) Wei. Design of a integrated servo-flap main rotor. In *American Helicopter Society 59th Annual Forum Proceedings*, page 11, Phoenix, AZ, May 6-8 2003.

[16] F. S. Wei and R. Jones. Optical design application on the advanced aeroelastic rotor blade. pages 1–14, Moffett Field, CA,, November 7-9 1984. Proceedings of Decennial Specialists' Meeting on Rotorcraft Dynamics.

[17] N. D. Ham. Helicopter individual-blade-control and its applications. In *American Helicopter Society 39th Annual Forum Proceedings*, pages 613–623, St. Louis, MO, May 9-11 1983.

[18] J. Shaw, N. Albion, E. J. Hanker, and R. S. Teal. Higher harmonic control: Wind tunnel demonstration of fully effective vibratory hub forces suppression. *Journal of the American Helicopter Society*, 34(1):14–25, January 1989.

[19] Khanh Nguyen. *Higher Harmonic Control Analysis for Vibration Reduction of Helicopter Rotor Systems*. PhD thesis, University of Maryland, at College Park, 1989.

[20] Rendy P. Cheng, Colin R. Theodore, and Roberto Celi. Effects of two/rev higher harmonic control on rotor performance. *Journal of the American Helicopter Society*, 48(1):18–27, January 2003.

[21] Andreas P. F. Bernhard. *Smart Helicopter Rotor with Active Blade Tips*. PhD thesis, University of Maryland, College Park, MD, 2000.

[22] J. Hobbs. *Bristol Helicopters: A Tribute to Raoul Hafner*. Frenchay Publications, Bristol, UK, 1984.

[23] R.P. Pescara. Screw propeller of helicopter flying machines. U.S. Patent 1,449,129, March 1923.

[24] C. d'Ascanio. U.S. Patent 1,960,141, May 1934.

[25] C.H. Kaman. Aircraft of rotary wing type. U.S. Patent 2,455,866, December 1948.

[26] Andrew Z. Lemnios and Robert Jones. The servo flap – an advanced rotor control system. In *Proceedings of AHS and NASA Ames Research Center Vertical Lift Aircraft Design Conference*, San Francisco, CA, January, 17-19 1990.

[27] Fu-Shang (John) Wei. Design of soft torsion rotor systems at kaman aerospace corporation. In *American Helicopter Society 58th Annual Forum Proceedings*, pages 1264–1273, Montreal, Canada, June 11-13 2002.

[28] Inderjit Chopra. Perspectives in aeromechanical stability of helicopter rotors. *Vertica*, 14(4):457–508, 1990.

[29] L. Dadone, J. Cowan, and F. J. McHugh. Variable camber rotor study. Technical Report NASA-CR-166382, 1982.

[30] Friedrich K. Straub. A feasibility study of using smart materials for rotorcraft. *Smart Materials and Structures*, 5(1):1–10, 1995.

[31] A. Bueter, U.-C. Ehlert, D. Sachau, and E. Breitbach. Adaptive rotor blade concepts: Direct twist and camber variation. *Active Control Technology for Enhanced*

Performance Operational Capabilities of Military Aircraft, Land Vehicles and Sea Vehicles, page 11, June 2001.

[32] S. S. Houston. Identification of autogyro longitudinal stability and control characteristics. *Journal of Guidance, Control, and Dynamics*, 21(3):391–399, May-June 1998.

[33] Fu-Shang Wei and Robert Jones. Correlation and analysis for SH-2F 101 rotor. *Journal of Aircraft*, 25(7):647–652, July 1988.

[34] Robert A. Ormiston. Aeroelastic considerations for rotorcraft primary control with on-blade elevons. In *American Helicopter Society 57th Annual Forum Proceedings*, Washington, D.C., May 9-11 2001.

[35] Inderjit Chopra. Status of application of smart structures technology to rotorcraft systems. *Journal of the American Helicopter Society*, 45(4):228–252, October 2000.

[36] T.A. Millott and P.P. Friedmann. Vibration reduction in helicopter rotors using an actively controlled partial span trailing edge flap located on the blades. Technical Report CR 4611, NASA, June 1994.

[37] Judah Milgram, Inderjit Chopra, and Friedrich Straub. Rotors with trailing edge flaps: Analysis and comparison with experimental data. *Journal of the American Helicopter Society*, 43(4):319–332, October 1998.

[38] Nikhil A. Koratkar and Inderjit Chopra. Wind tunnel testing of a Mach-scaled rotor model with trailing-edge flaps. *Journal of the American Helicopter Society*, 47(4):263–272, October 2002.

[39] Jinwei Shen and Inderjit Chopra. Aeroelastic modeling of trailing-edge flaps with smart material actuators. In *Proceedings of the 41st AIAA/ASME/ASCE/AHS/ASC structure, structural dynamics, and materials conference*, AIAA-2000-1622, page 14, Atlanta, GA, April, 3-6 2000.

[40] Friedrich K. Straub and Bruce D. Charles. Aeroelastic analysis of rotors with trailing edge flaps using comprehensive codes. *Journal of the American Helicopter Society*, 46(3):192–199, July 2001.

[41] Bingling Wang, James D Baeder, and Rajneesh K Singh. A computational study of trailing-edge flap aerodynamics and acoustics. In *AHS International 55th Annual Forum Proceedings*, pages 1414–1435, Montreal, Canada, May 25-27 1999.

[42] Fu-Shang (John) Wei and Frank Gallagher. Servo-flap rotor performance flight testing and data identification. In *American Helicopter Society 57th Annual Forum Proceedings*, pages 596–603, Washington, D.C., May 9-11 2001.

[43] B. Rocconella and F. S. Wei. Wind tunnel model testing of the improved k-max servo-flap blade section. In *American Helicopter Society 57th Annual Forum Proceedings*, Washington, D.C., May 9-11 2001.

[44] P. R. Payne. Higher harmonic rotor control. *Aircraft Engineering*, 30(354):222–226, August 1958.

[45] A. Z. Lemnios and F. K. Dunn. Theoretical study of multicyclic control of a controllable twist rotor. Technical Report NASA-CR-151959, Moffett Field, California, April 1976.

[46] A. Z. Lemnios, H. E. Howes, and W. E. Nettles. Full scale wind tunnel tests of a controllable twist rotor. pages 1–17, Essington, PA, August 11-13 1976. American Helicopter Society Mideast Symposium on Rotor Technology.

[47] J. L. McCloud and A. L. Weisbrich. Wind-tunnel test results of a full-scale multicyclic controllable twist rotor. In *American Helicopter Society 34th Annual Forum Proceedings*, Washington, DC, May 1978.

[48] F. S. Wei and A. L. Weisbrich. Multicyclic controllable twist rotor data analysis. Final Report NASA-CR-152251, 1979.

[49] E.F. Prechtl and S.R. Hall. An X-frame actuator servo-flap actuation system for rotor control. In *SPIE Symposium on Smart Structures and Materials, Conference on Smart Structures and Integrated Systems*, San Diego, CA, March 1998.

[50] Taeoh Lee and Inderjit Chopra. Design of a bidirectional piezoelectric actuator for blade trailing-edge flap. In *SPIE Symposium on Smart Structures and Materials, Conference on Smart Structures and Integrated Systems*, number 4327-05, Newport Beach, CA, March 2001.

[51] Andreas Bernhard and Inderjit Chopra. Trailing edge flap activated by a piezo-induced bending-torsion coupled beam. *Journal of the American Helicopter Society*, 44(1):3–15, January 1999.

[52] Mark V. Fulton and Robert A. Ormiston. Hover testing of a small-scale rotor with on-blade elevons. *Journal of the American Helicopter Society*, 46(2):96–106, April 2001.

[53] P. Janker, V. Kloppel, F. Hermle, T. Lorkowski, S. Storm, M. Christmann, and M. Wettemann. Development and evaluation of a hybrid piezoelectric actuator for advanced flap control technology. In *Proceedings of the 25th European Rotorcraft Forum*, Rome, Italy, September 1999.

[54] Judah Milgram and Inderjit Chopra. Dynamics of an actively controlled plain trailing edge flaps system for a modern bearingless rotor. In *Twenty-third European Rotorcraft Forum*, Dresden, Germany, September 16-18 1997.

[55] N. Hariharan and J. G. Leishman. Unsteady aerodynamics of a flapped airfoil in subsonic flow by indicial concepts. *Journal of Aircraft*, 33(5):855–868, September-October 1996.

[56] A. Bagai and J. G. Leishman. Rotor free-wake modeling using a pseudo-implicit technique - including comparisons with experimental data. *Journal of the American Helicopter Society*, 40(3), July 1995.

[57] Friedrich K. Straub. Active flap control for vibration reduction and performance improvement. In *American Helicopter Society 51st Annual Forum Proceedings*, Fort Worth, TX, May 9-11 1995.

[58] Timothy F. Myrtle and Peretz P. Friedmann. Vibration reduction in rotorcraft using actively controlled trailing edge and issue related to practical implementation. In

AHS International 54th Annual Forum Proceedings, Washington, D.C., May 20-22 1998.

[59] Timothy F. Myrtle and Peretz P. Friedmann. New comprehensive time domain unsteady aerodynamics for flapped airfoils and its application to rotor vibration reduction using active control. In *American Helicopter Society 53rd Annual Forum Proceedings*, Virginia Beach, VA, April 29 - May 1 1997.

[60] Jianhua Zhang, Edward C. Smith, and K. W. Wang. An active-passive hybrid method for optimization of rotor blades with trailing edge flaps. In *Proceedings of the 40th AIAA/ASME/ASCE/AHS/ASC Structures, Structural Dynamics and Materials Conference*, AIAA-99-1222, St. Louis, Missouri, April 1999.

[61] Friedrich K. Straub and Ahmed A. Hassan. Aeromechanic considerations in the design of a rotor with smart material actuated trailing edge flaps. In *American Helicopter Society 52nd Annual Forum Proceedings*, Washington, D.C., June 4-6 1996.

[62] Wayne Johnson. Rotorcraft dynamics models for a comprehensive analysis. In *AHS International 54th Annual Forum Proceedings*, Washington, D.C., May 20-22 1998.

[63] Wayne Johnson. Rotorcraft aerodynamics models for a comprehensive analysis. In *AHS International 54th Annual Forum Proceedings*, Washington, D.C., May 20-22 1998.

[64] Theodore Theodorsen and I. E. Garrick. Nonstationary flow about a wing-aileron-tab combination including aerodynamic balance. Technical Report No. 736, NACA, 1942.

[65] Eric F Prechtl and Steven R Hall. Design of a high efficiency, large stroke, electromechanical actuator. *Smart Materials and Structures Journal*, 8(1):13–30, February 1999.

[66] Andreas Bernhard and Inderjit Chopra. Hover test of a Mach-scale rotor model with active blade tips. *Journal of the American Helicopter Society*, 47(4):273–284, October 2002.

[67] Jeanette J. Epps and Inderjit Chopra. In-flight tracking of helicopter rotor blades using shape memory alloy actuators. *Smart Materials and Structures Journal*, 10(1):104–111, February 2001.

[68] Jinwei Shen and Inderjit Chopra. A parametric design study for a swashplateless helicopter rotor with trailing-edge flaps. In *American Helicopter Society 58th Annual Forum Proceedings*, page 15, Montreal, Canada, June 11-13 2002.

[69] Roberto Celi. Stabilization of helicopter blades with severed pitch links using trailing-edge flaps. *Journal of Guidance, Control, and Dynamics*, 26(4):585–592, July-August 2003.

[70] Jinwei Shen and Inderjit Chopra. Aeroelastic stability of trailing-edge flap helicopter rotors. *Journal of the American Helicopter Society*, 48(4):236–243, October 2003.

[71] Marco Lovera, Patrizio Colaneri, Carlos Malpica, and Roberto Celi. Closed-loop aeromechanical stability analysis of hhc and ibc, with application to a hingeless rotor helicopter. In *Proceedings of the 29th European Rotorcraft Forum*, pages 43.1–43.14, Friedrichshafen, Germany, September 16-18 2003.

[72] E.G. Broadbent. The elementary theory of aero-elasticity, part iii. flutter of control surfaces and tabs. *Aircraft Engineering*, 12(13):145–153, May 1954.

[73] Y.C. Fung. *An Introduction to the Theory of Aeroelasticity*. Dover Publications, Inc, 1993.

[74] Theodore Theodorsen. General theory of aerodynamic instability and the mechanism of flutter. Technical Report No. 496, NACA, 1935.

[75] Edwin W. Aiken, Robert A. Ormiston, and Larry A. Young. Future directions in rotorcraft technology at ames research center. In *American Helicopter Society 56th Annual Forum Proceedings*, pages 1–21, Virginia Beach, VA, May 2-4 2000.

[76] Fu-Shang Wei. Advanced servo flap rotor using variable blade index angle control. In *Proceedings of 38th AIAA/ASME/ASCE/AHS/ASC Structures, Structural Dynamics, and Materials Conference and Exhibit, and AIAA/ASME/AHS Adaptive Structures Forum*, pages 876–884, Kissimmee, FL, April 7-10 1997.

[77] F.K Straub and B.D Charles. Preliminary assessment of advanced rotor/control system concepts (arcs). Technical Report 90-D03, USA AVSCOM, August 1990.

[78] MD Helicopters, Mesa, Arizona. *MD Explorer Technical Description*, August 1999.

[79] C Lanczos. *The variational Principles of Mechanics*. Dover Publications, Inc, New York, NY, 1970.

[80] Gunjit Bir and Inderjit Chopra. University of Maryland Advanced Rotor Code (UMARC) theory manual. Technical Report UM-AERO 94-18, Center for Rotorcraft Education and Research, University of Maryland, College Park, July 1994.

[81] Mark W. Nixon. *Aeroelastic Response and Stability of Tiltrotors with Elastically-Coupled Composite Rotor Blades*. PhD thesis, University of Maryland, College Park, MD, 1993.

[82] D.H. Hodges and E.H. Dowell. Nonlinear equations of motion for the elastic bending and torsion of twisted nonuniform blades. Technical Report TND-7818, NASA, December 1974.

[83] D.H. Hodges, R.A. Ormiston, and D.A. Peters. On the nonlinear geometry of euler-bernoulli beams. Technical Report TP 1566, NASA, April 1980.

[84] Judah H. Milgram. *A Comprehensive Aeroelastic Analysis of Helicopter Main Rotors with Trailing Edge Flaps for Vibration Reduction*. PhD thesis, University of Maryland, College Park, 1997.

[85] Ahmed A. Hassan, Friedrich K. Straub, and Kevin W. Noonan. Experimental/numerical evaluation of integral trailing edge flaps for helicopter rotor applications. In *American Helicopter Society 56th Annual Forum Proceedings*, pages 84–102, Virginia Beach, VA, May 2-4 2000.

[86] Anita L. Tracy and Inderjit Chopra. Aeroelastic analysis of a composite bearingless rotor in forward flight using a improved warping model. *Journal of the American Helicopter Society*, 40(3):35–51, 1995.

[87] Hyeonsoo Yeo and Inderjit Chopra. Modeling issues related to vibration prediction of a coupled rotor/fuselage system. In *Proceedings of the 38th AIAA/ASME/ASCE/AHS/ASC Structures, Structural Dynamics and Materials conference*, Kissimmee, FL, April 1997.

[88] Hyeonsoo Yeo. *A comprehensive vibration analysis of a coupled rotor/fuselage system*. PhD thesis, University of Maryland, College Park, MD, 1999.

[89] Gopal K. Gupta, Ron Sacks-Davis, and Peter E. Tischer. A review of recent developments in solving odes. *Computing Surveys*, 17(1):5–47, 1985. March.

[90] W. Johnson. Self-tuning regulators for multicyclic control of helicopter vibration. Technical Report TP 1996, NASA, March 1982.

[91] I. Chopra and J. L. McCloud. A numerical simulation study of open-loop, closed-loop and adaptive multicyclic control systems. *Journal of the American Helicopter Society*, Jan 1983.

[92] Khanh Nguyen, Dan Lauzon, and Vaidyanathan Anand. Computation of loads on the McDonnell Douglas advanced bearingless rotor. In *American Helicopter Society 50th Annual Forum Proceedings*, pages 337–346, Washington, D.C., May 11-13 1994.

[93] Michael McNulty, Stephen Jacklin, and Benton Lau. A full-scale test of the mc-donnell douglas advanced bearingless rotor in the nasa ames 40- by 80-ft wind tunnel. In *American Helicopter Society 49th Annual Forum Proceedings*, pages 1535–1544, St. Louis, MO, May 19-21 1993.

[94] Khanh Nguyen, Michael McNulty, Vaidyanathan Anand, and Dan Lauzon. Aeroe-lastic stability of the Mcdonnell Douglas advanced bearingless rotor. In *American Helicopter Society 49th Annual Forum Proceedings*, pages 1283–1290, St. Louis, MO, May 19-21 1993.

[95] Wayne Johnson. Technology drivers in the development of camrad ii. In *American Helicopter Society Aeromechanics Specialists Conference*, San Francisco, CA, January 19-21 1994.

[96] Khanh Nguyen and Benton Lau. Dynamics of the mcdonnell douglas large scale dynamic rig and dynamic calibration of the rotor balance. Technical Memorandum 108855, NASA Ames Research Center, Moffett Field, California 94035-1000, Oc-tober 1994.

[97] James M. Wang. Correlation of vibratory hub loads for a Skiorsky full-scale bear-ingless main rotor. In *American Helicopter Society 50th Annual Forum Proceed-ings*, Washington, D.C., May 11-13 1994.

[98] S. Dawson and F.K. Straub. Design, valdiation, and test of a model rotor with tip mounted active flaps. In *American Helicopter Society 50th Annual Forum Pro-ceedings*, Washington, D.C., May 11-13 1994.

[99] Judah Milgram and Inderjit Chopra. A parametric design study for actively controlled trailing edge flaps. *Journal of the American Helicopter Society*, 43(2):110–119, April 1998.

[100] Sighard F. Hoerner and Henry V. Borst. *Fluid-Dynamic Lift*, chapter Characteristics of Airplane Control Surfaces, pages 9–1–9–30. Hoerner fluid dynamics, Bakersfield, CA, 1975.

[101] Kenneth S. Brentner, Guillaume Perez, Guillaume A. Bres, and Henry E. Jones. Toward a better understanding of maneuvering rotorcraft noise. In *AHS International 58th Annual Forum Proceedings*, page 11, Montreal, Canada, June 11-13 2002.

[102] Beatrice Roget and Inderjit Chopra. Individual blade control methodology for a rotor with dissimilar blades. *Journal of the American Helicopter Society*, 48(3):176–185, July 2003.